QUANTIFYING INFORMATION AND UNCERTAINTY OF ROCK PROPERTY ESTIMATION FROM SEISMIC DATA

A DISSERTATION
SUBMITTED TO THE DEPARTMENT OF GEOPHYSICS
AND THE COMMITTEE ON GRADUATE STUDIES
OF STANFORD UNIVERSITY
IN PARTIAL FULFILLMENT OF THE REQUIREMENTS
FOR THE DEGREE OF
DOCTOR OF PHILOSOPHY

Isao Takahashi
May 2000

I certify that I have read this dissertation and that in my opinion it is fully adequate, in scope and quality, as a dissertation for the degree of Doctor of Philosophy.

Gary Mavko
(Principal Adviser)

I certify that I have read this dissertation and that in my opinion it is fully adequate, in scope and quality, as a dissertation for the degree of Doctor of Philosophy.

Amos Nur

I certify that I have read this dissertation and that in my opinion it is fully adequate, in scope and quality, as a dissertation for the degree of Doctor of Philosophy.

Jack Dvorkin

Approved for the University Committee on Graduate Studies:

Abstract

Geophysical prospecting consists of making a quantitative inference about subsurface properties from geophysical measurements. Due to many ineluctable difficulties, observed data are almost always insufficient to uniquely specify the rock properties of interest. Hence, inevitable uncertainty remains after the estimation. The sources of the uncertainty arise from many factors: inconsistency in data acquisition conditions, insufficient available data as compared to the subsurface complexities, limited resolution, imperfect dependence between observed data and target rock properties, and our limited physical knowledge. While the uncertainty has been identified for a long time, quantitative framework to discuss the uncertainty has not been well established.

The objective of this dissertation is to *quantify uncertainty of rock property estimation* and to reduce it by using multiple seismic observables. Using existing laboratory data and rock physics model parameters, we establish the general relationships between rock properties and pairs of seismic attributes. We show how optimal selections of seismic attributes allow us to better distinguish different rock property effects. One of the novel innovations in this work is to combine statistical formulations—information theory and Bayes decision theory—with rock physics models to quantitatively describe the dependence of seismic attributes on several important rock properties. Various sources of uncertainty about rock property estimation are quantified using the developed formulations. Furthermore, We propose a method of combining stochastic simulations and Bayes inversion to quantify the uncertainty about the dependence between seismic observables and target rock properties, caused by ignorance of other rock properties. We apply this method to explore scale effects

on sand/shale ratio estimation from seismic reflectivity. One of the new results of this investigation is to show from the full probability density function that the effective medium average tends to overestimate the sand/shale ratio when reservoirs are randomly layered. The proposed framework of quantifying information given by seismic data will serve as a *decision making guideline* in various exploration stages.

Acknowledgements

I have been blessed with friends and professors during my stay at Stanford. I would like to thank all the people in and out of the school who made my last student life pleasant and successful. Without their encouragement and support, this dissertation would have been impossible.

I wish to express my foremost gratitude to my adviser, Gary Mavko. His having the door open to me for stimulating discussions, generosity with new ideas, and always pinpointing and cheering advices have kept me highly motivated for research. Gary showed me how to give such an entertaining lecture and how to live as a researcher in such an enjoyable way.

Amos Nur's everlasting hunger for new researches and his ways to ask questions taught me how to anticipate what happens next. He attracted many good students and visitors to SRB from all over the world, whom I associated with. I greatly appreciate the comments and suggestions from Jack Dvorkin. Many ideas of this dissertation occurred to me from the discussions in the seminars led by Jack, as well as the class Jack taught and I TA'ed. I am also indebted to Jerry Harris who first accepted me to join Stanford and has been supporting me ever since. Jon Claerbout and Biondo Biondi allowed me to participate in some of the activities of Stanford Exploration Project, and have reminded me to be open-minded to different perspectives of exploration geophysics. Special thanks go to Tapan Mukerji, who always gave clearcut answers to all the questions I brought every two hours everyday for the past three years. Margaret Muir has been such a great help whenever I needed some assistance.

I am grateful to all my friends in Stanford Rock Physics Laboratory. Keeping company with the friends from diverse background disciplines and cultures was an exciting and priceless experience, and has made my viewpoint broader than before. The sunny Californian sky and the even sunnier fellows, Alex, Andres, Carlos, Diana, Elizabeth, Emma, Ezequiel, Haibin, Madhumita, Mario, Mike, Per, Sandra, Wendy, and Youngseuk, have mitigated the stress from my work.

Noboru Tezuka of JNOC had propelled me to pursue the higher educational opportunity, before I jumped over the Ocean to Stanford in 1997. My dear geologists, Yasuhisa Kanehara, Hideki Hayakawa, and Takeshi Nakanishi, had opened my rather engineer-like eyes to the wonderland of earth sciences, in front of seismic sections and over drinks.

Last but not least, I could not thank more to my mother, Choko, and my father, Toshio, for instilling in me the importance of learning and diligence, and for their unceasing assistance. They have been my great spiritual support.

The data from the Alba oil field used in chapter 7 of this dissertation was provided by Chevron U.K. and the Alba partners. In particular, I acknowledge John Toldi and Rex Hanson from Chevron for their helpful information about the data. Financial support of this work was from JNOC and the sponsors of Stanford Rock Physics and Borehole Geophysics Project.

Contents

List of Tables

List of Figures

Chapter 1

Introduction

The objective of geophysical measurements is to estimate spatial distributions of subsurface properties. In exploration geophysics, subsurface properties of interest include the reservoir architecture, porosity, fluid saturation, pore pressure, lithology, and permeability. In the procedure of the subsurface property estimation, it is usual that geophysicists first produce spatial distributions of seismic attributes from observed seismic data, such as seismic velocity, impedance, amplitude, and traveltime, through data processing and inversion. Then from the derived seismic attributes, we estimate subsurface properties of interest using rock physics theories and/or statistical methods, along with well-log data. In spite of our hope and efforts of accurately estimating subsurface properties, the estimation—both the first process from observed seismic data to seismic attributes, and the second from seismic attributes to subsurface properties—is almost always non-unique and subject to a significant amount of uncertainty (Tarantola and Valette, 1982; Mavko and Mukerji, 1998; Claerbout, 1999). The uncertainty arises because of many inevitable causes; inconsistent data acquisition conditions, limited availability of data as compared to the subsurface heterogeneity, restricted bandwidth of seismic waves, imperfect dependence between seismic attributes and subsurface properties, insufficient rock physics knowledge, and many others. The uncertainty in geophysical prospecting has been identified for a long time. However, until recently, data quality had been too poor and available data had been too sparse to

quantitatively discuss the uncertainty. Hence, quantitative framework to describe the uncertainty has not been well established.

One simple but powerful way of increasing information and therefore reducing uncertainty about rock properties, is using more than one seismic attribute for an estimation. Recent advancements in seismic data acquisition and processing techniques have enabled us to obtain non-conventional seismic data in addition to conventional P-P reflection profiles, and thereby provide us with multiple seismic attributes. For example, a new seismic tool of ocean bottom multicomponent receivers enables us to obtain P-S converted wave data and provides us with new seismic attributes of the P-S reflectivity and the P-S pseudo-impedance. Combinations of different seismic observables convey more information about subsurface properties than single observables. The goal of this thesis is to understand the relation between rock properties and multiple seismic attributes, and to quantify their dependence.

Chapter 2 explores the relationships between rock properties and combinations of seismic attributes. Rock physics research, both theoretical and experimental, has enabled us to understand the relations between rock properties and seismic velocities (Hilterman, 1998; Mavko et al., 1998). However, the effects of rock properties on other attributes and on the dependences between attributes are much less investigated. In order to understand the rock property effects on several combinations of seismic attributes, we use laboratory data samples from various geological conditions. Our results show that rock properties indistinguishable by an attribute pair can be distinguished by optimal selection of a different attribute pair. Moreover, we show that some rock physics model parameters describe well the experimental relations between rock properties and seismic attributes, and help us extrapolate the limited laboratory measurements. The established relationships between rock properties and seismic attributes will enable us to better interpret rock properties from multiple seismic observables. In chapter 3, by focusing on the dependences of $V_p - V_s$ relations on lithology, we investigate how the relation between seismic attributes can tell us about the microstructures of rocks.

Due to the non-unique relation between observed seismic data and objective rock properties, any estimates of rock properties derived from seismic data is no more than one possible answer satisfying given data and given conditions. Data available to us almost never

give sufficient information to specify the subsurface properties of interest. Hence, quantitatively understanding the dependence between seismic attributes and rock properties—how seismic data constrain our information about target rock properties—is crucial. Chapter 4 explores statistical formulations of information theory and Bayes decision theory to describe the dependence between seismic attributes and rock properties of interest (Middleton, 1960; Ash, 1965; Fukunaga, 1972; Duda and Hart, 1973). The formulations using probability density functions enable us to integrate uncertainties arising from various causes, and to evaluate the information about rock properties provided by seismic data. The results show that acquired data, physical theories, and geological knowledge are sources of information about rock properties, which reduce uncertainty of their estimation. However, data manipulations do not bring about any new information if the process is a Markov chain (Cover and Thomas, 1991).

Information provided by seismic data is influenced by many factors. The factors include type and number of seismic attributes, sensitivity of the attributes to the objective properties, natural variability of the target rock properties, and accuracy of derived seismic attributes. In chapter 5, we apply the formulation developed in chapter 4 and quantitatively discuss how information carried by seismic data is influenced by these factors. We show that the selection of optimal attributes is variable, depending on target rock properties. No single choice of attributes is optimal for estimating all rock properties. The proposed framework of quantifying information given by seismic data will serve as a *decision making guideline* in various exploration stages.

Chapter 6 proposes a method of evaluating uncertainty about rock property estimation caused by ignorance of other properties, specifically, the scale effect on the relation between seismic reflectivity and the sand/shale ratio of reservoirs. Any seismic properties is dependent on the scale of heterogeneity of the media (Mukerji, 1995). Hence, ignorance of the scale increases uncertainty about the rock property estimation. A combination of stochastic simulation and seismic forward modeling enables us to non-parametrically realize Bayes inversion. The method establishes a bivariate probability density function to describe the relation between seismic reflectivity and the sand/shale ratio when scale of heterogeneity of a reservoir is variable (Tarantola and Valette, 1982; Gastaldi et al., 1998). The generality of the proposed method makes it applicable to any estimation problems

which are accompanied by uncertainty.

In chapter 7, we explore well log and seismic data from the North Sea and investigate how the P-S converted wave seismic data constrain rock properties as compared to the conventional P-P data. Results from quantitative investigation of the well data show that a combination of P-P near and far offset impedances is as informative as a combination of P-P near and P-S impedances, when the measurements are error-free. However, a comparison of the impedances derived from seismic data reveals that the P-S impedance is more informative, confirming the effectiveness of P-S surveys in reservoir characterization in the field investigated in this study.

Chapter 2

Interpreting Rock Properties on Seismic Attribute Domains

Abstract

Developments in seismic data acquisition and processing, especially in multi-component techniques, have enabled us to extract various seismic attributes from seismic data than before. Hence, physical understanding of the relation between seismic attributes and rock properties is becoming more crucial for seismic interpretation.

In this chapter, we investigate existing laboratory and well data in relation to rock physics models so that we may better understand the effect of rock property changes on various seismic attributes and the interdependence between attributes. Our results show that a combination of seismic attributes enables us to interpret rock properties even when more than one rock property is variable. Furthermore, rock properties indistinguishable in some attribute domains can be distinct by optimal selection of seismic attributes. We find that the $V_p - V_s$ and AVO attribute combinations can predict pore fluids even when other rock properties are uncertain. On the other hand, combinations of acoustic impedance and elastic impedance (non-zero offset impedance) may separate two geological processes, diagenesis and textural variation.

We then explore the dependence of several rock physics model parameters, pore stiffness, Biot coefficient, pore aspect ratio, and critical porosity, with respect to the rock property changes. We find that contours of pore stiffness and Biot coefficient approximate textural variation, whereas constant-aspect ratio and constant-critical porosity curves mimic diagenetic trends. The rock physics model parameters help us extend our understanding of rock physics to various attribute domains and serve as physical bases in interpreting rock properties from seismic attributes.

2.1 Introduction

2.1.1 Motivation

Estimating the spatial distribution of heterogeneous reservoir properties, such as porosity, lithology, and pore fluids, from seismic data is critical for economic oil field development and management. For the purpose of seismic interpretation *away from wells* where only seismic data are available, the relation between rock properties and seismic properties must be well established. Effects of individual rock properties on P-wave velocity, as well as on bulk modulus, have been studied extensively in rock physics (Mavko et al., 1998; Hilterman, 1998). Figure 2.1 concisely summarizes effects of various rock properties on the seismic velocity.

When seismic attributes are influenced by more than one rock property, as in many cases, a single seismic attribute may not be enough to predict a particular objective rock property reliably. For example, porosity estimation from seismic velocity becomes difficult when the clay content is variable. Furthermore, predictability of fluid saturation from velocity suffers when the pore pressure is unknown.

Use of two or more seismic attributes in rock property estimation allows us to extract more information from seismic data than single attributes. During the past decade, the improvements in data acquisition and processing methods have enabled us to extract seismic information beyond conventional zero-offset P-wave reflectivity. The recently developed data acquisition methods include long offset surveys to obtain AVO attributes for large

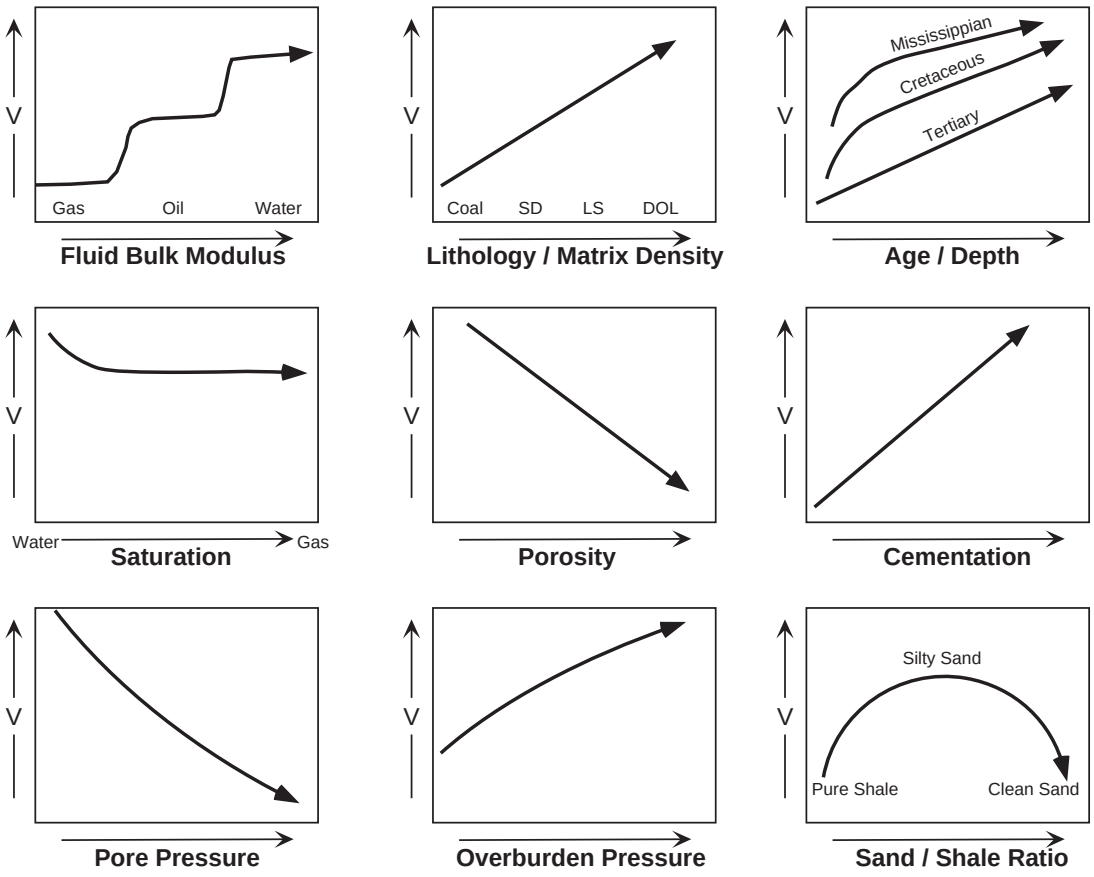

Figure 2.1: Schematics of various rock property effects on seismic velocity. (Modified from Hilterman (1998))

incidence angles, ocean bottom surveys to acquire converted wave P-S data, and 9 component land surveys to record full elastic wavefields. Thanks to this progress, many kinds of seismic attributes are becoming available for rock property estimation. However, the inter-relations among different attributes are less understood, and only empirical statistical correlations of seismic attributes and target rock properties at calibration wells are usually emphasized in seismic reservoir property estimation (Kalkomey, 1997).

In this chapter, we extend existing rock physics knowledge of reservoir properties to various seismic attributes and pairs of attributes. Using well-log and laboratory data, we explore the signatures of important rock properties on various seismic attribute domains, so that we may better understand how the rock properties influence the interdependence

among these attributes. The rock properties that we investigate include diagenesis, textural variation, pressure, and pore fluids. We will see that combinations of seismic attributes help us to interpret rock properties more reliably, even when more than one rock property is variable. Our results show that rock property effects indistinguishable in some attribute domains can be distinctive by optimal selection of attributes. Furthermore, we interpret the rock property effects in terms of several rock physics model parameters, such as pore stiffness, Biot coefficient, pore aspect ratio, and critical porosity. The model parameters provide us with the physical validation of the rock property effects in seismic attribute domains identified in the laboratory data, and enable us to extend laboratory observations to field seismic attributes.

In chapter 4, we will introduce statistical formulations, information theory and Bayes decision analysis, to quantify the dependence between rock properties and seismic attributes. Combination of the results from this chapter—*rock physics*—and chapter 4—*quantitative formulation*—will provide a guideline for quantitative interpretation of seismic attributes.

2.1.2 Chapter Outline

In section 2.2, we summarize effects of four important rock properties (*i.e.*, diagenesis, textural variation, pressure, and pore fluids) on the $K-\phi$ (bulk modulus - porosity) domain, where many rock physics theories have been investigated and many rock property effects are relatively well understood. Section 2.3 explores effects of the individual rock properties across five different seismic attribute domains. We use laboratory sandstone data from the Gulf of Mexico measured by Han (1986) and show how porosity, clay, pressure, and saturation can be distinguished in different attribute domains. We also investigate the rock property seismic signatures in North Sea sandstone data and find similar characteristics as identified in Han's data. In section 2.5, we introduce several rock physics model parameters and summarize their relationships with the rock properties in the $K-\phi$ domain. We then extend the model parameters to seismic attribute domains so that we may better understand the effects of rock property changes in each domains.

2.2 Effect of Rock Property Changes on Bulk Modulus and Porosity

Various rock property effects on the $K - \phi$ (Bulk modulus - porosity) relation have been extensively studied by many rock physicists (Mavko et al., 1998; Hilterman, 1998). Figure 2.2 shows typical examples of the $K - \phi$ dependence of four major rock property changes identified in Han's sandstone data (1986). The samples are well-consolidated sandstones from the Gulf Coast. The samples have various porosities (3% to 30%), as well as various clay contents (0% to 55%). Ultrasonic measurements of these samples were performed at a range of effective pressures from 5 MPa to 40 MPa in both dry and water-saturated conditions.

We divide the entire data into subgroups and investigate the effect of each single rock property on the $K - \phi$ relation, while other rock properties are maintained constant. In the data set, decreasing porosity with the remaining properties (*i.e.*, clay content, pressure, and pore fluid) maintained constant mimics trends of increasing diagenesis (*e.g.*, cementation and mechanical compaction). Similarly, increasing the clay content within a sub-group having the same sampled depth, effective pressure, and pore fluid, but with variable porosities, approximates textural variation (*i.e.*, good sorting to poor sorting).

When the variation of porosity is controlled by diagenesis, the $K - \phi$ relation tends to have a steep slope, as shown in Figure 2.2-A. This effect can be described by the modified Voigt line (Nur et al., 1995) or by Han's regressions (1986). On the other hand, when the variation of porosity is due to the textural variation, the bulk modulus is less sensitive to the porosity. The $K - \phi$ relation is flatter and can be mimicked by the modified lower Hashin-Shtrikman bound (Hashin and Shtrikman, 1963; Dvorkin and Nur, 1996; Avseth et al., 1998a; Avseth et al., 2000) as shown in Figure 2.2-B. The effective pressure trend in the $K - \phi$ relation is quasi-vertical, since increasing an increment of effective pressure stiffens rocks with a little decrease of the porosities (Figure 2.2-C). Furthermore, the pore fluid trend is vertical in the $K - \phi$ domain; a change in the fluid bulk modulus does not directly influence the porosity, but it changes the bulk modulus of the rock (Figure 2.2-D).

The four rock physics effects are schematically summarized in Figure 2.3. According

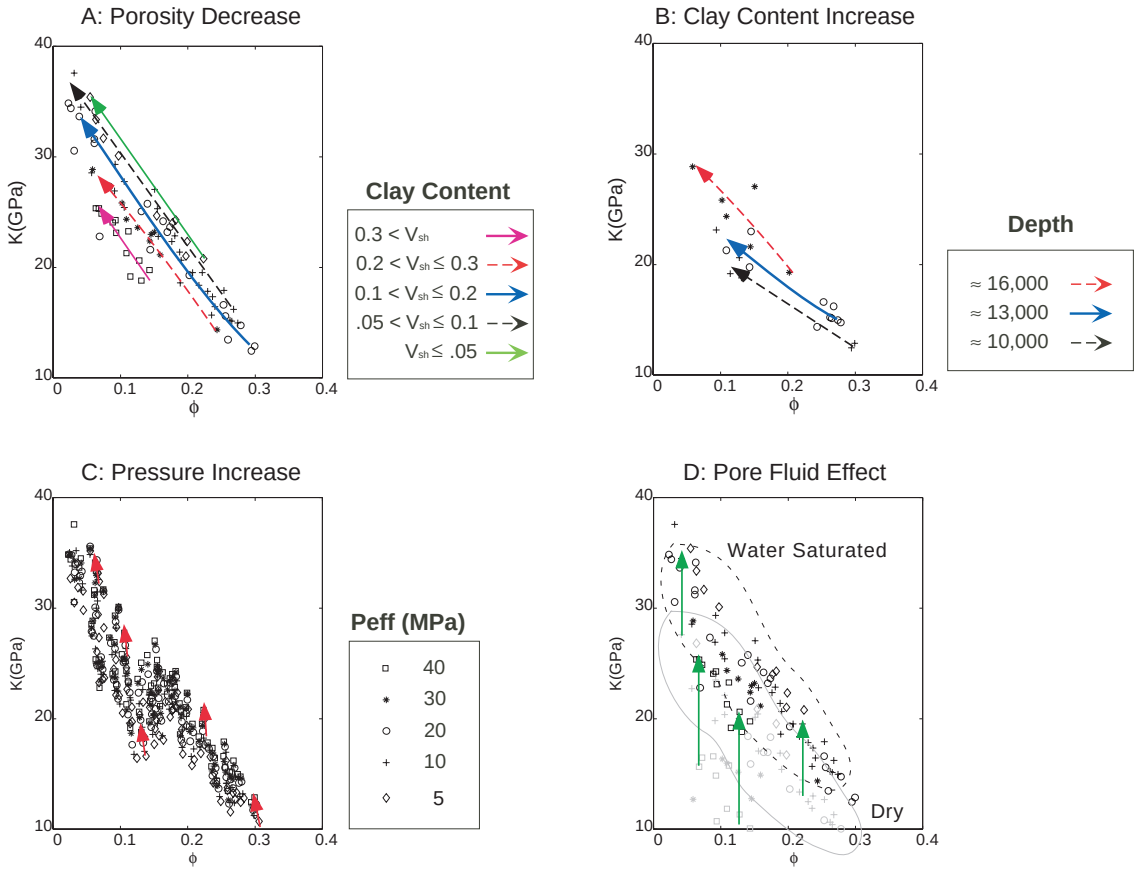

Figure 2.2: Effects of rock property changes on the $K - \phi$ relation in Han's sandstone: A) Diagenesis effect (Increasing depth) for different clay content subgroups (water-saturated samples with an effective pressure of 40 MPa), B) Textural variation (Increasing clay content) for different depth subgroups (water-saturated samples with an effective pressure of 40 MPa), C) Pressure (Increase effective pressure), and D) Pore fluid (From dry to water-saturated samples at an effective pressure of 40 MPa).

to the critical porosity model (Nur et al., 1991; Nur, 1992; Nur et al., 1995), rocks generally have porosities lower than their critical porosities, ϕ_c, where they change from the suspension state to load-bearing state. The critical-porosity point and the mineral point are the high-porosity and zero-porosity end members of these rocks, respectively. The $K - \phi$ relation follows a linear trend from the critical porosity point to the mineral point, if diagenesis controls the porosity decrease. In contrast, the $K - \phi$ relation can be approximated by modified lower Hashin-Shtrikman bounds when the porosity is controlled by the textural

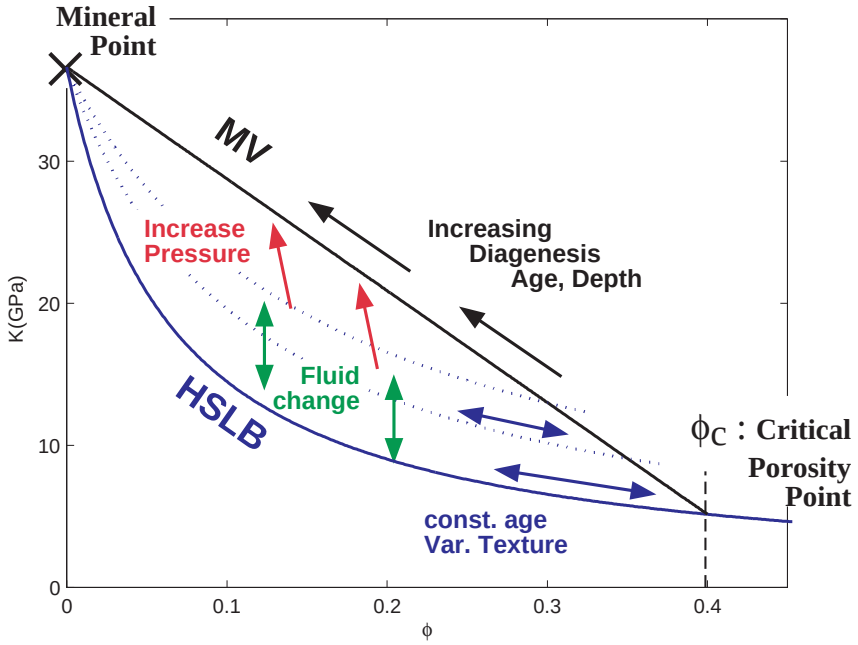

Figure 2.3: Effects of four rock property changes on the $K - \phi$ relation. Two important geological effects, diagenesis and texture, have different slopes; Diagenesis, mimicked by the modified Voigt model, produces a steeper slope than the textural variation, mimicked by the modified Hashin-Shtrikman bounds. Pressure varies bulk stiffness with little influence on the porosity, while fluid only affects the bulk stiffness. MV and HSLB denote the modified Voigt model and the Hashin-Shtrikman lower bound, respectively.

variation. Effective pressure increases the bulk modulus with small decrease of the porosity. The pore fluid only influences the bulk modulus without any change of the porosity.

A combination of porosity and bulk modulus enables us to interpret these different rock properties, since each effect has a different slope in the $K - \phi$ domains. However, when only the bulk modulus is available and two or more rock properties are variable, the rock property interpretation is non-unique.

The rock physics effects on the $V_p - \phi$ domain are similar to those on the $K - \phi$ domain, since V_p and K are usually well correlated. Hence, these effects can also be characterized by arrows of different slopes as in Figure 2.4. Measurement of V_p only may not be enough to identify the types of rock property causing the velocity change, again. For example, high-porosity, cemented, and well-sorted sandstones may have similar V_p as low-porosity,

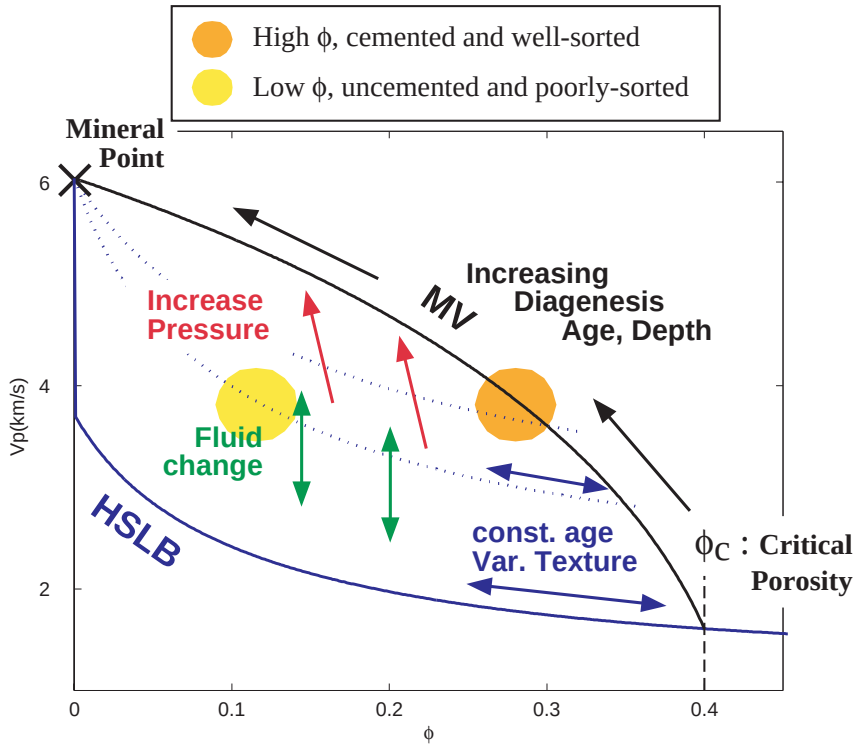

Figure 2.4: Effects of four rock property changes on the $V_p - \phi$ relation. High-porosity, cemented, and well-sorted sandstones (orange) may have similar V_p as low-porosity, un-cemented, and poorly-sorted sandstones (yellow), as indicated by two circles.

un-cemented, and poorly-sorted sandstones, as indicated by two circles in Figure 2.4. These two facies are indistinguishable only from V_p.

2.3 Effects of Rock Properties on Seismic Attribute Pairs in Gulf Coast Data

In this section, we derive various seismic attributes from Han's measurements of P- and S-wave velocities and density, to investigate the effects of rock properties on various combinations of attributes. Five typical pairs of attributes are investigated, including, $V_p - V_s$, $\lambda - \mu$ (Lamé's constant-shear modulus), $AI_p - V_p/V_s$ (P-wave acoustic impedance-V_p/V_s ratio), $AI_p - EI(30)$ (P-wave acoustic impedance - Elastic impedance at 30 degree angle

of incidence (Mukerji et al., 1998)), and $G - RC(0)$ (AVO gradient-AVO intercept). These attributes are nonlinear transforms of the measured basic observations, namely, V_p, V_s, and density. For AVO attributes representing boundary properties, homogeneous shaly caprock is assumed. Elastic and acoustic impedances, AVO coefficients, and P- and S-velocities can be directly derived from seismic data, and hence are of practical importance.

Our purpose is extending our understanding about the effects of the four rock properties discussed in Figure 2.3 to various seismic attribute domains, so that we may better interpret the rock properties from observed seismic attributes. We investigate rock physics effects on multiple seismic attribute domains, which may be expressed as

$$\left.\frac{\partial Attributes}{\partial RockProp.}\right|_{const.otherprop.} \tag{2.1}$$

i.e., partial derivative of seismic attributes with respect to a rock property, while other rock properties are maintained constant. Using multiple attributes, we hope to distinguish the individual rock property effects, which is impossible from only one seismic observable. Later in section 2.4 we perform a similar investigation on another sandstone data from the North Sea, and compare the results with this section.

2.3.1 Diagenesis and Texture

We first investigate effects of two major classes of geological processes that affect porosity—diagenesis and textural variation—on the five pairs of attributes, namely, $V_p - V_s$, $\lambda - \mu$, $AI_p - V_p/V_s$, $AI_p - EI(30)$, and $G - RC(0)$. As shown in Figure 2.2-A, we assume that the diagenetic trend in Han's data is mimicked by varying porosity with the other properties maintained constant. Similarly, we presuppose that the textural variation in Han's data is mimicked by varying the clay content with the depth maintained constant, as in Figure 2.2-B.

Effect of Porosity (Diagenesis)

In Figure 2.5, the arrows show the overall trajectories of the points when porosity is decreased in each subgroup having the same clay content and the same measurement conditions (water-saturated samples at a constant effective pressure of 40 MPa). This effect may be expressed as $-\frac{\partial \mathbf{A}}{\partial \phi}|_{clay}$, where $\mathbf{A}$ is each pair of attributes.

In the cross-plots of $V_p - V_s$ and $G - RC(0)$ in Figures 2.5-A and E, the parallel and slightly overlapped arrows show the stationarity of the porosity effect in these domains with respect to the clay content. In contrast, the directions of the arrows are radially variable in the $\lambda-\mu$ domain (Figure 2.5-B); data corresponding to higher clay content are characterized by a steeper slope of λ with respect to μ. The $AI_p - V_p/V_s$ plot (Figure 2.5-C) shows that the V_p/V_s ratio decreases when porosity decreases. The nearly vertical arrows in $AI_p - EI(30)$ demonstrate that $EI(30)$ is not sensitive to porosity changes in this data set (Figure 2.5-D).

Effect of Clay Content (Texture)

The dependence of attributes on clay contents in different depth subgroups is shown by arrows in Figure 2.6. These lines may be expressed as $\frac{\partial \mathbf{A}}{\partial clay}|_{depth/age}$.

In the $V_p - V_s$ and $G - RC(0)$ domains (Figures 2.6-A and E), the orientation of the clay effect is similar to the effects of porosity in Figure 2.5. In contrast, in the $\lambda - \mu$, $AI_p - V_p/V_s$, and $AI_p - EI(30)$ domains (Figures 2.6-B,C, and D), the clay effects are oblique to the porosity effects, when the sample is relatively shallow. This difference implies the separability of the porosity and clay effects in these domains for shallow rocks. Figure 2.6 shows that the V_p/V_s ratio for shallow samples increases when the clay content increases. This observation is consistent with the dependence of the V_p/V_s ratio on sorting identified by Avseth et al. (1998a); poor sorting increases the V_p/V_s ratio. For deep samples, however, the V_p/V_s ratio slightly decreases as the clay content increases.

For the $\lambda-\mu$ and $AI_p-EI(30)$ domains, in which the data are more scattered than in the other three, the contours of porosity and clay content are illustrated as shown in Figure 2.7. For the $AI_p - EI(30)$ domain (Figures 2.7-A and C), porosity decreases towards the upper right, and the clay content increases towards the right. These results show that in Han's data, the elastic impedance is a good indicator of shaliness, while acoustic impedance is more dependent on porosity. In contrast, in the $\lambda - \mu$ domain (Figures 2.7-B and D),

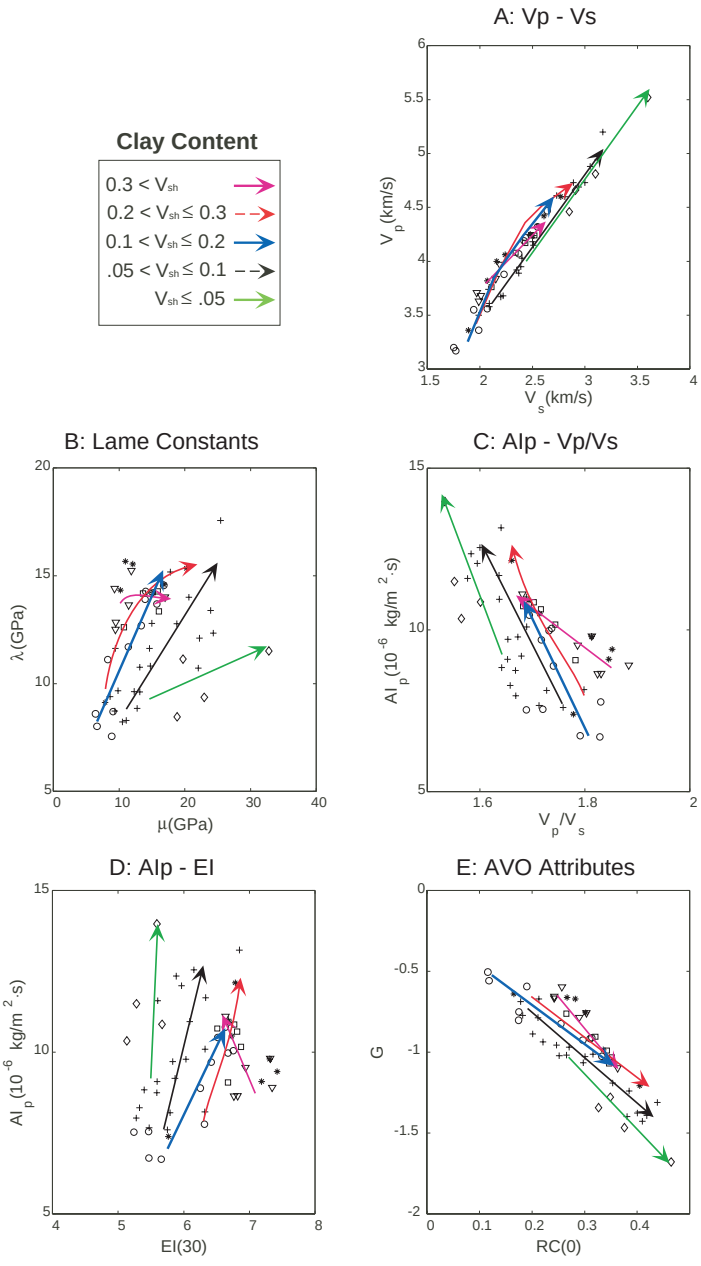

Figure 2.5: The effects of porosity changes on combinations of seismic attributes in water-saturated conditions at an effective pressure of 40 MPa. Arrows show the trajectories of decreasing porosity in each subgroups with the same clay contents. In the $\lambda - \mu$ and $AI_p - EI(30)$ domains, the porosity effects depend on the clay contents. In contrast, the porosity effects are uniform throughout all clay contents in the $V_p - V_s$ and AVO domains.

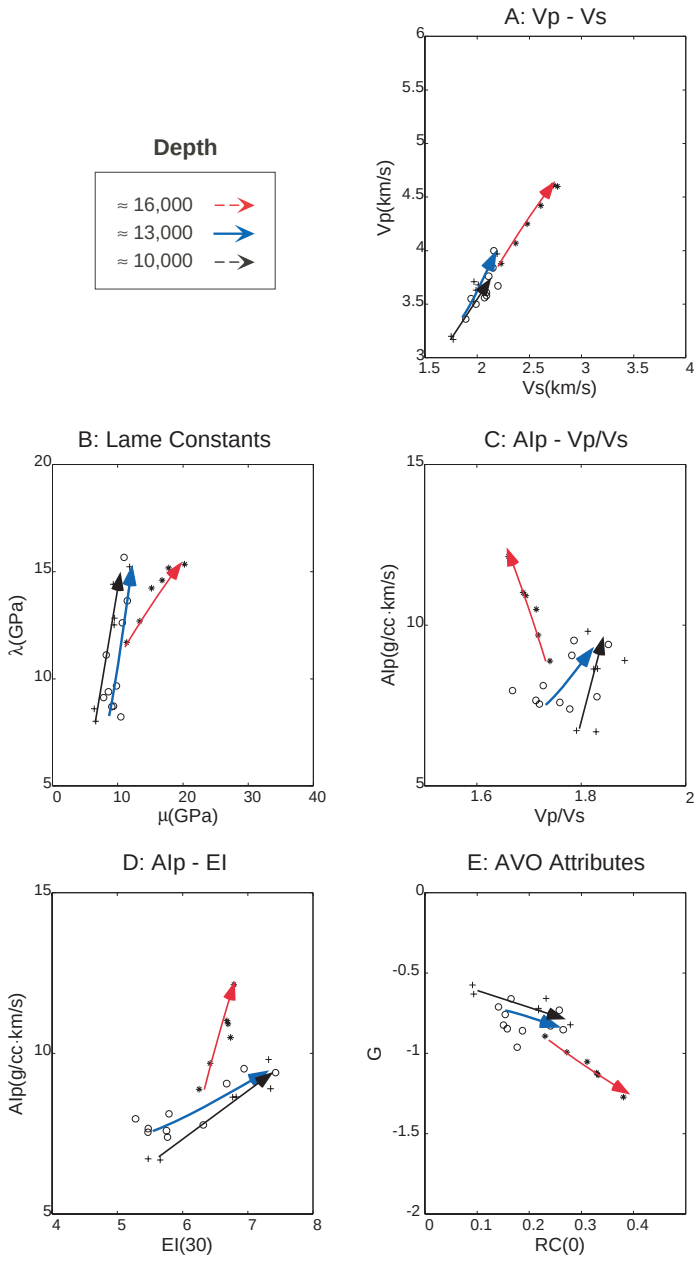

Figure 2.6: Clay content dependence on combinations of seismic attributes in water-saturated conditions at an effective pressure of 40 MPa. Arrows show the trajectories of clay effects on each depth subgroup. In the $\lambda - \mu$ and $AI_p - EI(30)$ domains, the clay effects can be normal to the porosity effects, while the clay and porosity have similar effects on the other three domains.

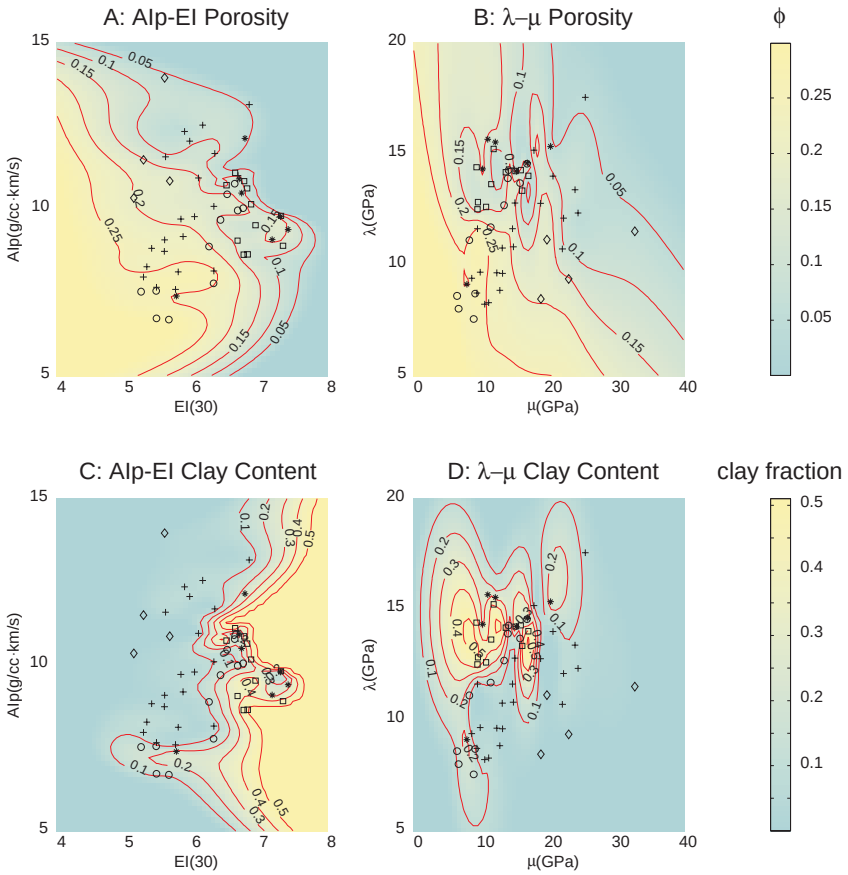

Figure 2.7: Contour maps of porosity and the clay content in the $AI_p - EI$ and $\lambda - \mu$ domains

porosity decreases towards the upper right and clay content increases towards the upper left. These contours are *purely empirical*, and therefore, only valid within the data analyzed here.

2.3.2 Pressure Change

We discuss the dependence of seismic attributes on effective pressure, as shown in Figure 2.8. The arrows show the trajectories of increasing the effective pressure in each sample.

In all domains, the pressure effects are small compared to the total variation caused by

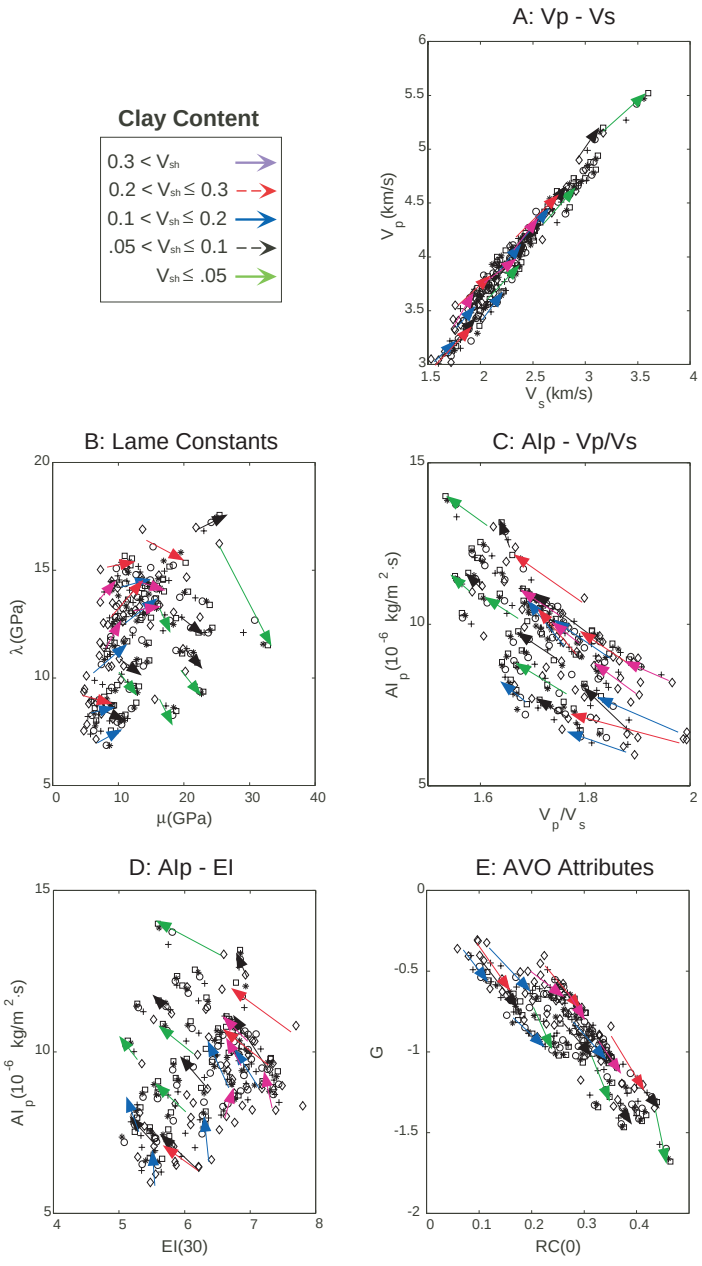

Figure 2.8: Effective pressure dependence of combinations of seismic attributes in water-saturated conditions. Arrows show the trajectories of increasing the effective pressure in each clay content subgroups. The pressure effect depends on the clay content in the $\lambda - \mu$ domain. The effects of pressure are generally small compared to the scatter of the data.

diversity of porosity and clay content. Figure 2.8 shows that the directions of the pressure effect are almost uniform within each attribute domain, except in $\lambda - \mu$ (Figure 2.8-B). The dependence of λ on the effective pressure varies with the clay content; if the clay content is large, the λ increases with the effective pressure. In contrast, λ decreases with the effective pressure if the sample is clean. As a result, the arrows showing the pressure effect rotate as the clay content changes.

The observation in Figure 2.8-B means positive $\frac{\partial \lambda}{\partial P}$ for large clay contents and negative $\frac{\partial \lambda}{\partial P}$ for small clay contents. Considering $\lambda = K - \frac{2}{3}\mu$, where K and μ are the bulk and shear modulus, respectively, dependence of the Lamè's constant on the effective pressure (P) can be expressed as

$$\frac{\partial \lambda}{\partial P} = \frac{\partial K}{\partial P} - \frac{2}{3} \cdot \frac{\partial \mu}{\partial P} \tag{2.2}$$

Hence, we can deduce that $\frac{\partial K}{\partial P} > \frac{2}{3} \cdot \frac{\partial \mu}{\partial P}$ (*i.e.*, the bulk modulus is more sensitive to pressure than the shear modulus) for small clay contents and $\frac{\partial K}{\partial P} < \frac{2}{3} \cdot \frac{\partial \mu}{\partial P}$ (*i.e.*, the shear modulus is more sensitive to pressure than the bulk modulus) for large clay contents.

2.3.3 Pore Fluid Effect

In this section, we discuss the relation between seismic attributes and pore fluids. Figure 2.9 shows five cross-plots of the same data as in Figure 2.2. Arrows represent the effect of increasing water saturation on each porosity subgroup. In Figure 2.9, the water-saturated samples are clearly separated from the dry samples in any of the five attribute domains. The directions of arrows imply that the V_p/V_s ratio and the elastic impedance are more sensitive to pore fluids than AI_p. The fluid effect becomes greater for more compliant rocks with greater porosity.

2.3.4 Discrimination of Rock Physics Effects

We combine the results from the previous sections to investigate which pairs of attributes can best discriminate the various rock properties of interest. Figure 2.10 summarizes typical trends of the four different rock physics effects, porosity (diagenesis), clay

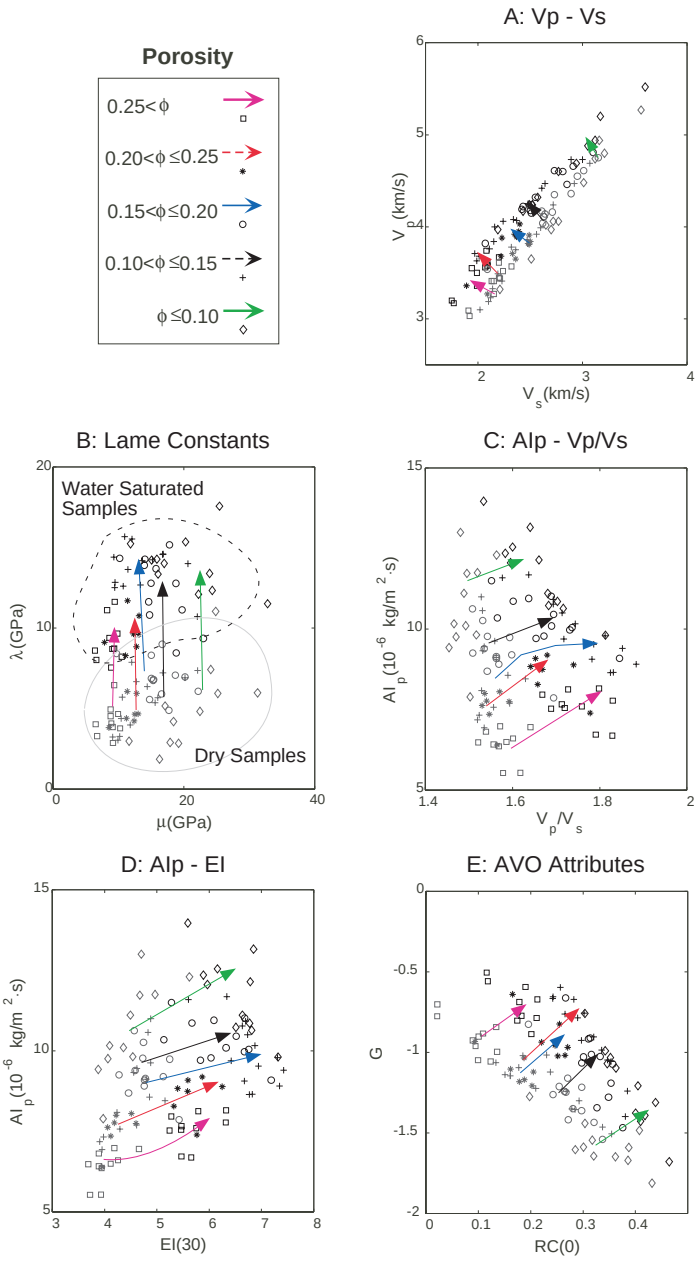

Figure 2.9: The fluid saturation dependence of combinations of seismic attributes at an effective pressure of 40 MPa. Arrows show the effect when water saturation is increased in each porosity subgroup. Water-saturated and dry samples are clearly separated in all five domains.

content (texture), effective pressure, and pore fluid, in the five seismic attribute domains, borrowed from Figures 2.5 through 2.9.

According to Figures 2.10-A and E, the $V_p - V_s$ and $G - RC(0)$ domains have several similar features: the trends for variation in porosity, the clay content, and the effective pressure are similar, while the pore fluid trend is roughly perpendicular to these three properties. Therefore, discrimination among the former three effects might be difficult, whereas the pore fluid effect might be more separable from others. That is, even when porosity, clay content and/or pressure are diverse, pore fluid prediction can be possible in these domains.

In the $AI_p - V_p/V_s$ cross-plot (Figure 2.10-C), the pore fluid trend is again roughly perpendicular to the other three effects. In addition, the clay trend can be distinguishable from the porosity and pressure trends at the shallow depth (soft rock matrix), although its direction is similar to the two at the deeper depth (stiff rock matrix).

The $\lambda - \mu$ and $AI_p - EI(30)$ cross-plots share similar features. The porosity and clay effects are parallel to each other at the deeper depth, but oblique at the shallow depth, where their separation might be possible. However, the pore fluid trend is normal to none of the three rock physics effects and almost parallel to the clay content variation at the shallow depth. Therefore, when any of the three properties has large variability, the prediction of pore fluid becomes more difficult in these domains. The pressure trend in the $\lambda - \mu$ domain is very characteristic; it rotates as the clay content decreases.

2.4 Rock Physics Effects in North Sea Sandstones

We analyze well and laboratory data from the North Sea in a way similar to that discussed in section 2.3. The data include ultrasonic laboratory measurements of high porosity deltaic sandstone of early to middle Jurassic age (Strandenes, 1991) and middle to late Jurassic shallow marine poorly consolidated sandstone (Blangy, 1992). Well log data of Paleocene turbiditic sandstone consisting of cemented and unconsolidated facies (Avseth et al., 2000) are also analyzed. The information about the analyzed data are summarized in Table 2.1.

Figure 2.11 shows the North Sea data plotted in the five seismic attribute domains, as well as in the $K - \phi$ domain. The Gulf Coast sandstone investigated in section 2.3 are

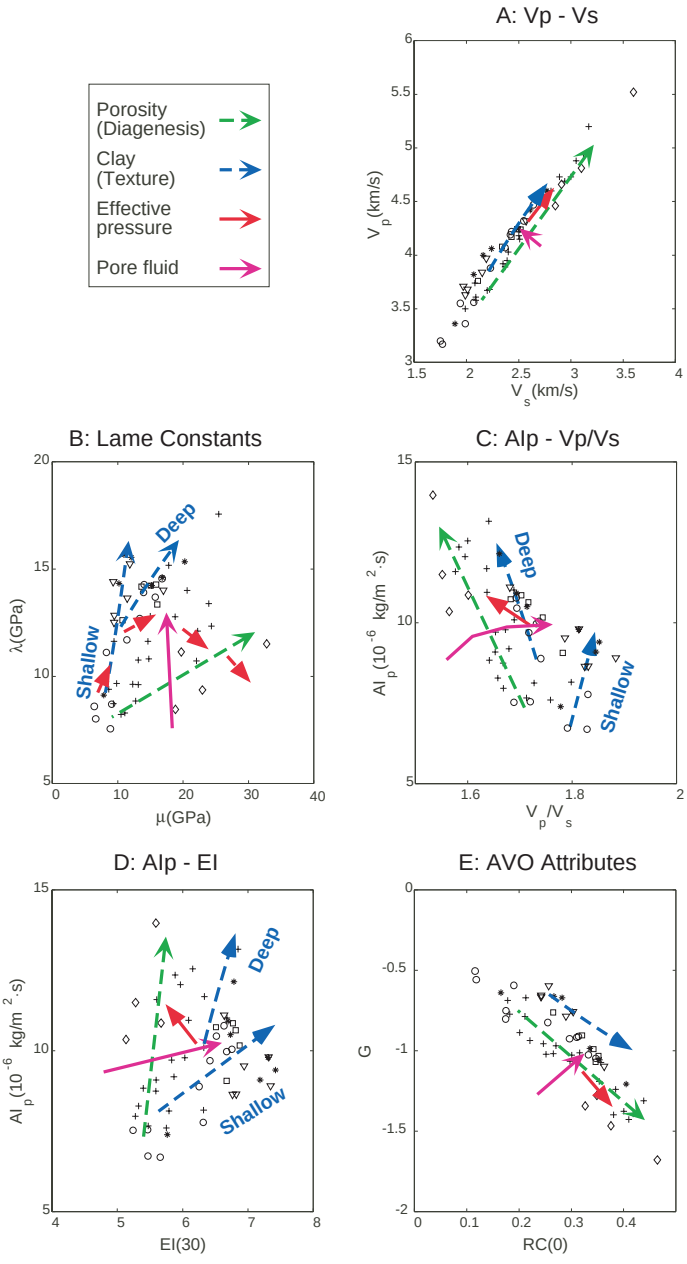

Figure 2.10: Summary of rock physics effects on seismic attributes. Arrows show the trends of each rock property variations, borrowed from Figures 2.5 through 2.9. The pore fluid effects can be distinguished from the other three effects in the $V_p - V_s$ and $G - RC(0)$ domains. The clay effect can be oblique to the porosity effect in the $\lambda - \mu$ and $AI_p - EI(30)$ domains.

Name	Age	Depos. Env.	Depth (km)
NS High porosity	Early/Middle Jurassic	Deltaic	2.5
NS Poorly consolidated	Middle/Late Jurassic	Shallow marine	1.5
NS Paleocene	Paleocene	Deep sea turbidite	2

Table 2.1: Geological information of North Sea sandstones used in the study.

overlain.

We interpret trends of three effects, diagenesis, the textural variation, and the effective pressure. The upper-right envelop of the entire data set in the $K-\phi$ domain (Figure 2.11-A) is assumed as the diagenesis trend. Also, trends of porosity decrease within individual data set are assumed as the trends for the textural variation, *i.e.*, good sorting to poor sorting. The pressure trends are derived only from the laboratory data, in which measurements at several effective pressures are available. Figure 2.12 consists of the same data plots as in Figure 2.11, as well as the interpretation of the three rock physics effects highlighted by arrows.

The effects of the three rock property changes on the seismic attribute domains are consistent with those identified in the Gulf Coast sandstone as in Figure 2.10. In the $V_p - V_s$ and AVO domains (Figures 2.11 B and F), the data are linearly well correlated. The trend of the three effects for diagenesis, texture, and pressure, are along similar directions. In the $AI_p - V_p/V_s$ domain, the increase of the V_p/V_s ratio due to poor sorting can be apparently identified. The $\lambda-\mu$ and AI_p-EI domains show more conspicuous separation of the diagenesis trend from the textural trends in the North Sea (Figure 2.12) than in the Gulf Coast data (Figure 2.10). In both data sets, λ and EI are characterized by strong dependence on the texture, while μ and AI_p are more influenced by diagenesis. The $\lambda-\mu$ domain, again, produces distinctive pressure dependence. Increasing the effective pressure increases λ when μ is small, whereas it decreases λ when μ is large.

The two sandstone facies indistinguishable only from the bulk modulus—high-porosity, cemented, and well-sorted sandstone and low-porosity, un-cemented, and poorly-sorted sandstone—can be separable by using combinations of seismic attributes.

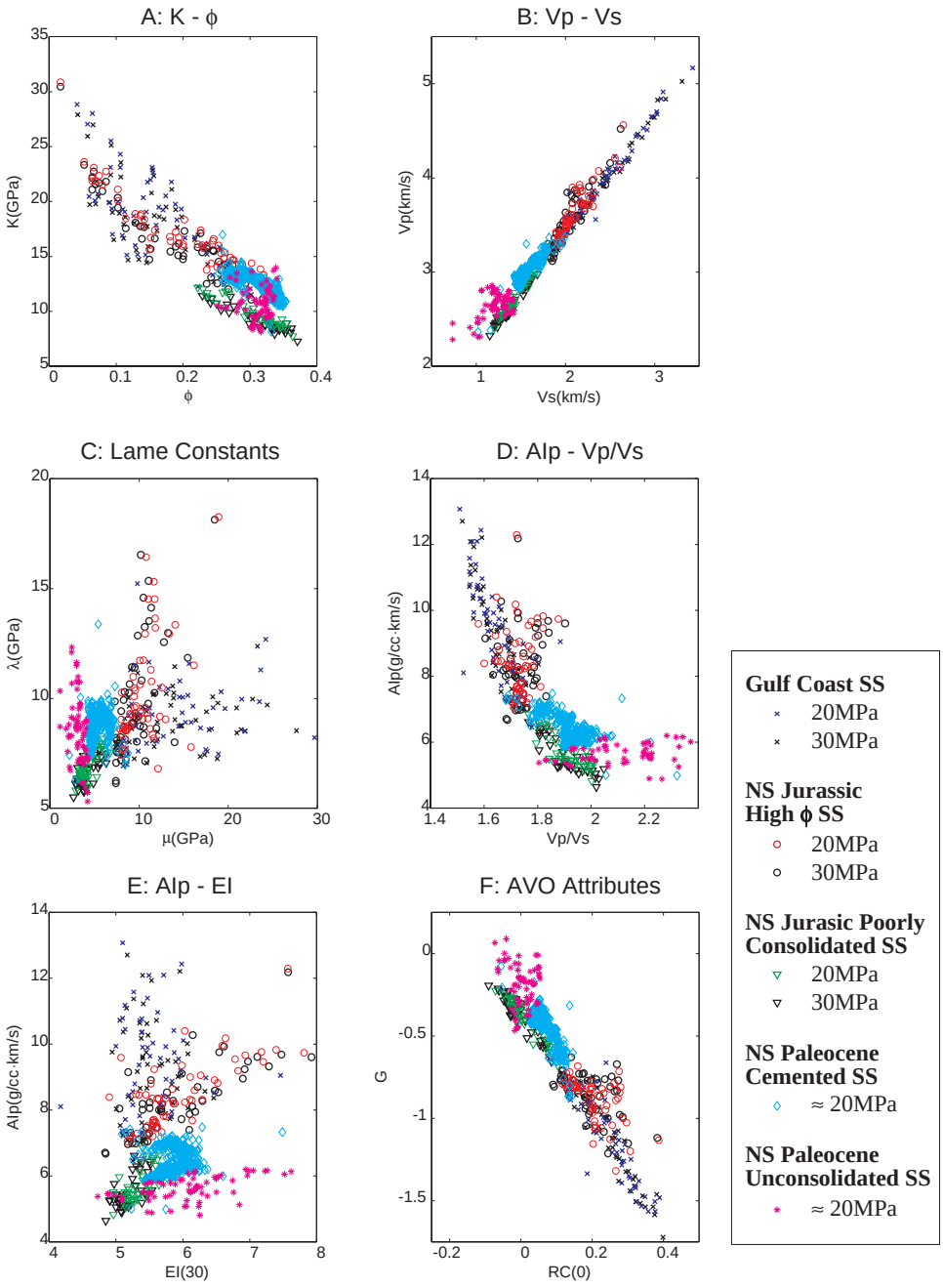

Figure 2.11: Seismic attribute crossplots of four North Sea sandstones. Han's Gulf Coast sandstone is also overlain. Colored data are values measured at 20 MPa and black data are at 30 MPa.

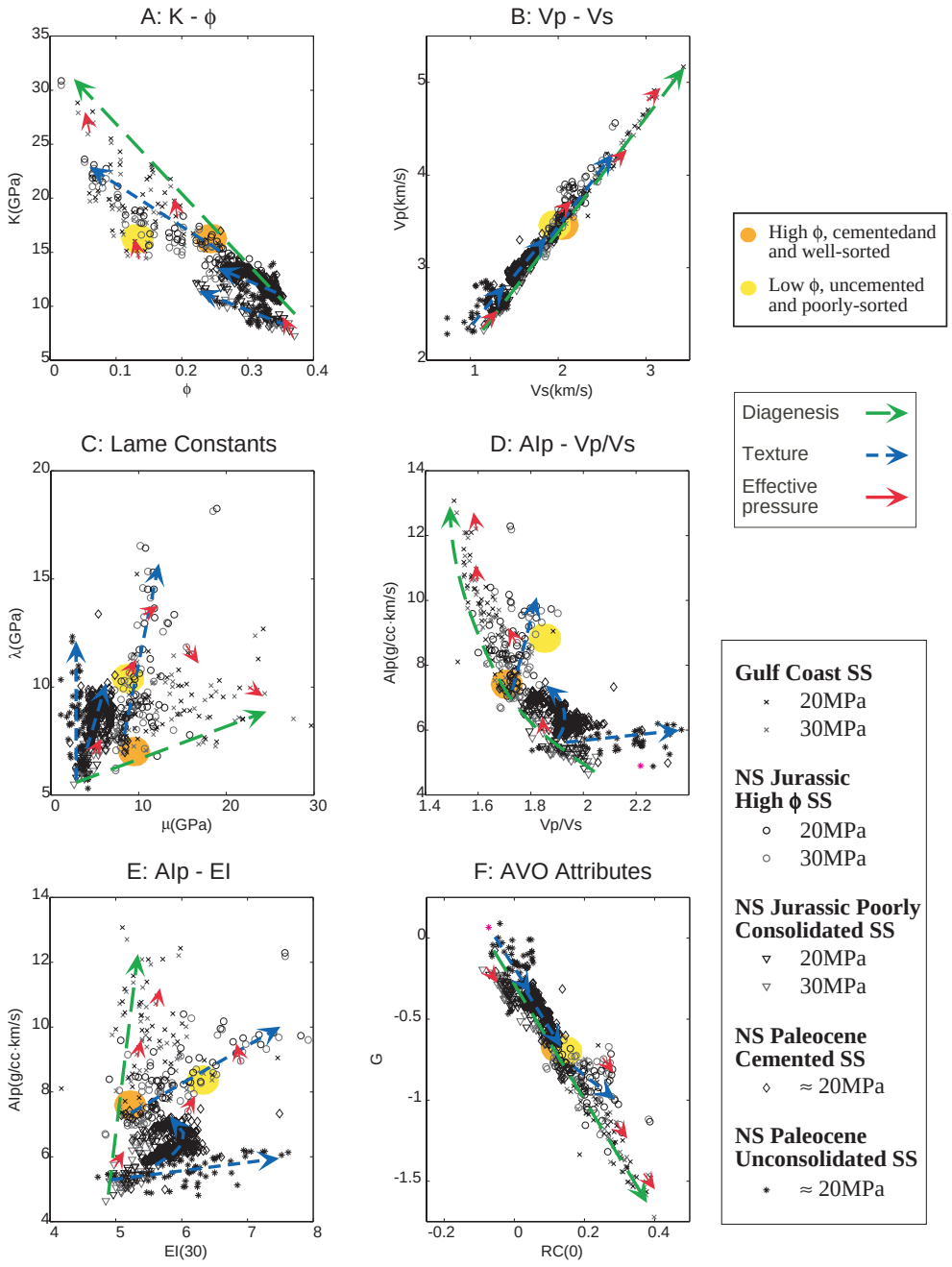

Figure 2.12: Interpretation of three rock physics effects, diagenesis, the textural variation, and the pressure in six attribute domains. Arrows show trends of individual rock property changes on each domain. Two sand facies indistinguishable only from K can be separated by using pairs of seismic attributes.

2.5 Parameterization of Rock Physics Relations

Rock physics models predict rock property relations for idealized geometries of constituent phases under particular physical conditions. Measured rock properties, such as the bulk modulus and porosity, are used to estimate unknown parameters of individual rock physics models by data fitting. For example, by observing the $V_p - \phi$ relation, a pore aspect ratio may be estimated using self-consistent models (Berryman, 1980) or a cement fraction may be predicted from the cementation model (Dvorkin and Nur, 1996). Some physical parameters, such as pore stiffness and Biot coefficient, represent mechanical properties of porous rocks under particular conditions.

Rock physics model parameterization also helps us understand effects of rock property changes in individual seismic attribute domains. A constant rock physics model parameter corresponds to a curve in a two-attribute domain, and a set of parameters produces a set of curves in the domain. Different parameterizations produce different sets of curves, hence observed properties can be interpreted in several different ways.

2.5.1 Rock Physics Model Parameters in The $K - \phi$ Domain

In this section, we investigate the characteristics of four rock physical model parameters—pore stiffness, Biot coefficient, pore aspect ratio, and critical porosity—and their behaviors in the $K - \phi$ domain.

Pore Stiffness, K_ϕ

Among several measures of compressibilities of porous media, the pore stiffness of a rock is defined as the ratio of the fractional change in the pore volume, v_p, to an increment of the applied external hydrostatic stress, σ, at a constant pore pressure, P_{pore} (Zimmerman, 1991; Mavko et al., 1998).

$$\frac{1}{K_\phi} = \frac{1}{v_p}\frac{\partial v_p}{\partial \sigma}\bigg|_{P_{pore}} = \frac{1}{\phi}\Big[\frac{1}{K_{dry}} - \frac{1}{K_o}\Big] \tag{2.3}$$

where K_{dry} and K_o are dry frame bulk modulus of the rock and the bulk modulus of the constituent mineral, respectively.

Contours of constant-K_ϕ/K_o curves in the $K-\phi$ domain are depicted in Figure 2.13. The curves are a set of hyperbolas that go through the mineral point, $(\phi, K) = (0, K_o)$. The curve for $K_\phi = 0$ matches the lower Hashin-Shtrikman bound exactly. The constant-K_ϕ curves may violate the upper Hashin-Shtrikman (HS) bound for large K_ϕ and/or large porosity. Comparison of Figure 2.13 with Figures 2.2 and 2.3 shows that constant-K_ϕ

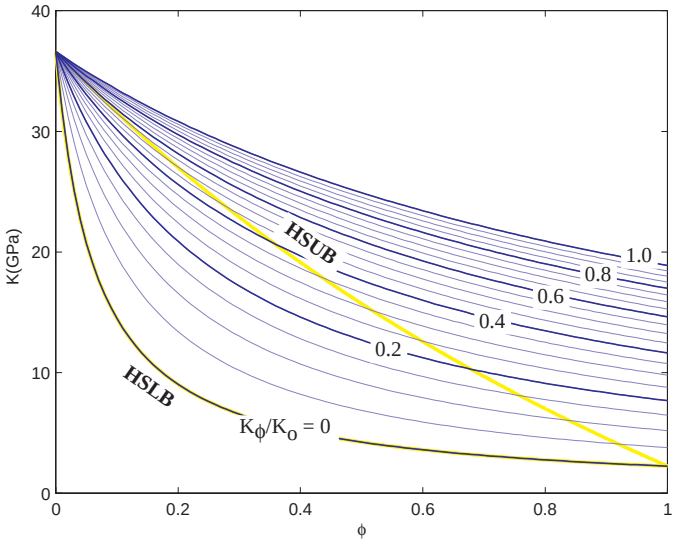

Figure 2.13: Contours of constant-K_ϕ curves in the $K-\phi$ domain. HSUB and HSLB are the Hashin-Shtrikman upper and lower bounds, respectively.

curves mimic trends of textural variation at a constant age or a constant degree of diagenesis. Diagenesis and effective pressure correspond to an increase in K_ϕ.

Biot Coefficient, β

The Biot coefficient, β, is defined as the ratio of pore volume change, Δv_p, to the bulk volume change, ΔV, at a constant pore pressure, due to an incremental applied external

hydrostatic stress.

$$\beta = \left.\frac{\Delta v_p}{\Delta V}\right|_{P_{pore}} = \frac{\phi K_{dry}}{K_\phi} = 1 - \frac{K_{dry}}{K_o} \tag{2.4}$$

As clear from the definition, β is a negative measure of the pore stiffness, *i.e.* increasing β corresponds to softening the rock's matrix frame.

Contours of constant-β lines in the $K - \phi$ domain are shown in Figure 2.14. They are similar to constant-K_ϕ curves in Figure 2.13, but steeper at low porosities and flatter at higher porosities. The line for $\beta = 1$ is exactly the same as the constant-K_ϕ line for $K_\phi = 0$, and matches the lower HS bound. Curves of constant-β mimic trends of textural

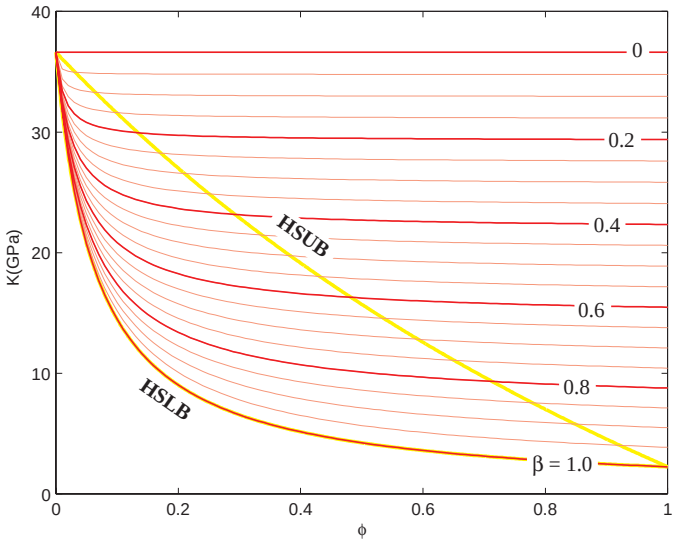

Figure 2.14: Contours of constant-β curves in the $K - \phi$ domain. Note that β is a negative measure of stiffness.

variation, as do the curves of constant-K_ϕ. Increases of diagenesis and effective pressure correspond to a decrease in β.

Pore Aspect Ratio, α_{pore}

The self-consistent models, as well as differential effective medium models, predict elastic moduli of aggregates whose pores and grains are modeled by spherical/ellipsoidal

inclusions (Berryman, 1980; Mavko et al., 1998). The $K - \phi$ relations of Berryman's self-consistent approximation for various pore aspect ratios, α_{pore}, are shown in Figure 2.15. Overlain on the curves are Han's Gulf Coast sandstone data (1986), grouped by the clay content.

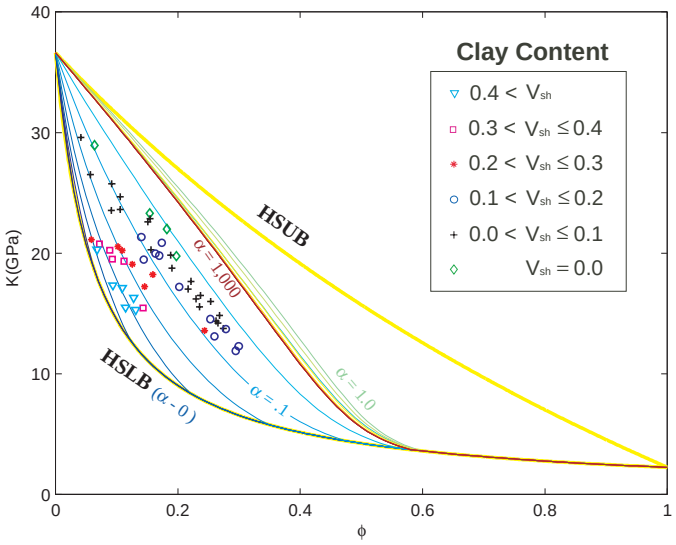

Figure 2.15: Contours of constant-α_{pore} curves using Berryman's self-consistent approximation (1980). The aspect ratio of the grain phase is maintained to be 1. Overlain are Han's sandstone data (1986), colored by the clay contents. The constant-α_{pore} curves mimic the constant-clay content trends of Han's data.

A rock with very thin crack, *i.e.*, $\alpha_{pore} \approx 0$, approaches the HS lower bound. Up to $\alpha_{pore} = 1$, increasing the pore aspect ratio increases the rock's bulk modulus. Curves of constant-α_{pore} are roughly parallel to the diagenesis trend in Figure 2.3. The textural variation, *i.e.*, poor sorting or more clay content, corresponds to a decrease in α_{pore}. On the other hand, increasing effective pressure corresponds to an increase in α_{pore}, which can be explained by a closing of the thin cracks and an increase in the average pore aspect ratio.

Critical Porosity, ϕ_{cr}

Nur (1992) and Nur et al. (1991; 1995) found that the relation between elastic modulus and the porosity of rocks in the load-bearing state can be approximated by a linear trend, whose one end is the mineral modulus and the other end is the suspension at the

critical porosity. The critical porosity, high-porosity end member, and the average mineral modulus, zero-porosity end member, are variable depending on the clay content of the rock (Marion, 1990; Mavko et al., 1998).

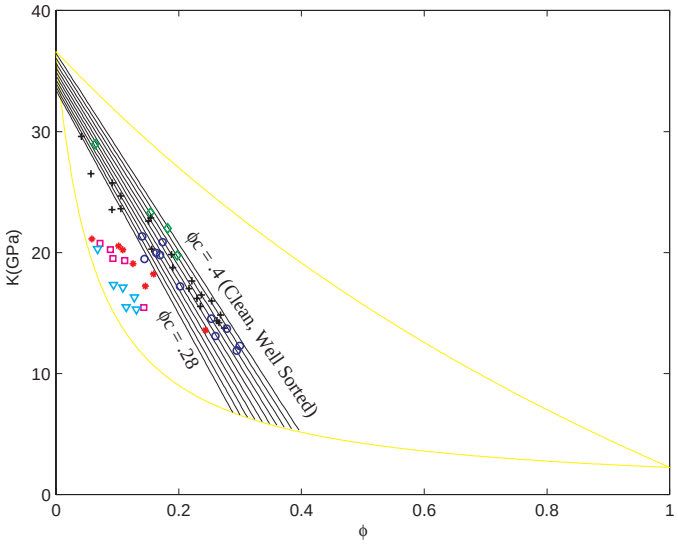

Figure 2.16: Modified Voigt lines for various clay content. The high-porosity end member, critical porosity, and zero-porosity end member, mineral point, is dependent on the clay content; The critical porosity decreases and mineral bulk moduli, modeled by Hill's average, decreases as the clay content increases. Overlain are Han's sandstone data colored by the clay contents.

As mentioned by Nur et al.(1991; 1995), modified Voigt lines approximate trends of porosity decrease controlled by diagenesis. Poor sorting corresponds to a decrease in the critical porosity of the modified Voigt model (Marion, 1990). Increasing effective pressure is mimicked by an *apparent* increase in the critical porosity.

2.5.2 Dependence of Rock Physics Model Parameters on Rock Properties

We summarize the dependence of the four rock physics model parameters on changes of three rock properties (*i.e.*, diagenesis, textural variation, and effective pressure) in Table 2.2, based on the patterns recognized in Figures 2.13 through 2.16.

		Model Parameters			
Rock Property	Directions	K_ϕ	β	α	ϕ_{cr}
Diagenesis	Increasing Depth/Age	$\Uparrow$	$\Downarrow$	$\approx$	$\approx$
Texture	Poor Sorting	$\approx$	$\approx$	$\Downarrow$	$\Downarrow$
Pressure	Increasing Effective Pressure	$\Uparrow$	$\Downarrow$	$\Uparrow$	$\Uparrow$

Table 2.2: Dependence of rock physics model parameters on rock property changes. The pressure effect on the critical porosity is only apparent.

Changes in the rock physics model parameters, for a fixed porosity, are related to matrix stiffness or softness of rocks. However, their behavior with respect to the three rock property changes are variable. The relations in Table 2.2 are used to interpret dependence of rock properties in seismic attribute domains in section 2.5.3.

2.5.3 Rock Physics Model Parameterization in Seismic Attribute Domains

We extend the contours of the four rock physics model parameters in the $K-\phi$ domain (as shown in Figures 2.13 through 2.16) to the five seismic attribute domains, V_p-V_s, $\lambda-\mu$, $AI_p - V_p/V_s$, $AI_p - EI$, and $G - RC(0)$ (as discussed in sections 2.3 and 2.4). We then compare the characteristics of the model parameters with the trends of each rock property change in each attribute domain.

For the conversion of the contours for K_ϕ, β, and ϕ_{cr}, the dry Poisson's ratio is assumed to be equal to the mineral Poisson's ratio (Picket, 1963), *i.e.*,

$$\nu_{dry} = \nu_{min} \tag{2.5}$$

This assumption tends to under-predict the Poisson's ratio of sandstones (Walton, 1987). Since the self-consistent models, per se, predict shear modulus for each pore aspect ratio, the conversion of the constant-α_{pore} contours is straightforward. Because of the different assumptions in the relation between bulk and shear modulus in the α_{pore} contours and other three model parameters, two separate data points in a domain may correspond to a single

point in another domain.

$V_p - V_s$ domain

Figure 2.17 shows four sets of contours for the pore stiffness (K_ϕ), the Biot coefficient (β), the pore aspect ratio (α_{pore}), and the critical porosity (ϕ_{cr}) in the $V_p - V_s$ domain.

On the whole, three model parameters, *i.e.*, K_ϕ, α_{pore}, and ϕ_{cr}, produce contours roughly parallel each other, while constant-β contours are roughly perpendicular to the other three sets of contours. According to Table 2.2, the trends along α_{pore} and ϕ_{cr} contours represent trajectories of diagenesis for different textures. Approaching towards the mineral point along these trends correspond to a decrease in β.

If the effective pressure increases and K_ϕ, ϕ_{cr}, and α_{pore} increase, the three contours shift towards lower right, and the V_p/V_s ratio thereby decreases. In contrast, Table 2.2 shows that poor sorting decreases α_{pore} and ϕ_{cr}, maintaining β to be nearly constant, which is realized by moving towards upper left along the β contours, hence increasing the V_p/V_s ratio.

$\lambda - \mu$ domain

Figure 2.18 shows the same four sets of contours in the $\lambda - \mu$ domain.

Contours of ϕ_{cr} and α_{pore} (for large α_{pore}) in Figures 2.18-D and C, respectively, mimic trends for diagenesis identified in Figures 2.10 and 2.12. These trends correspond to an increase in β contours in Figure 2.18-B, which is consistent with Table 2.2. Also, constant-K_ϕ contours in Figure 2.18-A approximate textural variations in Figures 2.10 and 2.12.

Contours of K_ϕ and α_{pore} are convex-shaped and non-linear. Their peaks where both K_ϕ and α_{pore} are small, correspond roughly to the clay-rich zone of Han's data observed in Figure 2.7-D. In addition, the convexity of the K_ϕ and α_{pore} contours explains the intriguing behavior of the effective pressure in both Han's data and the North Sea data (Figures 2.8 and 2.12); the effective pressure increases K_ϕ and α_{pore}, as well as shear modulus, μ, making a rotation in the $\lambda - \mu$ relation. The monotonous increase of μ and rather chaotic behavior of λ by pressure can also be understood by β contours; effective pressure decreases β and, hence, increases μ, but does not have a fixed effect on λ.

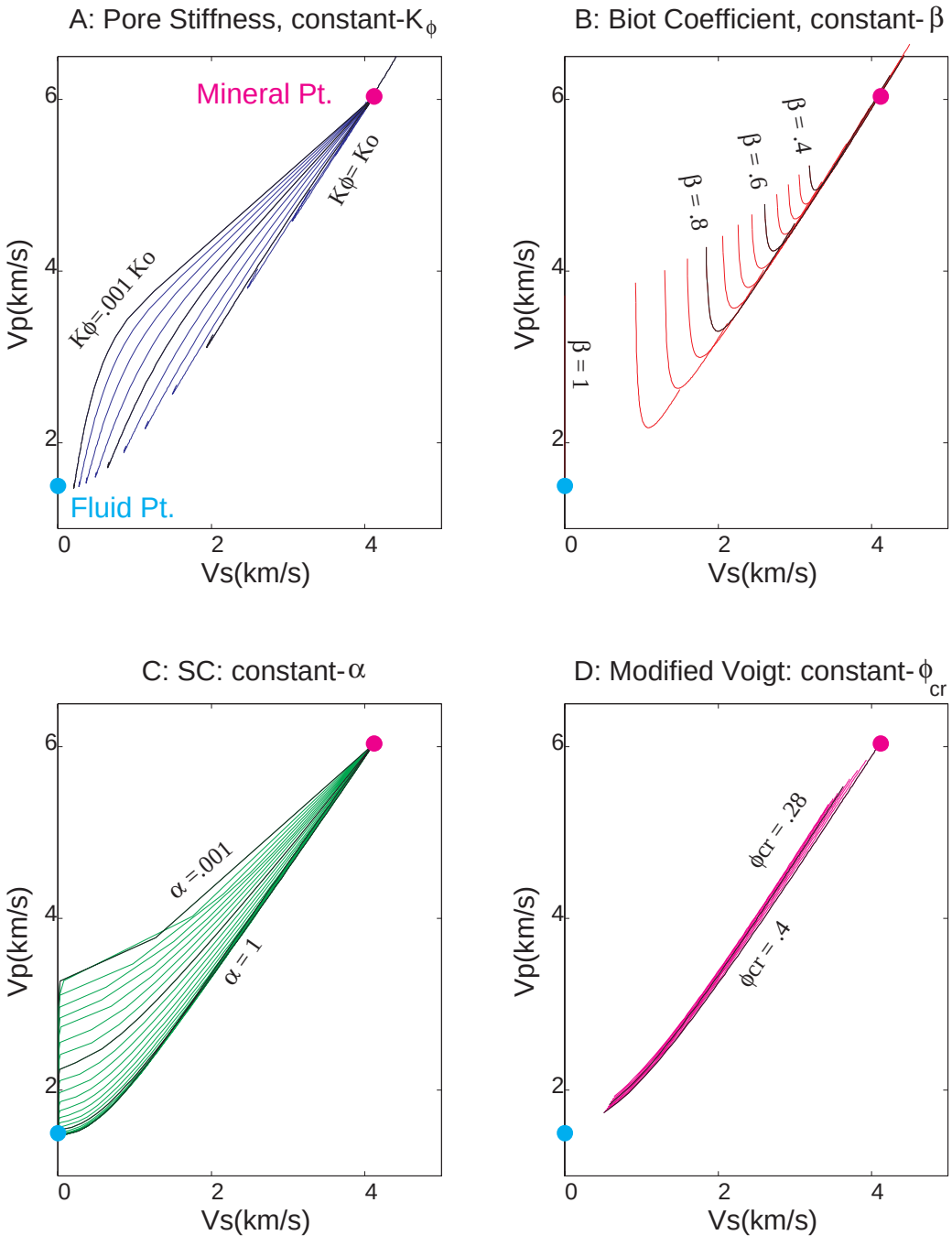

Figure 2.17: Rock physics model parameters in $V_p - V_s$ domain.

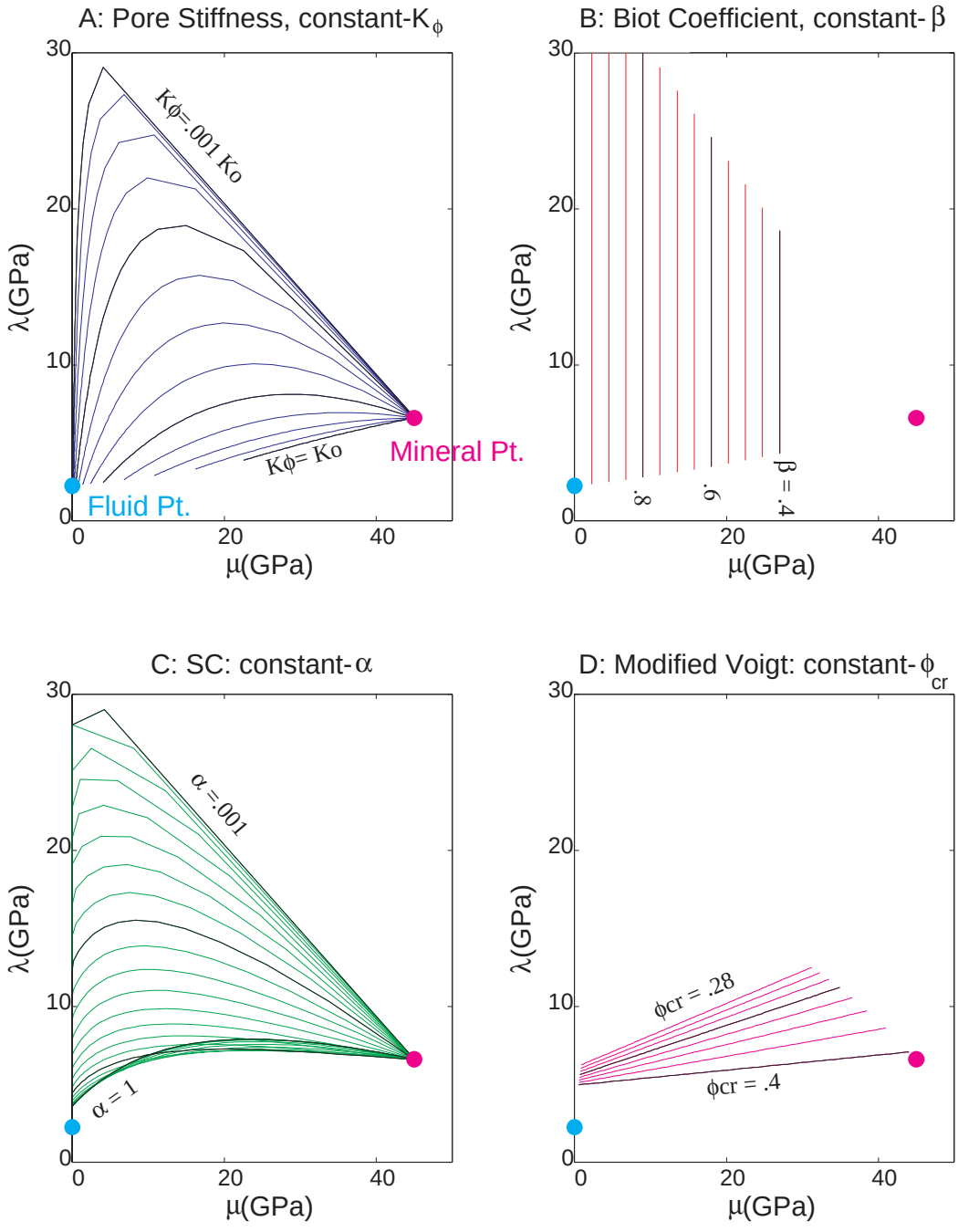

Figure 2.18: Rock physics model parameters in $\lambda - \mu$ domain.

$AI_p - V_p/V_s$ domain

Figure 2.18 shows the same four sets of contours in the $AI_p - V_p/V_s$ domain.

Again, contours of ϕ_{cr} and α_{pore} for large α_{pore} mimic diagenetic trends of clean sandstone. The diagenetic trends in Figure 2.5-C correspond to an increase in K_ϕ in Figure 2.19-A, as well as a decrease in β in Figure 2.19-B. These observations are consistent with Table 2.2. The textural variation is mimicked by β contours for high porosities, although not for low porosities. The increasing pressure shifts data towards stiffer matrix (*i.e.*, larger K_{phi}, α_{pore}, and ϕ_{cr}, and smaller β) and decreases the V_p/V_s ratio.

$AI_p - EI$ domain

Figure 2.20 shows the four sets of contours in the $AI_p - EI$ domain. Contours of ϕ_{cr} and α_{pore} (for large α_{pore}) in Figures 2.20-C and D not only mimic the diagenetic trend of clean sandstones in Figures 2.5 and 2.12, but also imply little dependence of EI on the diagenesis effect. In Figure 2.21, the rock physics model parameter contours are overlain onto arrows for the rock physics effects observed in Han's data, borrowed from Figure 2.10-D. The rotating trend for textural variation depending on the depth of the samples is well mimicked by the curved K_ϕ contours. The effective pressure acts normal to the β contours and increasing K_ϕ and α_{pore}.

AVO Gradient - AVO Intercept domain

The characteristics of the contours in the AVO domain shown in Figure 2.22 are similar to the $V_p - V_s$ domain in Figure 2.17. In Figure 2.23, the rock physics model parameter contours are overlain onto arrows for the rock physics effects observed in Han's data, borrowed from Figure 2.10-E. The linear trend for diagenesis is mimicked by the constant ϕ_{cr} and constant α_{pore} contours for large α_{pore}. The dense intervals of the ϕ_{cr} contours imply little effect of textural variation in the domain. The diagenesis and effective pressure are realized by crossing the β contours towards the mineral point, *i.e.*, stiffer matrix.

Pore Fluid Effect

Since the four rock physics model parameters explored in this section are measures of the pore and matrix stiffness of rocks, they are not suitable for investigations of pore fluid

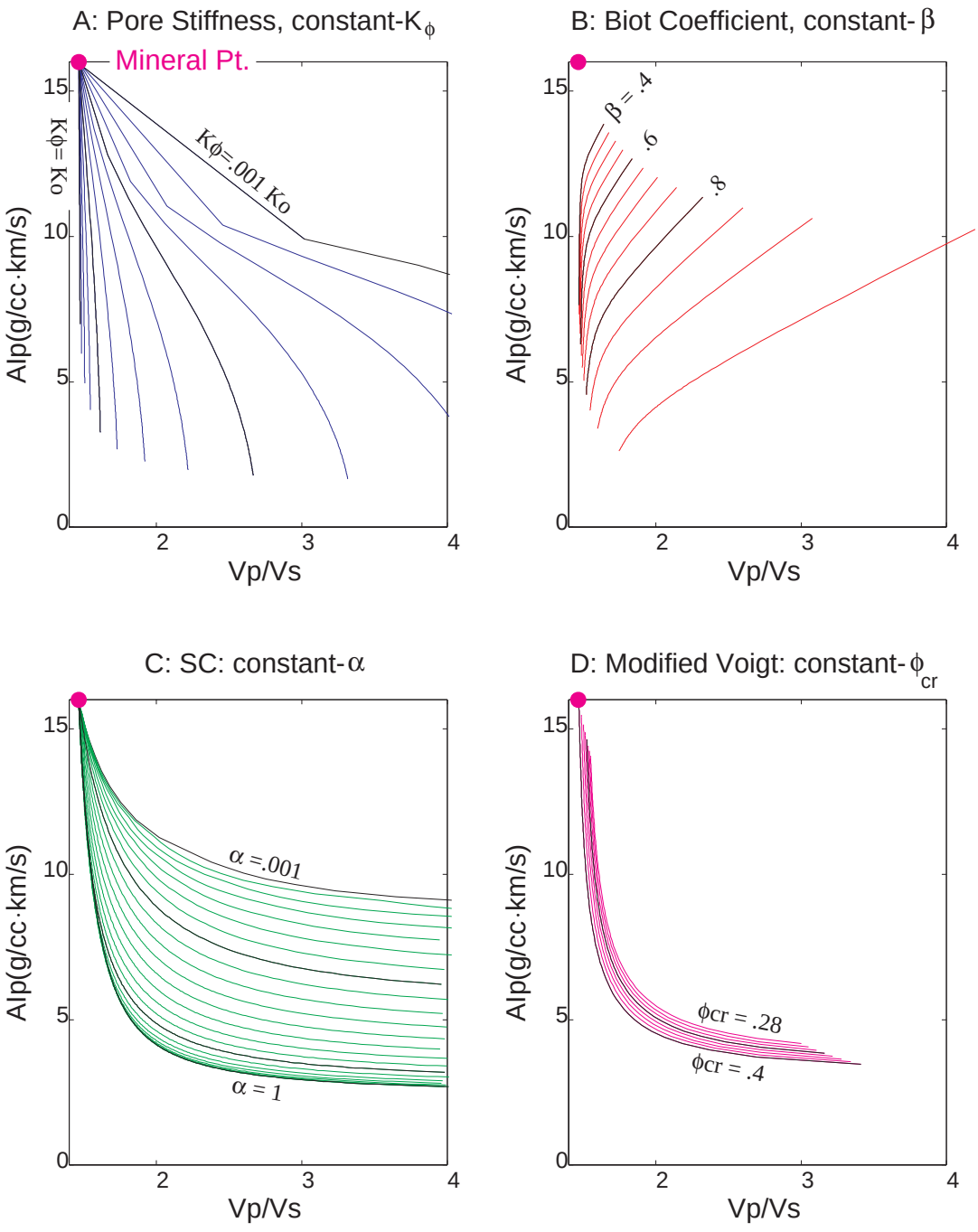

Figure 2.19: Rock physics model parameters in the $AI_p - V_p/V_s$ domain.

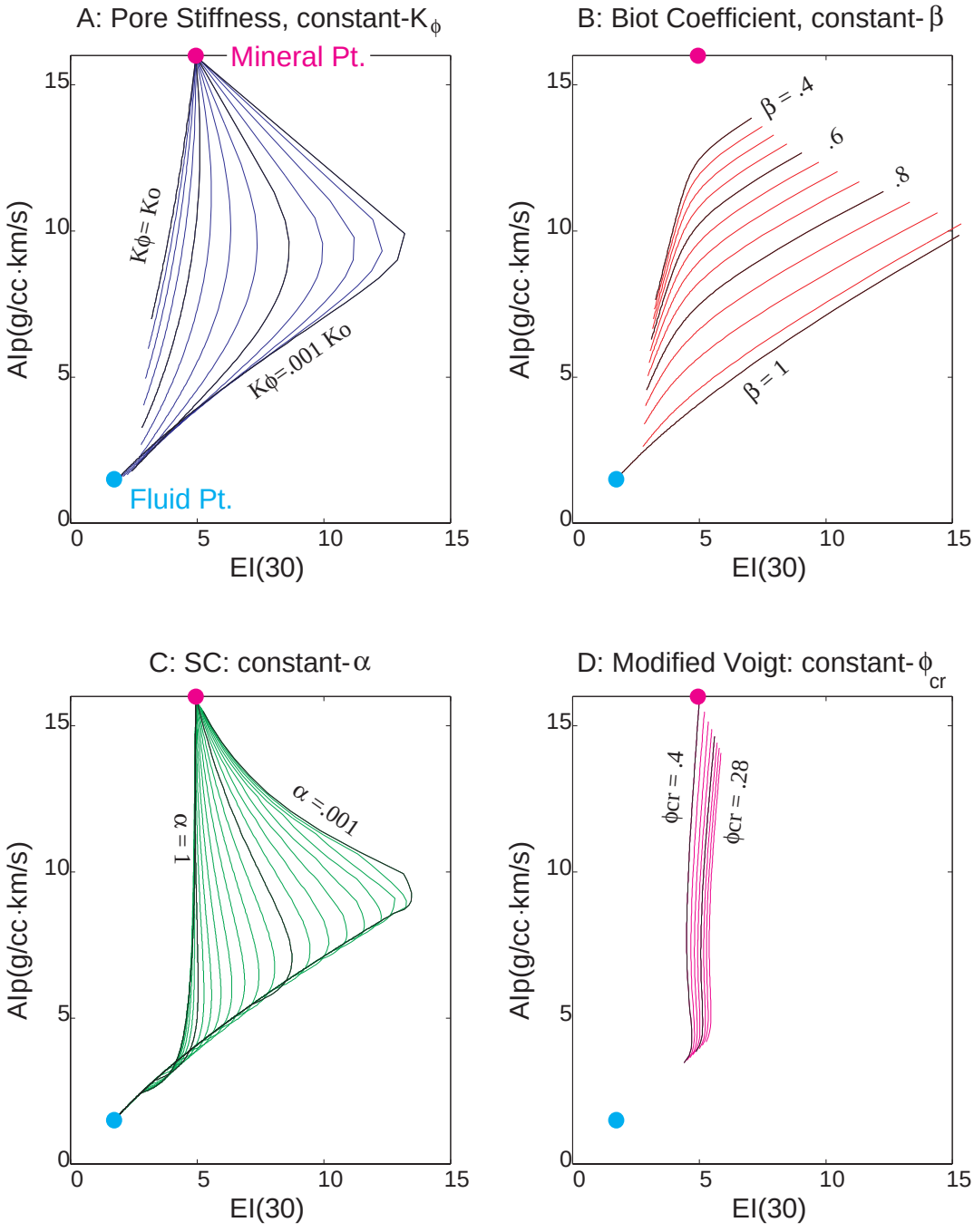

Figure 2.20: Rock physics model parameters in the $AI_p - EI$ domain.

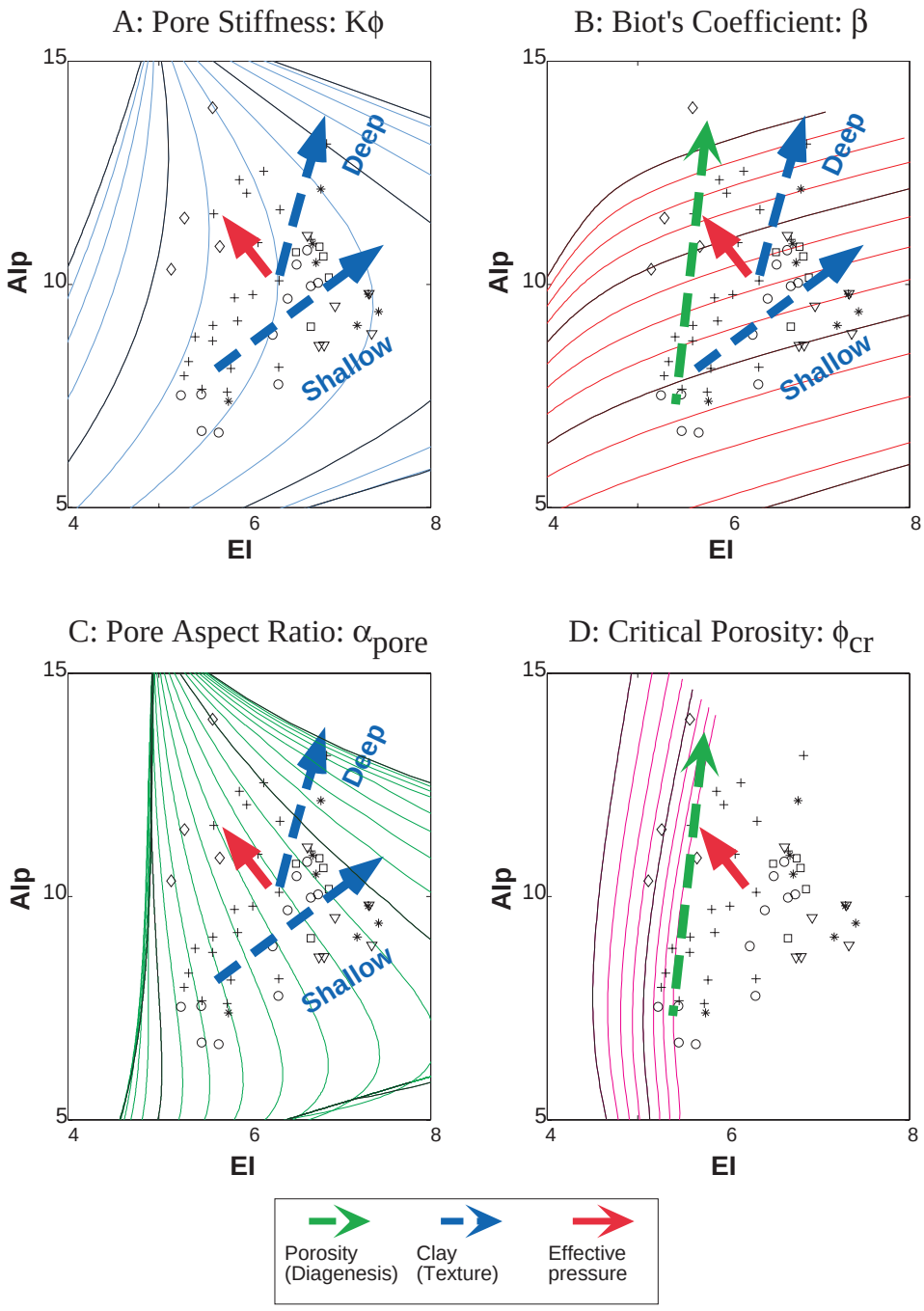

Figure 2.21: Rock physics model parameters and rock physics effects observed in Han's data in the $AI_p - EI$ domain.

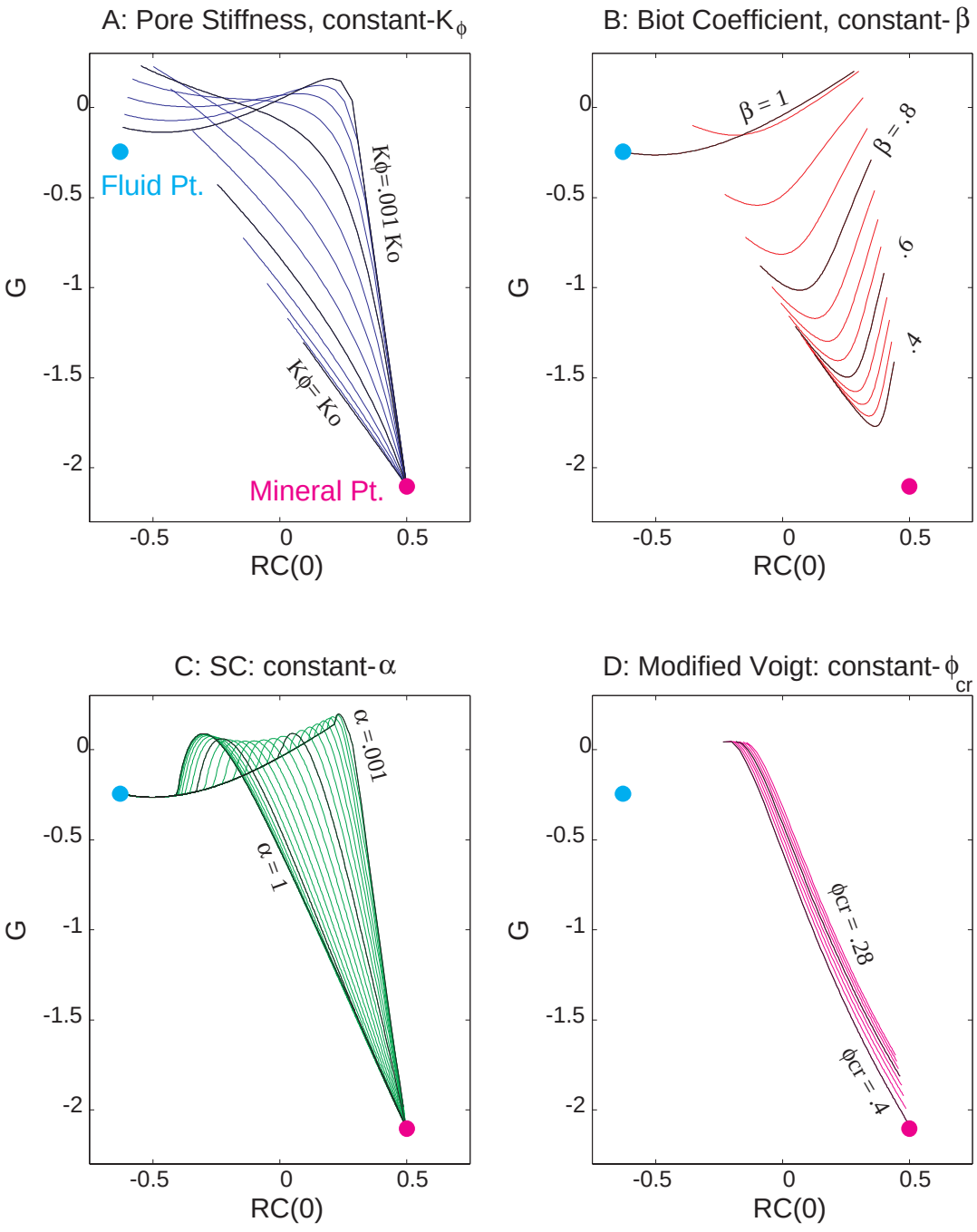

Figure 2.22: Rock physics model parameters in AVO crossplot.

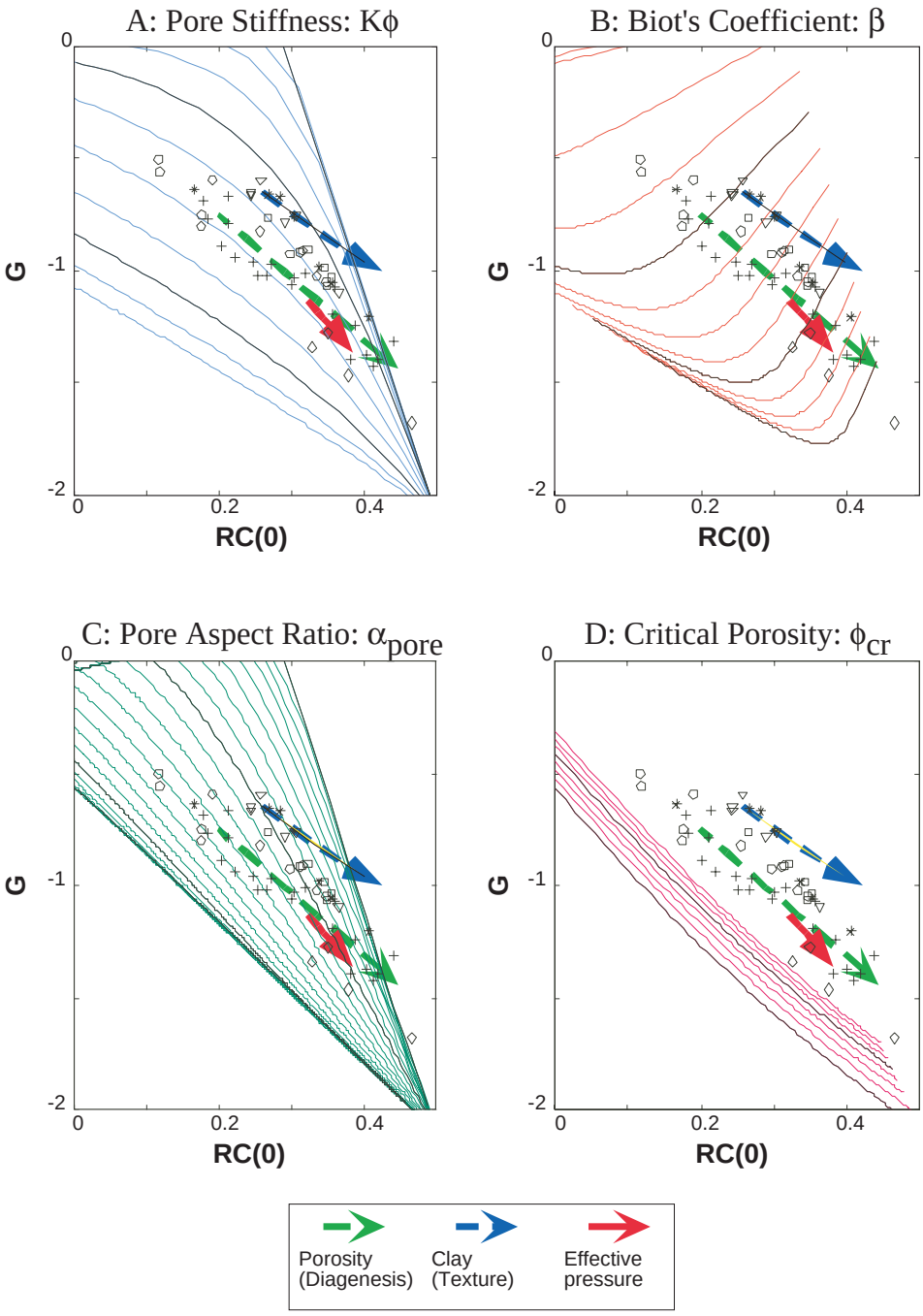

Figure 2.23: Rock physics model parameters and rock physics effects observed in Han's data in the AVO domain.

effects on seismic attributes.

Gassmann's theory states that substitution of pore fluid to stiffer one increases bulk modulus but maintains a constant shear modulus. Mavko and Mukerji (1995) proposed a simple method to realize Gassmann's substitution in the $K - \phi$ domain using constant K_ϕ contours: Gassmann fluid substitution is equivalent to jumping K_ϕ contours with the porosity held constant. The shear modulus is, of course, unchanged.

In contrast, stiffening of the matrix bulk modulus, either caused by diagenesis, textural variation, or effective pressure, is almost always accompanied by stiffening of the shear matrix stiffness. Because of this inherent difference, the parameters representing pore matrix stiffness do not describe the pore fluid effect, unless we look only at bulk stiffness properties. Actually, comparison of Figure 2.9 and Figures 2.17 through 2.22 shows that substitution to stiffer pore fluid corresponds to a decrease in apparent K_ϕ in multi-attribute domains.

2.6 Conclusions

We investigated the dependence of physical seismic attributes on rock property changes, using laboratory and well log measurements. Our results show that each seismic attribute pair is good at predicting different rock properties. Combinations of $V_p - V_s$ and AVO attributes (*i.e.*, $G-RC(0)$) are helpful in predicting pore fluids even if other rock properties, such as porosity, clay content, and the effective pressure, are heterogeneous. However, discrimination among porosity, clay content, and pressure is difficult in these domains. The $\lambda - \mu$, and $AI_p - EI(30)$ cross-plots can discriminate diagenesis and pressure effect from textural variation, though uncertainty about porosity, clay content, and pressure may make fluid detection erroneous. In particular, the $AI_p - EI$ and $G - RC(0)$ pairs are of practical significance, since both can be directly derived from seismic data.

The investigation of rock physics model parameters, pore stiffness, Biot coefficient, pore aspect ratio, critical porosity, provided us with physical understanding of the dependence of seismic attributes on rock property changes; constant-pore stiffness and constant-Biot coefficient curves tend to mimic the textural variation, while constant-aspect ratio and

constant-critical porosity contours approximate the diagenetic trends. The model parameters also help us extrapolate the observed relations between rock properties and seismic attributes to whole attribute domains.

Chapter 3

Elastic Properties of Sandstones and Carbonates: The $V_p - V_s$ Relations and Their Implication About Pore Structures

Abstract

The importance of S-wave information in addition to P-wave is becoming more widely recognized with emerging advancements in multi-component data acquisition and processing techniques. Better prediction of lithology from multiple seismic observables is one of the expected outcomes. Hence, greater understanding of $V_p - V_s$ relations of various rock types is essential. V_p and V_s of typical reservoir rocks are known to be *well correlated* as well as dependent on lithology; sandstones tend to have *linear* $V_p - V_s$ relations, while carbonates' are *quadratic*. Although these distinctive characters have been observed in many measurements, the physical reason for the difference, except the obvious one of mineralogy, is not well understood.

In this chapter, we first extend the definitions of Hashin-Shtrikman bounds to the $V_p - V_s$ domain and show that V_p and V_s of monomineralic rocks must be well correlated. We then amplify the bounding average method to introduce *bulk* and *shear stiffness indices* (w_k and w_μ), which extract information about pore structure and pore stiffness of rock matrices. Investigation of the stiffness indices of various sandstone and carbonate samples

reveals a conspicuous distinction between the two rock types; bulk stiffness indices for sandstones are greater than or equal to the shear indices, while carbonates have greater shear indices than bulk indices. Comparison of this result with various rock physics models in the stiffness index domain leads to the conclusion that the difference of sandstones and carbonates in the $V_p - V_s$ relation is due to either the difference in their pore shape or the difference in tangential stiffness at the grain-to-grain contacts.

3.1 Introduction

3.1.1 Motivation

Lithology is one of the important factors influencing seismic signatures, in addition to porosity, pore fluid, textural variation, and pressure, which are explored in chapter 2. Figure 3.1 shows the distributions of seismic attributes for various types of two typical reservoir rocks: sandstone and carbonate. The plotted data include Gulf Coast well-consolidated sandstone (Han, 1986), North Sea high-porosity sandstone (Strandenes, 1991), North Sea poorly-consolidated sandstone (Blangy, 1992), tight-gas sandstone from East Texas (Jizba, 1991), limestone (Cadoret, 1993; Lucet, 1989; Yale and Jamieson, 1994), dolomite (Geertsma, 1961; Yale and Jamieson, 1994), and chalk (Brevik, 1995). The individual attribute domains produce different distributions for each rock type. For example, in the $V_p - V_s$ domain in Figure 3.1-A, sandstones and carbonates have obliquely crossing linear trends, while the distribution of the two rock types are the most scattered in $AI_p - V_p/V_s$ domain, shown in Figure 3.1-C.

In this chapter, we discuss how inter-dependence between seismic signatures carries information about the internal properties of rocks. We focus on the $V_p - V_s$ relations of sandstones and carbonates and investigate the inherent difference in micro-structures between the two rock types. The physical insight of the $V_p - V_s$ relations can lead to better understandings of the behaviors of sandstones and carbonates in various seismic attribute domains, shown in Figure 3.1.

We explore the elastic properties of the two rock types in relation to the Hashin-Shtrikman bounds (Hashin and Shtrikman, 1963). We first amplify the Hashin-Shtrikman

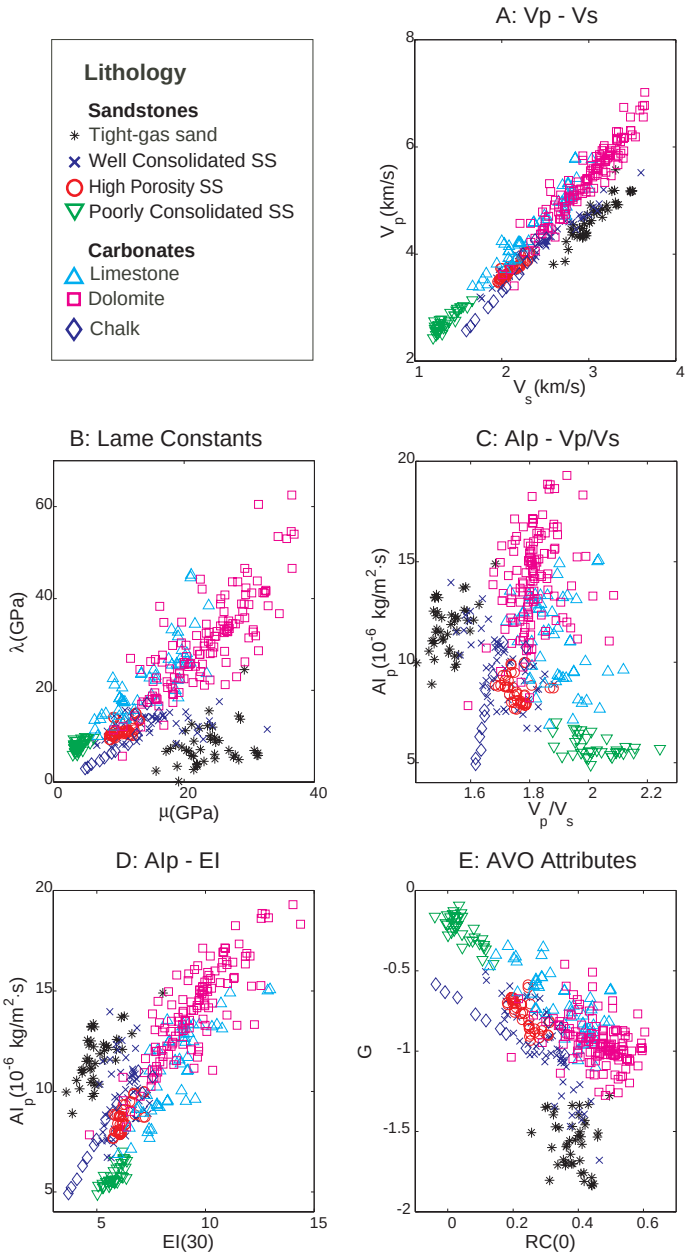

Figure 3.1: Sandstone and carbonate in five seismic attribute domains, A: $V_p - V_s$, B: $\lambda - \mu$ (Lamé's constant - Shear modulus), C: $AI_p - V_p/V_s$ (Acoustic impedance - V_p/V_s ratio), D: $AI_p - EI$ (Acoustic impedance - Elastic impedance), E: $G - RC(0)$ (AVO gradient - AVO intercept).

bounding theory and reveal that V_p and V_s of monomineralic rocks must be well correlated. We then extend the bounding average method (Marion and Nur, 1991) to define *stiffness indices*; parameters which quantify the bulk and shear stiffnesses of pore structures. By comparing existing laboratory data with rock physics theories in the stiffness index domain, we interpret the difference in micro-structure between sandstones and carbonates.

3.1.2 $V_p - V_s$ Relations of Sandstones and Carbonates

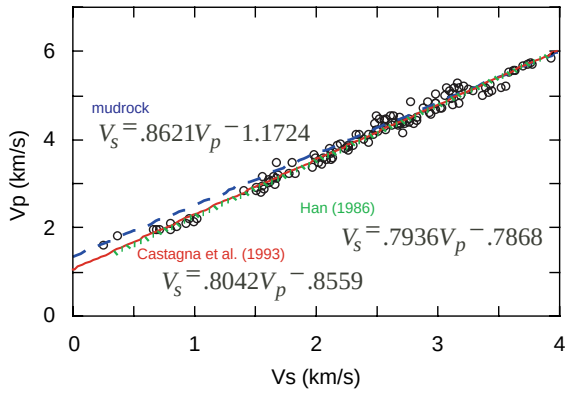

Figure 3.2: $V_p - V_s$ relation of water-saturated sandstone (modified from Mavko et al., 1998).

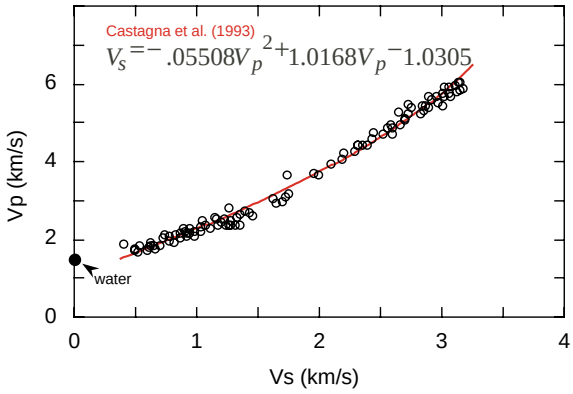

Figure 3.3: $V_p - V_s$ relations of water-saturated limestone (modified from Mavko et al., 1998).

$V_p - V_s$ relations of sandstones and carbonates from various data sources are shown in Figures 3.2 and 3.3. Overlain on these figures are linear and non-linear regressions proposed by several authors (Castagna et al., 1985; Castagna et al., 1993; Han, 1986). In both rock types, V_p and V_s are *well correlated*. The relation tends to be *linear in sandstones and quadratic in carbonates*. In spite of these and many similar observations, the physical reason for these distinctive characteristics is not yet well understood.

3.2 Extensions of Hashin-Shtrikman Bounds

3.2.1 Hashin-Shtrikman Bounds

Hashin-Shtrikman (HS) bounds (Hashin and Shtrikman, 1963) define the upper and lower limits of elastic moduli of isotropic aggregates. In monomineralic rocks consisting of a mineral phase as the stiffer constituent and a fluid phase as the softer constituent, bounds of bulk and shear moduli are given by

$$K^{HS\pm} = K_1 + \frac{f_2}{(K_2 - K_1)^{-1} + f_1(K_1 + \frac{4}{3}\mu_1)^{-1}} \tag{3.1}$$

$$\mu^{HS\pm} = \mu_1 + \frac{f_2}{(\mu_2 - \mu_1)^{-1} + \frac{2f_1(K_1+2\mu_1)}{5\mu_1(K_1+\frac{4}{3}\mu_1)}} \tag{3.2}$$

where K, μ, and f represent the bulk modulus, shear modulus, and volume fraction of each constituent for either of the phases, denoted by suffixes 1 and 2. The upper bound is realized when the mineral phase is termed 1 in Equation 3.2 and forms the outer shell of the concentric spheres in Figure 3.4. The lower bound is realized when the mineral phase is termed 2 and is in the inner core in Figure 3.4.

The upper and lower bounds of bulk and shear moduli for water-saturated sandstone (quartz-water mixture) are shown in Figure 3.5 as examples. The parameters in Table 3.1 are used hereafter. Figure 3.5 includes data from ultrasonic laboratory measurements of well-consolidated Gulf Coast sandstone (Han, 1986), high-porosity North Sea sandstone (Strandenes, 1991), and poorly-consolidated North Sea sandstone (Blangy, 1992). The data are plotted certainly within the upper and lower bounds.

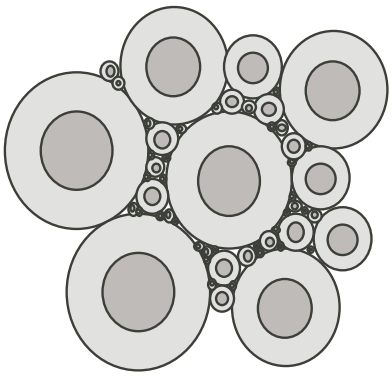

Figure 3.4: Physical realization of Hashin-Shtrikman bounds.

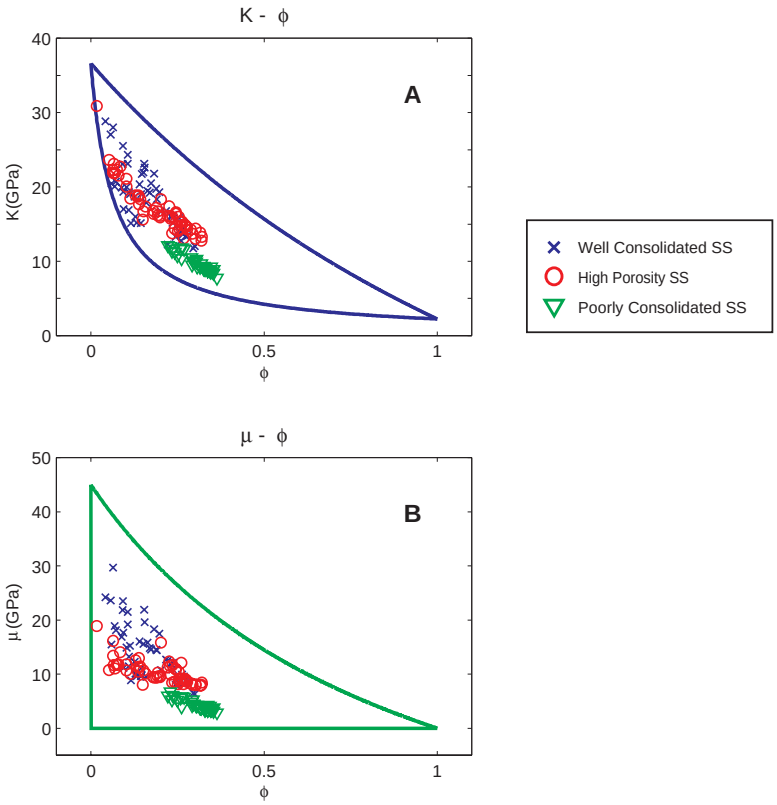

Figure 3.5: Hashin-Shtrikman upper and lower bounds of the bulk modulus (A) and the shear modulus (B) for water-saturated quartz sandstone. Data points from ultrasonic laboratory measurements are overlain onto the bounds.

Constituents	K (GPa)	μ (GPa)	ρ (g/cc)
Quartz	36.6	45.0	2.65
Water	2.25	0	1.0

Table 3.1: Properties of constituents used for elastic property modeling.

3.2.2 Bounds in the $K - \mu$ Domain

We combine the HS bounds of bulk and shear moduli and define HS bounds in the $K - \mu$ domain as shown in Figure 3.6. For a given porosity, the possible extent of (K, μ) is within a rectangle defined by (K^{HS-}, μ^{HS-}) as the lower left corner and (K^{HS+}, μ^{HS+}) as the upper right corner (Berryman, 1995). As the porosity changes, the rectangle slides up or down since the HS bounds depend on porosity. The envelope of the rectangles for all the porosity outlines the overall HS bounds in the $K - \mu$ domain.

Figure 3.7 show the bounds overlain by the data shown in Figure 3.5. The real data cover limited region near the center within the bounds. Figure 3.7 shows that HS bounds do not allow arbitrary combination of bulk and shear moduli; shear moduli close to the upper end member (the mineral shear modulus) may not coexist with bulk moduli close to the lower end member (the fluid bulk modulus), though bulk moduli close to the upper end member (the mineral bulk modulus) can coexist with shear moduli close to the lower end member (the fluid shear modulus, *i.e.*, 0).

3.2.3 Bounds of the Poisson's Ratio

A straightforward extension of the $K - \mu$ bounds using Equation 3.3 leads to bounds of the Poisson's ratio, shown in Figure 3.8.

$$\nu = \frac{K/\mu - 2/3}{2K/\mu + 2/3} \tag{3.3}$$

Equation 3.3 states that the Poisson's ratio is a deterministic function of K/μ, the slope of the line connecting a point and the origin in the $K - \mu$ domain. Hence the Poisson's ratio has large values when the (K, μ) stays in the upper-left quadrant in the $K - \mu$ domain, and

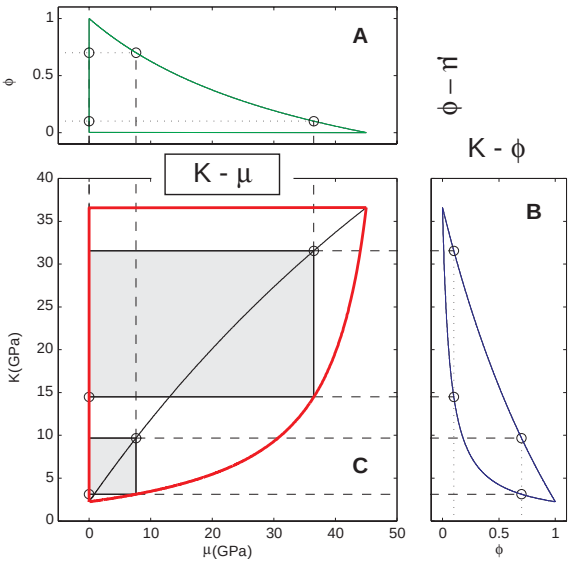

Figure 3.6: Hashin-Shtrikman bounds for water-saturated quartz sandstone in the $K - \mu$ domain are illustrated by the thick outline. For a given porosity, upper and lower bounds for the bulk modulus (K^{HS+} and K^{HS-}) and the shear modulus (μ^{HS+} and μ^{HS-}) can be determined individually from Equation 3.2 as in A (top) and B (right), respectively. Bounds in the $K - \mu$ domain for the porosity is a rectangle, whose upper-right corner is (K^{HS+}, μ^{HS+}) and the lower-left corner is (K^{HS-}, μ^{HS-}). The envelope of the rectangle as the porosity changes define the bounds in the $K - \mu$ domain. Top and bottom rectangles inside the thick outline in C are bounds of (K, μ) when the porosities are 0.1 and 0.7, respectively.

small values when the (K, μ) stays in the lower right quadrant. The bounds in Figure 3.8 show that the Poisson's ratio can be smaller than that of the low-porosity end member (the Poisson's ratio of the mineral) in intermediate porosities. More generally, Poisson's ratios of mixtures can be either greater or smaller than the Poisson's ratios of the end members, depending on the pore structures. Although the possible range of the Poisson's ratio of elastic materials is $-1 < \nu \leq 0.5$ from energy considerations, Figure 3.8 shows that the Poisson's ratio of an isotropic quartz-water mixture has narrower bounds, about $-0.324 \leq \nu \leq 0.5$. That is, HS theory limits the lower possible values of the Poisson's ratio. The Poisson's ratio of most natural reservoir rocks are greater than 0, such as the data points overlain on Figure 3.8.

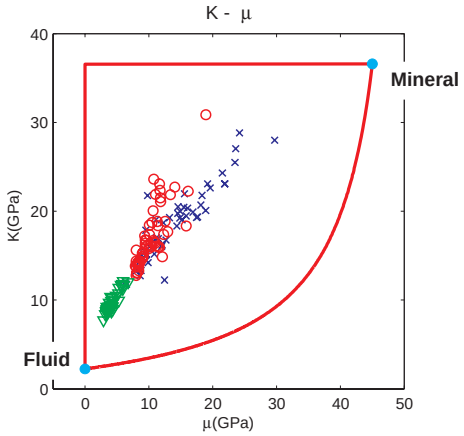

Figure 3.7: Hashin-Shtrikman bounds for water-saturated quartz sandstone in the $K - \mu$ domain. Data points from ultrasonic laboratory measurements are overlain onto the bounds.

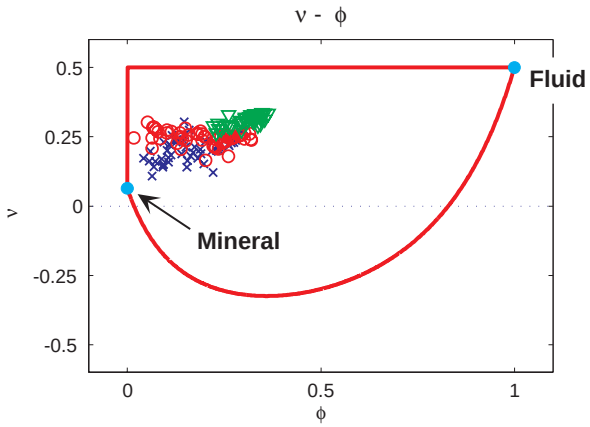

Figure 3.8: Hashin-Shtrikman bounds of the Poisson's ratio for water-saturated quartz-sandstone as a function of porosity. Data points from ultrasonic laboratory measurements are overlain onto the bounds.

3.2.4 Bounds in the $V_p - V_s$ Domain

Furthermore, Equation 3.4 enables us to extend the bounds in the $K - \mu$ domain to the bounds in the $V_p - V_s$ domain in Figure 3.9.

$$V_p = \sqrt{\frac{K + \frac{4}{3}\mu}{\rho}}, \qquad V_s = \sqrt{\frac{\mu}{\rho}} \tag{3.4}$$

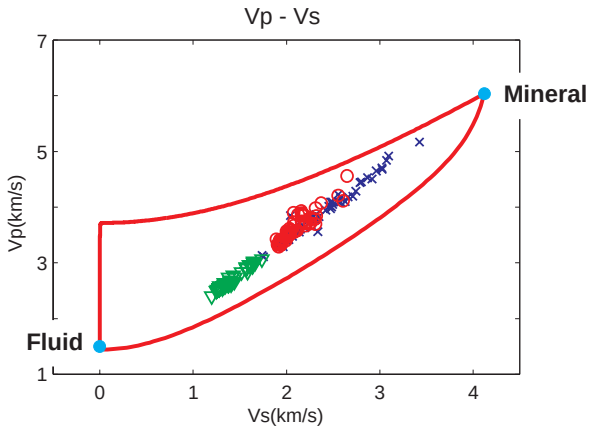

Figure 3.9: Hashin-Shtrikman bounds for water-saturated quartz sandstone in the $V_p - V_s$ domain. Data points from ultrasonic laboratory measurements are overlain onto the bounds.

The wedge-shaped outline in Figure 3.9 defines the HS bounds in the $V_p - V_s$ domain; (V_p, V_s) pairs of clean wet sandstone must be within the outline. The narrowly confined configuration of the bounds indicates that the V_p and V_s of sandstone must be well correlated (Takahashi et al., 1999c). Furthermore, as shown by laboratory data points overlain onto the bounds, the V_p and V_s of natural rocks are located along a linear trend and cover a limited region within the bounds.

Figure 3.10 illustrate the HS bounds in the $V_p - V_s$ domain for water-saturated limestone and chalk (calcite-water mixture). The difference of mineralogy makes the bounds for limestone and chalk fatter than the bounds for quartz-sandstone in Figure 3.9. The well-log and laboratory data overlain on the bounds in Figure 3.10 shows that V_p and V_s of natural limestone and chalk cover limited distribution within the bounds.

Figure 3.11 is the complete description of the Hashin-Shtrikman bounds for water-saturated quartz sandstone, shown in three dimension, V_p, V_s, and porosity. The wedge-shaped volume defines all possible elastic properties of a quartz-water mixture. The thinly limited volume of the wedge implies a high correlation between V_p, V_s, and porosity. The HS bounds in any two dimensions is a projection of the three-dimensional bounds.

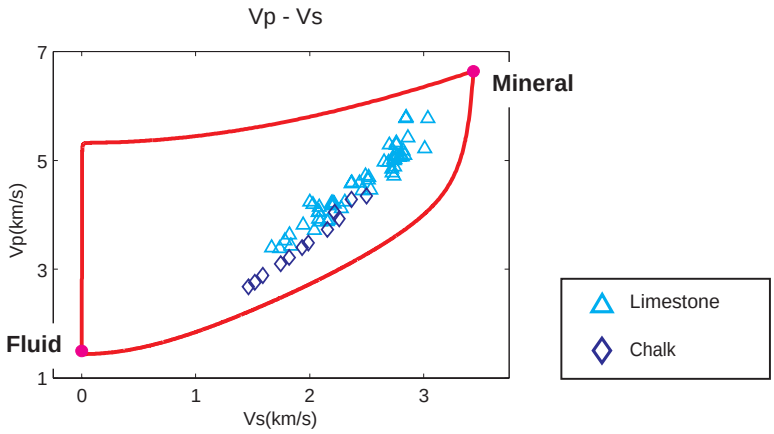

Figure 3.10: Hashin-Shtrikman bounds for water-saturated limestone in the $V_p - V_s$ domain. Data points from well-log and laboratory measurements are overlain onto the bounds.

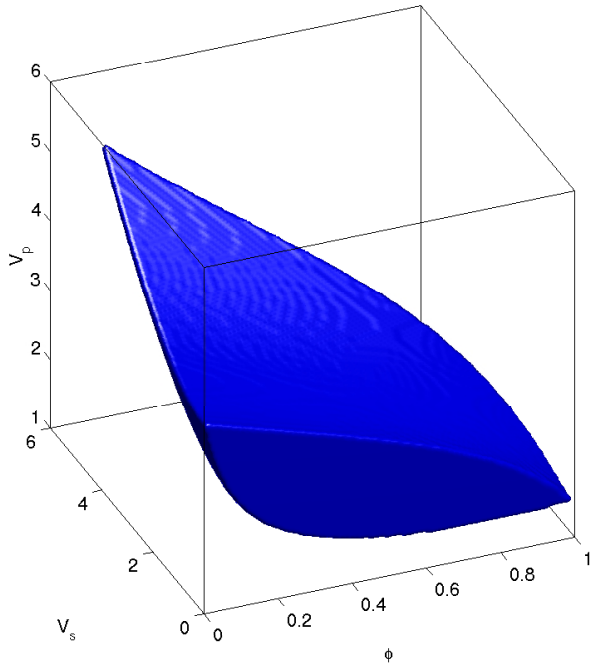

Figure 3.11: Hashin-Shtrikman bounds for water-saturated quartz sandstone in the $V_p - V_s - \phi$ domain. The volume inside the blue surface is the physically realizable combination of V_p, V_s, and porosity.

3.3 Stiffness Indices: Parameters to Extract the Pore Structure Information

3.3.1 Bounding Average Method

According to Marion and Nur (1991), values of elastic moduli relative to the corresponding HS upper and lower bounds (w in Equation 3.5) carry information about the stiffness of pore structures.

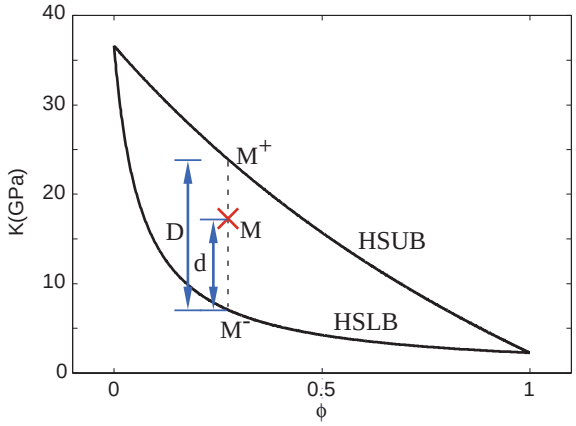

Figure 3.12: Bounding average method. The ratio of d relative to D represents the stiffness of the pore structure.

$$w = \frac{M - M^-}{M^+ - M^-} = \frac{d}{D} \tag{3.5}$$

where M is the elastic modulus of a sample and M^+ and M^- are the corresponding HS upper and lower bounds, respectively. Elastic moduli of monomineralic rocks, in general, are dependent on 1) mineralogy, 2) porosity, and 3) geometric details of the pore structure. The index, w, which ranges from 0 to 1, extracts and quantifies the information about the pore geometry; values close to 0 and 1 indicate softer and stiffer pore microstructures, respectively. Marion and Nur used this method to approximate Gassmann's theory and estimated bulk moduli after fluid substitution.

3.3.2 Stiffness Indices of Sandstones and Carbonates

We extend the bounding average method to extract information about the pore structure in relation to the shear stiffness, as well as about the bulk stiffness. We apply Equation 3.5 to bulk and shear moduli of various sandstone and carbonate samples and derive the *bulk* and *shear stiffness indices*, w_k and w_μ. Since w_k and w_μ are quasi-independent of mineralogy, the $w_k - w_\mu$ relation enables us to compare the pore structures of sandstones and carbonates. The data we use consist of well-consolidated sandstones (Han, 1986), high-porosity sandstones (Strandenes, 1991), poorly-consolidated sandstones (Blangy, 1992), limestone (Cadoret, 1993; Lucet, 1989; Yale and Jamieson, 1994), chalk (Urmos and Wilkens, 1993; Brevik, 1995), and dolomite (Geertsma, 1961; Yale and Jamieson, 1994) from various regions.

From Figures 3.13 and 3.15, we derive the stiffness indices—w in Equation 3.5—using the corresponding HS bounds for bulk and shear moduli. Figures 3.14 and 3.16 show cross-plots of w_k and w_μ for the sandstones and carbonates, respectively.

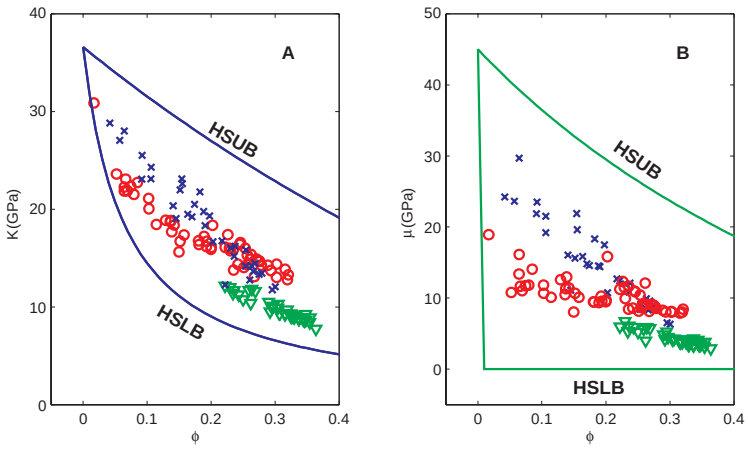

Figure 3.13: Sandstone data and the corresponding Hashin-Shtrikman upper bound (HSUB) and lower bound (HSLB) in the $K - \phi$ domain (A) and in the $\mu - \phi$ domain (B).

A comparison of sandstones and carbonates in the stiffness index domain shows a conspicuous distinction between the two rock types (Takahashi et al., 1999c). In sandstones,

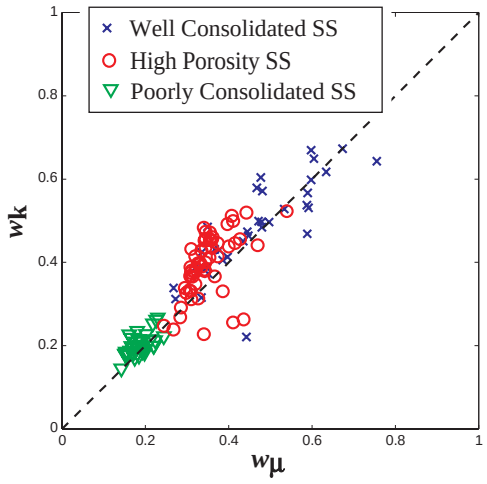

Figure 3.14: Stiffness indices of sandstones. The distribution is around the dashed $w_k = w_\mu$ line.

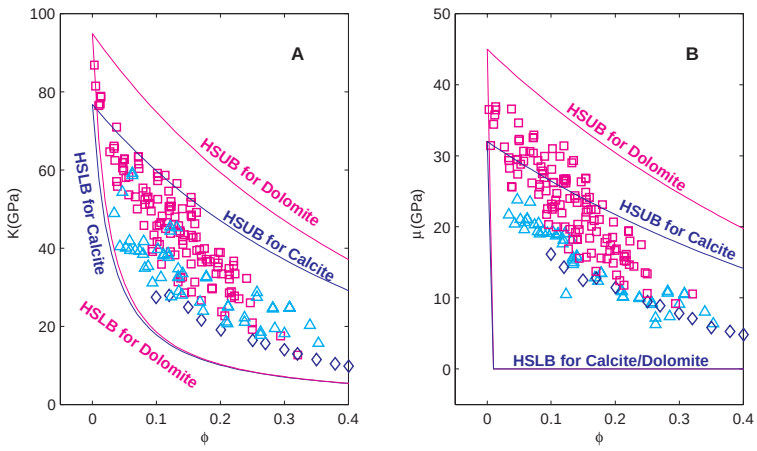

Figure 3.15: Carbonate data and the corresponding Hashin-Shtrikman upper bound (HSUB) and lower bound (HSLB) in the $K - \phi$ domain (A) and in the $\mu - \phi$ domain (B). HSUB/HSLB for calcite are used for the limestone and chalk, while the dolomite has its own bounds.

bulk stiffness indices, w_k, are greater than or equal to shear indices, w_μ, whereas w_μ are greater than w_k in carbonates. This is in contrast to the overlap of the $V_p - V_s$ relations of the same two data sets in Figure 3.1-A. The difference shows that pore structures of the

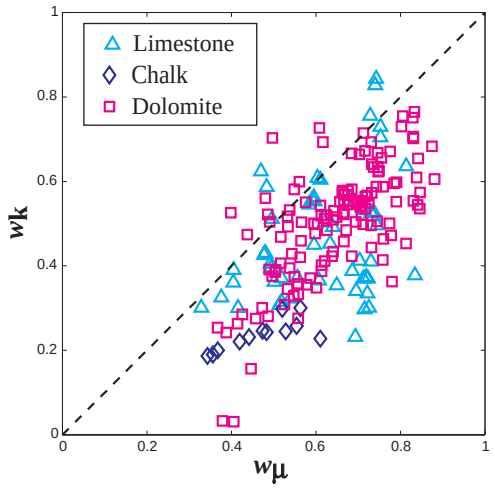

Figure 3.16: Stiffness indices of carbonates. The distribution is mainly in the lower-right quadrant.

sandstones are stiffer for volumetric deformations than for shear, while the carbonate pore structures are stiffer for shear deformations. The distinction in the $w_k - w_\mu$ domain gives rise to the different behaviors in their $V_p - V_s$ relations; distribution of the $w_k - w_\mu$ of carbonates in the lower-right quadrant makes their $V_p - V_s$ near the curved lower-right bound in Figure 3.10, while the centered $w_k - w_\mu$ of sandstones gives rise to a linear $V_p - V_s$ relation. We can also observe relatively large shear moduli of carbonates by comparing the $K - \phi$ and $\mu - \phi$ relations as shown in Figures 3.13 and 3.15. However, the stiffness indices amplifies the difference between sandstones and carbonates.

3.3.3 Rock Physics Models in the Stiffness Index Domain

We investigate the relation between the stiffness indices of various rock physics models, including both contact models and inclusion models (Wang and Nur, 1992), so that we may physically interpret the distinction between sandstones and carbonates observed in Figures 3.14 and 3.16.

Contact Models

The contact models we explore include the Hertz-Mindlin model (Mindlin, 1949), Walton's infinitely rough grain surface model and perfectly smooth grain surface model (1987), and Dvorkin and Nur's cementation model (1996). In the four models considered, Walton's smooth surface model assumes slippery grain-to-grain contacts with no tangential stiffness, whereas grain-to-grain contacts are completely locked together with infinite tangential stiffness in the other three models.

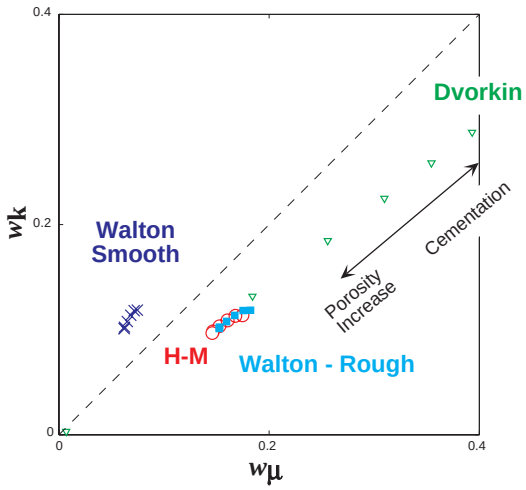

Figure 3.17: Stiffness indices of four contact models, the Hertz-Mindlin model, Walton's smooth contact model, Walton's rough surface model, and Dvorkin and Nur's cementation model.

Figure 3.17 shows that the models with locked contacts have greater w_μ than w_k, while the smooth contact model has greater w_k than w_μ. The $w_k - w_\mu$ relation for sandstones in Figure 3.14 remain between the two groups, implying a mixture of smooth and rough contacts in natural rocks (Bachrach, 1998). This observation is consistent with the fact that models with locked contacts tend to over-predict the V_s of sandstones (Dvorkin and Nur, 1996). In contrast, carbonates are well mimicked by the rigid contact models.

The difference in the contact shear rigidity can be explained by the relatively high diagenetic potential of carbonates; chemical activeness of carbonate minerals tends to create more cementation and dissolution in carbonates, making grain-to-grain contacts bonded together (Anselmetti and Eberli, 1997). On the other hand, quartz cementation in sandstones

occurs in later stages of diagenetic process (Surdam et al., 1993).

Inclusion Models

Figure 3.18 summarizes $w_k - w_\mu$ relations of two inclusion models, the self-consistent model (SC) (Berryman, 1980) and the differential effective medium model (DEM) (Berryman, 1992), for various pore aspect ratios. Depending on the pore aspect ratio, the inclusion

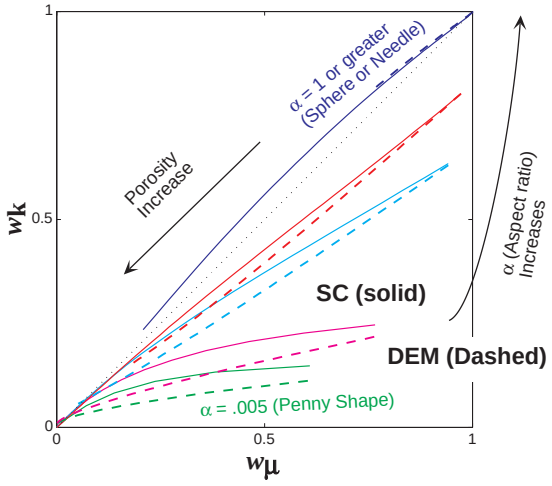

Figure 3.18: Stiffness indices of inclusion models. Different colors represent different pore aspect ratios. Solid and dashed lines are for the self-consistent model and the differential effective medium model, respectively.

models cover a wide range of $w_k - w_\mu$, comparable to the extent of natural rocks observed in Figures 3.14 and 3.16. Using the inclusion models, we can explain different $w_k - w_\mu$ relations of sandstones and carbonates by their pore shapes. Sandstones are well predicted by spherical or prolately-ellipsoidal (needle-like) inclusions, *i.e.*, $w_k \approx w_\mu$, whereas oblately-ellipsoidal (penny-shaped) inclusions mimic carbonates, *i.e.*, $w_k < w_\mu$.

3.4 Conclusions

We explored $V_p - V_s$ relations of sandstones and carbonates to infer information about their pore structures. By combining the bounds defined for the bulk and shear moduli, we

extended the Hashin-Shtrikman theory and showed that the $V_p - V_s$ relation of monomineralic rocks must be well correlated. We then introduced bulk and shear stiffness indices, w_k and w_μ, which quantify information about pore structure and enable comparison between sandstones and carbonates. Using the stiffness indices, we revealed that the pore structures of sandstones are stiffer in compression than in shear, *i.e.*, $w_k \geq w_\mu$, whereas the pore structures of carbonates are stiffer in shear than in compression, *i.e.*, $w_\mu > w_k$. Finally, investigation of the stiffness indices of various rock physics models showed that either the difference in the types of grain-to-grain contacts or the difference in the pore shapes could be responsible for the different $V_p - V_s$ relations of sandstones and carbonates.

Chapter 4

Information and Uncertainty in Rock Property Estimation

"Any physical theory is a kind of guesswork. There are good guesses and bad guesses. The language of probability allows us to speak quantitatively about some situation which may be highly variable, but which does have some consistent average behavior.

. . .

Our most precise description of nature must be in terms of probabilities."

— Richard Phillips Feynman

Abstract

Subsurface property estimation from geophysical measurements is always subject to uncertainty because of many inevitable difficulties in data acquisition, processing, and interpretation. In this chapter, we present methods to express quantitatively information and uncertainty in rock property estimation from seismic data. Probability density functions enable us to describe quantitatively the state of knowledge about objective rock properties and the relationships between rock properties, including their inherent uncertainty. We present a procedure to retrieve pdfs from available data by taking account of the spatial sampling and the measurement error. We also discuss how to extend available data to establish the pdfs of non-observed physical conditions.

After exploring non-linear statistical measures of information and uncertainty, such as information entropy, mutual information, and the Bayes error, we discuss what gives us information about rock properties and what does not. Investigations using the statistical measures reveal that information about rock properties cannot be gained by mere data manipulations. Instead, geophysical data, physical theories, and geological knowledge bring us information and reduce uncertainty about rock properties.

4.1 Introduction

Estimation of subsurface properties from geophysical data is inherently subject to uncertainty. Hence, geophysical prospecting is a process that reduces uncertainty, thereby increasing information about objective subsurface properties rather than finding absolutely correct values of rock properties. In order to reduce uncertainty about subsurface properties, we acquire geophysical data, apply adequate physical laws, and combine available geological knowledge.

In this chapter, rock property estimation problems and their inherent uncertainty are quantitatively expressed by statistical formulations of probability theory and information theory (Tarantola and Valette, 1982; Tarantola, 1987). In these theories, the probability density function (pdf) is used to express the *"state of knowledge"* about our objectives, that is, *how well we know the objectives* and *how uncertain our objectives are*. We also discuss how to estimate the pdf from available data, with emphasis on the physical implication of the estimation. Finally, using the statistical formulations, we quantitatively investigate the sources of information in rock property estimation.

4.2 Using PDFs to Describe the *State of Knowledge*

In estimation problems, the probability density function, pdf, expressed by the likeliness of each parameter value, provides us with the complete and quantitative description of the *"state of knowledge"*, information and uncertainty about objectives (Feynman et al., 1963; Gouveia et al., 1996; Gouveia, 1996; Scales and Snieder, 1997; Scales and Tenorio, 1998).

4.2.1 Uncertainty About Rock Properties

The two curves in Figure 4.1 illustrate the pdfs of porosity of two different reservoirs. The probability density values represent the likeliness of each porosity value in each reser-

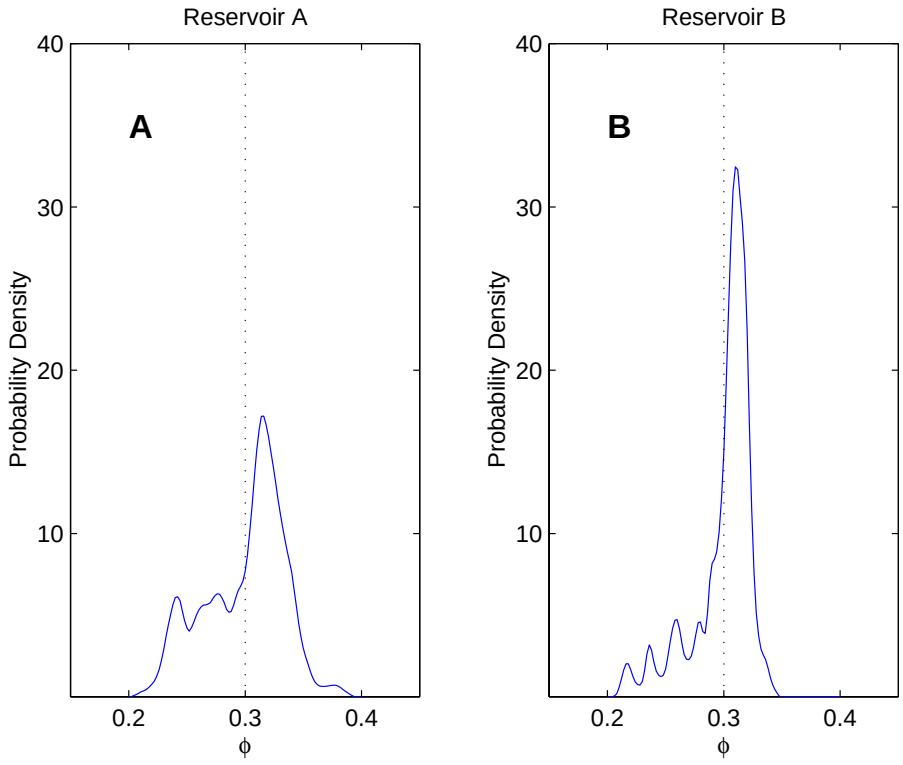

Figure 4.1: Probability density functions of porosity in two reservoirs, A and B. The pdfs represent *"state of knowledge"* about porosity. Reservoir A has larger uncertainty about porosity than reservoir B.

voir. The peaks of the functions correspond to the mostlikely porosities, and the ranges where the functions have non-zero values show possible ranges of porosity values. In reservoir A, the pdf has a smoother and broader shape, while the distribution is more peaky and taller in reservoir B. A comparison of the pdfs reveals a difference in uncertainty. The uncertainty in porosity is greater for reservoir A than for reservoir B, since porosity values close to the peak are more probable in B, while possible porosity has a wider range in A.

Using the pdf, we can express a perfect knowledge about a porosity value by the Dirac's delta function (Gouveia et al., 1996), *i.e.*, $p(\phi) = \delta(\phi - \phi_o)$, as shown in Figure 4.2-A.

This occurs when we are completely sure that the porosity is equal to ϕ_o, which is virtually impossible in geophysical prospecting. On the other hand, complete ignorance of porosity can be described by the uniform function, $p(\phi) = const.$, over the entire porosity range. From the physical definition, porosity of any rock must be in the range $0 \leq \phi \leq 1$, hence the uniform prior is $p(\phi) = 1$, as in Figure 4.2-B. The uniform function represents the case when all possible porosity values are equally likely; we have the least knowledge about porosity.

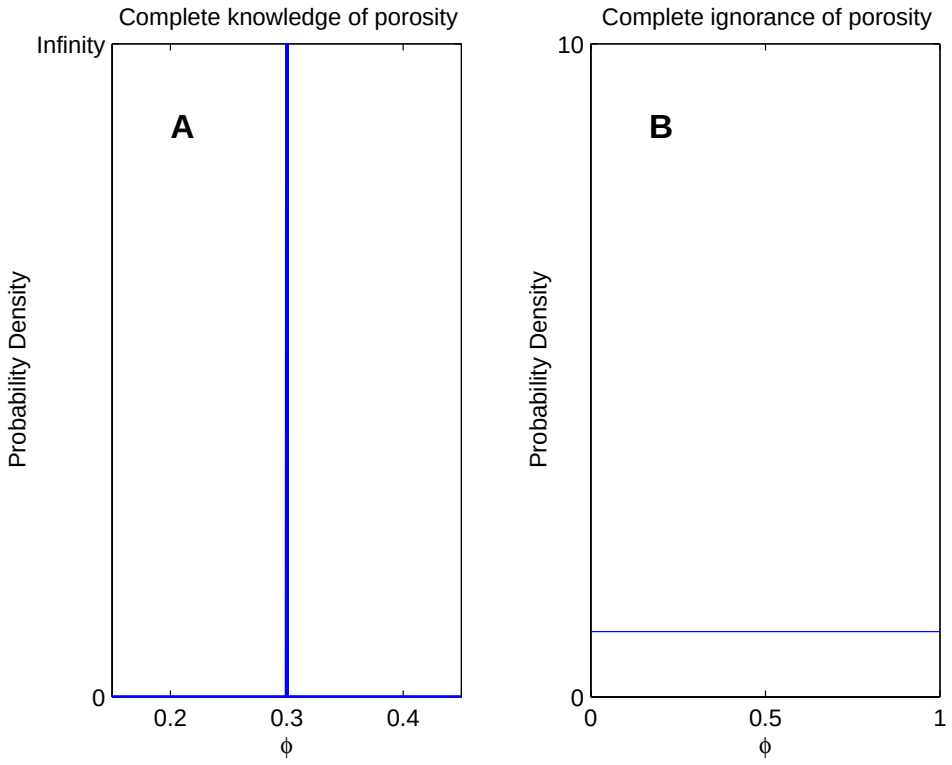

Figure 4.2: Probability density functions of porosity with complete knowledge (A) and complete ignorance (B) about porosity, described by the Delta function and the uniform function, respectively.

In spite of our hopes and efforts, *no geophysical measurement can provide us with perfect knowledge about subsurface properties*. This limitation is because of restricted data acquisition geometry, random and coherent noise, our limited physical knowledge, the large complexity of Nature, and many other inevitable difficulties. Hence, practical and

reachable objectives of geophysical prospecting are constraining the knowledge about subsurface properties and minimize their uncertainty, rather than aiming for absolutely correct values of subsurface properties. In view of this point, unique values are not sufficient to describe the answers of our estimation, but the pdfs are needed to describe the answers.

Furthermore, rock properties expressed by pdfs, along with considerations of their economical values, are essential input for the decision analysis and the risk analysis. Typically in oil exploration and development, the pdf of oil reserves of undrilled prospects is estimated from the pdfs of individual reservoir properties, before it is used to evaluate whether the prospect is worth drilling (Steinmetz, 1992).

4.2.2 Dependence Between Rock Properties

Probability density functions are also helpful in describing the dependence between two or more subsurface parameters that are non-linear and non-unique. When we deal with real data, the relations between rock properties are rarely well fit by deterministic functions, but they are usually scattered (such as the V_p-porosity relation of a North Sea reservoir in Figure 4.3).

The scatter in Figure 4.3 illustrates the range of V_p that can correspond to one porosity value, as well as the range of porosity possible for one V_p. Because of the diversity, a linear regression line poorly describes the $V_p - \phi$ dependence. The dispersions of rock property relations are often due to geological heterogeneity within the reservoir. In other words, the variability of rock properties other than these plotted (*i.e.*, pore pressure, clay content, and types of saturating fluid) causes scattering. Since the geological heterogeneity is the inherent characteristic of many reservoirs, we need to take it into account in rock property estimation.

Using pdfs, we can fully describe the dependence between two or more rock properties, *including its inherent non-uniqueness and non-linearity*. Figure 4.4 is a bivariate pdf of porosity and P-wave velocity, $p(V_p, \phi)$, derived from the scattered data in Figure 4.3. The broadness of the pdf expresses the non-uniqueness of the relation.

Also, bivariate pdfs contain a full description of the individual properties, comprising two dimensions of the pdfs. Given the bivariate pdf in Figure 4.4, $p(V_p, \phi)$, the univariate

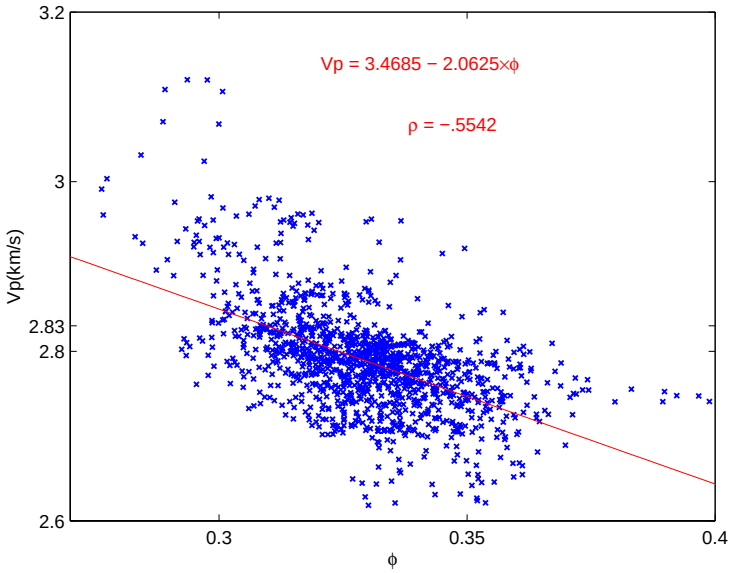

Figure 4.3: $V_p - \phi$ relations of a North Sea reservoir. Scatter of the relation shows heterogeneity of the reservoir. A linear regression line and its equation are overlain.

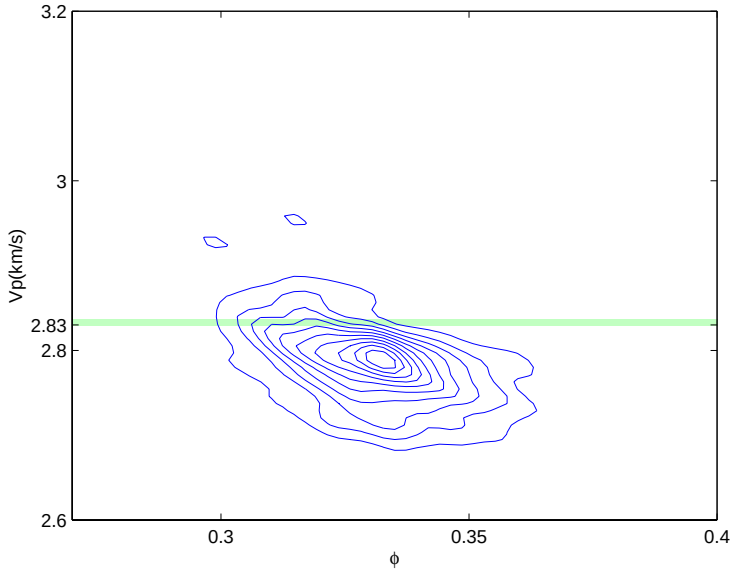

Figure 4.4: Bivariate pdf of V_p and ϕ, $p(V_p, \phi)$ of a North Sea reservoir. The broad shape describes inherently non-deterministic relations between porosity and V_p.

pdf of porosity can be derived by the integration along the V_p dimension as

$$p(\phi) = \int p(V_p, \phi) dV_p \tag{4.1}$$

$p(\phi)$, shown in Figure 4.5, is the marginal pdf of the bivariate pdf, which expresses a prior state of knowledge about porosity without V_p observations. Typical regression lines predict unique values of porosity for a given velocity, as shown in Figure 4.3. For example, for an observed velocity of 2.83 km/s, the predicted porosity is 0.31. In contrast, from the bivariate pdf, the estimate of porosity can be given by the conditional pdf of porosity given the velocity, $p(\phi|V_p)$, as shown in Figure 4.5. In fact, a deterministic relation, such as the linear regression in Figure 4.3, can be expressed using a Delta function as an extreme case, $p(V_p, \phi) = \delta(V_p - 3.4685 + 2.0625\phi)$. Graphically, the conditional pdf is realized by taking a horizontal section of the bivariate pdf along the given velocity, followed by normalization.

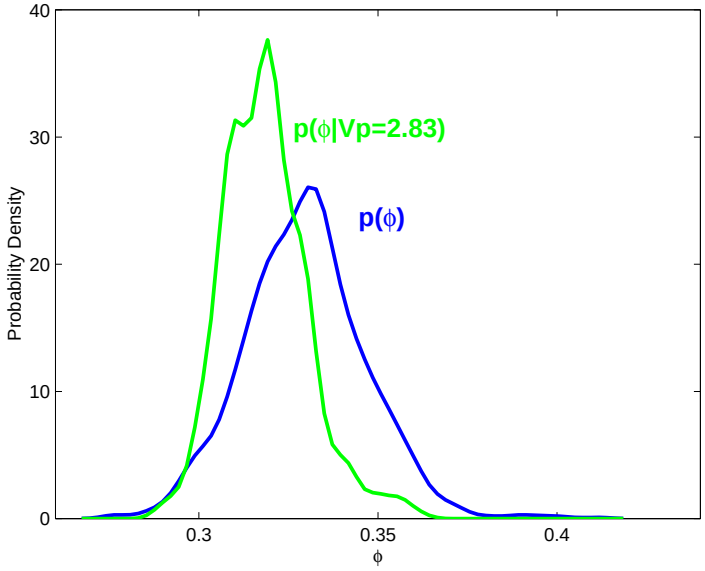

Figure 4.5: The conditional pdf of porosity given a velocity and the marginal pdf of porosity. Velocity data condition porosity information and reduce its uncertainty.

The conditional pdf represents the state of knowledge about porosity after observing a V_p of 2.83 km/s. The mostlikely porosity for a given velocity is the one that maximizes the conditional pdf, $p(\phi|V_p)$, which is $\phi_{m.l.} = 0.32$ for V_p =2.83 km/s. A comparison between

the conditional pdf ($p(\phi|V_p = 2.83)$) and the marginal pdf of porosity ($p(\phi)$) in Figure 4.5 demonstrates that uncertainty about porosity is reduced by the velocity observation, since the conditional pdf has a sharper and narrower shape than the marginal pdf. The width of the conditional pdf expresses the remaining uncertainty after the velocity observation, *i.e.*, velocity observation does not guarantee a unique porosity value, but it *conditions* or *constrains* our knowledge about porosity. We describe precise and quantitative measures of uncertainty in section 4.4.

4.3 Estimation of Non-Parametric PDFs

Probability density functions represent our knowledge about subsurface properties. They should be consistent with measured data, rock physics theories, and our geological ideas about objective rocks. In seismic reservoir characterization, well data along with rock physics models may be used to build pdfs.

4.3.1 Retrieving PDFs of In-situ Conditions

If we allow ourselves to describe subsurface properties with a pdf, data acquisition of physical properties can be considered as sampling from the pdf. Assuming that measured data are non-biased samples from the pdf, we can retrieve the pdf by smoothing their sample histograms. The smoothing is to account for the following two different *physical limitations of available data*: spatial sampling and measurement errors.

Spatial Interpolation

Data we obtain are properties of discrete points in a large volume of target rocks. Well data, in general, are sparse laterally, although they are densely sampled in the vertical direction.

When sampling is relatively sparse for a heterogeneous target rock, properties of the target are not well represented by the data. Therefore, the data samples need to be *interpolated* to recover the pdf, which must picture the properties of the whole target. Mathematically, a complete continuous function can be retrieved from its samples by convolution with the

sinc function, $sincx = \frac{\sin \pi x}{\pi x}$, when the sampling interval is uniform (Bracewell, 1921). However, since pdfs cannot have negative values, a Gaussian function is often used (Silverman, 1986) because of its similarity to the sinc function, as well as the positiveness. The width of the smoothing function should be consistent with the sparseness of data sampling.

Measurement Errors in Data Acquisition

Any subsurface physical measurement, including well logs, involves measurement errors due to imperfect acquisition conditions and limited resolution of acquisition tools. Hence, data we acquire may not completely represent even the properties of the sampled points. In order to describe the incompleteness of the measurement rigorously, we can again use a pdf.

The two pdfs of porosity shown in Figure 4.6 are information given by a single measured porosity of 0.3 with different measurement errors. When the error is small, as in A, only porosity values close to the measured value of 0.3 are likely. A wider range of porosity values are possible when the error is large, as in B. The shape of the error function can be arbitrary, depending on the types of errors in the measurement system. In many cases, a Gaussian function may be used whose width is consistent with the measurement error.

Smoothing discrete data to build pdfs is often done with very little physical consideration of the two points above. However, it should be noted that the smoothing with a specific function is equivalent to assuming that errors and interpolation are represented by the particular smoothing function.

4.3.2 Coordinate Transform

Some rock properties are interrelated to each other by deterministic physical relations. For example, the acoustic impedance is defined as the product of density and velocity, and the bulk modulus can be given by V_p, V_s, and density. In fact, any two pairs of elastic properties can be exactly derived from any other pairs (Mavko et al., 1998). In rock property estimation, we sometimes use those relations back and forth to change variables in order

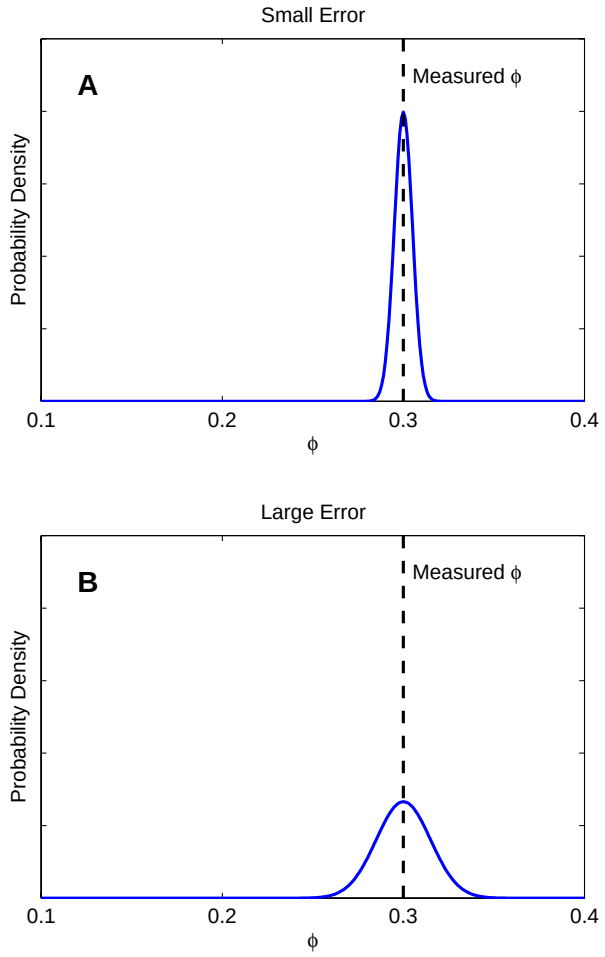

Figure 4.6: Probability density functions to express information given by erroneous data. Measured porosity of 0.3 can be described by a pdf with a high peak if the error is small (A). The pdf becomes broad when the expected error is large (B).

to compare observed data with other data or with theoretical models. The coordinate transformation of probability density functions (pdfs) and probability mass functions should be conducted with consideration of the following points.

Probability Density Function

If we want to transform a pdf in one coordinate to a mathematically equivalent one in a new coordinate system, the coordinate transform should observe the following relation:

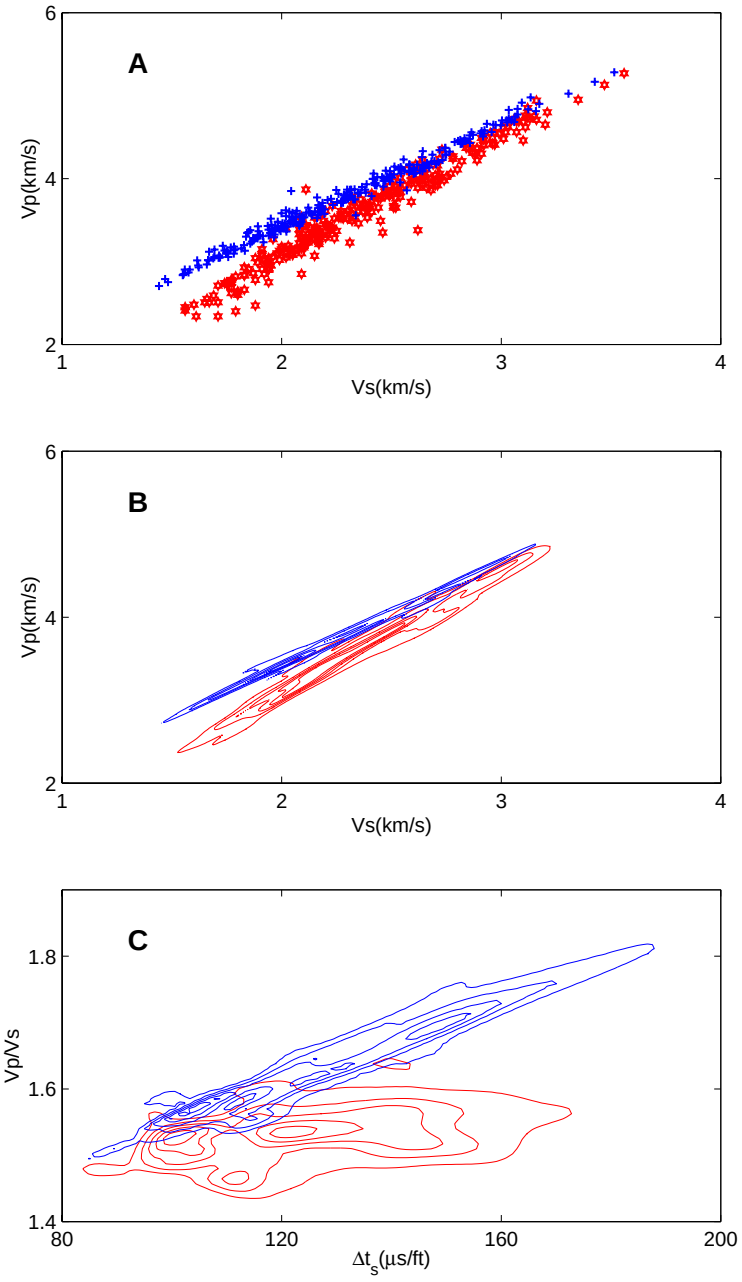

Figure 4.7: Observed discrete data (A) and the bivariate pdf (B) of V_p and V_s of gas and water-saturated sandstones. The equivalent bivariate pdf of B in $V_p/V_s - \Delta t_s$ domain is derived by Equation 4.2 and shown in C.

If a random variable, $\mathbf{N}$, is a function of another random variable, $\mathbf{M}$, as $\mathbf{N} = \mathbf{N}(\mathbf{M})$, and if we can assume one-to-one correspondence between the $\mathbf{M}$ and $\mathbf{N}$ domains, the multi-dimensional pdf in $\mathbf{M}$ domain, $p(\mathbf{m})$, and the equivalent pdf in the $\mathbf{N}$ domain, $p(\mathbf{n})$, are related by

$$p(\mathbf{m}) = p(\mathbf{n}) \left| \frac{\partial \mathbf{n}}{\partial \mathbf{m}} \right| \tag{4.2}$$

In a non-linear coordinate transform when the Jacobian, $\left| \frac{\partial \mathbf{m}}{\partial \mathbf{n}} \right|$, is not constant, the configuration of the pdf is different from one coordinate system to another. Furthermore, *linear statistical characters, such as mean, variance, standard deviation, correlation coefficient, covariance, etc. are variant with respect to the non-linear transform*. On the other hand, non-linear measures, such as Bayes error, information entropy, and mutual information, which are described in the next sections, are invariant with a non-linear change of variables.

Likewise, a stationary smoothing function in one domain changes to a non-stationary function in another domain when the transform is non-linear. When building pdfs in two non-linearly related domains, we may be tempted to first coordinate transform discrete data, before smooth-filtering in the two different domains. However, the two pdfs created from this procedure are not equivalent to each other, because physical assumptions of errors and interpolation become different unless the smoothing function observes Equation 4.2. The correct procedure is to smooth discrete data and create the pdf in one domain, then transform the coordinate of the pdf, using Equation 4.2.

Figure 4.7 shows an example of the equivalent pdfs in two different domains, $V_p - V_s$ and V_p/V_s ratio-Δt_s (S-wave slowness). Since the V_p/V_s ratio and Δt_s can be deterministically derived from V_p and V_s, the transforms are no more than mathematical manipulations. Hence, the significance of the two pdfs in terms of predictability of rock properties are exactly equivalent, in spite of their different appearances.

Probability Mass Function

Although probability density functions are variant with respect to non-linear coordinate transforms, probability mass functions are invariant, if discretization of the pdfs in the two

domains are equivalent. When a probability mass function, $P(\mathbf{m}_i)$, is defined using V_i, the ith sub-volume of the $\mathbf{M}$ domain, as

$$P(\mathbf{m}_i) = \int_{\mathbf{m}\in\mathbf{V}_i} \cdots \int p(\mathbf{m}) d\mathbf{m} \tag{4.3}$$

the probability mass function is transformed to the $\mathbf{N}$ domain as

$$\begin{aligned} P(\mathbf{m}_i) &= \int_{\mathbf{n}\in\mathbf{U}_i} \cdots \int p(\mathbf{m}(\mathbf{n})) \left| \frac{\partial \mathbf{n}}{\partial \mathbf{m}} \right| d\mathbf{m} \\ &= \int_{\mathbf{n}\in\mathbf{U}_i} \cdots \int p(\mathbf{n}) d\mathbf{n} \\ &= P(\mathbf{n}_i) \end{aligned} \tag{4.4}$$

where U_i is the sub-volume of $\mathbf{N}$ equivalent to V_i in the $\mathbf{M}$ domain. Equation 4.4 states that probabilities of the corresponding bins in the two domains are identical, *i.e.*, the probability mass function is invariant with respect to non-linear coordinate transforms if the bins are transformed appropriately to the corresponding ones.

Figure 4.8 shows changes of bin sizes by a non-linear transform, from the $V_p - V_s$ to the $V_p/V_s - \Delta t_s$ domain. The boxes of same colors are corresponding bins in each domain. Although the probability density functions are variant with respect to the non-linear transform, as discussed earlier, the probabilities within each corresponding bin are identical, since the change in bin size takes care of the changes of the probability densities.

4.3.3 Deriving PDFs From Physical Modeling

Since the number of data are usually limited as compared to the volume of target rocks, we may not be able to obtain data for every possible physical condition of the targets, especially in terms of the time dimension when changes in the physical state are expected after data acquisition. One common example is the prediction of seismic velocity after fluid injection in feasibility studies of seismic reservoir monitoring. Sometimes the difference in physical conditions between the past measurement, whose data are used to establish the

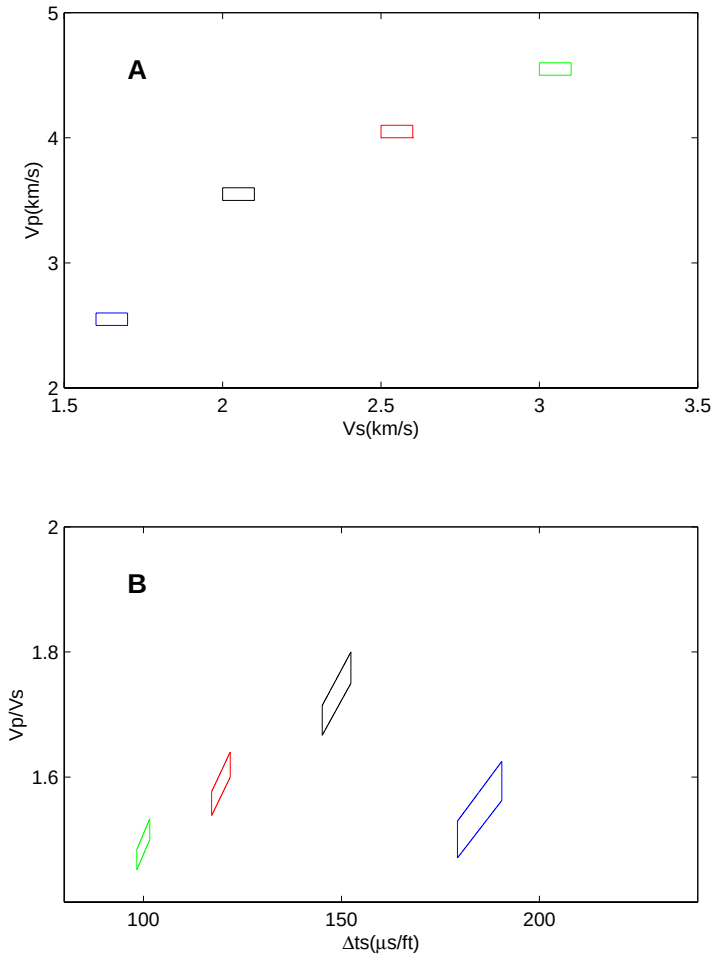

Figure 4.8: Changes of bin sizes in coordinate transform of probability mass function. Because of the non-linearity of the relation between the two coordinates, V_p-V_s in A and V_p/V_s-Δt_s in B, the corresponding bin sizes vary.

pdf, and the future measurement, whose data will be used for predicting rock properties, can be significant. Typically, pdfs of seismic responses, which will be used for rock property estimation, are predicted from pdfs established from well log measurements. In such cases, the difference of resolution between the two tools, sonic and surface seismic, can be significant. In these two situations, physical modeling helps *extend* the available data base to predict the pdf at unobserved physical conditions.

Deterministic Model

If the relations between observed data and data in non-observed conditions are deterministically described by theoretical equations, such as Gassmann's equation in fluid substitution problems, derivations of the pdf at new physical conditions are simple coordinate transforms. For example, in a case of estimating the P-wave velocity of an oil-saturated reservoir from data of the same reservoir saturated with brine, the oil reservoir's V_p is a deterministic function of the brine reservoir's V_p, as $V_{p_{oil}} = G(V_{p_{brine}})$ (G being Gassmann's equation), if the porosity, the compressibilities of brine and oil, the densities of brine and oil, and the bulk modulus of the mineral are exactly known. Therefore, the relation between the two pdfs is

$$p(V_{p_{brine}}) = p(V_{p_{oil}}) \left| \frac{\partial V_{p_{oil}}}{\partial V_{p_{brine}}} \right| = p(G(V_{p_{brine}}))G'(V_{p_{brine}}) \tag{4.5}$$

In order to obtain the pdf, $p(V_p, fluid)$, which may be used to predict fluid types from V_p, we also need to consider the prior probabilities as

$$p(V_p, Fluid = oil) = p(V_p|Fluid = oil)p(Fluid = oil) = p(V_{p_{oil}})p(oil) \tag{4.6}$$

$$p(V_p, Fluid = brine) = p(V_p|Fluid = brine)p(Fluid = brine) = p(V_{p_{brine}})p(brine) \tag{4.7}$$

where $p(oil)$ and $p(brine)$, the prior probabilities of oil and brine, respectively, represent information about fluid types prior to the V_p observations. Figure 4.9 shows an example of a data-derived pdf, $p(V_p, Fluid = brine)$, and a pdf derived from Gassmann's modeling, $p(V_p, Fluid = oil)$.

Probabilistic Model

More generally, rock property relationships may be defined by a combination of many theories or given by experimental relations. When physical properties in unobserved conditions, $\mathbf{m}$, are modeled from observed physical properties, $\mathbf{n}$, the relation between $\mathbf{m}$ and $\mathbf{n}$ can be expressed by a multi-dimensional pdf, $p(\mathbf{m}, \mathbf{n})$ (Tarantola and Valette, 1982; Tarantola, 1987). The pdf of rock properties in unobserved conditions can then be derived by

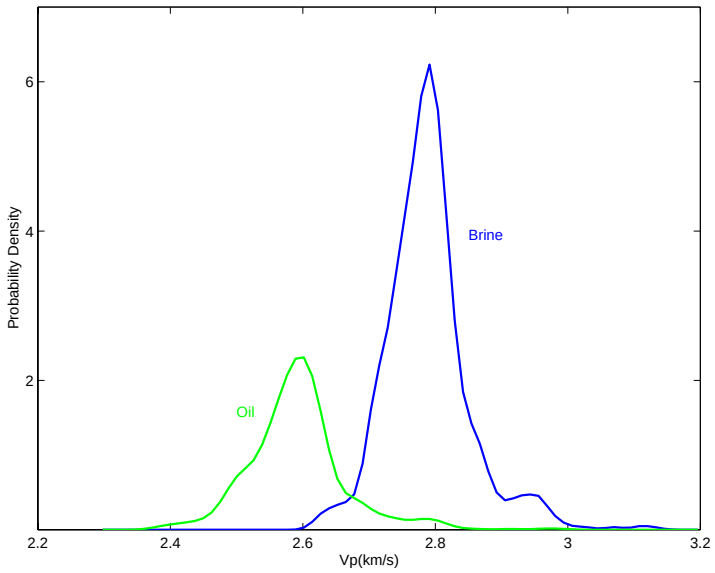

Figure 4.9: The pdfs of V_p for brine-saturated and oil-saturated reservoirs, $p(V_p, fluid = brine)$ and $p(V_p, fluid = oil)$. The pdf of the oil reservoir is derived from Gassmann's modeling using Equation 4.5. The area under the brine pdf is larger than the area under the oil pdf, observing $p(brine) > p(oil)$.

taking the marginal pdf of the multivariate pdf as

$$p(\mathbf{m}) = \int \cdots \int p(\mathbf{m}, \mathbf{n}) d\mathbf{n} = \int \cdots \int p(\mathbf{m}|\mathbf{n}) p(\mathbf{n}) d\mathbf{n} \tag{4.8}$$

In practice, when the pdfs have arbitrary form, the integration in Equation 4.8 can be accomplished by Monte Carlo simulations (Omre and Tjelmeland, 1997; Tjelmeland and Omre, 1997; Takahashi et al., 1999a; also discussed in chapter 6 of this thesis), in which many sampled realizations out of the pdfs are used for physical forward modeling. Equation 4.8 reduces to Equation 4.5 when the physical modeling is described by deterministic equations.

4.4 Non-linear Statistical Measures of Uncertainty and Information

Statistical formulations with pdfs help us express our state of knowledge about rock properties and the relationships between rock properties. It is useful to have parameters that represent certain characters of the complete pdfs. In this section, we discuss non-linear statistical measures of information and uncertainty, information entropy, mutual information, and the Bayes error.

4.4.1 Information Theory

Information theory, introduced by Shannon (1948), has been developed extensively in the communication industry and deals with the data transmission and the data compression. At the same time, because of its all-encompassing inference, the theory has been amplified in physics and statistics, as well as applied to computer science and economics (Ash, 1965; Cover and Thomas, 1991; Gouveia et al., 1996).

Since geophysical prospecting, from a certain viewpoint, is a process of increasing information about subsurface properties, many ideas in information theory help us to understand and describe its problems (Mavko and Mukerji, 1998; Takahashi et al., 1999b). We apply the theory to quantify information and uncertainty in subsurface property estimation.

Information Entropy

In information theory, uncertainty is quantified by a parameter called *information entropy*. Information entropy about a random variable, $\mathbf{M}$, is defined as

$$H(\mathbf{M}) = -\sum_i P(\mathbf{m}_i) \log_e P(\mathbf{m}_i) \tag{4.9}$$

where $P(\mathbf{m}_i)$ is the probability mass function of $\mathbf{M}$ defined in Equation 4.3.

In the example shown in Figure 4.1, the entropy value is 4.17 in reservoir A and 3.63 in reservoir B, showing that the uncertainty is greater in A. Minimum and maximum values of the information entropy occur for complete knowledge and complete ignorance about

objectives, as shown in Figure 4.2. Information entropy is *invariant with respect to non-linear coordinate transforms*, since the probability mass function is invariant if each bin is correctly transformed to the equivalent one in the other domain.

Since the information entropy is defined from the probability mass function, not from the probability density function, it is not unique to a pdf, but it depends on how we discretize a given pdf to produce the mass function (Middleton, 1960). Bin sizes in the discretization should be consistent with the expected accuracy of the estimation. The entropy values increase when the bin sizes are decreased.

Relative Entropy

Relative entropy represents the difference of uncertainty of a pdf relative to a reference pdf, and it is *free from discretization*.

$$D(p||q) = -\int p(\mathbf{m}) \log_e \frac{p(\mathbf{m})}{q(\mathbf{m})} d\mathbf{m} \tag{4.10}$$

where $p(\mathbf{m})$ is the pdf of objective properties, $\mathbf{m}$, and $q(\mathbf{m})$ is a reference pdf in the $\mathbf{M}$ domain. As the reference, the uniform function, $q = const.$, is often used, which corresponds to the complete ignorance about the objectives.

Although the pdf is variable with respect to non-linear coordinate transformations, the relative entropy is invariant. This can be demonstrated by

$$\begin{aligned} D(p(\mathbf{m})||q(\mathbf{m})) &= -\int p(\mathbf{m}) \log_e \frac{p(\mathbf{m})}{q(\mathbf{m})} d\mathbf{m} \\ &= -\int p(\mathbf{n}) \left|\frac{\partial \mathbf{n}}{\partial \mathbf{m}}\right| \log_e \frac{p(\mathbf{n}) \left|\frac{\partial \mathbf{n}}{\partial \mathbf{m}}\right|}{q(\mathbf{n}) \left|\frac{\partial \mathbf{n}}{\partial \mathbf{m}}\right|} d\mathbf{m} \\ &= -\int p(\mathbf{n}) \log_e \frac{p(\mathbf{n})}{q(\mathbf{n})} d\mathbf{n} \\ &= D(p(\mathbf{n})||q(\mathbf{n})) \end{aligned} \tag{4.11}$$

i.e., the relative entropy in the $\mathbf{M}$ domain, $D(p(\mathbf{m})||q(\mathbf{m}))$, is equivalent to the relative entropy in the $\mathbf{N}$ domain, $D(p(\mathbf{n})||q(\mathbf{n}))$.

Mutual Information

Observation of geophysical data reduces uncertainty about objective rock properties. In the example shown in Figures 4.4 and 4.5, a velocity observation of 2.83 km/s decreases information entropy from $H(\phi) = 3.44$ to $H(\phi|V_p = 2.83) = 3.06$. The reduced entropy represents the information provided by the velocity data.

Likewise, the dependence between properties can in general be quantified by the expected entropy decrease of one property by observing the other, which is called *mutual information*. The mutual information of random variables $\mathbf{M}$ and $\mathbf{D}$ is defined as

$$I(\mathbf{M}|\mathbf{D}) = H(\mathbf{M}) - H(\mathbf{M}|\mathbf{D}) \tag{4.12}$$

where $H(\mathbf{M})$ is the entropy of $\mathbf{M}$ and $H(\mathbf{M}|\mathbf{D})$ is the conditional mean entropy of $\mathbf{M}$ given $\mathbf{D}$ defined by

$$H(\mathbf{M}|\mathbf{D}) = -\sum_j P(\mathbf{d}_j) H(\mathbf{H}|\mathbf{D} = \mathbf{d}_j) = -\sum_j \sum_i P(\mathbf{m}_i, \mathbf{d}_j) \log_e P(\mathbf{m}_i|\mathbf{d}_j) \tag{4.13}$$

The conditional mean entropy, $H(\mathbf{M}|\mathbf{D})$, is the expected entropy of $\mathbf{M}$ when $\mathbf{D}$ is given. Hence mutual information expresses difference in uncertainty about $\mathbf{M}$ before and after knowing $\mathbf{D}$.

The mutual information may be normalized to show the information relative to the uncertainty at the prior state as

$$I_n(\mathbf{M}|\mathbf{D}) = I(\mathbf{M}|\mathbf{D})/H(\mathbf{M}) = 1 - \frac{H(\mathbf{M}|\mathbf{D})}{H(\mathbf{M})} \tag{4.14}$$

$$0 \le I_n(\mathbf{M}|\mathbf{D}) \le 1, \qquad \because 0 \le I(\mathbf{M}|\mathbf{D}) \le H(\mathbf{M})$$

Since $H(\mathbf{M})$ is the information required to predict the target rock properties, the normalized information represents completeness of the estimation.

In the example in Figures 4.4 and 4.5, mutual information about porosity carried by V_p, $I(\phi|V_p)$, is 0.22 and the normalized information, $I_n(\phi|V_p)$, is 0.07. Seismic velocity does not constrain porosity very much in this case. Since the mutual information is derived from the information entropy, it is invariant with respect to coordinate transforms.

4.4.2 Bayes Decision Theory

Pdfs provide us with not only the mostlikely prediction of rock properties for given data, but also with the reliability of the predictions and the probability of their errors (Duda and Hart, 1973; Box and Tiao, 1992; Houck, 1999). The following example describes the decision criterion and its error when discriminating oil sand from brine sand using seismic P-wave velocity.

Bayes Decision Criterion

Each curve in Figure 4.9 shows the pdfs of V_p for brine sand and oil sand, $p(V_p, Fluid = brine)$ and $p(V_p, Fluid = oil)$, from a North Sea reservoir. The area under each curve represents the marginal probability of each pore fluid, *i.e.*,

$$p(brine) = \int p(V_p, Fluid = brine) dV_p \tag{4.15}$$

$$p(oil) = \int p(V_p, Fluid = oil) dV_p \tag{4.16}$$

The larger area under the brine pdf than the oil pdf—$p(brine) > p(oil)$—represents an a priori assumption that brine sand is more likely to exist than oil sand without velocity observation.

From the pdfs, the conditional pdf of pore fluid given an observed V_p can be derived as

$$p(Fluid|V_p) = \frac{p(V_p, Fluid)}{p(V_p)} = \frac{p(V_p, Fluid)}{\sum_i p(V_p, fluid_i)} \tag{4.17}$$

In the example in Figure 4.9 with two possible fluid types, brine and oil, the probability of each fluid type for a given V_p is

$$p(brine|V_p) = \frac{p(V_p, Fluid = brine)}{p(V_p, Fluid = brine) + p(V_p, Fluid = oil)} \tag{4.18}$$

$$p(oil|V_p) = \frac{p(V_p, Fluid = oil)}{p(V_p, Fluid = brine) + p(V_p, Fluid = oil)} \tag{4.19}$$

Two curves in Figure 4.10 show the probabilities of the two pore fluids for all possible V_p.

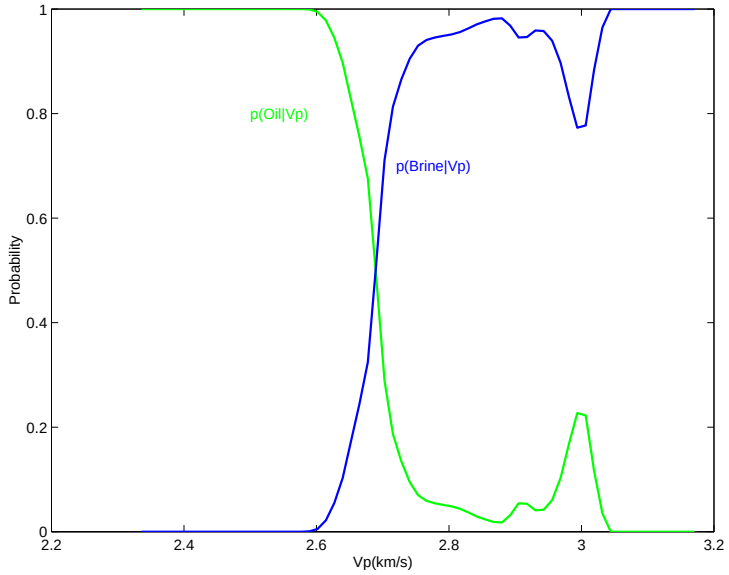

Figure 4.10: The conditional pdfs V_p given fluids. The conditional pdfs intersect each other at $V_p = 2.67$, which is the decision boundary between prediction of oil and gas.

The *Bayes decision criterion* states that, for any given V_p, the mostlikely pore fluid is the one with the largest $p(Fluid|V_p)$ (Duda and Hart, 1973). More generally, when we estimate a set of rock properties, $\mathbf{m}$, from a set of observables, $\mathbf{d}$, the mostlikely estimate of $\mathbf{m}$ for any given $\mathbf{d}$ is the one that has maximum conditional pdf, $p(\mathbf{m}|\mathbf{d})$. In the example in Figure 4.10, V_p= 2.67 km/s (=$V_{p_{th}}$) is the decision boundary of Bayes criterion; oil sand should be predicted when $V_p < V_{p_{th}}$, while brine sand should be predicted when $vp > V_{p_{th}}$.

Bayes Estimation Error

Overlap of the pdfs in Figure 4.9 implies that the rocks with the two different saturating fluids can have the same V_p. Therefore, perfect prediction of pore fluids from V_p only is impossible. This is true for any geophysical rock property estimation; geophysical data do not allow perfect predictions of rock properties, but there are always inevitable interpretation errors. The *Bayes decision criterion of selecting the maximum likelihood rock properties guarantees minimum prediction errors*, as compared to other decision criteria.

In Figure 4.11, colored areas under the pdfs represent the probabilities of errors for the

example in Figure 4.9. They are either predicting brine when the true fluid is oil (A), or predicting oil when the true fluid is brine (B). In this case, the probability of error is

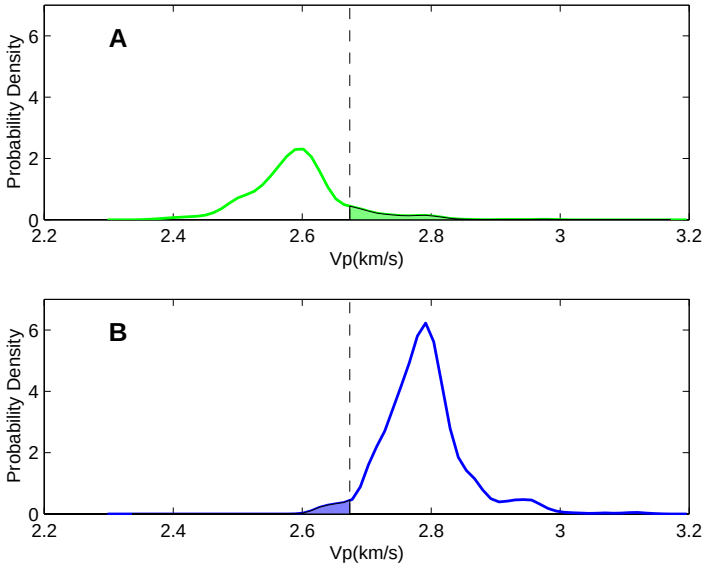

Figure 4.11: The Bayes interpretation errors. Dashed line is the decision boundary of fluid prediction. The interpretation errors happen either when predicting brine for true fluid of oil (A, false negative) or when predicting oil for true fluid of brine (B, false positive).

$$p(error|V_p) = p(brine|V_p), \quad \text{if} \quad p(oil|V_p) > p(brine|V_p) \quad i.e., V_p < V_{p_{th}} \tag{4.20}$$

$$p(error|V_p) = p(oil|V_p), \quad \text{if} \quad p(brine|V_p) > p(oil|V_p) \quad i.e., V_{p_{th}} < V_p \tag{4.21}$$

The average probability of making any prediction error can be written as

$$p(error) = \int_{V_p < V_{p_{th}}} p(V_p, Fluid = brine) dV_p + \int_{V_{p_{th}} < V_p} p(V_p, Fluid = oil) dV_p \tag{4.22}$$

Table 4.1 summarizes probabilities of correct and wrong predictions in the example. The Bayes error can be considered a negative measure of dependence between objective rock properties and observed physical properties. When the observed properties completely depend on the objective properties, there is no error. On the other hand, a Bayes error of

Observed Velocity	$V_p < V_{p_{th}}$	$V_{p_{th}} < V_p$	$p(Fluid)$
	$p(o\|V_p) > p(b\|V_p)$	$p(b\|V_p) > p(o\|V_p)$	
Predicted Fluid	Oil	Brine	
True: Oil	0.267 Correct	0.033 *False negative error*	0.300
True: Brine	0.017 *False positive error*	0.683 Correct	0.700
Total	0.284	0.716	1.000

Table 4.1: Probability of correct/false prediction estimated from the pdf, $p(V_p, Fluid)$.

0.5, in this example of two possible categories, implies there is no information about the objectives provided by the observation. (More generally, the Bayes error for non-informative data is $1/n$ when there are n possible categories of rock properties.) In addition, the Bayes error is invariant with respect to non-linear coordinate transform, as discussed later.

When a particular reservoir property is economically more favorable than others, such as the example above in which oil sand is more preferable than brine sand, it is valuable to make the distinction between *false positive errors* and *false negative errors* (Duda and Hart, 1973; Houck, 1999). *False positives* are errors when predictions of more favorable properties turn out to be false, which corresponds to Equation 4.20 in the example. On the other hand, *false negatives* are when predictions of unfavorable property turn out to be false, such as Equation 4.21. The distinction between the two types of errors is important when evaluating economical impacts of decisions, especially when the economical values of the two errors, which may be quantified by *loss functions*, are asymmetric. In such cases, the decision boundary may not be at the intersection of the two conditional pdfs (Fukunaga, 1972).

4.4.3 Comparison With Linear Measures

So far, non-linear measures of uncertainty, information entropy and relative entropy, measures of dependence between parameters, mutual information and Bayes error, and non-linear Bayes decision criterion have been described. In this section, they are compared

with the common linear statistical counterparts: variance, covariance, linear regression, and discriminant analysis using Mahalanobis distance (Fukunaga, 1972).

We use an example from a North Sea reservoir to show the advantages of the non-linear measures as compared to their linear counterparts. Contours in Figure 4.12-A show the bivariate conditional pdfs of V_p and V_s for six different lithofacies found in a North Sea reservoir. The pdf was estimated from the discrete samples overlain on the contours. Colors in Figures 4.12-B and C show the predicted facies for each pair of V_p and V_s, according to the Bayes criterion and minimum-Mahalanobis-distance classifier, respectively.

The advantages of non-linear measures as compared to linear correspondents can be summarized below.

- Flexible representation of the state of knowledge of rock properties.

  Non-linear measures are based on non-parametric pdfs, which allow complete and flexible description of rock properties. As shown in Figure 4.12, pdfs can honor arbitrary rock property relations in observed data.

- Non-linear dependence can be analyzed.

  Mutual information and the Bayes error quantify the dependence between non-linearly and non-uniquely related variables, which are characteristic of most natural rocks.

- Categorical properties can be used.

  Rock properties can be categorical, such as lithofacies and pore fluid types, as well as continuous, while variance and covariance only work for continuous properties. In the example, the dependence between the two velocities and lithofacies can be quantified by the mutual information, $I(lithofacies|V_p, V_s) = 1.38$, or the normalized information, $I_n(lithofacies|V_p, V_s) = 0.23$.

- Invariance with respect to change of variables.

  Linear measures, as well as linear discriminant criterion, are variable with respect to non-linear coordinate transforms, while the non-linear measures and Bayes criterion are invariant.

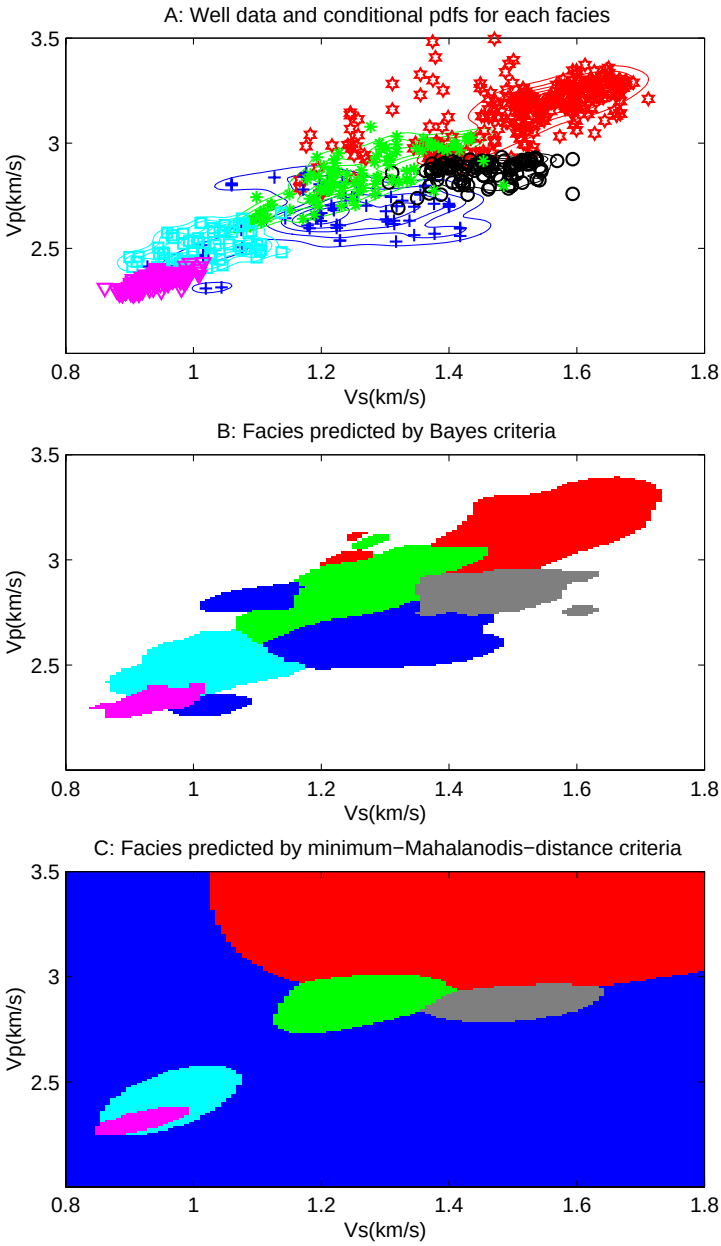

Figure 4.12: Comparison between the Bayes decision criterion and the minimum-Mahalanobis-distance discriminant criteria. Contours in A show the bivariate pdf of V_p and V_s for six different lithofacies, derived from the overlain discrete data. B and C show predicted lithofacies at each (V_p, V_s) pair from the Bayes criteria and the minimum-Mahalanobis-distance criteria, respectively.

- Bayes criteria guarantee minimum estimation error.

  For a given pdf, the Bayes decision criterion guarantees minimum prediction error. In Figure 4.12, the prediction error using the Bayes and the minimum-Mahalanobis-distance criteria are 17% and 26%, respectively. Minimum-Mahalanobis-distance classifier gives the best result only if the pdfs are Gaussian functions, when the decision criteria are equivalent to the Bayes criteria.

More importantly, the estimation of a non-parametric pdf explicitly requires consideration of the effects of spatial sampling, measurement errors, and the prior pdf, which are very often overlooked in linear analyses.

When available data are insufficient as compared to the heterogeneity of target rocks, or when we deal with multiple (more than five) rock properties at once, however, estimation of the pdfs can be highly difficult. In such cases, we may decide that only simple statistical parameters of the data, such as mean, variance, and covariance, are reliable, when the linear measures work as well as the non-linear ones.

4.5 Source of Information in Rock Property Estimation

The main objective of geophysical prospecting is to increase information, thereby reducing uncertainty about target subsurface properties. Using statistical formulations discussed earlier, we quantitatively discuss what brings us information in rock property estimation and what does not.

4.5.1 Sources of Information

Rock Physics Theories

Rock physics theories constrain our knowledge about subsurface rock properties. Absolute constraints come from physical definitions of parameters. For example, porosity must observe $0 \leq \phi \leq 1$ by definition. Moreover, most rocks have porosity values less than the critical porosity, ϕ_{cr}, introduced by Nur et al. (1991; 1992; 1995), *i.e.*, $0 \leq \phi \leq \phi_{cr}$.

Other theories also define bounds of rock properties for certain conditions. For example, the Hashin-Shtrikman theory defines bounds of elastic moduli of isotropic aggregates for given volume fractions (Hashin and Shtrikman, 1963). Figure 4.13 shows the upper and lower bounds of V_p for wet sandstone (*i.e.*, mixtures of quartz and water) as a function of porosity. The theory helps us infer bounds of porosity for an observed seismic velocity, even when we have no porosity information. As illustrated in Figure 4.13, if we know the

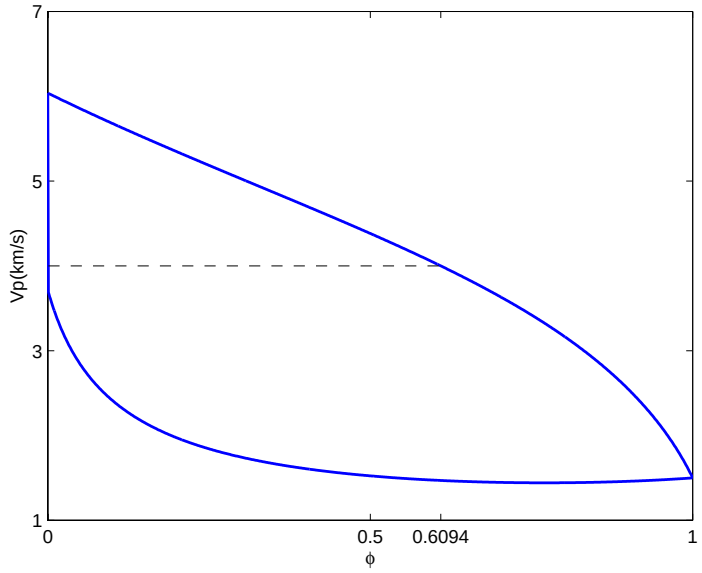

Figure 4.13: Hashin-Shtrikman bounds of V_p for quartz-water aggregate. The bounds limit possible range of porosity for given velocity. When V_p is 4 km/s and it is known that the target rock is clean wet sandstone (quartz-water mixture), porosity must be lower than 0.609.

rock is sandstone, quartz-water mixture, and when the measured V_p is 4 km/s, the theory limits the possible range of porosity to $0 \leq \phi \leq 0.6094$ and reduces information entropy from 6.91 to 6.41.

Other rock physics theories predict rock property relationships for well-defined conditions, such as Gassmann's prediction of elastic moduli after fluid substitution (Gassmann, 1951; Mavko et al., 1998). These theories help estimate the pdfs of rock properties in non-observed physical states, as discussed in section 4.3.3.

Prior Geological Information

Geophysical subsurface property estimation is usually a very under-constrained and ill-posed problem because of the large heterogeneity of the objectives compared to available information. Hence, the prior geological knowledge is used either explicitly or implicitly to condition the estimation.

Some implicit assumptions which are frequently presupposed in seismic data processing are random vertical layering in deconvolution and velocity increase with depth in velocity estimation. Additionally, local geological knowledge may be established from outcrop data, well data, and regional stratigraphy, from which we may estimate the *prior probabilities* to reduce uncertainty. Further investigation of the example in Figure 4.11 and Table 4.1, in which pore fluids are estimated from velocity measurements, show the influence of the prior probability on uncertainty. In the previous example, the prior probabilities of oil and brine were assumed to be 0.3 and 0.7. Table 4.2 summarizes the Bayes errors of pore fluid prediction, as well as the mutual information about pore fluid given by the velocity, when the prior probabilities are changed and the conditional pdf, $p(V_p|Fluid)$, is kept identical.

$p(oil)$	$p(brine)$	Total Bayes Error (%)
0.3	0.7	5.0
0.15	0.85	3.4
0.05	0.95	1.6
0.00	1.00	0.0

Table 4.2: Dependence of the Bayes Error on prior probability.

The Bayes error decreases as the difference between the prior probabilities for the two fluids becomes greater. When existence of oil is geologically impossible, such as when there is no source rock to produce oil or when the up-dip of the reservoir is found wet, the prior probability of oil is 0, hence there is no uncertainty about the pore fluid.

Measured Data

Measured data are the most important information in reducing uncertainty about rock properties. Two or more types of measured data may reduce the uncertainty even more.

The reduction of uncertainty by additional data can be shown by an example from the North Sea, in which the relationships between the porosity, V_p, and the V_s of the reservoir are described by a trivariate pdf in Figure 4.14. Conditioning of porosity information by velocities is summarized in Figure 4.15. The unconditioned prior pdf changes to narrower and taller conditional pdfs, $p(\phi|V_p)$ and $p(\phi|V_p, V_s)$, by velocity information. The velocity observation decreases the information entropy of porosity, as shown in Table 4.3.

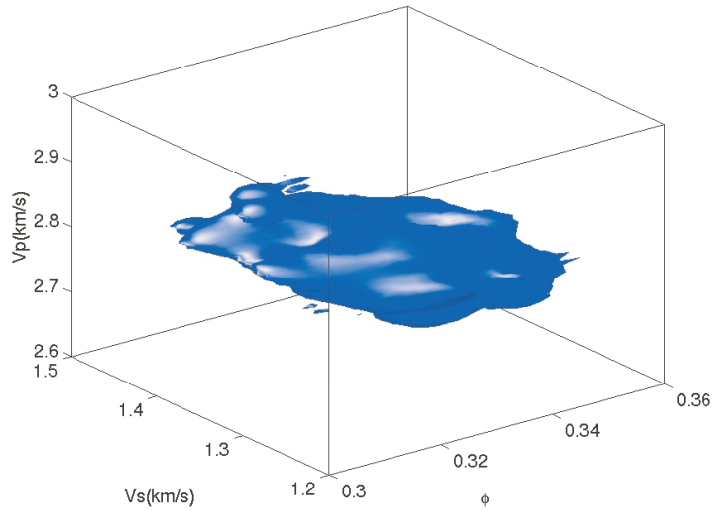

Figure 4.14: The trivariate pdf of porosity, V_p, and V_s, $p(\phi, V_p, V_s)$, in a North Sea reservoir. The surface corresponds to an iso-probability-density contour of the trivariate pdf.

Data	Information Entropy about Porosity
-	3.44
V_p=2.83	3.06
V_p=2.83 V_s=1.34	2.89

Table 4.3: Reduction of information entropy about porosity by seismic velocity observations.

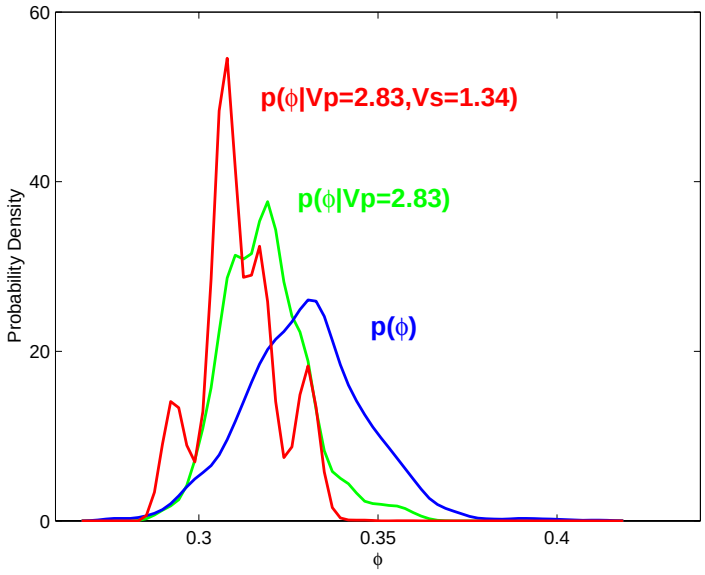

Figure 4.15: Conditioning of porosity pdf by V_p and V_s information, corresponding to the trivariate pdf in Figure 4.14.

4.5.2 No Source of Information

Data Manipulation

Recently, transforms of observed data to other coordinates have been used for rock property discrimination. Such transforms include (V_p, V_s) to $(\rho/\lambda, \mu/\lambda) = (1/({V_p}^2 - 2{V_s}^2), {V_s}^2/({V_p}^2 - 2{V_s}^2))$, or P- and S-impedances (I_p and I_s) to $(\rho\lambda, \rho\mu) = (I_p^2 - 2I_s^2, I_s^2)$ (Berryman, 1999; Goodway et al., 1999) (λ and μ denote Lamé's elastic constant and shear modulus, respectively). However, from the information-theoretic view point, these data manipulations do not increase information about rock properties.

Invariance of Prediction Error

The lack of additional information gained by data manipulations is demonstrated by the invariance of the Bayes prediction error, with respect to non-linear coordinate transformation. The following example attempts to distinguish oil sand from brine sand in the (I_p, I_s) domain and in the (L, M) domain, where L and M are any functions of I_p and I_s, as $L(I_p, I_s)$ and $M(I_p, I_s)$. If the Bayes criterion predicts oil sand when $(I_p, I_s) \in R$ and

brine sand when $(I_p, I_s) \in \bar{R}$), the total Bayes error in the (I_p, I_s) domain can be related to the total Bayes error in the (L, M) domain as

$$\begin{aligned} p_{I_p,I_s}(error) &= \iint_R p(brine, I_p, I_s) dI_p dI_s + \iint_{\bar{R}} p(oil, I_p, I_s) dI_p dI_s \\ &= \iint_S p(brine, L, M) dL dM + \iint_{\bar{S}} p(oil, L, M) dL dM \\ &= p_{L,M}(error) \end{aligned} \tag{4.23}$$

where S is an area in the (L, M) domain corresponding to R in the (I_p, I_s) domain. Equation 4.23 states that the Bayes error is invariant when we change variables from (I_p, I_s) to any domain that can be derived from (I_p, I_s) alone. Figure 4.16 shows the bivariate pdfs of oil sand and brine sand in the (I_p, I_s) and in the $(\rho\lambda, \rho\mu)$ domains. The latter is produced by data manipulation of the former, observing Equation 4.2.

In spite of the different shapes of the pdfs, each one is no more than a non-linearly stretched version of the other. The Bayes errors in both domains, as well as estimation errors of the minimum-Mahalanobis-distance discriminant, are summarized in Table 4.4. The minimum-Mahalanobis-distance discriminant produces different estimation errors in

Domain	Bayes Error (%)	Error of MD-based Discriminant (%)
$I_p - I_s$	5.4	6.3
$\rho\lambda - \rho\mu$	5.5	7.2

Table 4.4: Estimation errors of Bayes and minimum-Mahalanobis-distance discriminant criteria in $I_p - I_s$ and $\rho\lambda - \rho\mu$ domains.

the two domains, since it is based on the covariances of the pdfs which are variant with respect to non-linear coordinate transforms. However, the difference in the Bayes errors is smaller than discretization errors of the computation, showing the invariance of the Bayes error. In addition, the Bayes errors are smaller than the linear correspondent in both domains.

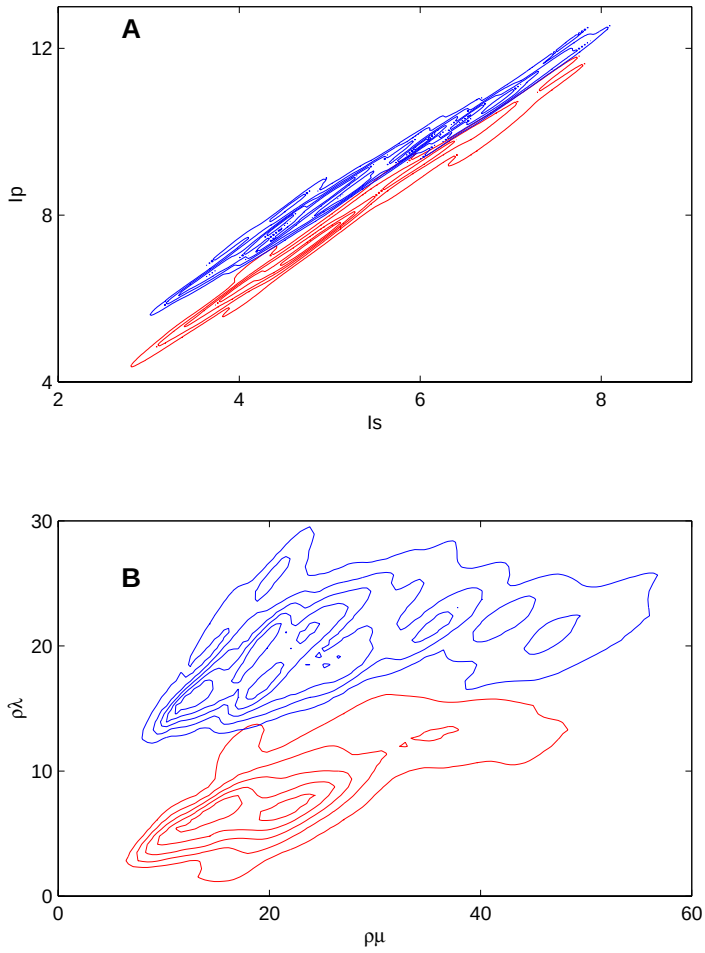

Figure 4.16: The bivariate pdfs of I_p and I_s, for brine and gas sand (A) and the equivalent pdfs in $(\rho\lambda, \rho\mu)$ domain (B). In spite of the different shapes, the ability to discriminate pore fluids is identical.

Data Processing Inequality

As Cover and Thomas (1991) correctly state, " *No clever manipulation of data can improve the inference that can be made from the data.*", the data processing inequality in the information theory explicitly shows that no information can be gained by data manipulations.

If random variables, $\mathbf{X}$, $\mathbf{Y}$, and $\mathbf{Z}$, form a Markov chain in that order, information about

$\mathbf{X}$ given by $\mathbf{Y}$ is greater than or equal to the information about $\mathbf{X}$ given by $\mathbf{Z}$.

$$\begin{aligned} \text{If} \quad & \mathbf{X} \rightarrow \mathbf{Y} \rightarrow \mathbf{Z} \\ \text{then} \quad & I(\mathbf{X};\mathbf{Y}) \geq I(\mathbf{X};\mathbf{Z}) \end{aligned} \tag{4.24}$$

$\mathbf{X}$, $\mathbf{Y}$, and $\mathbf{Z}$ form a Markov chain if and only if

$$p(\mathbf{x},\mathbf{z}|\mathbf{y}) = p(\mathbf{x}|\mathbf{y})p(\mathbf{z}|\mathbf{y}) \tag{4.25}$$

i.e., $\mathbf{X}$ and $\mathbf{Z}$ are conditionally independent given $\mathbf{Y}$.

In practice, Markov chains can be found in cases when we simply manipulate observed data to produce other parameters, as in Figure 4.17. For example, it happens when we compute a pair of attributes, L and M, only from measured P and S impedances, I_p and I_s, by mere manipulation. In that case, subsurface rocks ($\mathbf{X}$), impedances ($\mathbf{Y}$), and attributes after manipulation ($\mathbf{Z}$) form a Markov chain, since only information contained in $\mathbf{Y}$ and no other information is used for deriving $\mathbf{Z}$. In this case, the information about the rocks given

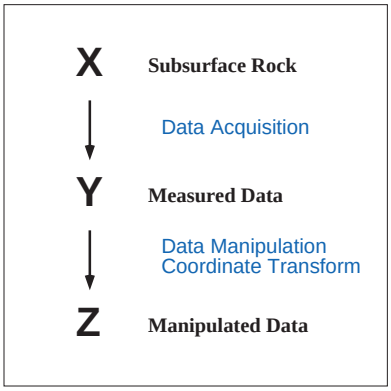

Figure 4.17: Information transfer in Markov chain.

by the measured impedances, $I(\mathbf{X}|\mathbf{Y})$, is greater than or equal to the information given by the attributes derived from the impedances, $I(\mathbf{X}|\mathbf{Z})$. That is, *data manipulation does not increase information*. In the example in Figure 4.16, in which variables are transformed

from (I_p, I_s) to $(\rho\lambda, \rho\mu)$,

$$I(fluid|I_p, I_s) = I(fluid|\rho\lambda, \rho\mu) = 0.56 \tag{4.26}$$

i.e., the information given by the impedances, I_p and I_s, is equal to the information given by the derived attributes, $\rho\lambda$ and $\rho\mu$.

In chapter 2, we discussed rock property effects in various seismic attribute domains. The pairs of attributes explored in chapter 2 are not products of data manipulations from other pairs, hence each of them carries different information. For example, AVO attributes can not be determined from V_p and V_s only, but density values are needed.

It should be noted that *the data processing inequality does not apply to general geophysical data processing.* Essentially, most data processing in geophysics are not mere data manipulations, but procedures to combine information from measured data, physics theories, and geology. For example, in seismic data processing, migration a priori assumes particular wave propagation patterns from a scatterer, based on the physics of waves. In the same way, deconvolution a priori assumes that reflected waves are approximated by the convolution model. In addition in many processing procedures, noise is suppressed under the assumption of its randomness and unbiased character. In those cases, data processing attaches additional information to measured data, information that comes out of a priori physical and geological assumptions, as shown in Figure 4.18, *i.e.*, subsurface properties ($\mathbf{X}$), measured data ($\mathbf{Y}$), and processed data ($\mathbf{Z}$) do not form a Markov chain.

Non-Physical Attributes

Recent developments in seismic technology have enabled us to use multiple seismic attributes for the interpretation of rock properties (Brown, 1996; Chen and Sidney, 1997). Although some attributes are reported to be advantageous in rock property estimation (White, 1991; Dilay and Eastwood, 1995; Lewis, 1997), most of the seismic attributes have poorly established physical relationships with rock properties. In many cases, empirical statistical correlation between seismic attributes and objective rock properties are established from well data. Then the seismic attributes that have high statistical correlation with objective properties are selected for seismic interpretation.

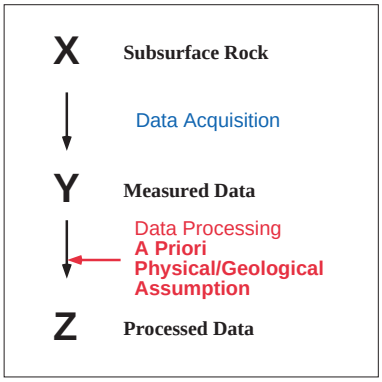

Figure 4.18: Information transfer in geophysical data processing.

According to Kalkomey (1997), small numbers of calibrating well data can result in spurious good correlations between rock properties and seismic attributes, even when they do not have any dependence. This is because the estimation of true reservoir statistics becomes difficult when available data are limited. It becomes virtually impossible for high dimensional pdf when we deal with many rock properties at once. Selection of seismic attributes from only empirical statistics can lead to incorrect rock property prediction. Hence, physical relationships between seismic attributes and rock properties need to be emphasized, especially when the number of calibrating data are limited.

4.6 Conclusions

In this chapter, we explored the methods to quantify information and uncertainty in rock property estimation. Probability density functions enable complete representation about our knowledge about objective rock properties, and thereby are suitable to describe estimated rock properties, as well as the relations between rock properties. We also present a procedure to establish pdfs about rock properties from available data with emphasis on the physical implications.

Non-linear statistical parameters, such as information entropy, mutual information, and the Bayes error, provide us with measures of uncertainty and information about non-linearly and non-uniquely dependent rock properties. Investigation using these parameters

clearly revealed that uncertainty about rock properties cannot be reduced by data manipulations. Instead, data acquisition, physics, and geological knowledge bring information about rock properties. Popular linear statistics can lead to spurious conclusions unless they are used with enough awareness about their limitations.

Chapter 5

Rock Physics Effects on Estimation Uncertainty in Various Scenarios

Abstract

In seismic exploration, seismic attributes are usually used as interim products in estimating reservoir properties from seismic data. Important factors affecting the predictability of reservoir properties from seismic attributes include types and numbers of available seismic attributes, sensitivity of the seismic attributes to the target reservoir properties, natural variability of the reservoir properties, and accuracy of deriving the seismic attributes. In this chapter, we use statistical formulations presented in chapter 4 and quantitatively investigate how these factors influence the uncertainty of reservoir property estimation. Furthermore, using probability density functions of various seismic observations derived from well data, we quantify information about reservoir properties, namely, lithofacies, pore fluid, and porosity, carried by each attribute. As optimal attributes, we choose those which convey maximum information.

Application of these methods serves as a quantitative decision analysis guide for evaluating various data acquisition, processing, and interpretation options. It can help to analyze which kinds of additional data would best reduce the uncertainty about reservoir properties.

5.1 Introduction

Estimation of rock properties consists of making an inference of the rock properties using available information. Figure 5.1 systematically summarizes the process of estimating rock properties from seismic data. From data acquisition and processing, we obtain processed seismic volumes, which are the reflectivity profiles of 5 dimensions or more (x, y, z, offset, azimuth, time, etc.). Then seismic attributes (*e.g.*, velocities, impedances, and AVO attributes) are extracted from the processed data through various inversion techniques. Finally, seismic attributes (including the reflectivity profiles obtained in the first step) are used for rock property estimation, along with well data and rock physics theories. In this procedure, seismic attributes act as *interim products* to connect seismic data and target rock properties. Unfortunately, geophysicists sometimes skip the second step (from seismic attributes to target rock properties) and consider attributes as *final* products. The attributes provide us with information extracted from the seismic data in a form that is ready for rock property estimation.

The estimation uncertainty of target rock properties from seismic attributes is related to 1) types and numbers of available seismic attributes, 2) sensitivity of the seismic attributes to the target rock properties, 3) variability of the target rock properties, 4) accuracy of measurement of the seismic attributes, and many other factors. Quantitative understanding of the uncertainty is essential in making exploration and production decisions.

In this chapter, we use the quantitative measures of information presented in chapter 4 and explore how the estimation uncertainty of reservoir properties is related to individual sources. We define pdfs from laboratory and well data for various estimation scenarios, reservoir conditions, measurement conditions, and from these we quantify information and uncertainty of the reservoir properties. Furthermore, we explore which kinds of seismic attributes are appropriate for various rock property estimation scenarios, *e.g.*, estimation of lithofacies, pore fluid, and porosity. The methods proposed in this chapter enable us to incorporate *rock physics* into *decision making* in various stages of oil exploration and production.

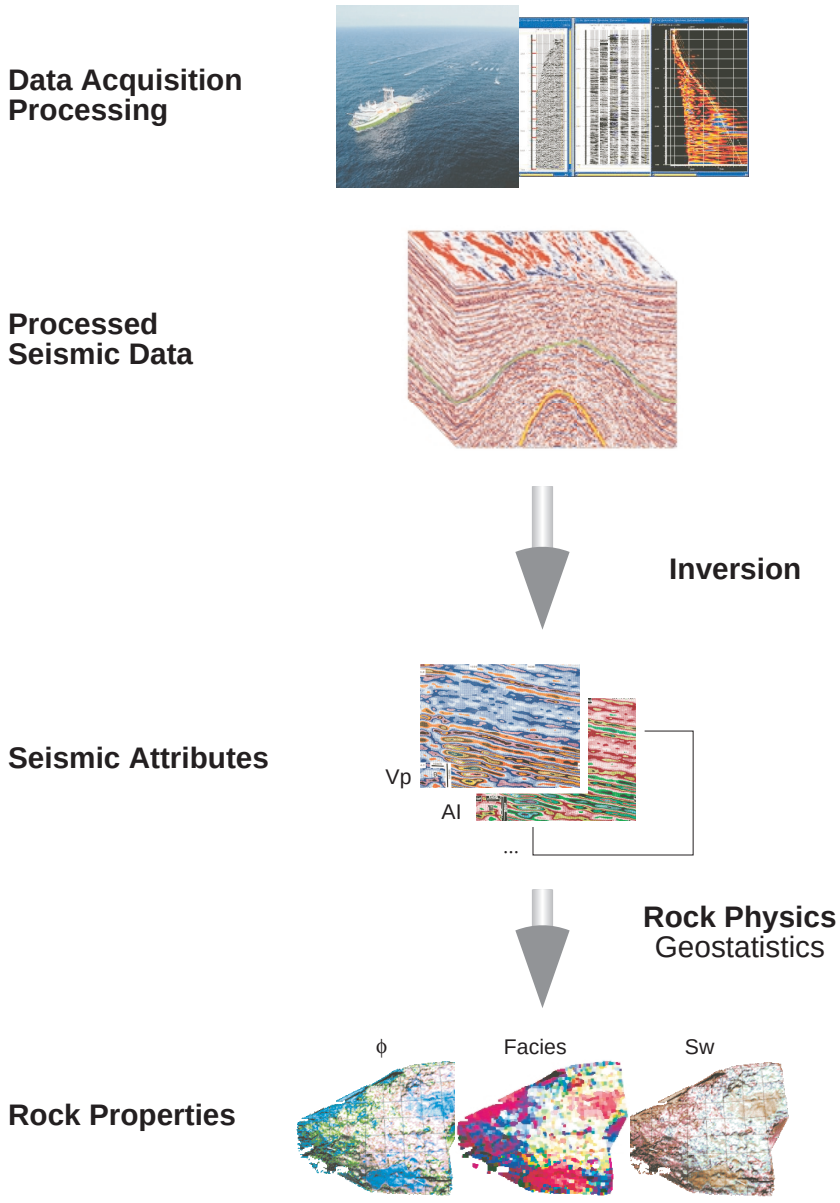

Figure 5.1: The process of rock property estimation from seismic data. Seismic data acquisition and processing produce processed seismic data (top). The processed data consist of reflection profiles, which are multidimensional. From the data, seismic attributes, such as impedance or AVO coefficients, are extracted through inversion procedures. Then from the seismic attributes, rock properties, *e.g.*, porosity, lithofacies, and fluid saturation, are estimated using rock physics theories and statistical methods.

5.2 Sources of Uncertainty in Rock Property Estimation

Measured data, rock physics theories, and geological knowledge are what give us information about subsurface properties, as discussed in chapter 4. Chapter 2 described how seismic attributes extracted from seismic data are dependent on rock properties. In this chapter, we combine the methods proposed in chapters 2 and 4 and quantitatively explore the effects of individual sources of uncertainty.

For several scenarios of pore fluid prediction—*e.g.*, distinction of gas-saturated reservoir from water-saturated reservoir—we establish pdfs using Han's laboratory sandstone data (1986). We then quantify the information and uncertainty of the pore fluid prediction in each scenario using the non-linear statistical measures that were presented in chapter 4.

5.2.1 Limited Information

Elasticity theory describes wave propagation through most rocks and thereby is the basis of most seismic analysis. Under the assumption of elasticity and isotropy, any combination of three seismic parameters, such as V_p, V_s, and density, completely describe the seismic signatures of rocks, as long as none of the three can be deterministically derived from the other two. Once the combination of three elastic properties is given, we can derive any other elastic property, *e.g.*, λ (Lamé's constant), μ (shear modulus), and ν (Poisson's ratio). Hence, perfect measurements of any three seismic properties provide us with the maximum information about rock properties seismic data carry. In other words, there is an inevitable upper limit of information that we can extract from seismic data, even when the measurements are error-free. Furthermore, use of less than three seismic measurements would mean abandoning part of the limited information seismic data can convey.

The two clouds in Figure 5.2 are the trivariate pdf of V_p, V_s, and density for gas- and water-saturated sandstones, derived from Han's data set (1986). We suppose they represent the pdfs of error-free measurements for pore fluid prediction. Hence the diversity of the pdfs comes from the natural variability of the reservoir properties. Figure 5.3 shows the corresponding bivariate pdfs of V_p and V_s, as well as the univariate pdfs of V_p, and V_s. The bivariate pdfs are projections of the trivariate pdf along the density axis and the univariate pdfs are projections of the bivariate pdfs.

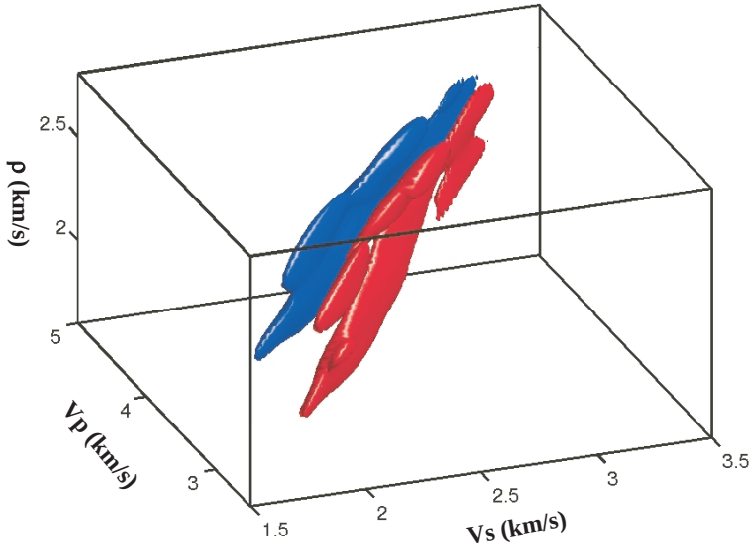

Figure 5.2: The trivariate pdf of V_p, V_s, and density for gas-saturated (red) and water-saturated (blue) sandstones. The surfaces represent iso-probability-density surfaces of the pdfs.

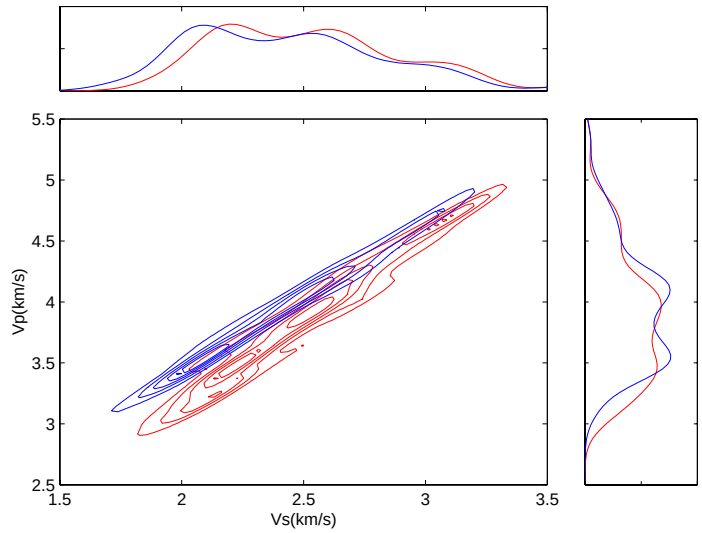

Figure 5.3: The bivariate pdf of V_p and V_s for gas-saturated (red) and water-saturated (blue) sandstones. The univariate pdfs of V_p (right) and V_s (top) are also shown.

The univariate pdfs in Figure 5.3 show overlaps for gas and water, although the pdfs become much more separated in the bivariate case. Also from the comparison between the trivariate and the bivariate pdfs, we can observe that higher dimensional pdfs (*i.e.*, more information) have smaller overlap between gas-sand clouds and water-sand cloud than lower dimensional pdfs. Table 5.1 summarizes statistical measures of the predictability for one, two, and three measurements, in terms of mutual information and the Bayes errors.

Attributes used	Mutual Information $I(fluid\|Attributes)$	Normalized Inf. $\mathrm{I_n(fluid\|Attributes)}$	Bayes Error
V_p	0.01	0.02	0.453
V_s	0.01	0.02	0.445
V_p, V_s	0.41	0.59	0.127
V_p, V_s, ρ	0.53	0.76	0.069

Table 5.1: Information about pore fluid given by one, two, and three parameters. Bayes errors in pore fluid prediction using one, two, and three parameters are also shown.

According to Table 5.1, the more measurements we use for classification, the more information we can extract, hence the less estimation errors. Although individual single measurements of V_p and V_s provide little information about pore fluids, the combination of the two enables their distinction. Three measurements (adding density information) give the most information and the least Bayes error. Since any additional seismic properties can be deterministically derived from the three, and the three measurements are assumed error-free in this case, no information can be added by further seismic measurements. However, even the three measurements cannot perfectly predict pore fluids in this case—the normalized information is less than 1 and the Bayes error is greater than 0—because the dependence between pore fluid types and the three attributes are not complete.

In practical situations, using more than three measurements can be beneficial, since no measurement is error-free. Additional measurement with higher data quality and/or denser data sampling can bring supplemental information about rock properties and reduce their uncertainty via redundancy.

For rocks which have more complicated characteristics than isotropic and elastic media, a possible way to increase the information extractable from seismic data is to use more

rigorous physical models. For example, measuring seismic wave attenuation enables us to employ viscoelastic models for absorptive rocks, and to extract information about pore fluids (*e.g.*, permeability). Hence, additional measurement of quality factors, Q, increases the dimensionality of the information from three to four. Alternatively, if the rocks are anisotropic, measuring seismic properties in more than one orientation expands the maximum extractable information from seismic data.

5.2.2 Sensitivity of Seismic Properties on Target Rock Properties

Predictability of rock properties from seismic attributes depends on the sensitivity of the seismic attribute value to the target rock properties—how much the attributes are varied by a change in the rock property. The following example shows how the uncertainty of pore fluid prediction is influenced by the sensitivity between pore fluids and seismic velocities.

Figure 5.4 shows the pdfs of V_p and V_s for gas- and water-saturated sandstones with low porosity (**A**) and high porosity (**B**), derived from Han's data set (1986). The low-porosity data and the high-porosity data have identical porosity variability (± 0.05), but different mean porosity values ($\bar{\phi} = 0.10$ in **A** and $\bar{\phi} = 0.25$ in **B**). Error-free measurements of the attributes are again assumed.

In these data, the sensitivity of velocities to pore fluids is greater in high-porosity sandstone than in low-porosity. Consequently, the separation between the gas-sand cloud and the water-sand cloud is larger in **B** than in **A**, although the porosity ranges of the two cases are identical. Table 5.2 summarizes statistics of the pore fluid detection in both cases.

Table 5.2 shows that information about pore fluid carried by seismic velocities is larger in high porosity (**B**) than in low porosity (**A**), quantitatively illustrating better prediction of pore fluid in higher porosity. In both cases, the combination of V_p and V_s drastically decreases the uncertainty about pore fluids.

The example above focuses on the impact of porosity on the pore fluid dependence of velocities. In general, however, rock properties other than porosity (*e.g.*, rock matrix stiffness, overburden pressure, pore pressure, depth, the difference in fluid compressibilities, etc.) also influence the sensitivity of seismic velocities on pore fluids.

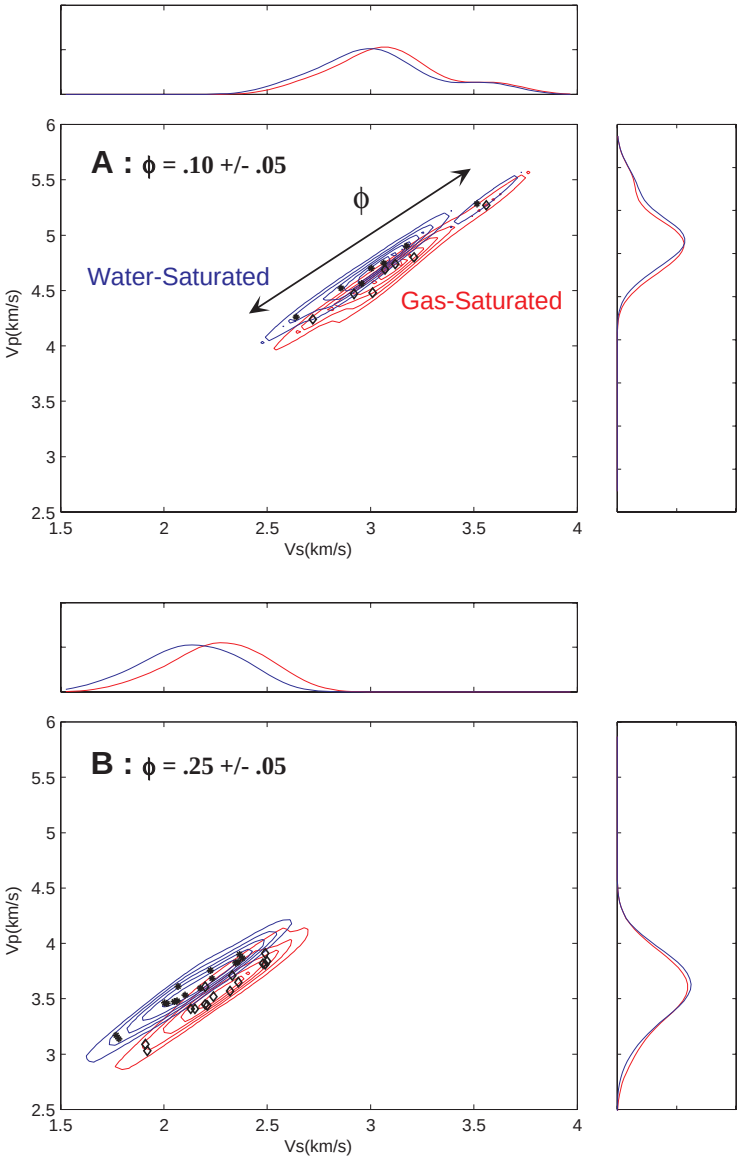

Figure 5.4: The pdfs of V_p and V_s for gas- and water-saturated sands. **A** is when the porosity range is $0.05 \leq \phi \leq 0.15$ and **B** is when $0.20 \leq \phi \leq 0.30$

5.2.3 Heterogeneity of Reservoirs

The relation between a rock property and seismic attributes becomes scattered when rock properties other than the objectives are heterogeneous, as discussed in chapter 4. For

		Mutual Inf.	Normalized Inf.	Bayes Error
V_p				
A	Low ϕ	0.00	0.00	0.468
B	high ϕ	0.00	0.00	0.48
V_s				
A	Low ϕ	0.01	0.01	0.451
B	high ϕ	0.04	0.05	0.395
V_p and V_s				
A	Low ϕ	0.34	0.49	0.164
B	high ϕ	0.46	0.66	0.106

Table 5.2: Information about pore fluid given by velocities and the corresponding Bayes errors in pore fluid prediction for cases **A** and **B** in Figure 5.4.

example, Figure 2.5 illustrates that the relation between seismic attributes and porosity can be variable depending on the clay content. The heterogeneities of reservoirs make rock property prediction non-unique and difficult.

Figure 5.5 shows pdfs of V_p and V_s for gas- and water-saturated sandstones of the same reservoir rocks with different variabilities in porosity, defined from Han's data. The mean porosities of the two reservoirs are identical ($\bar{\phi} = 0.32$, though porosity variations are ± 0.02 in **A** and ± 0.08 in **B**). Perfect measurements with no error are assumed. The statistics of the pore fluid prediction in both cases are summarized in Table 5.3.

	A			**B**		
Attributes	M. Inf.	N. Inf.	B. Error	M. Inf.	N. Inf.	B. Error
V_p	0.51	0.73	0.074	0.30	0.44	0.174
V_s	0.24	0.35	0.241	0.11	0.16	0.324
V_p, V_s	0.69	1.00	0.000	0.69	1.00	0.00

Table 5.3: Information about pore fluid given by velocities and the corresponding Bayes errors in pore fluid prediction for case **A** and **B** in Figure 5.5

In both cases, the combination of V_p and V_s data makes a perfect distinction between water sand and gas sand, since variability in porosity scatters the data along the direction approximately perpendicular to the fluid effects in the V_p-V_s domain, as discussed in chapter

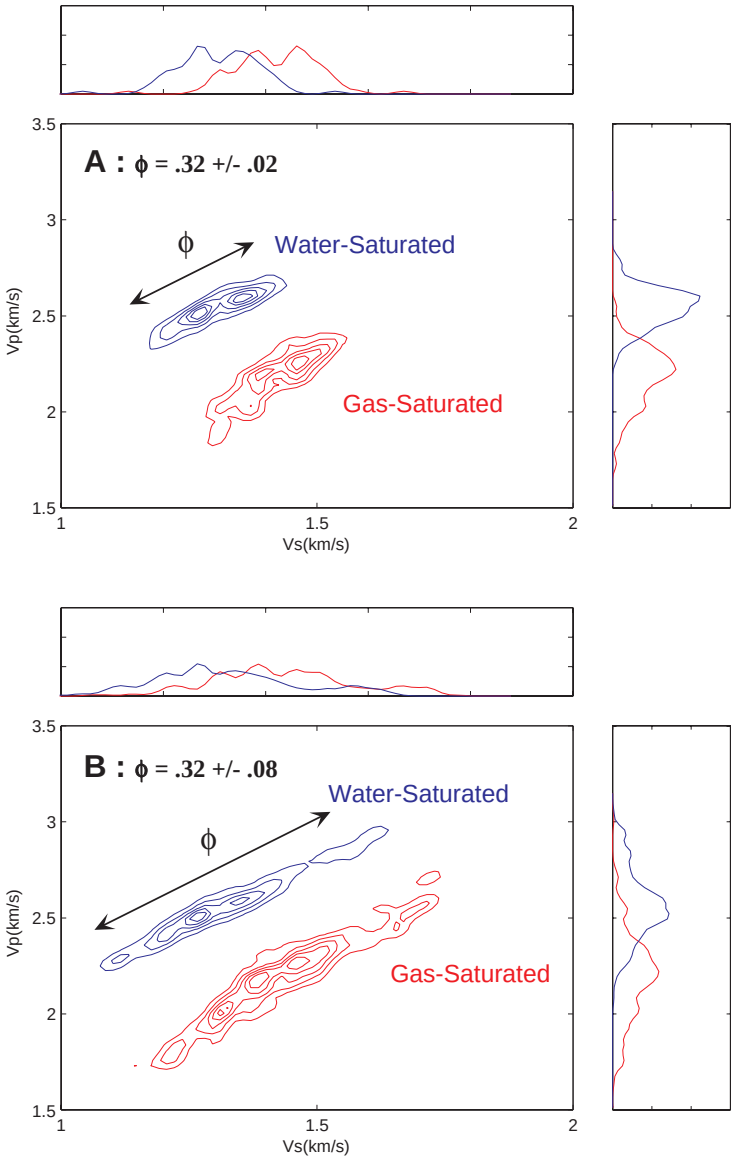

Figure 5.5: The pdfs of V_p and V_s for gas- and water-saturated sandstones. **A** has a smaller porosity variability than **B**, although the mean porosities are the same in both cases.

2. The univariate pdfs of V_p in Figure 5.5-**A** (right), as well as the statistics for V_p in Table 5.3-**A**, show that prediction of pore fluid using only V_p gives relatively good results when the formation variability is small. Hence, additional V_s information has little impact on the prediction in case **A**. In case **B**, on the other hand, prediction error using only V_p is

relatively large because of the broad overlaps of the pdfs. In this case, additional V_s data have a great effect on the prediction and significantly increase the predictability of pore fluids.

Although the difference between cases **A** and **B** are assumed to be due to the variability of reservoirs, it can also be considered as another scenario—the influence of geological knowledge. Well data and geological information may suggest specific distribution of rock properties and may define local pdfs as **A** for a sub-region of the entire reservoir, when the pdfs for the entire reservoir is estimated as **B**. In this case, the geological knowledge provides us with information about constraints on the intrinsic variability and reduces uncertainty about the pore fluid prediction, as summarized in Table 5.3.

5.2.4 Errors in Seismic Attributes

Seismic measurement and processing introduce errors related to ambient and coherent noise, geophone coupling, limited acquisition geometry, limitations in computer abilities, etc. A big issue is velocity estimation in laterally heterogeneous environment (Claerbout, 1999). As discussed in chapter 4, when these errors can be rigorously expressed by pdfs, we can include the errors into our information and uncertainty analysis. According to Figure 4.6, a pdf corresponding to a measured data value becomes broad when the measurement error becomes large. Simple assumptions are often made such as zero-mean Gaussian functions (Silverman, 1986).

Figure 5.6 shows the bivariate pdfs of V_p and V_s for the same gas- and water-saturated sandstones when measurement errors are different. The error pdfs are assumed to be Gaussian functions with different covariances. The error pdf for each case (*i.e.*, a pdf corresponding to a measured sample) is illustrated in the lower-right of each plot.

The statistics of the pore fluid prediction in the three cases are summarized in Table 5.4. The comparison of the statistics in **A** and **B**—pdfs with the same configurations but different width—demonstrates that an increase in measurement errors decreases the information provided by the measurement, and increases the estimation error. Case **C** shows that an uncorrelated error drastically increases the estimation uncertainty. It should be noted that the small uncorrelated measurement errors (**C**) make the prediction more difficult than the

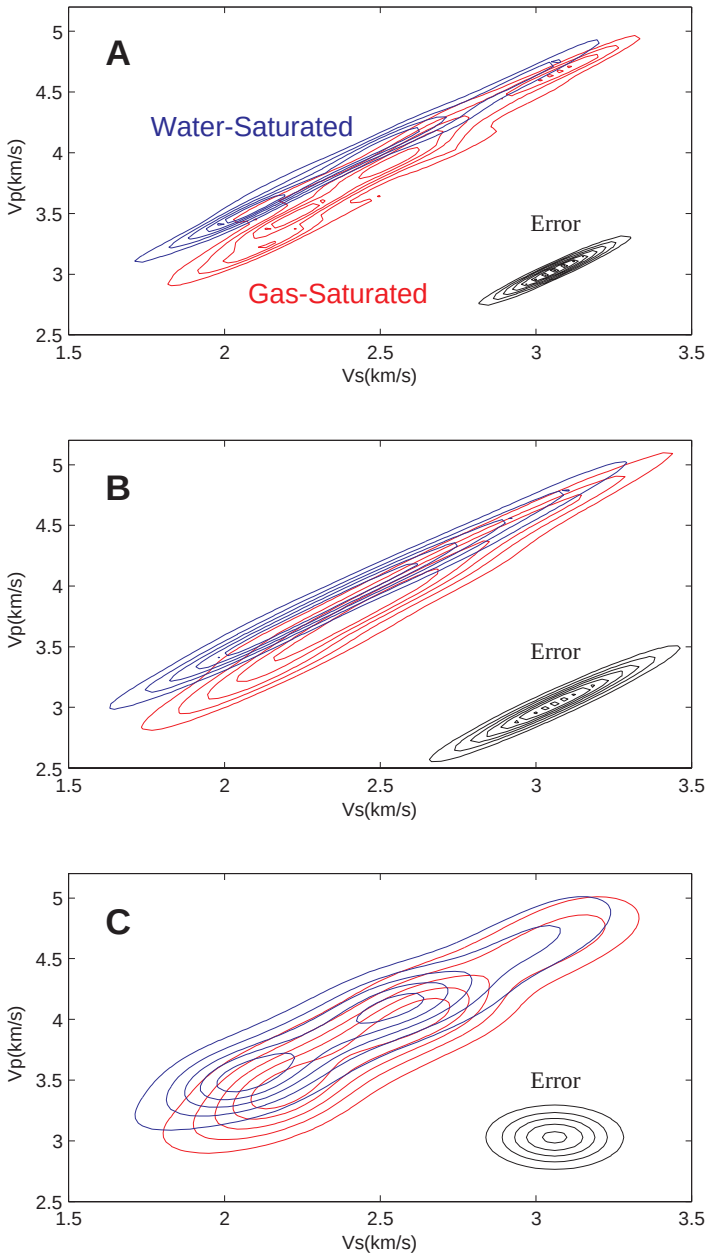

Figure 5.6: The bivariate pdfs of V_p and V_s for gas- and water-saturated sand with different measurement errors. The error pdfs are Gaussian functions shown by contours in the lower right of individual plots. In **A** and **B**, the errors for V_p and V_s are correlated, while the error is uncorrelated in case **C**. The correlation coefficient of the error is equal to the sample correlation coefficient in **A** and **B**. Standard deviations of the error pdfs along the V_p and the V_s axes are summarized in Table 5.4

large correlated errors (**B**). Knowledge about the error correlation conveys information.

		$\sigma_{V_p}^{error}$ (m/s)	$\sigma_{V_s}^{error}$ (m/s)	M. Inf.	N. Inf.	B. Error
A	correlated	115	152	0.37	0.54	0.143
B	correlated	186	253	0.30	0.44	0.183
C	uncorrelated	115	152	0.09	0.13	0.336

Table 5.4: Information and the Bayes error of pore fluid prediction from V_p and V_s, derived from the pdfs in Figure 5.6.

The width of error pdfs should be consistent with the specifications of the data acquisition, processing, and inversion used to derive the particular seismic attributes. The errors in attributes can be evaluated from the sensitivity between the attributes and the data, along with errors in the data space. For example, by exploring the traveltime equation for reflected waves, Uzcategui (1998) estimated the accuracy of seismic velocity analysis as a function of the frequency of the wave, the target depth, average subsurface velocity, and the maximum offset. Precise evaluations of the measurement/processing/inversion errors, as well as the relation between errors in different attributes, are difficult in practice. However, the framework for incorporating the errors as pdfs into the uncertainty analysis presented in chapter 4 is general and can be applied to arbitrary types of errors.

5.3 Optimal Seismic Attributes for Rock Property Estimations

Recent developments in seismic technology have enabled us to use seismic data not only for structural interpretation, but also for reservoir property estimation. Although many types of seismic attributes are used in practice, quantitative guidelines about which attributes should be used in particular conditions have not been well established.

Figure 5.7 shows well log profiles from a North Sea Tertiary turbiditic reservoir. These data points are also plotted in Figure 5.8 in four different combinations of seismic attributes. The colors represent six different siliciclastic facies within the reservoir, from clean sand to pure shale. The clustering and separability of the facies are different in each of the

attribute planes, since each pair contains different information. The question of which seismic attributes to use under which conditions is crucial for more reliable rock property estimation.

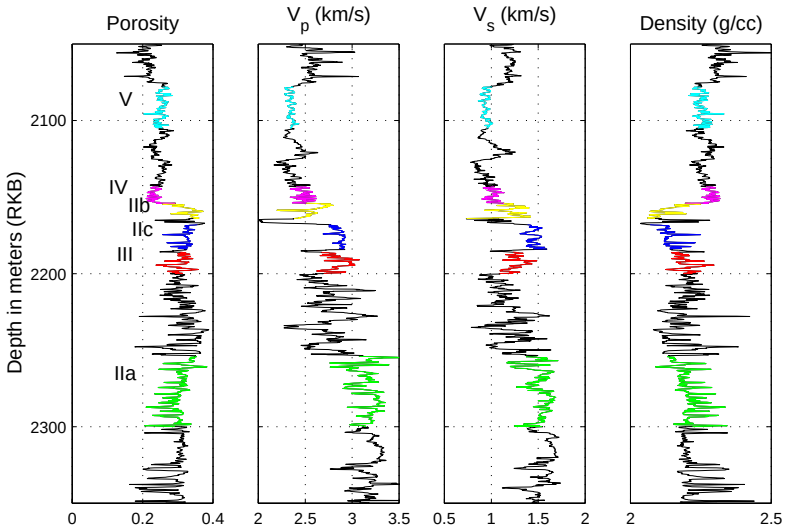

Figure 5.7: Well log profile of a Tertiary turbiditic reservoir in the North Sea. Six siliciclastic lithofacies are displayed in colors and Roman numerals: IIa: cemented sand, IIb: unconsolidated sand, IIc: laminated sand, III: interbedded sand and shale, VI: silty shale, V: pure shale.

In this section, we develop a strategy to find optimal seismic attributes for predicting particular reservoir properties, such as lithofacies and pore fluid types, combining rock physics and statistics. By using the concept of mutual information presented in chapter 4, we quantify the information about rock properties carried by seismic attributes (Ash, 1965; Cover and Thomas, 1991). Well data from the North Sea and Australian oil fields are used for the investigation.

The attributes studied are those that have established physical relations to either the interval properties of the reservoir, such as velocity and impedance, or the contrast of rock properties at certain boundaries, such as reflectivity and AVO attributes.

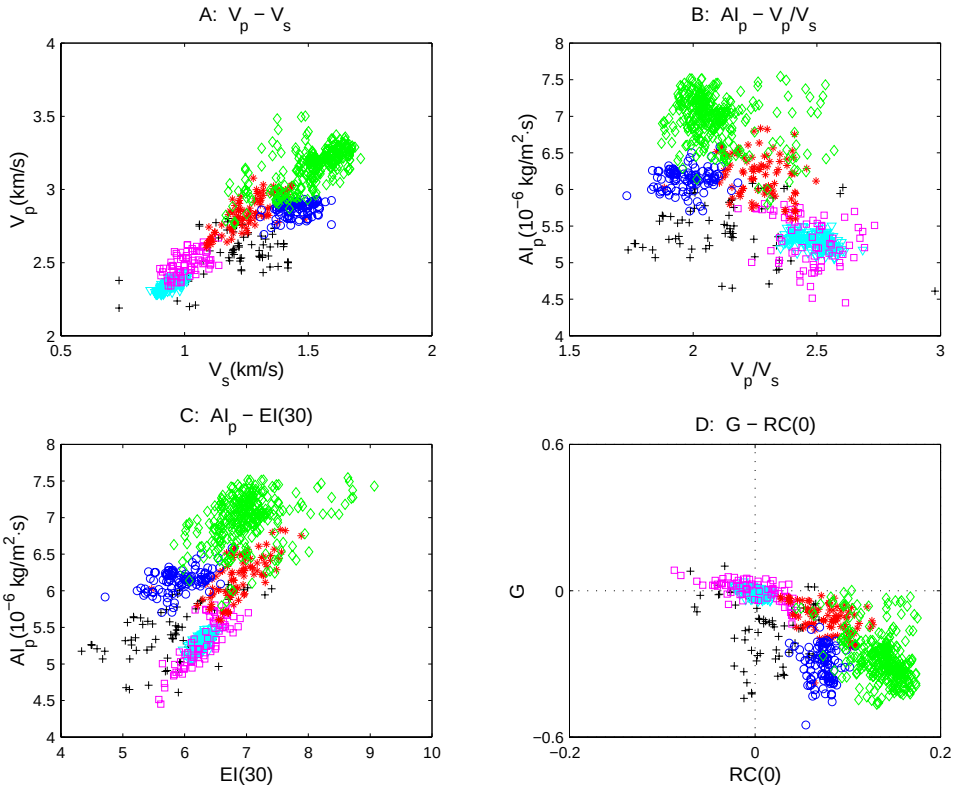

Figure 5.8: Four cross-plots of seismic attributes in a North Sea reservoir. A-D for V_p-V_s, acoustic impedance-V_p/V_s ratio, acoustic impedance-elastic impedance (see appendix 2), and AVO gradient-AVO intercept domains. The individual attribute domains show different behaviors. Refer to Figure 5.7 for the facies correspondence to the colors.

5.3.1 A Strategy to Find Optimal Seismic Attributes for Reservoir Property Prediction

The uncertainty of reservoir property estimation from seismic data is caused by two factors. The first is the imperfect dependence of rock properties and seismic properties. The second is the incompleteness of seismic attribute estimation from seismic data.

The strategy that we develop to quantify the information carried by seismic attributes consists of the following three major steps. The first step is estimation of the pdfs of seismic properties at in-situ reservoir conditions. The second step is evaluating errors of the forthcoming seismic data acquisition/processing/inversion of deriving seismic attributes from

observed data, and updating the pdfs. The final step is deriving the mutual information.

We first measure the information about lithofacies carried by seismic attributes, using the North Sea well data shown in Figure 5.7.

Step 1: Estimate PDFs of Attributes In-situ Conditions

From V_p, V_s, and density measurements at the well, we derive pdfs of seismic properties in perfect measurements for five lithofacies observed at the wells. Assuming that the well is representative of the entire reservoir, we interpolate the scattered data points (*e.g.*, as shown in Figure 5.8) to account for errors and lateral sampling of well log measurements, and estimate univariate and bivariate pdfs of the seismic properties. These seismic properties include linear and nonlinear transforms of the measured basic observations (V_p, V_s, and density), such as impedance, reflectivity, and elastic modulus. We assume homogeneous shaly caprock for properties representing boundary properties, such as reflectivity and AVO gradient. Four examples of the pdfs are shown in Figure 5.9.

In Figure 5.9, $RC(0)$ and $RC(30)$ denote the P to P reflectivity at normal and 30 degree incidence, respectively. Δt_p is the P-wave slowness, and PR is the modified AVO gradient defined by Hilterman (1989) (refer to appendix 2 for the definition). The lithofacies populations are distributed differently in different domains. Overlaps of each lithofacies demonstrate the non-uniqueness of the relation between seismic properties and lithofacies even in the error-free condition. The univariate pdfs of V_p has well separated peaks for the different facies, shaly sand (blue) and cemented sand (green), while the pdf of the V_p/V_s ratio shows more overlap between the facies. Similarly, the bivariate pdfs in $\Delta t_p - PR$ are more separated than in $RC(0) - RC(30)$. The pdfs imply more separability of lithofacies in V_p and $\Delta t_p - PR$ than in V_p/V_s and $RC(0) - RC(30)$, respectively, in error-free measurements.

Step 2: Estimate PDFs at Seismic Observation

Since the resolution and quality of seismic data are limited, attributes derived from seismic data may not describe the *true* values of the seismic properties, but can be erroneous representations of the properties. We assume errors in each seismic attribute as uncorrelated zero-mean Gaussian functions with 95% confidence intervals, as in Table 5.5.

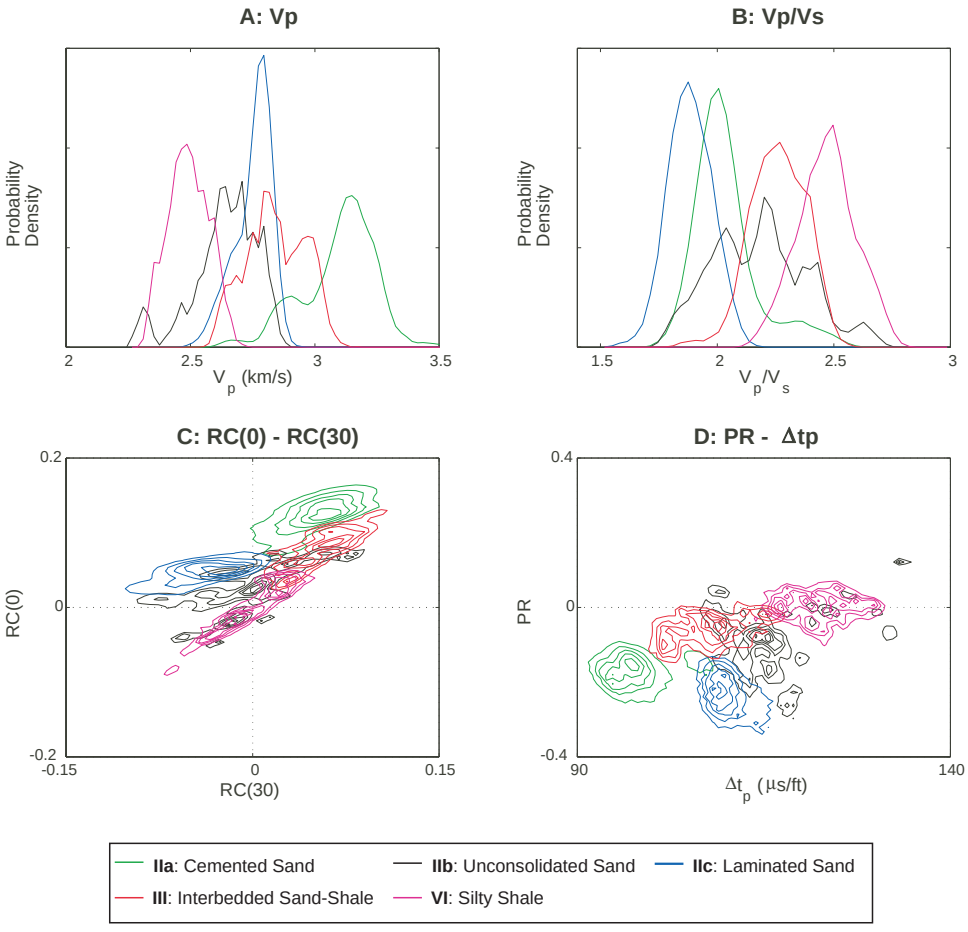

Figure 5.9: Univariate and bivariate pdfs at the in-situ condition in a North Sea reservoir. V_p and $PR - \Delta t_p$ show more separated peaks than V_p/V_s and $RC(0) - RC(30)$.

We smooth the pdfs at the in-situ condition (*e.g.* as shown in Figure 5.9) according to the assumed errors in Table 5.5. The estimated pdfs for seismic observations are shown in Figure 5.10. The pdfs at seismic accuracy are smoother and have more overlaps than at well log accuracy, showing that lithofacies estimation from seismic data is more uncertain than from acoustic well log data.

Step 3: Quantify Information

Finally, using the pdfs at seismic accuracy, we derive the mutual information carried by attributes, $I(facies|attributes)$, which are summarized in Figure 5.11. In this par-

Attribute	V_p	V_s	AI_p	AI_s	$EI(30)$	$RC(0)$	$RC(30)$	G	PR
Method	Stacking		Inversion			Conventional Processing		AVO	
Data	P	S	P	S	P				
Error (%)	15	20	7.5	12	10	7.5	10	12	12

Table 5.5: Assumed errors of individual attributes. The difference between the maximum and minimum observed attribute values are multiplied by the listed values and used as the 95% confidence intervals of Gaussian functions. The processing method and necessary data to derive each attribute are also listed. AI_p: P-wave acoustic impedance, AI_s: S-wave acoustic impedance, $EI(30)$: elastic impedance at the 30 degree incidence, $RC(0)$: zero-offset reflectivity, $RC(30)$: reflectivity at the 30 degree incidence, G: AVO gradient by Aki and Richards approximation (1980), PR: AVO gradient by Hilterman's approximation (1989).

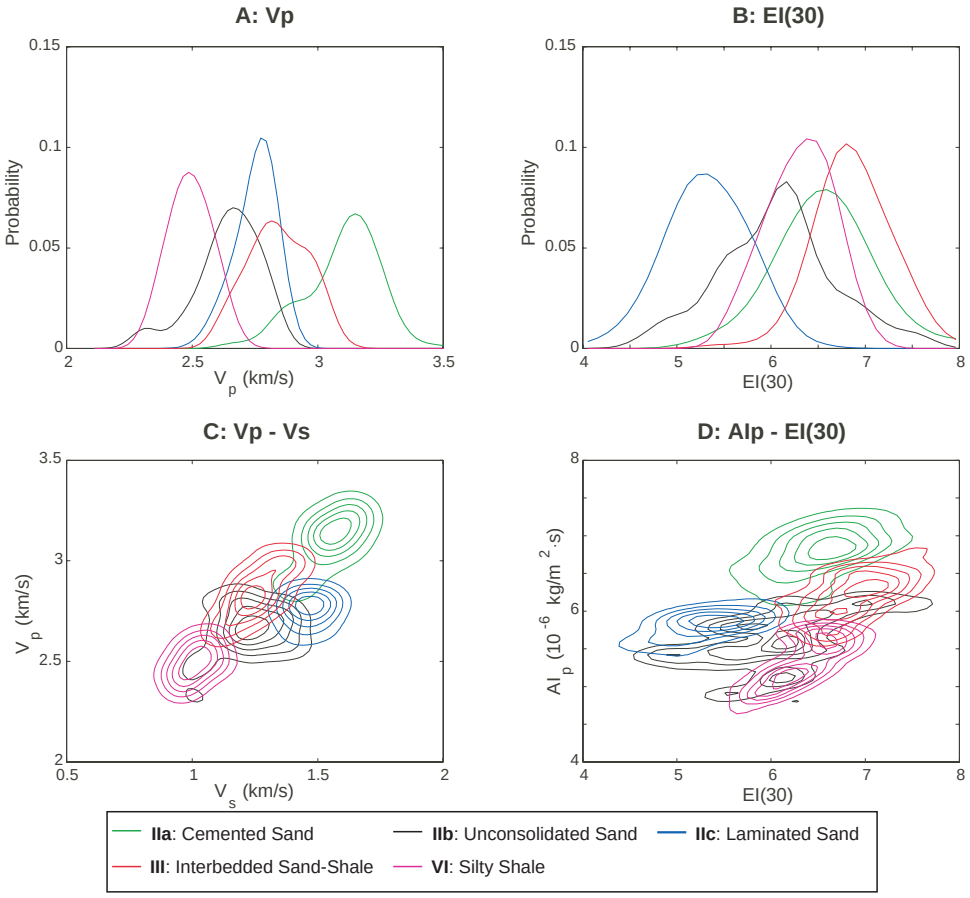

Figure 5.10: Univariate and bivariate pdfs at a seismic observation in a North Sea reservoir. The pdfs are smoother than in well log accuracy, shown in Figure 5.9.

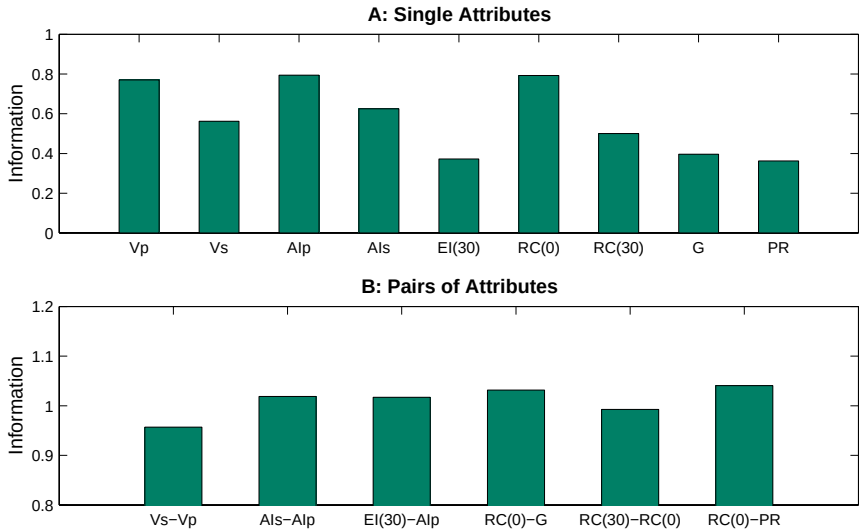

Figure 5.11: Information about lithofacies carried by single and pairs of seismic attributes, I(facies|attributes), in a North Sea reservoir. Attributes related to the volumetric stiffness, V_p, AI_p, and $RC(0)$, are good information carriers about lithofacies.

ticular Tertiary turbiditic reservoir that includes cemented and unconsolidated sand, V_p, AI_p (P-wave acoustic impedance), and $RC(0)$ (P-wave normal incidence reflectivity) are the most informative single attributes, which are related to the volumetric stiffness of the reservoir. On the other hand, single attributes related to the V_p/V_s ratio, such as $EI(30)$ (elastic impedance), G (AVO gradient by Aki and Richards (1980)), and PR (AVO gradient by Hilterman (1989)) are the least informative. All pairs of attributes provide more information than single attributes, which is consistent with the discussion in section 5.2.1. However, the differences between individual pairs of attributes are relatively small. This is because all the selected six pairs consist of both P-wave-related and S-wave-related attributes.

Optimal Seismic Attributes for Lithology Prediction in a Australian Reservoir

We also analyze the information about lithofacies carried by attributes using well data from Australia. Well log profiles in Figure 5.12 shows rather homogeneous characteristics of the reservoir and large contrast of the properties between the reservoir and the overlying shale. Relatively high velocity in the reservoir zone, below a sharp porosity boundary

around 2040 m, suggests stiff matrix frame of the reservoir rock. It is in contrast to the North Sea sands, where the reservoir sand have a relatively soft matrix frame. We select the optimal seismic attributes to classify sand from shale, following the procedure explained earlier.

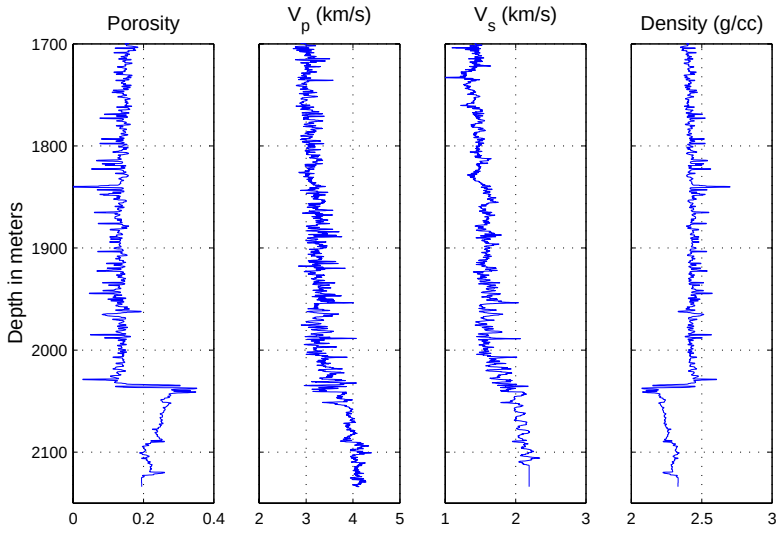

Figure 5.12: Well log profile of an Australian sandstone. Sharp boundary in porosity and density logs corresponds to the top of the reservoir.

Figure 5.13 shows examples of the estimated pdfs of sand and shale facies of the Australian reservoir. Figure 5.14 summarizes the mutual information about lithofacies provided by seismic attributes in the reservoir.

In the Australian reservoir, V_s, V_p, and G (AVO gradient) are better single information carriers about lithology, and V_p-V_s is the most informative pair. In contrast, attributes related to the V_p/V_s ratio, $EI(30)$ and $RC(30)$ (reflectivity at 30 degree of incidence), cannot distinguish sand from shale very well. Figure 5.13-B shows $EI(30)$ is almost independent of the lithofacies.

The mutual information about lithofacies classification of the North Sea and the Australian case cannot be directly compared, since the number of lithofacies are different. However, from a comparison between Figures 5.11 and Figure 5.14 we can conclude that P- and S-velocities are better information carriers about lithofacies than P- and S- impedances

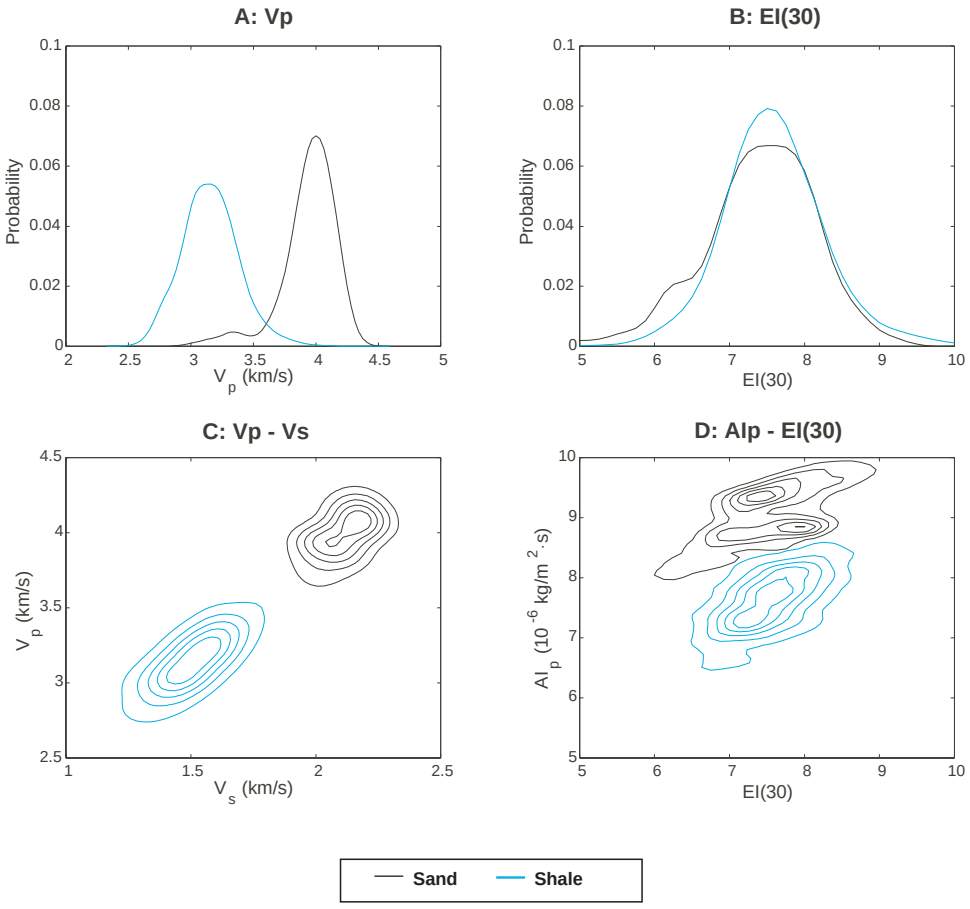

Figure 5.13: Univariate and bivariate pdfs at the seismic observation in an Australian reservoir. V_p shows clear separation between the sand and the shale, while they are overlapped in $EI(30)$.

in the Australian case, while the impedances are more informative than the velocities in the North Sea case. That is, the types of best attributes depend on local rock properties. Figures 5.11 and 5.14 can become quantitative input to decision analysis in exploration strategy making. The estimated information about lithofacies given by each attributes, along with cost estimates to obtain them, help us to decide which attributes—which acquisition/processing methods—to be used for lithofacies estimation.

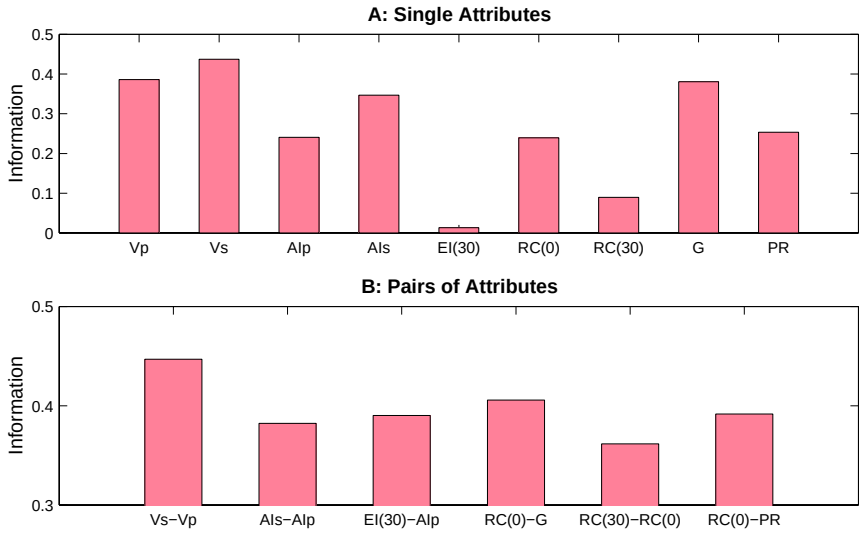

Figure 5.14: Information about lithofacies carried by single and pairs of seismic attributes in an Australian reservoir. V_s, V_p, and G are good information carriers.

5.3.2 Optimal Seismic Attributes for Various Scenarios

In this section, we apply the procedure presented in section 5.3 to rock properties other than lithofacies, namely, pore fluid and porosity, and investigate optimal seismic attributes for these scenarios.

Fluid Detection

We first study the information about pore fluid conveyed by various attributes. By applying Gassmann's formula and following the same procedure as described in section 5.3, we establish pdfs of sandstones saturated with three different pore fluids; brine, oil, and gas. That is, we derive seismic attributes in the unobserved conditions by extrapolating available data using Gassmann's theory.

Examples of the pdfs from the North Sea data are displayed in Figure 5.15. The fluid effect on seismic attributes, in general, is small as compared to the diversity of the pdfs. This causes large overlaps between the pdfs and makes pore fluid detection from seismic data difficult. Figures 5.16 and 5.17 summarize the information about pore fluids conveyed by single and pairs of seismic attributes in the North Sea, derived from the pdfs in Figure 5.15,

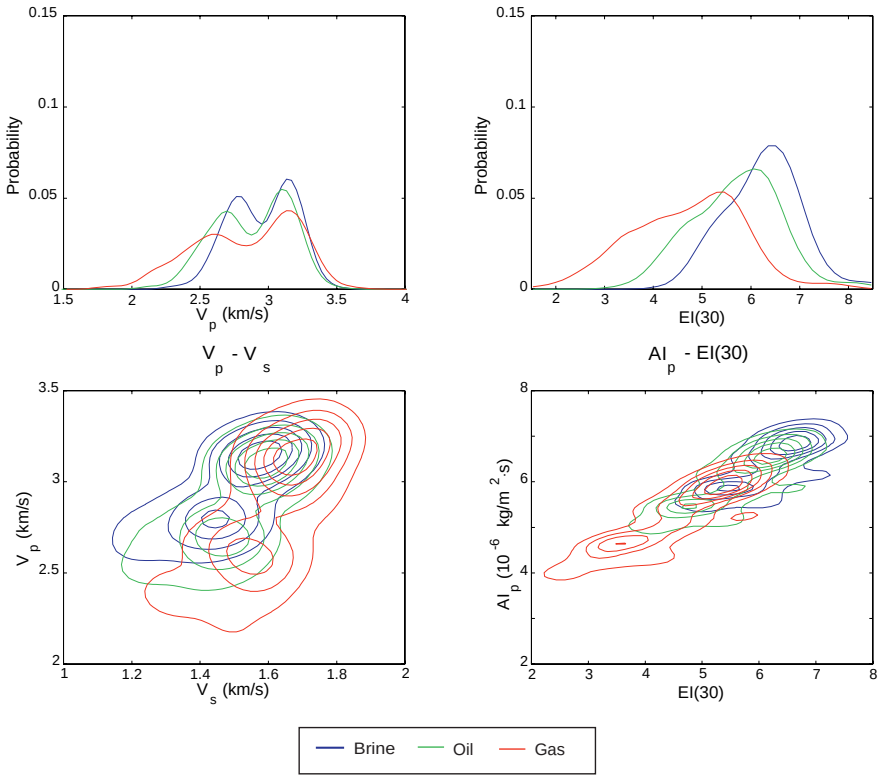

Figure 5.15: The pdfs of seismic attributes for three different pore fluids in a North Sea reservoir. $EI(30)$ is more sensitive to pore fluids than V_p.

as well as the Australian fields.

In the North Sea field, AI_p, $EI(30)$, $RC(0)$, and $RC(30)$ are the most informative single attributes about pore fluids. They depend on the density and/or the V_p/V_s ratio. In the Australian field, the information is generally smaller than the North Sea case, since a stiff matrix frame keeps elastic moduli of the reservoir insensitive to pore fluids, as discussed in section 5.2.2. (The mutual information of the two fields can be compared since the uncertainty about pore fluid prior to seismic observation is considered identical, *i.e.*, the same three fluids are considered possible in the two fields.) Hence, the attributes that are sensitive to density, such as V_s, AI_p, $RC(0)$, and $AI_s - AI_p$, are better information carriers than others in the Australian field.

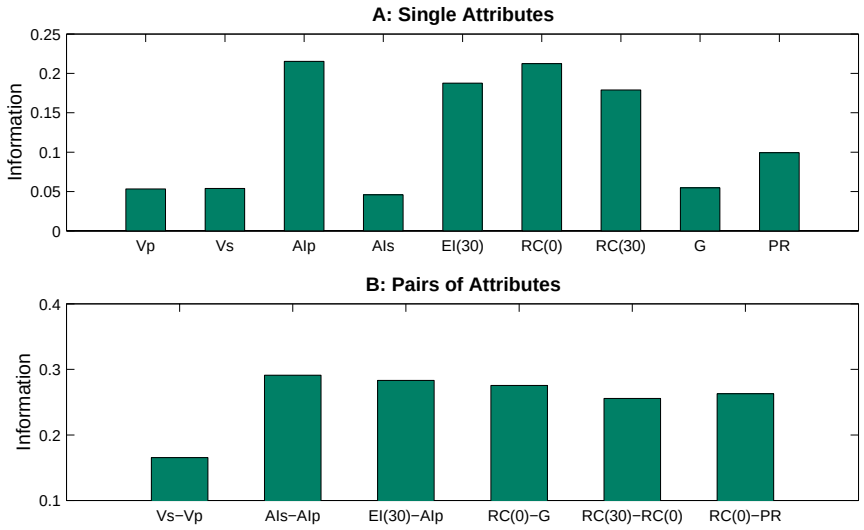

Figure 5.16: Information about pore fluids carried by single and pairs of seismic attributes in a North Sea reservoir. Attributes related to density and/or V_p/V_s, such as AI_p, $EI(30)$, $RC(0)$, and $RC(30)$, convey more information than others.

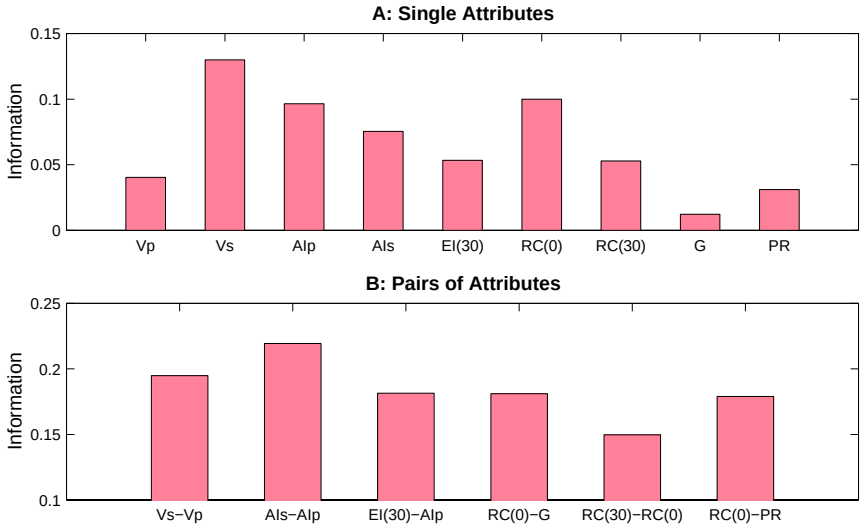

Figure 5.17: Information about pore fluids carried by single and pairs of seismic attributes in an Australian reservoir. Attributes dependent on density, V_s, AI_p, and $RC(0)$ are good information carriers.

Porosity Prediction

We next quantify the information about porosity of sandy facies carried by attributes. Figures 5.18 and 5.19 summarize estimated values of mutual information, $\mathrm{I}(\phi|\mathrm{attributes})$. For the purpose of porosity prediction in sands, AI_p and $RC(0)$ are the best single infor-

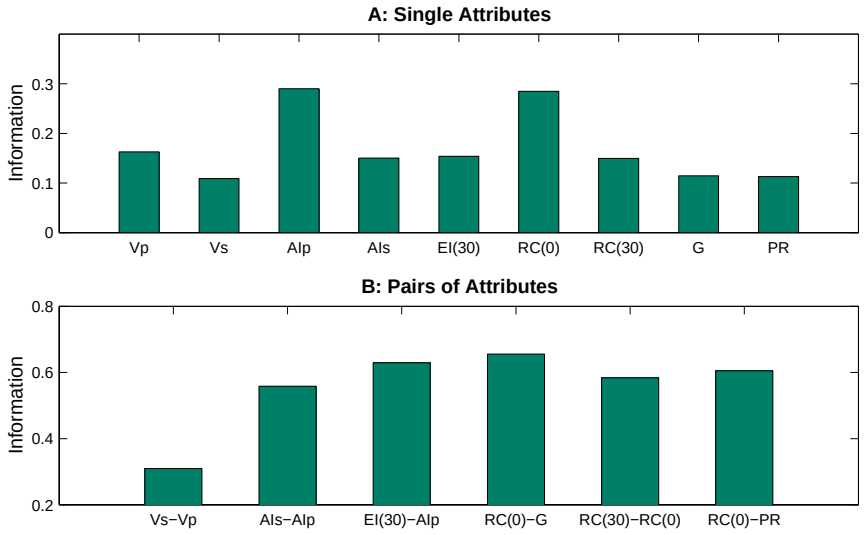

Figure 5.18: Information about porosity carried by single and pairs of seismic attributes in a North Sea reservoir. Attributes dependent on volumetric stiffness, AI_p, $RC(0)$, and V_p, convey more information than others.

mation conveyers in both the North Sea and the Australian fields. All of the selected pairs of attributes carry approximately the same information, except V_p-V_s. The mutual information is greater in the rather homogeneous Australian reservoir than the North Sea reservoir that comprises several lithofacies, although the overall sensitivity of attributes to porosity is similar in the two reservoirs.

5.3.3 Blind Tests

In statistical data mining, optimal choice of attributes is often made on the basis of performance on a test set of the data. The test set is a subset of the data kept aside from the training set. To verify that the mutual information indeed represents the ability of seismic attributes to predict rock properties, we perform blind classification tests for lithofacies

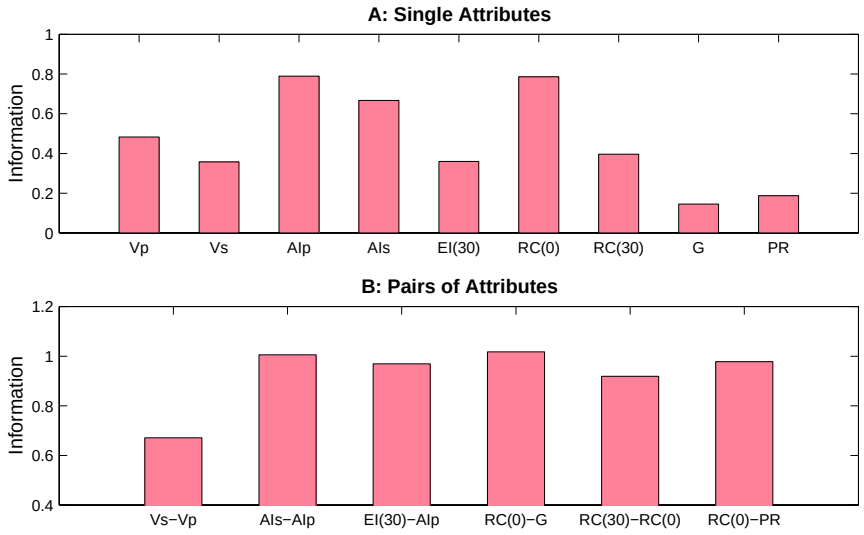

Figure 5.19: Information about porosity carried by single and pairs of seismic attributes in an Australian reservoir. Attributes dependent on volumetric stiffness, AI_p, $RC(0)$, and V_p, convey more information than other.

prediction and pore fluid detection. Using the North Sea well, we choose 80 percent of the data as training data and derive the pdfs of lithofacies, as described in section 5.3. We then classify lithofacies of the remaining 20 percent test data, compare the predicted facies with the true facies, and estimate the success rate of the prediction. We also conduct similar test classification for pore fluid detection. Figure 5.20 shows success ratios of the blind tests. The results are consistent with Figures 5.11 and 5.16, *i.e.*, the larger the mutual information,

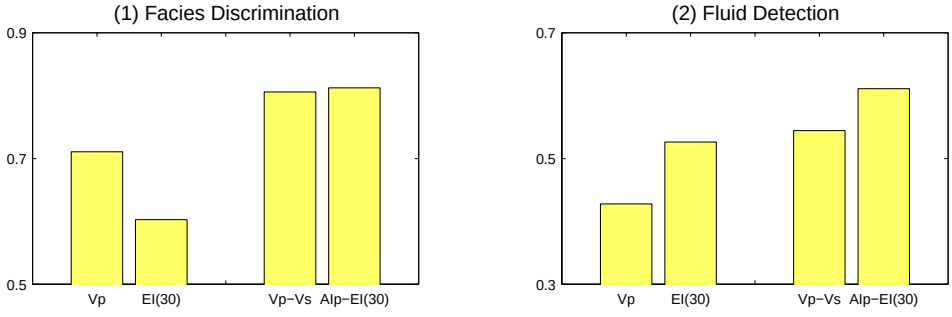

Figure 5.20: Success ratio of blind tests. The results are consistent with Figures 5.11 and 5.16, *i.e.*, the greater the information, the more successful prediction.

the more successful the classification, and the better the performance on the test data.

5.4 Conclusions

In this chapter, we quantitatively investigated how uncertainty in rock property estimation is influenced by individual sources of uncertainty. We showed that combinations of seismic attributes that can improve the predictability of rock properties, although there is an upper limit of information that seismic data can carry. The upper limit is due to imperfect dependence between seismic attributes and target rock properties. We also demonstrated that the predictability of rock properties from seismic attributes depends both on the sensitivity of the rock properties to the attributes, and the natural variabilities of the target rock properties. Furthermore, errors in deriving seismic attributes cause uncertainty in rock property estimation.

Using information theory, we then proposed a strategy to quantify the information conveyed by seismic attributes. Well data analysis showed that each seismic attribute and each pair of attributes carries different information about rock properties. Moreover, optimal seismic attributes for particular rock property prediction may differ from one field to another. In the particular cases of the North Sea and the Australian field, AI_p and $RC(0)$ are good information carriers for predicting lithology, pore fluids, and porosity. While pairs of attributes are usually better than single attributes, in some situations the small incremental information by additional attributes may not offset additional cost of acquiring the attributes. Application of the proposed methods serves as a *quantitative decision analysis guide* for evaluating various data acquisition and processing options.

Chapter 6

Scale Effects in Rock Property Estimation

Abstract

The scale of heterogeneity in the subsurface is one of the most important factors affecting seismic signatures. This chapter discusses how the fine-scale interbedding of sand and shale within a reservoir influences seismic reflectivity. Results from normal incidence seismic forward modeling demonstrate that reservoirs with identical average properties can give rise to a wide range of reflectivity, depending on the scale and distribution of layering. Although the reflectivity relies on the average reservoir property, its dependence is non-unique. This non-uniqueness prevents us from deterministically predicting rock properties from seismic reflectivity.

Combining Bayes inversion and stochastic simulation, we evaluate how seismic reflectivity can constrain the sand volume fraction of a reservoir. Assuming that all layer configurations statistically consistent with the spatial characteristics observed in the well are equiprobable, we establish a generalized relation between reflectivity and sand/shale ratio by seismic forward modeling. For a given seismic reflectivity, a probability density function (pdf) of possible sand/shale ratios is delivered as the answer, instead of one deterministic value. According to the results, the effective medium approximation in interpreting seismic reflectivity may result in systematic overestimation of the sand/shale ratio, if the reservoir

is randomly layered. The solution of the proposed method, a pdf of the sand/shale ratio, provides us with a quantitative and physical measure of uncertainty caused by small-scale heterogeneities.

6.1 Introduction

Subsurface geological formations have a wide scale range of heterogeneity, from microscopic and pore scale to macroscopic and sedimentary basin scale (Weber and Van Geuns, L.C., 1990). Seismic wave propagation is influenced by this diversity of the scale of heterogeneity, which makes rock property estimation non-unique, increasing the uncertainty. Marion et al. (1994), Watanabe et al. (1989), and Watanabe and Sassa (1995), among many others, demonstrated through both experiment and numerical modeling that the effective velocity of stratified media depends on the relation between wavelength and the scale of layering. This chapter extends their work to see how random interbedding affects seismic reflectivity, one of the most commonly used seismic attributes for predicting reservoir characters.

By combining Bayes theory and stochastic simulation, we propose a method to quantify how observed seismic reflectivity can constrain estimates of the sand/shale ratio of reservoirs, when the layer configurations are unknown. In general reservoir characterization, many subsurface properties (*e.g.*, porosity, clay content, pore fluid saturation) as well as small scale heterogeneities, influence seismic signatures and make rock property estimation uncertain. Although this chapter focuses on only one aspect of the non-uniqueness of one seismic attribute—the effect of small scale layering on reflectivity—the Bayes method proposed in this work is general and can be applied to any rock property prediction from seismic attributes, when dealing with non-uniqueness and uncertainty.

6.2 Scale Dependence of Seismic Velocities in Layered Media

The way seismic waves propagate through the Earth depends on the relation between the wavelength, λ, and the scale of heterogeneity, d, of the media (Marion et al., 1994).

6.2.1 Ray Theory Limit

When the wavelength is considerably smaller than the scale of heterogeneity, *i.e.*, $\lambda \ll d$, the wave propagation may be described by ray theory. The effective velocity perpendicular to the layers is given by

$$V_{RT} = \left[\sum_{i=1}^{N} \frac{f_i}{V_i} \right]^{-1} \tag{6.1}$$

where f_i and V_i are the volume fraction and velocity of the *i*th constituent material, respectively.

6.2.2 Effective Medium Theory Limit

When the wavelength is significantly larger than the scale of heterogeneity, *i.e.*, $\lambda \gg d$, the effective velocity is

$$V_{EMT} = \sqrt{\frac{M_{EMT}}{\rho_{ave}}} \tag{6.2}$$

where ρ_{ave} is the average density and M_{EMT} is the effective P-wave modulus of the medium. If the wave propagation is normal to the layers, M_{EMT} is the Backus average—the harmonic average of the P-wave moduli—of the constituent materials, M_i, as

$$M_{EMT} = \left[\sum_{i=1}^{N} \frac{f_i}{M_i} \right]^{-1} \tag{6.3}$$

By the nature of averaging, V_{RT} is always greater than V_{EMT}. Given a layered medium with constant volume fraction of constituent materials, V_{RT} and V_{EMT} correspond approximately to the upper and lower bounds of the velocity, respectively, although at intermediate scales, $\lambda \approx d$, Rayleigh and Mie scattering can give rise to velocities below V_{EMT} and above V_{RT} (Aki and Richards, 1980; Mavko et al., 1998).

Figure 6.1 shows the dependence of acoustic velocity on the wavelength relative to the scale of layering, observed in the ultrasonic transmission experiment by Marion et al. (1994).

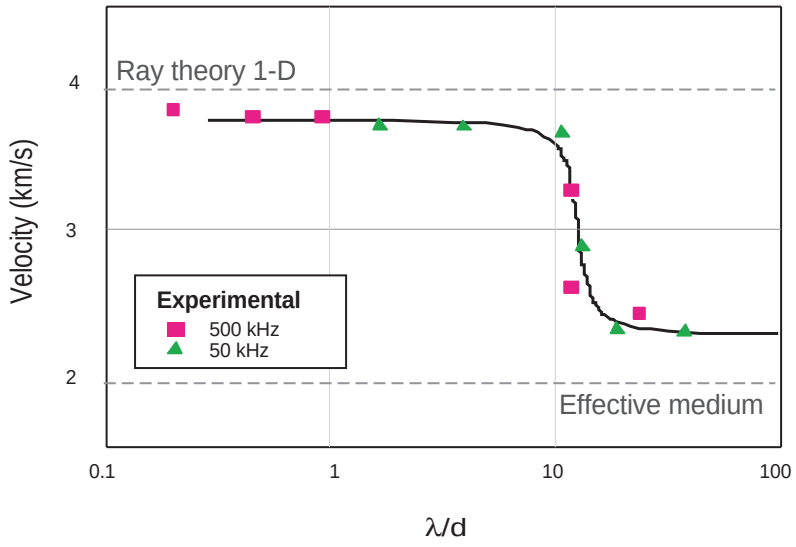

Figure 6.1: Dependence of acoustic velocity on the ratio of the wavelength relative to the scale of layering. All samples had the same volume fractions of two constituents (steel and plastic), but each one had different scale of layering (Modified from Marion et al. (1994))

Although all the measured velocities are for the models with equal volume fractions of two constituent materials, steel and plastic, velocities are variable depending on λ/d, the ratio of the wavelength relative to the scale of layering. When the wavelength is small compared to the scale of layering, *i.e.*, λ/d is small, the velocity is larger and close to the ray theory prediction. In contrast, when the wavelength is large relative to the scale of layering, *i.e.*, λ/d is large, the velocity is smaller and close to the effective medium theory prediction.

6.3 Seismic Forward Modeling

Since subsurface formations have a broad scale range of heterogeneity, neither ray theory nor effective medium theory can perfectly describe the wave phenomena. In order to clarify the dependence of seismic reflectivity on the scale of heterogeneity in layered media, we conduct normal incidence P-wave seismic modeling.

Our reservoir models simulate a Tertiary turbiditic reservoir in the North Sea (Avseth et al., 1998b). The depth to the top reservoirs and the total thicknesses of the reservoirs are 2,000 m and 200 m, respectively, for all models. The reservoirs are composed of interbedded sand and shale with various scales of layering, as well as variable volume fractions of the two facies.

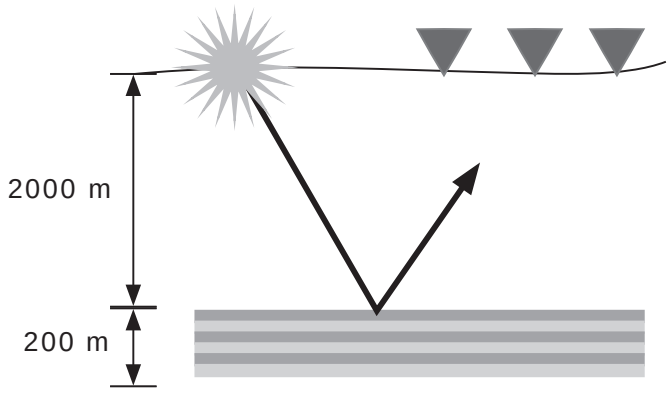

Figure 6.2: Schematic geometry of the numerical simulation. 200 m-thick reservoir, consisting of interbedded sand and shale is at a depth of 2,000 m. Normal incidence surface reflection survey is simulated.

Elastic parameters of sand and shale layers are kept constant. They are taken from typical values of well data in the field, as listed in Table 6.1.

Facies	V_p(km/s)	V_s(km/s)	ρ (g/cc)
Sandstone	3.0	1.6	2.1
Shale	2.3	1.0	2.25

Table 6.1: Reservoir model parameters for seismic forward modeling, taken from typical values in a North Sea field.

6.3.1 Periodically Layered Model

First we investigate the scale dependence of seismic amplitude using periodically layered reservoir models. Figure 6.3 shows ten reservoir models with the identical sand/shale ratio (50%) but different scales of layering. The sand and shale layer thicknesses are kept constant within each reservoir model. In the models, interbedding layer thickness changes from 2.5 m to 100m.

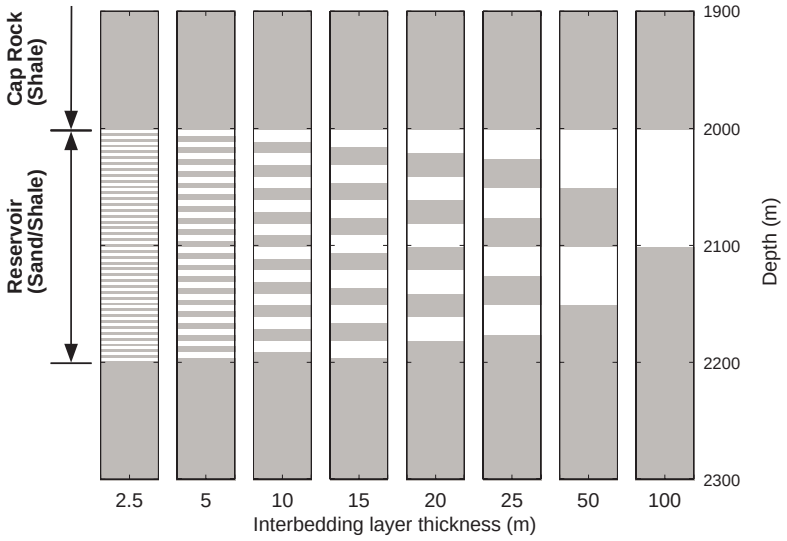

Figure 6.3: Periodically layered reservoir models. The sand/shale ratios of all models are 50%. The gray color is shale and the white represents sand. Only reservoir intervals of the models are displayed; homogeneous shale over-lies the reservoirs.

We carry out one-dimensional seismic forward modeling using the reservoir models to simulate zero offset surface seismic surveys. For the simulation, we use the invariant imbedding method introduced by Kennet (1974; 1983) to obtain the exact reflection seismograms, including all orders of multiple reflections. The input wavelet is a zero phase Ricker wavelet with a center frequency of 30 Hz, which is equivalent to a wavelength of 77 m and 100 m in the shale and the sand layers, respectively.

Figure 6.4 shows eight reflected seismograms simulated from the eight reservoir models in Figure 6.3. In both the thin and thick layer limits, the seismograms show two clear

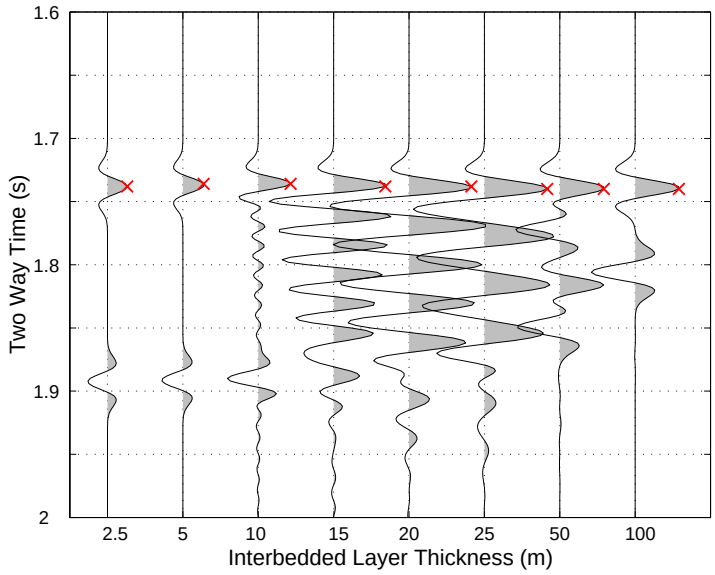

Figure 6.4: Reflected seismograms simulated from the periodically layered reservoir models in Figure 6.3. The seismograms show two clear peaks corresponding to the top and bottom reservoir in the thin-layer and thick-layer limits. However, the waveforms are chaotic in the intermediate layer thicknesses.

peaks corresponding to reflections from the top and bottom of the reservoir. In the intermediate layer thicknesses, however, interference of reflections from multiple layer boundaries makes the seismograms chaotic. The amplitudes of the top reservoir reflectors are picked, as shown by $\times$ marks, and plotted in Figure 6.5.

When the interbedded thickness, d, is smaller than 5 m, the reflectivity is almost consistent with the effective medium theory limit: the reflectivity between the overlying shale and the effective medium with a sand/shale ratio of 50%. In contrast, if d is large enough, the reflectivity is as predicted by the ray theory limit: the reflectivity between the overlying shale and the homogeneous sand. When d increases from the effective medium theory limit, the reflectivity increases and has a peak at around d = 25 m, when $d = \lambda/4$. The thickness corresponds to the *tuning thickness*, when the maximum constructive interference occurs (Widess, 1973). At this thickness, resonance of multiple reflections makes amplitudes larger than the ray theory limit.

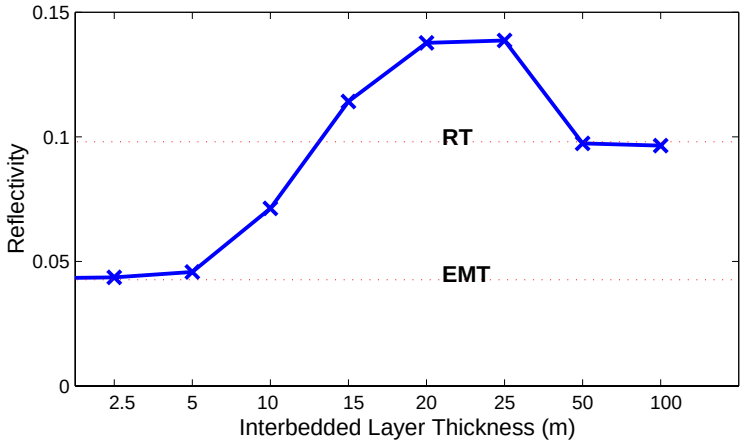

Figure 6.5: Reflection amplitudes at the top reservoir as a function of interbedded layer thickness, picked from Figure 6.4. The reflectivity is consistent with the ray theory and the effective medium theory limits in the thick-layer and thin-layer limits. The reflectivity is maximum when interbedded thickness is a quarter of the wavelength, corresponding to the tuning thickness.

6.3.2 Randomly Layered Model

Next we explore the scale dependence of reflectivity using randomly layered models. Using Monte Carlo simulation, we create 1,000 realizations of reservoir models for a fixed average layer thickness and sand/shale ratio. The individual layer thicknesses within the reservoirs are drawn from an exponential probability distribution with particular average values. In this case, the sand/shale stratifications follow a statistical model called a Poisson process. We keep the caprock as a homogeneous shale for all the models. Figure 6.6 shows ten examples of layered reservoir models, in which the average layer thickness (1 m) and the sand/shale ratio (50%) are identical. In a Poisson process, the distribution of individual layer thickness follows an exponential distribution, as shown in Figure 6.7.

We carry out normal incidence seismic modeling in the same way as explained in section 6.3.1. Figure 6.8 displays ten seismograms simulated from the reservoir models in Figure 6.6. Although the reservoir models in Figure 6.6 share the same average statistics, an average layer thickness of 1 m and a sand/shale ratio of 50%, the recorded waveforms are considerably variable. The individual layer thicknesses are significantly smaller than the wavelength ($\lambda/d \approx 10^2$ on average) in these models. However, waves propagate in

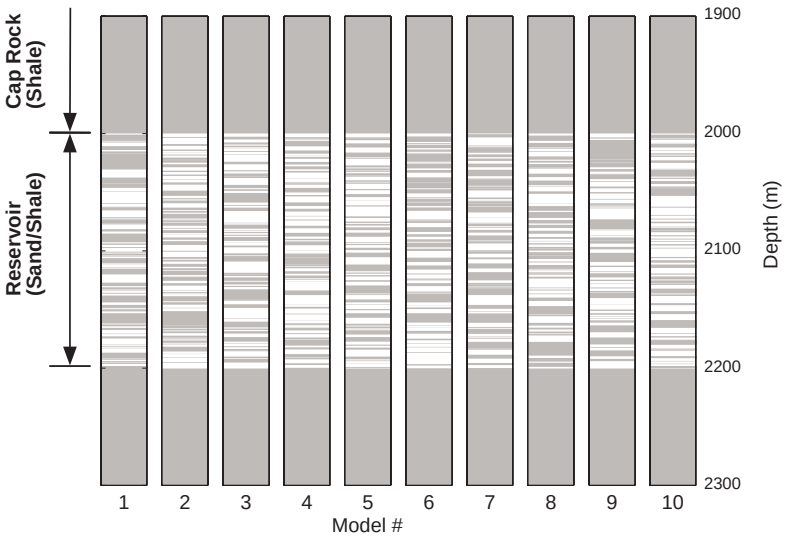

Figure 6.6: Examples of layered reservoir models from a Poisson process. The sand ratios are 50% and the average layer thicknesses are 1 m. The gray is shale and the white is sand.

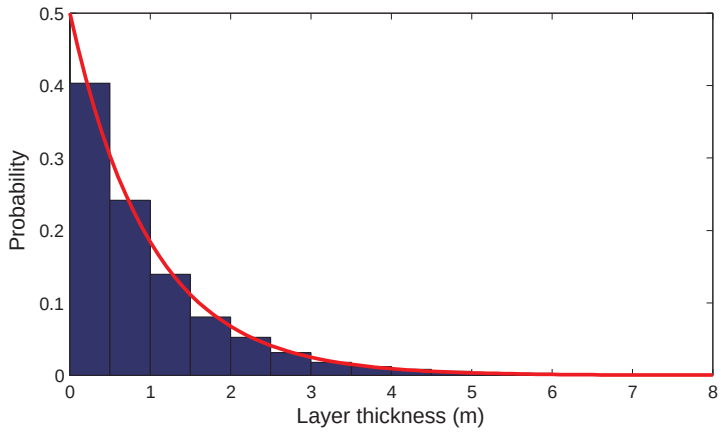

Figure 6.7: Layer thickness distribution in reservoir models from a Poisson process of average thickness of 1 m. The histogram follows an exponential function.

complicated ways in the randomly layered models. We pick amplitudes of the top reservoir reflectors from all the realizations, as shown by $\times$ marks in Figure 6.8.

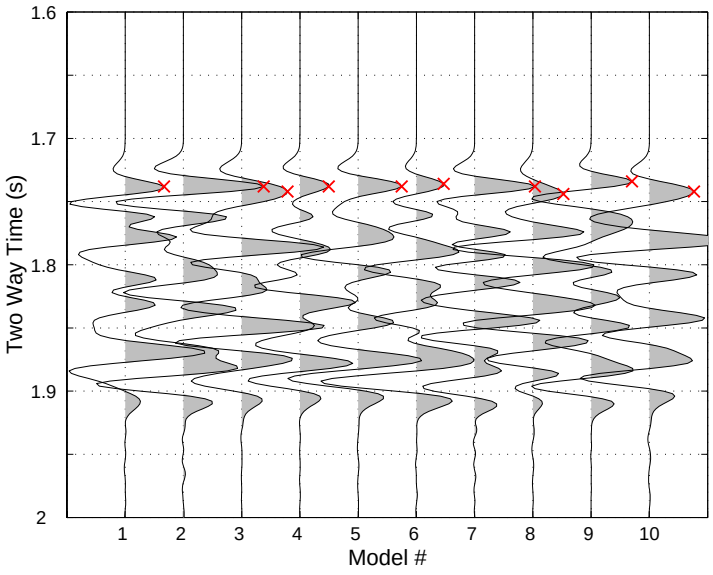

Figure 6.8: Zero offset reflected waves simulated from the reservoir models shown in Figure 6.6.

6.3.3 Effect of Layer Thickness on Reflectivity

First, we fix the sand/shale ratio, change the average layer thickness of the Poisson process, and investigate the dependence of the reflected amplitude on the average layer thickness. The curves in Figure 6.9 show the probability density functions, pdfs, of amplitude for a fixed sand/shale ratio of 50% and different average layer thicknesses, from 1 m to 50 m. Every distribution of reflectivity is computed from 1,000 simulated seismograms.

When the average layer thickness is the smallest, 1 m, the pdf of reflectivity has a peak around 0.043, which almost corresponds to the effective medium limit. As the layer thickness increases, the effective medium peak collapses and the distribution of reflectivity gradually shifts towards larger values. When the average thickness is over 10 m, a sharp peak appears, which corresponds to the ray theory limit. Although the two major populations of reflectivity can be well explained by the effective medium and ray theory limits, the randomness of layering makes the distribution of reflectivity diverse.

An intriguing point is that reflectivity outside high-frequency and low-frequency bounds is possible, *i.e.*, the reflectivity can be either smaller than the effective medium

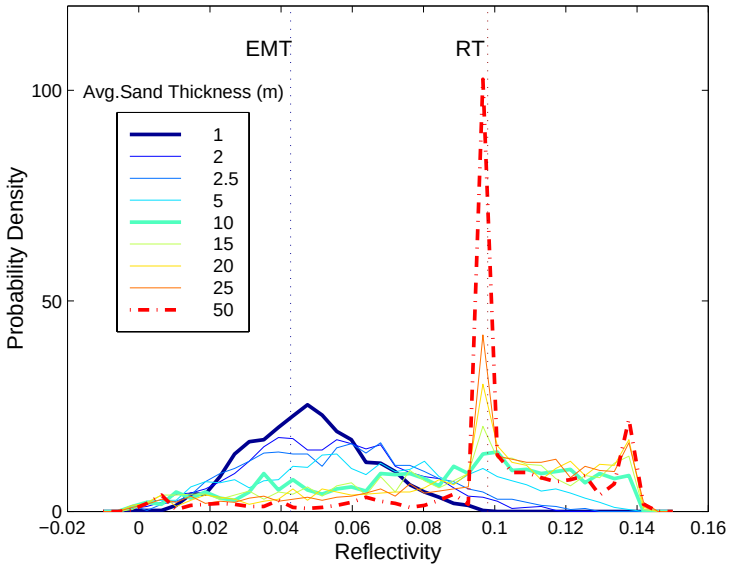

Figure 6.9: Distributions of reflectivity for various average interbedded thickness. Two peaks of reflectivity correspond to the ray theory and the effective medium theory limits. The reflectivity can be either smaller than the effective medium theory limit or larger than the ray theory limit, because of the random layering.

limit, or larger than the ray theory limit. This is in contrast to to the velocity of the transmitted wave, whose upper and lower bounds with respect to the scale of layering are given by the two theories (Marion et al., 1994).

6.3.4 Dependence of Reflectivity on Sand Ratio

In order to investigate the dependence of reflectivity on the sand/shale ratio, we next fix the average layer thickness to be 1 m ($\lambda/d \approx 10^2$) and vary the sand/shale ratio of reservoir models from 0% to 100%. Each curve in Figure 6.10 shows the pdf of reflectivity for different sand/shale ratios, picked from 1,000 simulated seismograms.

The two peaks on both sides show the reflectivity values of two limits when the sand/shale ratio is 0% and 100% (average layer thickness is not 1 m in these two limit cases). As the sand/shale ratio increases from 0%, the peak gradually collapses and the distribution shifts towards larger reflectivity. The distribution is the most dispersed when the sand/shale ratio is intermediate, and it becomes sharper as the sand/shale ratio approaches

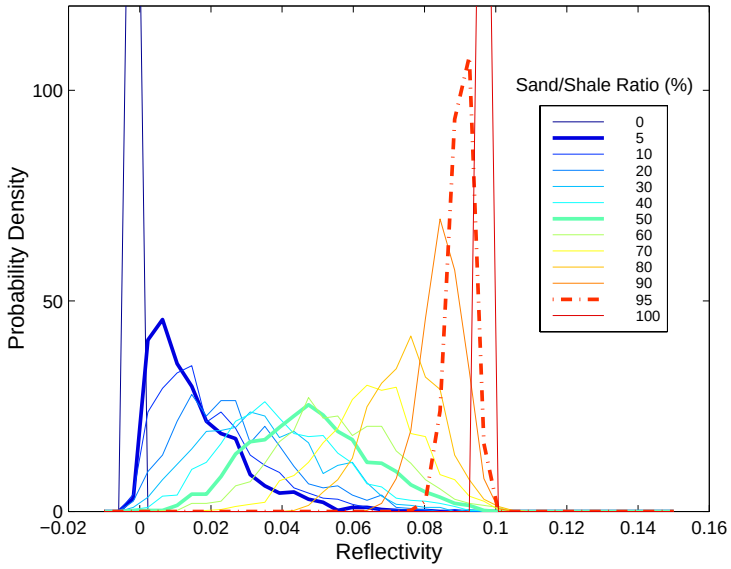

Figure 6.10: Distributions of reflectivity for various sand/shale ratio. The reflectivity is non-uniquely dependent on sand/shale ratio.

100%. The drift of the distribution implies that the reflectivity definitely depends on the sand/shale ratio. However, as the broad shapes of the pdfs implies, their relationship is non-deterministic and non-linear (Takahashi et al., 1999a).

6.4 Bayes Inverse Theory

In seismic reservoir characterization, we would like to estimate reservoir properties, such as the sand/shale ratio, from seismic attributes, such as reflectivity. Since the resolution of seismic data is limited, the seismic reflectivity represents the average character of a reservoir over a finite volume. As the results of our seismic forward modeling demonstrate, the dependence of reflectivity on the sand/shale ratio is non-unique if the layer configuration is variable. This non-uniqueness must be accounted for in any estimate of the sand/shale ratio for a given reflectivity. Because of the non-unique dependence, the perfect estimation of the sand/shale ratio from only seismic reflectivity is impossible. However, the reflectivity constrains the sand/shale ratio of a reservoir. One of the goals of this chapter is

to physically quantify the constraints.

General inverse problems deal with estimation of physical models from observed data (Tarantola, 1987). As discussed in chapter 4, using the probability density function (pdf) of subsurface properties, we can completely describe solutions of inverse problems including their inherent uncertainty (Tarantola and Valette, 1982; Box and Tiao, 1992). The problem of quantifying the constraint of reflectivity on the sand/shale ratio is equivalent to obtaining the conditional pdf of the sand/shale ratio (s) given reflectivity (r), which is denoted by $p(s|r)$. Bayes formulation in Equation 6.4 below enables us to replace inverse problems, estimation of the sand/shale ratio from a reflectivity, with forward problems, a sand/shale ratio to reflectivity.

$$p(s|r) = \frac{p(r|s)}{p(r)} p(s) = const. \cdot p(r|s) \cdot p(s) \tag{6.4}$$

where $p(r|s)$ is the conditional pdf of reflectivity given the sand/shale ratio, which is called the *likelihood function* in the Bayes theory and provides us with the relation between the sand/shale ratio and reflectivity. The last term, $p(s)$, is the prior pdf which is the information about sand/shale ratio independent of seismic reflectivity data. Gastaldi et al. (1998) used the Bayes approach to estimate reservoir thickness from seismic amplitude and reservoir isochron under tuning conditions. By applying the Bayes inversion to a number of synthetic models, Lörtzer (1990) predicted lithology, porosity, and pore fluid from observed seismic velocities and evaluated their uncertainties.

As discussed in the previous section, even in our simplified reservoir models, the relation between the sand/shale ratio and reflectivity is non-unique because of the variability of layer configurations. Hence, $p(r|s)$ is not simple and cannot be deterministically described. However, the following decomposition allows us to evaluate $p(r|s)$, since, in our models, seismic forward modeling provides us with a reflectivity value for each specific pair of a sand/shale ratio and a layer configuration.

$$p(r|s) = \int p(r, lyr|s) dlyr = \int p(r|lyr, s) p(lyr|s) dlyr \tag{6.5}$$

In practice, estimation of $p(r|s)$ is possible by the combination of stochastic simulation

and forward modeling (Takahashi et al., 1999a). The process is described as follows:

1. Produce a large number of equiprobable layered reservoir models, $\{lyr_1, lyr_2, ..., lyr_N\}$ for a fixed sand/shale ratio, s_1, such that $p(lyr|s)$ in Equation 6.5 is constant. When we can assume certain spatial statistical characters for the reservoir, geostatistical simulation will help create the equiprobable models.

2. Conduct seismic forward modeling for a set of a sand/shale ratio and a layer model, s_1 and lyr_1, and pick the reflected amplitude, $r(lyr_1, s_1)$.

3. Repeat step 2 for all layer models, $lyr_i, i = 1...N$.

4. Integrate the picked amplitudes for all the layered models, $\{r(lyr_1, s_1), r(lyr_2, s_1), ..., r(lyr_N, s_1)\}$. Normalization of the sum will produce the conditional pdf of reflectivity given a sand/shale of s_1, $p(r|s = s_1)$.

5. Repeat the step 1 through 4 for all possible sand/shale ratios, s_1 to s_k. Combination of all the conditional pdfs, $\{p(r|s_1), p(r|s_2), ..., p(r|s_k)\}$ produces the likelihood function, $p(r|s)$.

In general geophysical prospecting, we may need to estimate some rock properties, $\mathbf{m}$, from geophysical data, $\mathbf{d}$, without knowing other rock properties, $\mathbf{n}$, which influence the relation between $\mathbf{m}$ and $\mathbf{d}$. One simple example is the estimation of porosity from seismic velocity without knowing its lithology, which affects the porosity-velocity relation. In dealing with these problems, the following generalization of Equations 6.4 and 6.5 enables us to obtain the constraints of $\mathbf{m}$ given by $\mathbf{d}$, including the uncertainty caused by the ignorance of $\mathbf{n}$.

$$p(\mathbf{m}|\mathbf{d}) = const. \cdot p(\mathbf{d}|\mathbf{m}) \cdot p(\mathbf{m}) \tag{6.6}$$

$$p(\mathbf{d}|\mathbf{m}) = \int p(\mathbf{d}, \mathbf{n}|\mathbf{m}) d\mathbf{n} = \int p(\mathbf{d}|\mathbf{n}, \mathbf{m}) p(\mathbf{n}|\mathbf{m}) d\mathbf{n} \tag{6.7}$$

Equations 6.6 and 6.7 are very general formulations and can be applied to any estimation problems which are accompanied by uncertainty (Tarantola and Valette, 1982).

6.5 Estimation of Sand/Shale Ratio in North Sea Data

By applying the method proposed in section 6.4, we evaluate the constraints of the sand/shale ratio given by seismic amplitudes. We use well data from a North Sea oil field, where a Tertiary turbidite reservoir consists of interbedded sand and shale facies (Avseth et al., 1998b).

6.5.1 Reservoir Model

Figure 6.11 shows gamma ray profiles at three wells in the field. Wells 1, 2, and 3 are located at the feeder channel, the center of the lobe channel, and the margin of the lobe, respectively. As we progress from well 1 to 3, proximal to distal facies, the reservoir becomes more shaly.

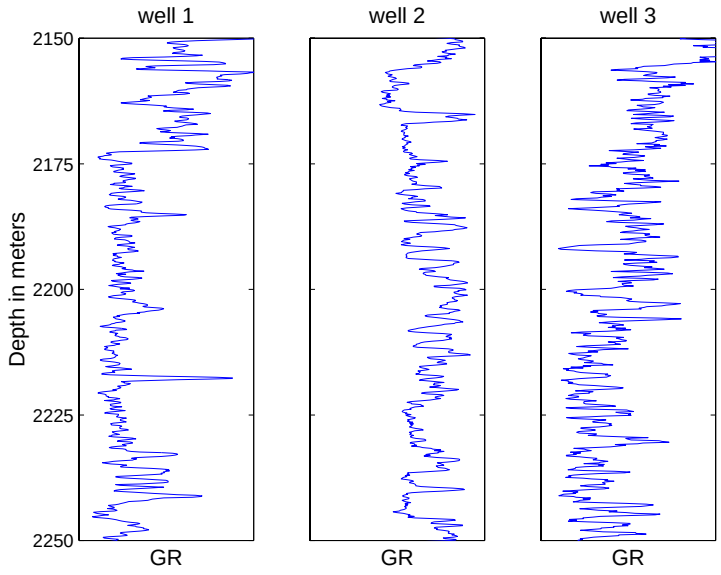

Figure 6.11: Gamma ray profiles in three North Sea wells.

We classify the interval to either sand or shale facies, using the gamma ray logs. Figure 6.12 shows interpreted facies at each well. We assume that any configuration of layered reservoir models which statistically has the same spatial character as seen at the three wells is possible in the inter-well region. We use the semivariogram, 2^{nd} order statistics, of the

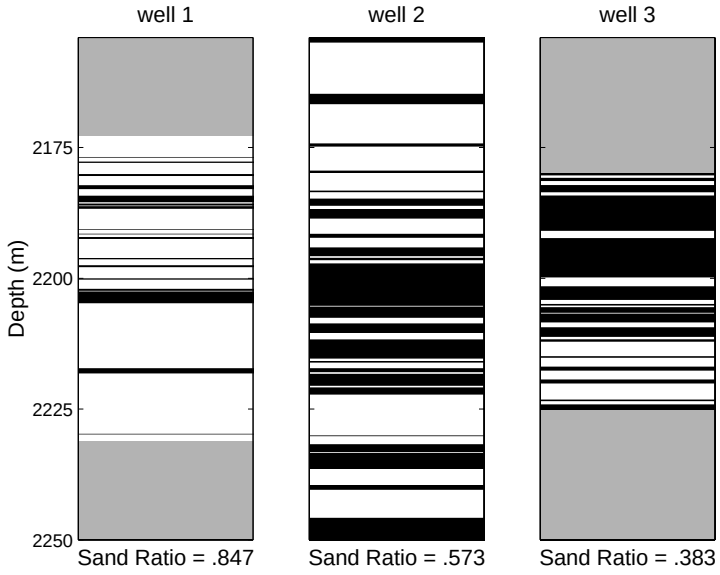

Figure 6.12: Sand-shale layering in three North Sea wells. The black color is shale and the white is sand. The gray is non-reservoir facies.

wells to investigate their spatial statistical characters. Figure 6.13 shows experimental indicator semivariograms of sand facies along the vertical direction, derived from the three wells. Our model of the vertical spatial correlation, also shown in Figure 6.13, is a spherical model with a range of 3 m and a nugget effect of 0.15 (Goovaerts, 1997).

$$\gamma(z) = 0.15 + 0.85 \cdot Sph(\frac{z}{3}) \tag{6.8}$$

We create 1,000 equiprobable reservoir models with the identical spatial variability for a fixed sand/shale ratio, using a geostatistical algorithm of the sequential indicator simulation (Deutsch and Journél, 1998). This method constrains both the 1^{st} order (sand/shale ratio) and the 2^{nd} order (spatial correlation) statistics of the layered models. Figure 6.14 shows ten examples of the simulated reservoir models with a sand/shale ratio of 50%.

In this study, we assume no lateral continuity of the reservoir models, *i.e.*, any layer model are assumed possible as long as it shares the 1^{st} and 2^{nd} order statistics with the wells.

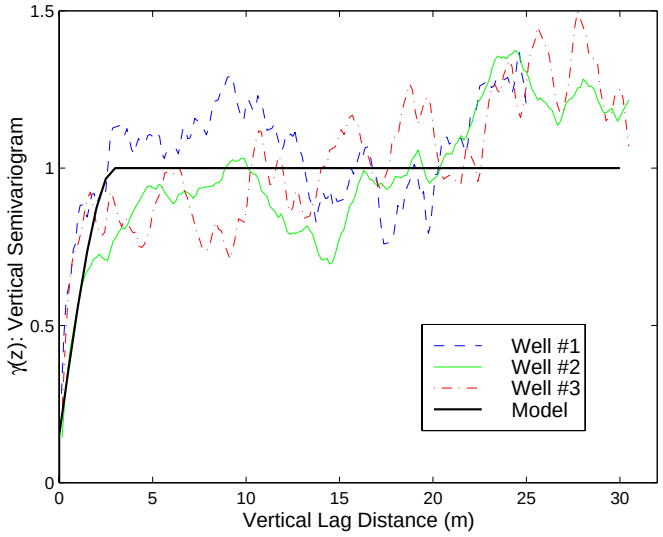

Figure 6.13: Experimental semivariograms at three wells and the model variogram.

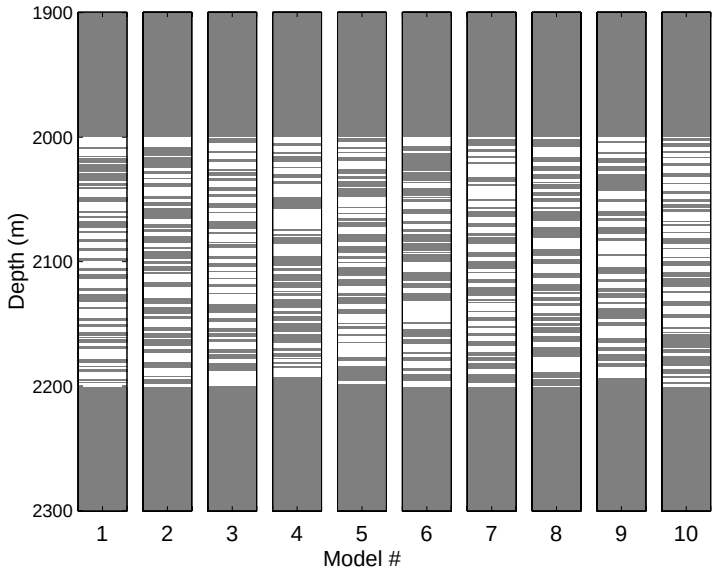

Figure 6.14: Ten realizations of reservoir models from a sequential indicator simulation based on the variogram model shown in Figure 6.13. The sand/shale ratio is 50%.

6.5.2 Forward Modeling

We perform one-dimensional seismic modeling to obtain reflected seismograms for all of the reservoir models in the same manner as in section 6.3.2. Figure 6.15 shows examples

of simulated reflected seismograms, corresponding to the models in Figure 6.14.

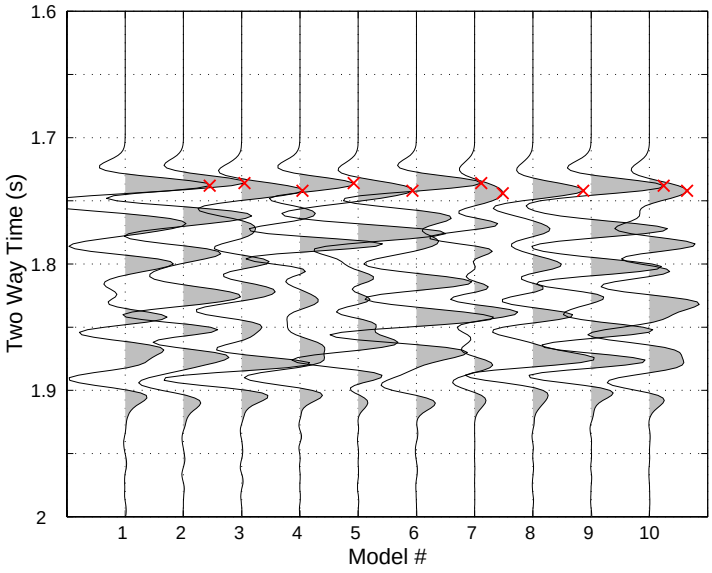

Figure 6.15: Simulated reflection seismograms for the ten reservoir models in Figure 6.14 with the stationary variogram model from the wells.

We vary the sand/shale ratio from 0% to 100%, repeat the above procedure, and pick the amplitudes from all the simulated seismograms. Figure 6.16 summarizes the pdfs of reflectivity derived from the forward modeling. Each curve illustrates the conditional pdf, $p(r|s = s_i)$ in Equation 6.5. A comparison of Figure 6.16 and Figure 6.10 demonstrates the dependence of the reflectivity distribution on the spatial variability models. Figure 6.10 is for the layered media distributed by a Poisson process, while Figure 6.16 is for layered media with a stationary spatial variogram from the wells.

By merging all the conditional pdfs, $p(r|s = s_i)$, for various sand/shale ratios, we establish the bivariate pdf of the sand/shale ratio and reflectivity, $p(r, s)$, shown in Figure 6.17. The bivariate pdf completely describes the dependence between reflectivity and the sand/shale ratio, including uncertainty of the relation caused by random thin layering. While the overall feature of the distribution exhibits a positive correlation between reflectivity and the sand/shale ratio, the broad shape of the distribution manifests the non-uniqueness of their relationship. Reflectivity values at the three well locations are also plotted by $\times$ marks in Figure 6.17. These observed data are just possible realizations among

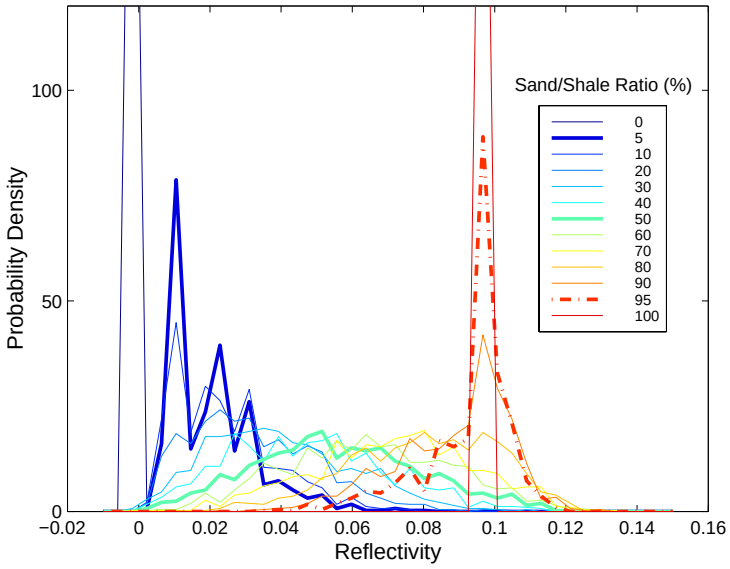

Figure 6.16: Distribution of reflectivity for different sand/shale ratio simulated from the reservoir models with stationary vertical correlation.

the whole coverage of the bivariate pdf. The reflectivity at well 3 is almost at the peak of the distribution, while the reflectivities at wells 1 and 2 are close to the high reflectivity limit.

By combining stochastic simulation and seismic forward modeling, we actually *extrapolated* the reflectivity-sand/shale relation from the three observations to all the possible layer configurations of the reservoir. This extrapolation is physically justified and cannot be accomplished by purely statistical methods. In addition, the two dashed lines over the contour map display the reflectivity in the effective medium theory limit (Backus average) and the most likely reflectivity, for all sand/shale ratios. The effective medium limit curve lies lower than the most likely curve, which corresponds to the ridge of the distribution. It implies that the effective medium average tends to overestimate the sand/shale ratio of a randomly layered reservoir.

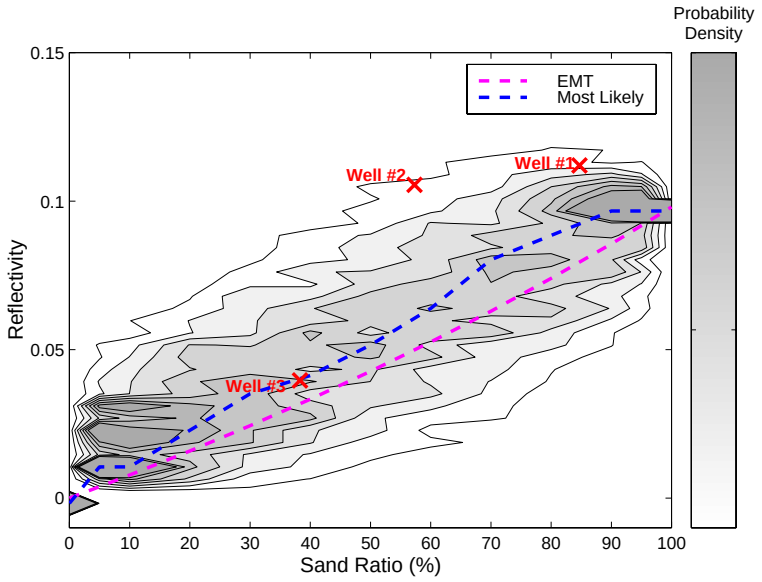

Figure 6.17: Bivariate pdf of reflectivity and the sand/shale ratio. Three $\times$ marks show the reflectivity at the three wells. The two dashed lines display the effective medium approximation of the reflectivity and the most likely reflectivity at each sand/shale ratio.

6.5.3 Scale Effect on PDFs

The bivariate pdf in Figure 6.17 can be considered the relation between seismic reflectivity and the sand/shale ratio at the seismic wavelength scale, since it is created through forward modeling mimicking surface seismic surveys. In contrast, since the well log tool sees the small scale characteristics of the reservoir, the pdf at the well log scale is a smoothed version of the properties of the two constituent rocks, *i.e.*, pure sand and pure shale, as shown in Figure 6.18,

The plot on the left in Figure 6.18 is the bivariate pdf corresponding to Figure 6.17 at the well log scale. The contrast of the elastic properties of the constituent rocks in Table 6.1 gives rise to the bimodal distribution of the pdfs. The peak of the contour in the upper right is for the pure sand, while the other peak in the lower left is for the pure shale. The broadness of the pdfs represent measurement errors. At the seismic scale, however, the pdf is continuous over the entire range of sand/shale ratios, because any volume fraction mixture of the two rock types can coexist within the seismic scale. In addition, reflectivity

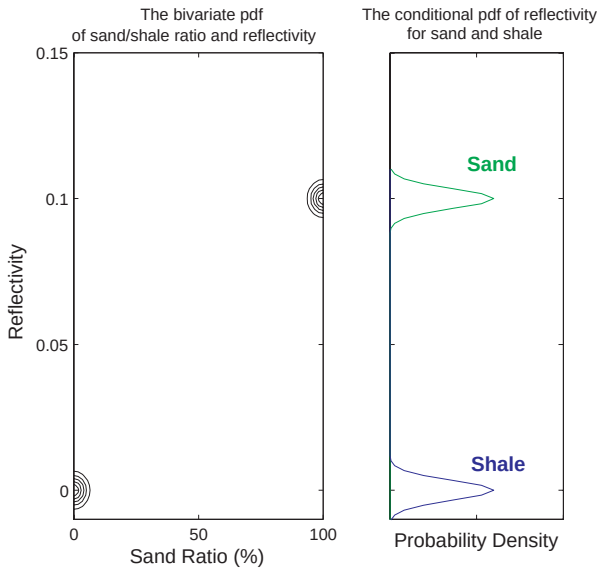

Figure 6.18: pdfs at well-log scale. Bivariate pdf of reflectivity and the sand/shale ratio (left), and the conditional pdfs of reflectivity for sand and shale facies (right). The univariate conditional pdfs are projections of the bivariate pdf onto the reflectivity axis.

at the seismic scale is influenced by the layer configuration, while the reflectivity at the well log scale is only a function of the interval elastic properties. Additional uncertainty about the layer configuration makes the seismic scale pdf broader than the well-log scale pdf, increasing uncertainty about the sand/shale ratio estimation. Furthermore, the seismic scale pdf in Figure 6.17 shows that reflectivities can be higher than both of the reflectivities of the constituent rock types, since reflected wave can constructively interfere each other in some layer configurations.

6.5.4 Bayes Inversion

Finally, assuming the prior pdf of the sand/shale ratio to be uniform, *i.e.*, $p(s) = const.$, we obtain $p(s|r)$, the conditional pdf of the sand/shale ratio given reflectivity, which is our answer to the inverse problem. The conditional pdf for each given reflectivity is shown in Figure 6.19. This can be realized by taking sections of the bivariate pdf in Figure 6.17 along horizontal lines corresponding to specific reflectivity values, before normalization.

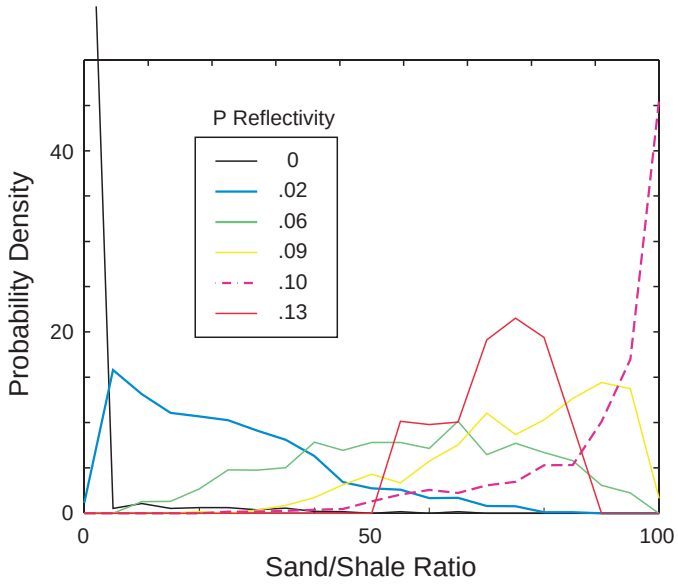

Figure 6.19: Conditional pdfs of the sand/shale ratio given P-wave reflectivity.

The conditional pdfs display how the seismic reflectivity constrains the sand/shale ratio estimation. When the reflectivity is 0, the sand/shale ratio is always 0% and there is no uncertainty. As the reflectivity increases, the distribution broadens and shifts towards larger sand/shale ratios. The distribution is the widest—hence the uncertainty about the sand/shale ratio is maximum—when the reflectivity is intermediate. The distribution sharpens again and the peak approaches 100%, as the reflectivity approaches 0.1. As a whole, the sand/shale ratio is not tightly constrained by seismic reflectivity.

Since geological formations tend to be laterally continuous, we may be able to assume certain lateral continuity of layer configuration, instead of no lateral continuity in this example. In such cases, the bivariate pdf of the sand/shale ratio and reflectivity in Figure 6.17 will be constrained by the additional information about the lateral continuity, and the answer of the estimation, $p(s|r)$, will become less uncertain.

6.5.5 Value of Additional Shear Measurement

As discussed in chapter 4, one method of increasing the information about rock properties is to acquire additional geophysical data. In this section, we investigate how S-wave reflectivity, in addition to P-wave data, constrains the sand/shale ratio.

S-wave velocities and densities of the sand and shale layers listed in Table 6.1 are used for modeling. We follow the same procedure as in the earlier section to establish the trivariate pdf of P- and S-wave reflectivity and the sand/shale ratio. For each layered models produced from geostatistical simulation, such as those shown in Figure 6.14, we conduct P-wave and S-wave normal incidence modeling and pick P and S amplitudes. Figure 6.20 shows an iso-contour surface of the trivariate pdf, $p(r_p, r_s, s)$. Similar to Figure 6.17, the

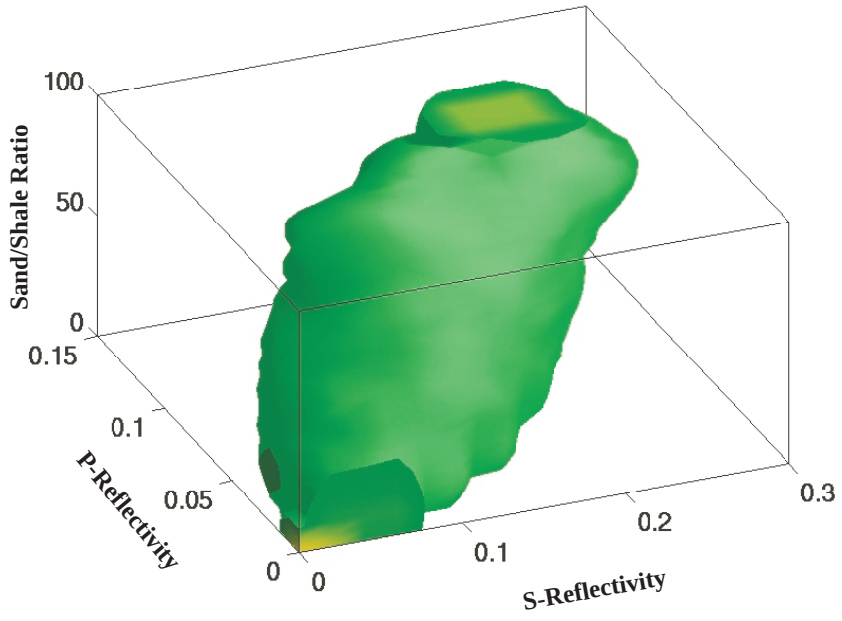

Figure 6.20: Trivariate pdf of P and S reflectivity and sand/shale ratio. The green blimp-shaped envelope is an iso-contour surface.

pdf is characterized by a positive correlation between the sand/shale ratio and reflectivities. The inner part of the blimp-shaped pdf has a higher probability. Projection of the trivariate pdf onto the $r_p - s$ domain produces the bivariate pdf of P-wave reflectivity and sand/shale

ratio in Figure 6.17.

Again assuming the uniform prior pdf of the sand/shale ratio, we estimate the conditional pdfs of the sand/shale ratio given P- and S-wave reflectivities, as in Figure 6.21. A comparison of Figure 6.21 with Figure 6.19 demonstrates that uncertainty about the

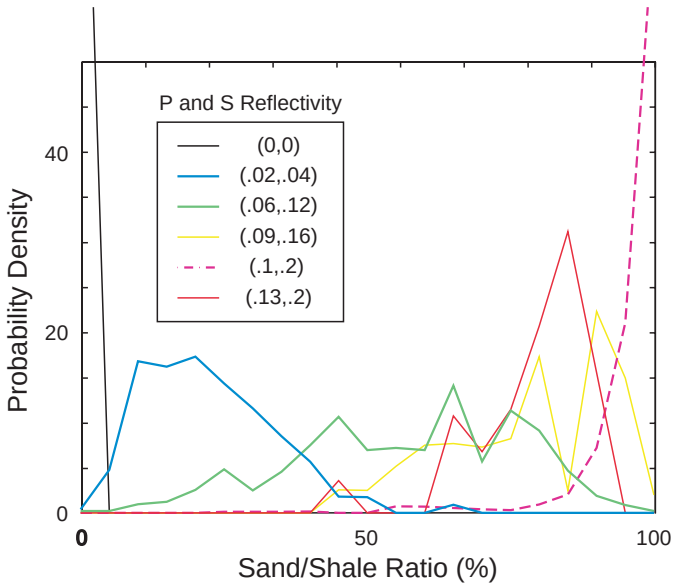

Figure 6.21: Conditional pdfs of sand/shale ratio given P-wave and S-wave reflectivity pairs.

sand/shale ratio is reduced by additional shear data, since each distribution is narrower and more peaky in Figure 6.21 than in Figure 6.19. However, due to the high correlation of P and S reflectivity, there is significant redundancy between information brought by P and S data.

Using a statistical parameter of mutual information defined in Equations 4.12 and 14, we quantify information about the sand/shale ratio given by P reflectivity only, S reflectivity only, and both P and S reflectivities, as shown in Table 6.2. Information given by two reflectivities is greater than the information given by either single reflectivities. That is, the combination of P and S information decreases the uncertainty about the sand/shale ratio.

	Mutual Inf.	Normalized Mutual Inf.
P only	0.78	0.30
S only	0.63	0.25
P and S	0.99	0.38

Table 6.2: Mutual information about the sand/shale ratio given by P-wave reflectivity only, S-wave reflectivity only, and both of P- and S-wave reflectivities.

6.6 Conclusions

This chapter demonstrated the dependence of seismic reflectivity on the scale of reservoir stratification. The results from the seismic forward modeling showed that random thin-layering within reservoirs makes the relationship between reflectivity and the average rock property non-unique. By applying Bayes inversion, we proposed a strategy to describe the relation between seismic data and rock properties, including the inherent non-uniqueness of the relation. The bivariate pdf, derived through combinations of stochastic simulations and seismic forward modeling, represented the dependence of reflectivity and sand/shale ratio. This includes the uncertainty caused by ignorance of layer configuration. The comparison of the seismic-scale pdf and the well log-scale pdf showed that the scale effect makes the pdf broader, hence increases uncertainty about the sand/shale prediction. According to our results, the effective medium average may result in systematic overestimation of sand/shale ratio if the layering within the reservoir is random. Our solution to the estimation problem, pdfs of rock properties given seismic data, is a truthful expression of information provided by seismic data and allows us to analyze the uncertainty of rock property estimation problems quantitatively and physically.

Chapter 7

Comparison Between P-P and P-S Seismic Information in the Alba Oil Field

Abstract

Converted shear (P-S) wave seismic data from multicomponent ocean bottom surveys have gained considerable industry attention, as they offer subsurface shear information more directly than the conventional P-P AVO analysis. Using P-S and P-P seismic data and well-log data from the Alba Field in the UK North Sea, we explore the significance of P-S data in rock property estimation.

We first diagnose the Alba reservoir using the V_p-porosity relation and compare it with rock physics models. Our results show that the porosity variation in the reservoir is well mimicked by a constant pore stiffness line, and thereby is controlled by the textural variation. A comparison of brine-saturated and oil-saturated sands disclose evidence of deceleration of cementation due to the oil accumulation in reservoirs—the water-saturated sands show systematically greater V_p and smaller porosity than the oil-saturated sands.

Quantitative investigation of the dependence of seismic impedances on lithology and pore fluids shows that the P-P near offset impedance (AI_p) is a better classifier of pore fluids than the P-P far offset impedance and the P-S pseudo-impedance. In contrast, the

P-P far offset impedance (EI) and the P-S pseudo-impedance (I_{ps}) distinguish lithology well. A combination of impedances from P-P near and far offset data ($AI_p - EI$) turns out to be as good a rock property predictor as does a combination of impedances from P-P near offset and P-S converted wave data ($AI_p - EI$), when the impedance measurements are error-free.

By comparing well-derived impedances and the impedances inverted from seismic data, we show that the errors of deriving the P-P far offset impedance is greater than the errors for the P-S pseudo-impedance. We estimate bivariate pdfs of impedances for three possible facies, define Bayes classification criteria, and predict the facies from the $AI_p - EI$ combination, as well as from the $AI_p - I_{ps}$ combination. The prediction from the $AI_p - I_{ps}$ is more consistent with a blind well and other geological information and confirms the advantage of using P-S converted wave data for rock property estimation in the Alba Field.

7.1 Introduction

This chapter explores the information about rock properties provided by P-S seismic data as compared to conventional P-P data, using well log and seismic data from the North Sea.

7.1.1 Motivation

Use of S-wave information in addition to P-wave information often enables us to better predict rock properties from seismic data, and ocean bottom seismic acquisition survey has thereby attained considerable industry attention as a tool to obtain converted wave S-wave data (MacLeod et al., 1999). On the other hand, conventional P-P data can indirectly provide us with shear information. Hilterman (1989), Castagna and Backus (1993), and many others have reported that AVO analysis is useful in predicting pore fluids and lithology. Mukerji et al. (1998) recently presented that pseudo-impedance derived from non-zero offset P-P data includes indirect shear information of layer intervals and can therefore be a good indicator of pore fluid and lithology.

Although both the ocean bottom P-S surveys and the conventional far-offset P-P

streamer surveys bring about S-wave information in addition to P-wave information, the costs of these two types of surveys are significantly different, *i.e.*, ocean bottom surveys are much more expensive than streamer surveys. Hence, it is an important question for exploration companies to decide which of the surveys to carry out.

In this chapter, we use P-P and P-S seismic data, as well as well-log data, of the Alba Field in the UK North Sea, and investigate how the two different seismic data can help us to predict lithology and pore fluids.

7.1.2 Alba Field

The Alba Oil Field (Figure 7.1), located in the UK North Sea, elongates along a NW-SE axis. The oil reservoir is 9 km long, 1.5 km wide, and up to 90 m thick at a depth of 1,900 m subsea (Mattingly and Bretthauer, 1992; Newton and Flanagan, 1993; Lonergan and Cartwright, 1999; MacLeod et al., 1999).

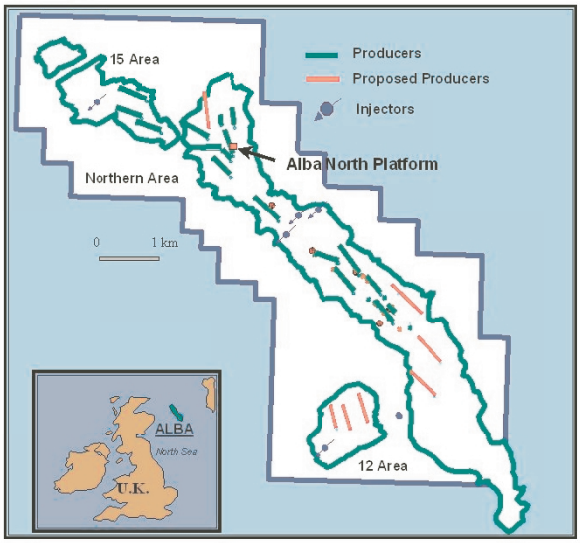

Figure 7.1: Alba Field location map (from MacLeod et al, 1999). Green outline shows the extent of oil sand. Well locations are marked.

The producing reservoir consists of unconsolidated high-porosity turbiditic sandstone

of Eocene age. The oil-bearing reservoir sand and the overlying shale have a very low P-wave acoustic impedance contrast, but make a significant S-wave velocity contrast. Hence the reservoir delineation using only normal incidence P-P seismic data is very difficult, and therefore the ocean bottom P-S converted wave survey was conducted.

We first explore well data and diagnose basic rock properties of the reservoir sandstone. We then estimate seismic attributes of the oil sand, brine sand, and shale from the well data, and quantitatively investigate how each facies is separated in different attribute domains, using the methods presented in chapters 4 and 5 in this thesis. We perform seismic inversion of the P-P and P-S seismic data and predict lithology and pore fluids from the derived impedances.

7.2 Rock Physics Diagnostics of the Alba Sandstone

In this section, we diagnose rock properties of the reservoir and compare them with several rock physics models using data from the key well (well 1), drilled in the northern part of the main channel.

7.2.1 The Alba Sandstone Compared with Other Sandstone Data and Rock Physics Models

Figure 7.2 shows vertical profiles of several rock properties at well 1. The boxcar-like volume-shale log shows massive and structureless characteristics of the reservoir. The sandstone has an average porosity of 35% and permeability of approximately 5 D. As the water saturation profile shows, the reservoir interval of this well is mostly oil saturated, with a thin water rim at the bottom section. The boundary between overlying shaly caprock and the oil-bearing sandstone has large contrasts in porosity, density, and V_s, but a very small contrast in V_p. In contrast, the oil-water contact (OWC) is characterized by a large increase in V_p and a small increase in V_s.

We use the well data to investigate fundamental rock properties of the reservoir in several rock physics domains. Figure 7.3 shows the V_p-porosity relation of the Alba sandstone, as well as other sandstone data from various ages and geological settings listed in Table 2.1.

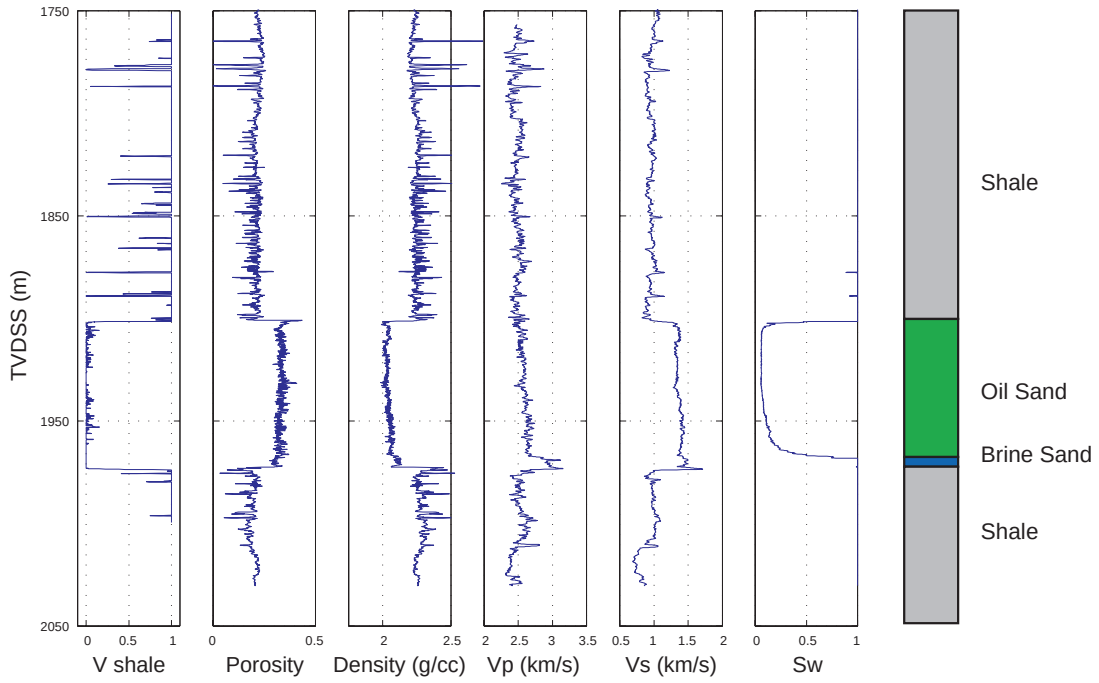

Figure 7.2: Well log profiles of the Alba reservoir at well 1. Lithology and pore fluid interpretation are shown on the rightmost column.

All the data are at an effective pressure of approximately 20 MPa. Gassmann's fluid substitution are performed such that the data represent properties for water-saturated conditions.

In Figure 7.3, the Alba sandstone shows a good correlation between V_p and porosity; the V_p slightly increases as the porosity decreases. As shown in Figure 2.4, the shallow $V_p - \phi$ trend of the Alba sandstone can be explained by variation in sorting. Figure 7.4 shows a comparison of the Alba sandstone with rock physics model curves. A constant K_ϕ curve for $K_\phi/K_o = 0.5$ (K_o is the mineral bulk modulus) well mimic the porosity variation of the Alba sandstone controlled by sorting.

Figure 7.5 summarizes the $V_p - \phi$ relations of sand and shale observed at several wells in the field, including well 1. The sand and shale clouds from each well overlap each other. Minor differences of the distributions between different wells can be explained by the depth of the reservoir at each well, *i.e.*, wells 1, 3, and 4 are deeper than well 2, and hence have larger velocities and lower porosities.

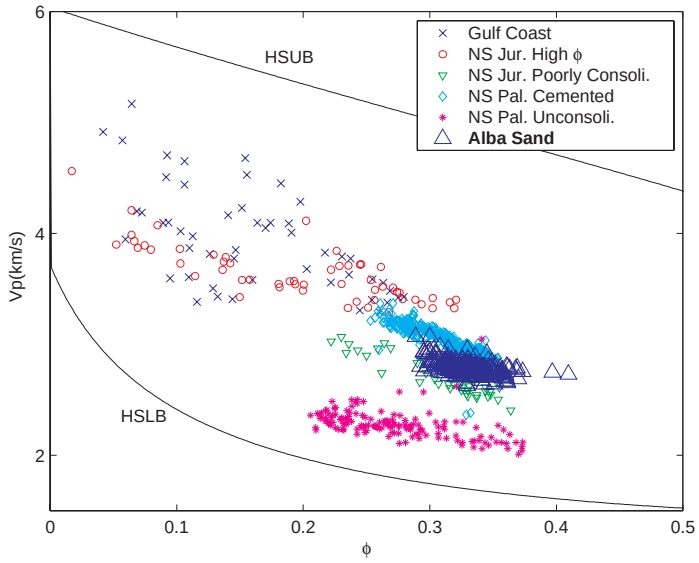

Figure 7.3: The $V_p - \phi$ relation of the Alba sandstone (well 1) combined with several other sandstone data. The data include Gulf Coast sands measured by Han (1986), North Sea high porosity sands (Strandenes, 1991), North Sea poorly consolidated sands (Blangy, 1992), and North Sea Paleocene cemented and unconsolidated sands (Avseth, 2000).

Figure 7.6 shows the $V_p - V_s$ relation of the Alba sandstone, as well as other sandstone data. All sand facies are for water-saturated conditions; Gassmann's fluid substitution is conducted for the originally oil-saturated zone. The $V_p - V_s$ relation of the Alba sandstone stays within the linear trend along with other sandstones. The trend is well predicted by Castagna's linear regression line (Castagna et al., 1993).

7.2.2 Sandstones Below and Above the OWC

We investigate the $V_p - \phi$ relation of the sandstone in more detail. We divide the reservoir into two groups: the zone originally oil-saturated (*i.e.*, above the original OWC) and the zone originally water-saturated (*i.e.*, below the original OWC). The different P-wave velocities between these two zones in the original data in Figure 7.2 are mostly due to the difference in fluid compressibilities (*i.e.*, oil versus water) (MacLeod et al., 1999). In this section, however, we investigate the $V_p - \phi$ relation of the two zones after normalizing

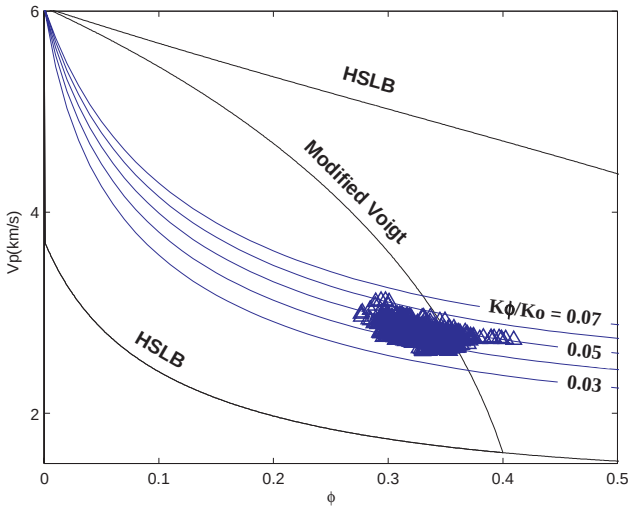

Figure 7.4: The Alba sandstone (well 1) compared with rock physics model curves. HSUB and HSLB are Hashin-Shtrikman upper and lower bounds, respectively. Constant pore stiffness curves for K_ϕ / K_o = 0.3 to 0.7 are included (K_ϕ and K_o are the pore stiffness and mineral bulk modulus, respectively.

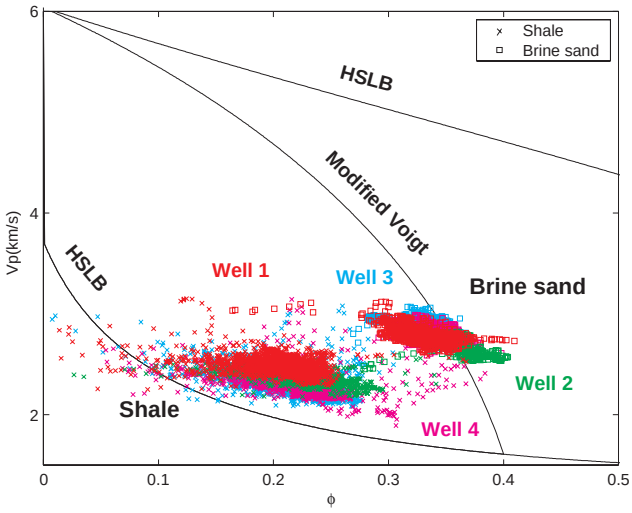

Figure 7.5: The $V_p - \phi$ relation of the Alba sandstone and shale at four different wells.

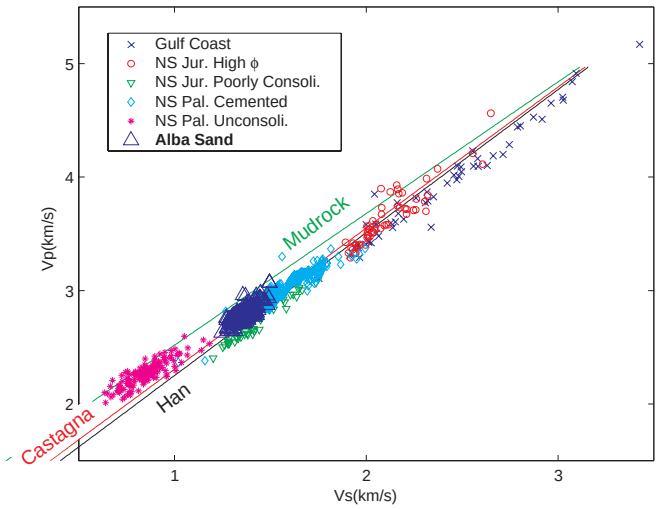

Figure 7.6: The $V_p - V_s$ relation of the Alba sandstone (well 1) plotted with other sandstone data and three linear regression lines.

the fluid compressibility discrepancy using Gassmann's theory (Gassmann, 1951; Johnstad and Dvorkin, 1999), and interpret the remaining difference in terms of cementation rate.

Figure 7.7 shows the $V_p - \phi$ relation of the two groups if they are in water-saturated condition, *i.e.*, Gassmann's fluid substitution is performed for originally oil-saturated facies above the OWC. The sandstone below the OWC is characterized by a higher V_p and a lower porosity than the sandstone above the OWC. Since both of the plotted data are for water-saturated conditions, the difference of the two groups due to fluid compressibilities has been removed, and Figure 7.7 highlights the difference in matrix properties.

One possible reason for the difference between the two facies is the prevention of quartz cementation due to oil accumulation above the OWC. According to Worden et al. (1998), oil emplacement in sandstone reservoirs halts quartz cementation either when silica is sourced externally or internally. In Figure 7.8, we overlay curves for the cementation model (Dvorkin and Nur, 1996) over the data.

The cementation model curves (red) are for three different critical porosities of 0.32, 0.35, and 0.38, an average contact number of 8, and the grain coating cementation scheme.

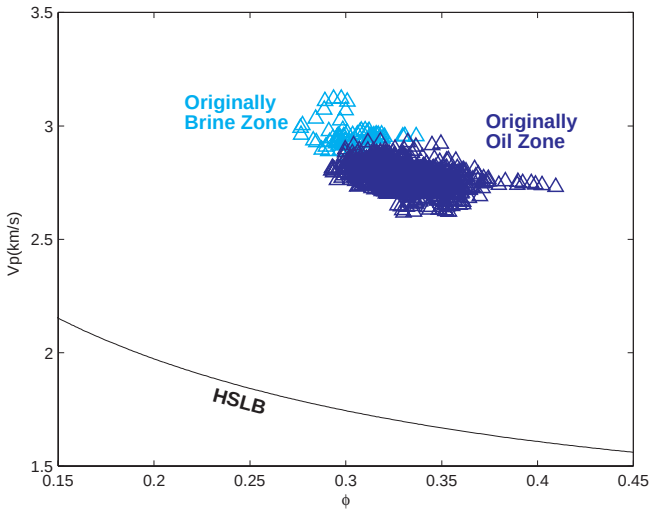

Figure 7.7: The $V_p - \phi$ relation of the two facies of the Alba reservoir—above the OWC and below the OWC—at well 1. The plotted data are for water-saturated condition after Gassmann's substitution for oil zone.

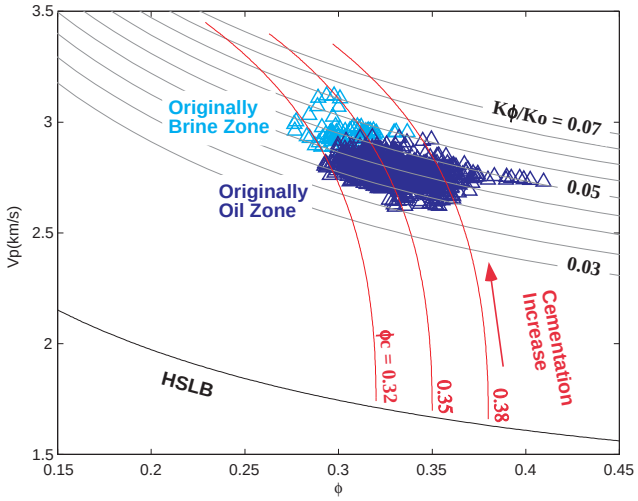

Figure 7.8: The $V_p - \phi$ relation of the two facies of the Alba reservoir—above the OWC and below the OWC—at well 1 overlain by Dvorkin and Nur's cementation curves (red) and constant pore stiffness curves (gray). The plotted data are for water-saturated conditions.

Increasing cementation increases V_p and decreases porosity along the trends. The difference between the two facies can be explained by the difference in cement fractions; the below-OWC facies has higher cement fractions by 2%. The constant pore stiffness (K_ϕ) curves (gray) mimic the trends within each group, corresponding to constant cementation rates.

Figure 7.9 shows similar comparison between sandstones above the OWC and sandstones below the OWC, using multiple well data shown in Figure 7.5. Sandstone data

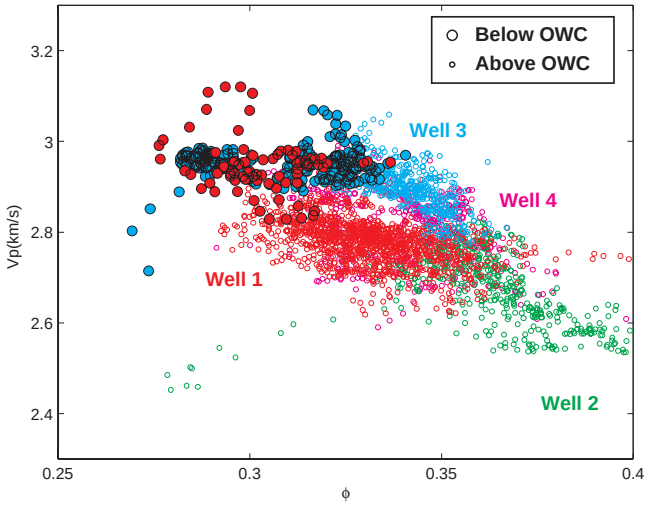

Figure 7.9: The $V_p - \phi$ relation of the two facies of the Alba reservoir—above the OWC and below the OWC—at various wells. The plotted data are for water-saturated conditions. Squares are sandstone below the OWC and small dots are above the OWC. Colors represent different wells.

below the OWC, observed at wells 1 and 3, have systematic distributions at the upper left of the total population—lower porosity and higher V_p—indicating their higher cementation rate. Figures 7.7, 7.8, and 7.9 display possible halts of quartz cementation due to oil emplacement in the reservoir. Several authors have reported that the internal characteristics of the Alba sandstone is massive and structureless (Newton and Flanagan, 1993; Lonergan and Cartwright, 1999), which supports our hypothesis that the difference in matrix properties below and above the OWC in Figures 7.7 and 7.9 is of diagenetic origin. However, it is still possible that the difference below and above the OWC is due to the difference in

depositional characteristics rather than the cementation effect.

7.3 Separability of Lithology and Pore Fluids Using P-P and P-S Seismic Data in Error-Free Conditions

In this section, we explore how lithology and pore fluids can be predicted from seismic observables, using the key well data. From the basic observations of V_p, V_s, and density at the well, we derive seismic attributes that could potentially be estimated from P-P seismic data, as well as P-S seismic data. We quantify the predictability of rock properties using the methods presented in chapters 4 and 5, namely information theory and Bayes decision theory. In this section, we do not take account of measurement errors of seismic data, discussed in section 4.3.1. Hence this section assumes perfect measurements of each seismic attribute at error-free conditions.

7.3.1 The $\mathrm{V_p} - \mathrm{V_s}$ Relation

Figure 7.10 shows the $V_p - V_s$ relation of the Alba sandstone and shale. Sandstone at two different fluid conditions—brine saturated (Sw = 100%) and oil saturated (Sw = 10%)—are plotted after the Gassmann's fluid substitution of the original well data.

Figure 7.10 shows clear separation of the three facies—oil sand, brine sand, and shale—when both V_p and V_s are available. A comparison of the oil and brine sands shows that V_s is barely influenced by the fluid change, while V_p can separate the oil and brine sands. On the other hand, we can distinguish the shale from the two sands using only V_s. V_p of the shale and the oil sand overlap each other, while the brine sand can be discriminated from the shale using V_p. These basic observations confirm that a combination of P- and S-wave data enables better prediction of lithology and pore fluids in the Alba Field.

7.3.2 Impedances from P-P Surveys

Figures 7.11 and 7.12 show the relation between the P-wave acoustic impedance (AI_p) and the elastic impedance at an incidence angle of 30 degrees ($EI(30)$), the two

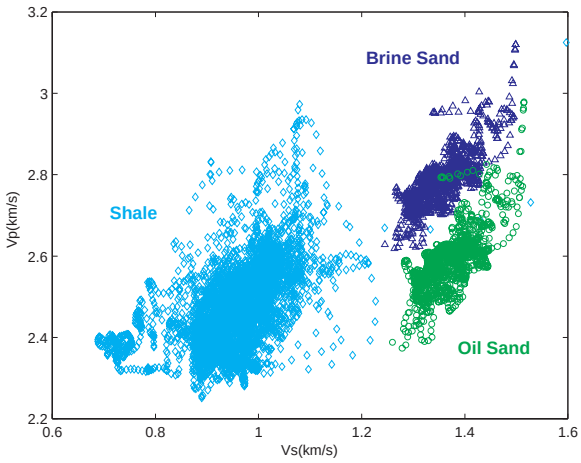

Figure 7.10: The $V_p - V_s$ relation of the Alba sandstone and shale. Two fluid conditions of the sandstone—brine saturated and oil saturated—are displayed.

impedances available from conventional near and far offset P-wave seismic surveys. The angle chosen for the elastic impedance (30 degrees) corresponds to the average incidence angle at the depth of the Alba sandstone (2,000 m), for the available P-P far-offset partial stack. Figure 7.11 is the scatter plot of the well data and Figure 7.12 is the bivariate and univariate pdfs of AI_p and $EI(30)$ derived from the well data.

Table 7.1 summarizes statistics of facies prediction. They are derived from the pdfs in Figure 7.12 and are for error-free measurement of the impedances. Both AI_p and $EI(30)$ are good discriminators of pore fluids, *i.e.*, oil sand from brine sand. However, $EI(30)$ is more sensitive to lithology than AI_p. This result is consistent with the observation in the Gulf Coast data discussed in section 2.3.1. A combination of the two impedances enables almost perfect facies discrimination for all cases, when their measurements are perfect and error-free.

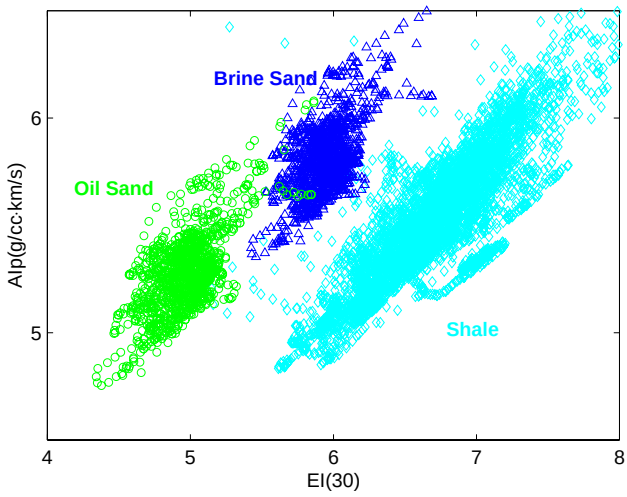

Figure 7.11: The relation between the P-wave acoustic impedance (AI_p) and the elastic impedance at an incidence angle of 30 degrees ($EI(30)$), for oil sand, brine sand, and shale.

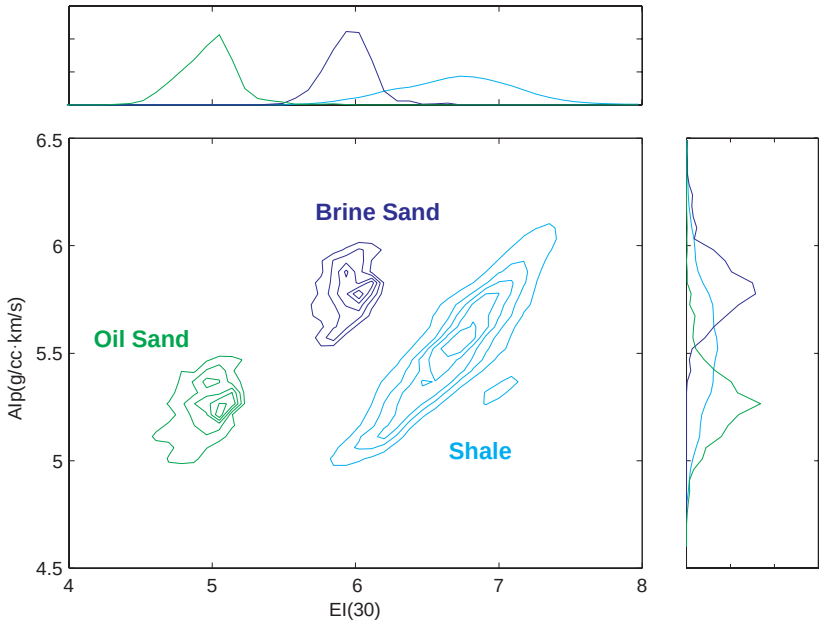

Figure 7.12: The univariate and bivariate pdfs of the acoustic impedance (AI_p) and the elastic impedance at an incidence angle of 30 degrees ($EI(30)$), for oil sand, brine sand, and shale.

Attribute	Success Rate	Mutual Inf. $I(facies\|attribute)$	Normalized Inf. $I_n(facies\|attribute)$
A: Discrimination of three facies (oil sand, brine sand, and shale)			
AI_p	0.67	0.39	0.35
$EI(30)$	0.93	0.91	0.83
AI_p & $EI(30)$	1.00	1.08	0.98
B: Discrimination of pore fluids (oil sand and brine sand)			
AI_p	0.94	0.53	0.76
$EI(30)$	0.99	0.66	0.95
AI_p & $EI(30)$	0.99	0.67	0.97
C: Discrimination of lithology (sand and shale)			
AI_p	0.60	0.03	0.05
$EI(30)$	0.92	0.49	0.71
AI_p & $EI(30)$	1.00	0.68	0.98

Table 7.1: Information about facies provided by P-P impedances at error-free conditions.

7.3.3 Impedances from P-S Surveys

We modify the approximated form of the P-S pseudo-impedance by Mukerji and Mavko (1999) and derive a new and more robust approximation of the P-S pseudo-impedance for cases when the average V_p/V_s ratio of the overlying layers is available. The approximate form is given as Equations B.15, B.16, and B.17, in appendix B.

Figures 7.13 and 7.14 show the relation between the P-wave acoustic impedance (AI_p) and the P-S pseudo-impedance. The angle of S-wave reflection chosen for the pseudo-impedance (22 degrees) corresponds to the average S-wave reflection angle at the target depth for the available P-S far-offset partial stack. We assume an average V_p/V_s ratio of 1.8—the same value as used in the converted wave data processing.

Table 7.2 summarizes success rates of facies prediction, as well as information about facies provided by the P-P near and P-S impedances. The statistics in Table 7.2 are derived from the pdfs in Figure 7.14 and are for error-free measurement of the impedances.

Figures 7.13 and 7.14 illustrate that the P-S pseudo-impedance has virtually no sensitivity to pore fluid change, although it is a good lithology discriminator. Table 7.2 displays that a combination of the two impedances enables almost perfect facies discrimination. A

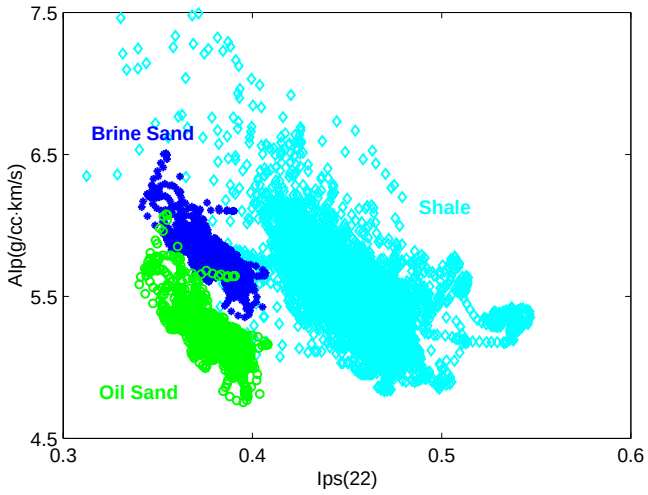

Figure 7.13: The relation between the P-wave acoustic impedance (AI_p) and the pseudo-impedance from P-S seismic data at a reflected angle of 22 degrees ($I_{ps}(22)$), for oil sand, brine sand, and shale.

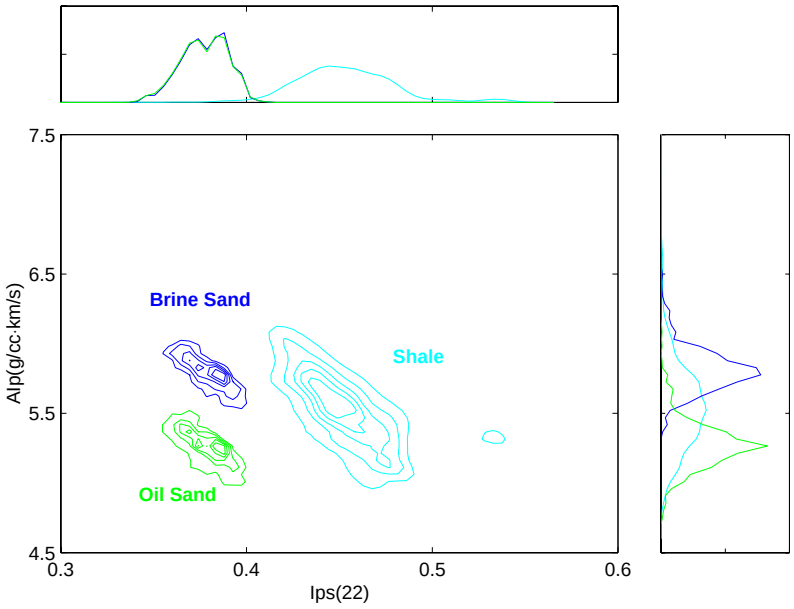

Figure 7.14: The univariate and bivariate pdfs of the P-wave acoustic impedance (AI_p) and the pseudo-impedance from P-S seismic data at a reflected angle of 22 degrees ($I_{ps}(22)$), for oil sand, brine sand, and shale.

Attribute	Success Rate	Mutual Inf. $I(facies\|attribute)$	Normalized Inf. $I_n(facies\|attribute)$
A: Discrimination of three facies (oil sand, brine sand, and shale)			
AI_p	0.67	0.39	0.35
$I_{ps}(22)$	0.66	0.59	0.54
AI_p & $I_{ps}(22)$	0.99	1.06	0.97
B: Discrimination of pore fluids (oil sand and brine sand)			
AI_p	0.94	0.53	0.76
$I_{ps}(22)$	0.51	0.00	0.00
AI_p & $I_{ps}(22)$	0.94	0.67	0.96
C: Discrimination of lithology (sand and shale)			
AI_p	0.60	0.03	0.05
$I_{ps}(22)$	0.98	0.63	0.92
AI_p & $I_{ps}(22)$	0.99	0.67	0.97

Table 7.2: Information about facies provided by P-P near and P-S impedances at error-free conditions.

comparison between Tables 7.1 and 7.2 shows that the impedances from P-P seismic data are as good of information carrier about pore fluids and lithology as are the impedances from P-P near and P-S data, in the cases when error-free impedance measurements are available.

7.4 Impedance Inversion

7.4.1 Seismic and Well Log Data

The 3D seismic data available for this study were acquired using 4-component ocean-bottom receivers—hydrophones and 3-component geophones—after 4 years of oil production and water injection. Figures 7.15 and 7.16 are seismic profiles of P-P near and far offset partial stacks, respectively, for a SW-NE section (section A). The section A transversely cuts through the Alba reservoir around well 1. In addition, on the southeast (left) of the reservoir is an isolated wet sand body, where well 5 was drilled (Newton and Flanagan, 1993).

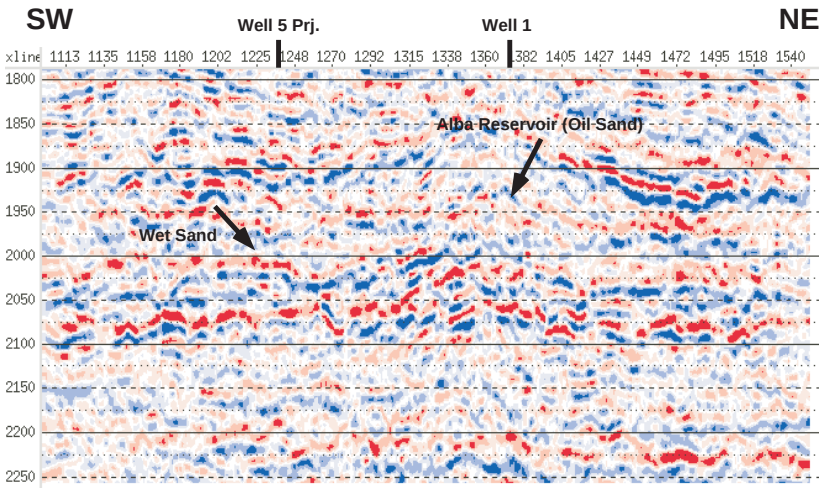

Figure 7.15: A SW-NE seismic section (section A) from P-P near offset stack.

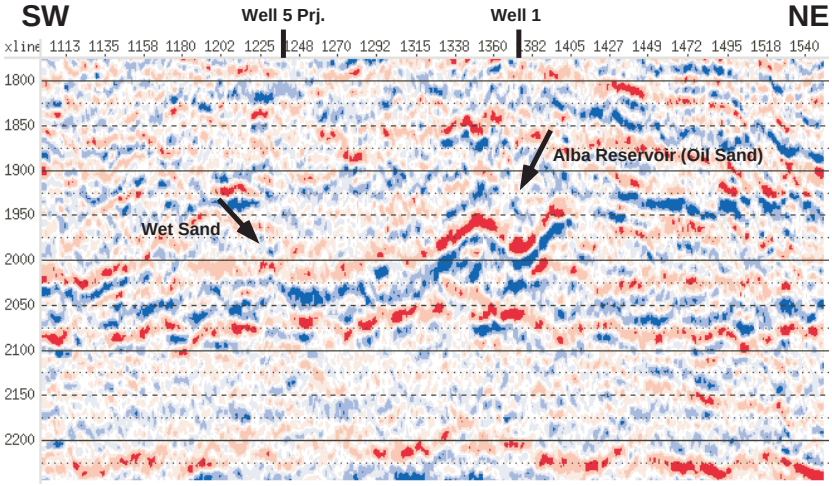

Figure 7.16: A SW-NE seismic section (section A) from P-P far offset stack.

The far offset stack corresponds to a 30 degree incidence angle at the target depth around 2,000 m. The P-P near stack in Figure 7.15 does not show a clear image of the Alba reservoir, although the wet sand in the southwest provides a weak amplitude anomaly. The P-P far stack in Figure 7.16 provides us with a weak amplitude anomaly as well, at the Alba sand.

In contrast, the P-S far-offset partial stack of section A in Figure 7.17, corresponding to a 22 degree reflection angle at the target, captures the image of the two sand bodies, although the frequency content of the P-S data is lower than the P-P data.

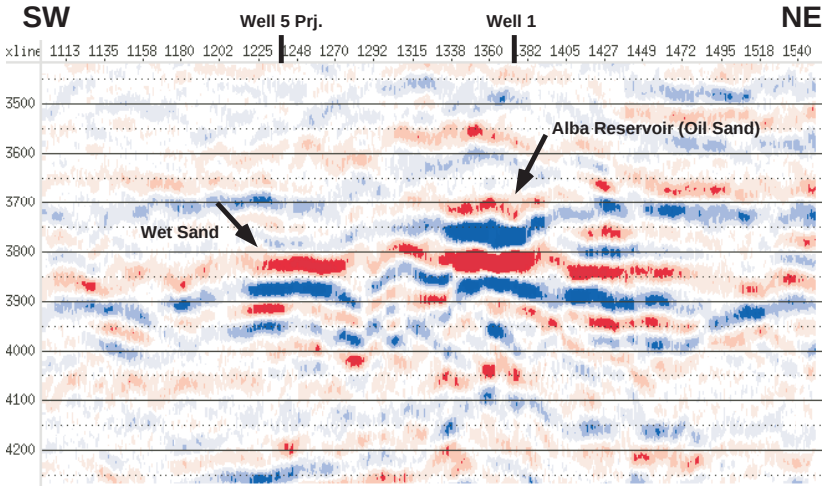

Figure 7.17: A SW-NE seismic section (section A) from P-S far offset stack.

The reservoir fluid conditions at the well-log data acquisition—before oil production—and at the time of seismic data acquisition—after 4 years of oil production—are different. Hence, we estimate well log profiles at the seismic acquisition, using outputs from reservoir flow simulation and performing Gassmann's fluid substitution. Figure 7.18 is the water-saturation profile—a vertical section cutting through well 1—at the time of seismic data acquisition (after oil production), output from the fluid-flow simulation. We extract the water-saturation profile at well 1 and estimate P- and S-wave velocities after oil production, as displayed in Figure 7.19. Figure 7.19 shows that the oil-water contact has risen from around 1,965 m to around 1,935 m due to the 4 years of oil production, although about 25% of residual oil remains in the swept zone. The change in velocities due to the production is relatively small because of the residual oil (Domenico, 1976; Murphy, 1982).

According to the corrected velocity and density logs at well 1, we derive bivariate pdfs of the acoustic impedance and the elastic impedance after oil production, as in Figure 7.20. In Figure 7.20, the brine sand pdf is for the zone below the OWC in Figure 7.19 after production, where the water-saturation is 25%. Because of the residual oil, the brine pdf

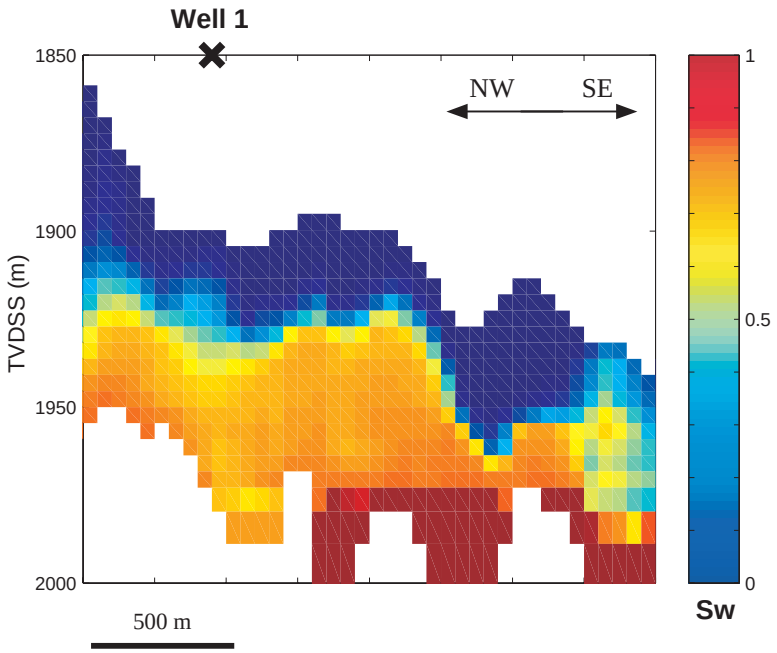

Figure 7.18: Water-saturation profile of the Alba reservoir—the longitudinal section (NW-SE) which go through well 1—after oil production, output from the flow simulation.

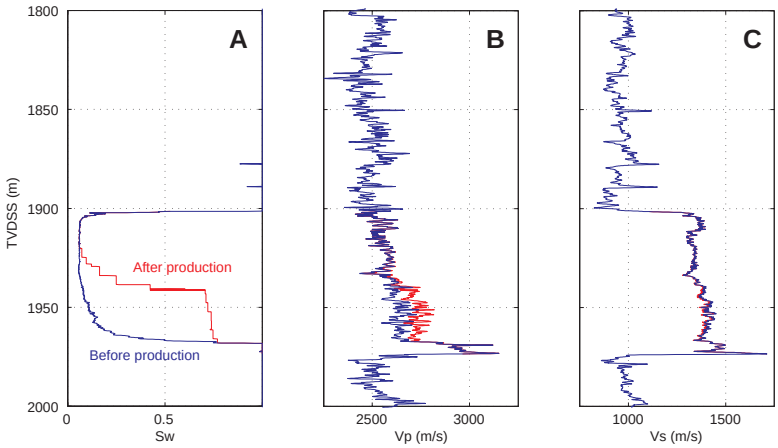

Figure 7.19: Water-saturation profile at well 1 before and after oil production (A), extracted from the eclipse output in Figure 7.18. P- and S-wave velocities before and after the production are shown in B and C. The velocities after oil production is estimated by Gassmann's modeling using the water-saturation profiles in A.

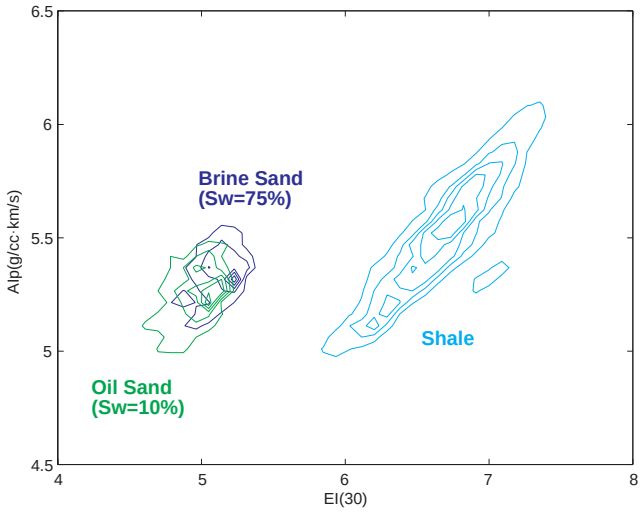

Figure 7.20: The bivariate pdf of the P-wave acoustic impedance and the elastic impedance for the reservoir condition after production. The three bivariate pdfs are for oil sand, brine sand (Sw = 25%), and shale.

and the oil pdf overlap each other and their discrimination is difficult.

We use the corrected velocity and density logs for calibration in seismic inversion performed in sections 7.4.2 and 7.4.3. Figure 7.21 is the correlation between the corrected well log and seismic section at well 1. The reflection at the top of the reservoir is not clear, although we can identify the positive and nearly flat reflector corresponding to the oil-water contact at around 2,010 ms.

7.4.2 P-P Data Inversion

Using the fluid-corrected well data to build a initial model, we conduct seismic inversion to derive seismic impedance profiles. We use only one well (well 1) for the calibration, where V_p, V_s, and density logs are available. A commercial software by Hampson Russell is used for the inversion. We create an initial impedance model from the well data—a horizontally layered model—and update the model using only seismic data as a constraint. A sparse spike inversion algorithm is used for the inversion, which tends to produce impedance models which are blocky along the vertical direction.

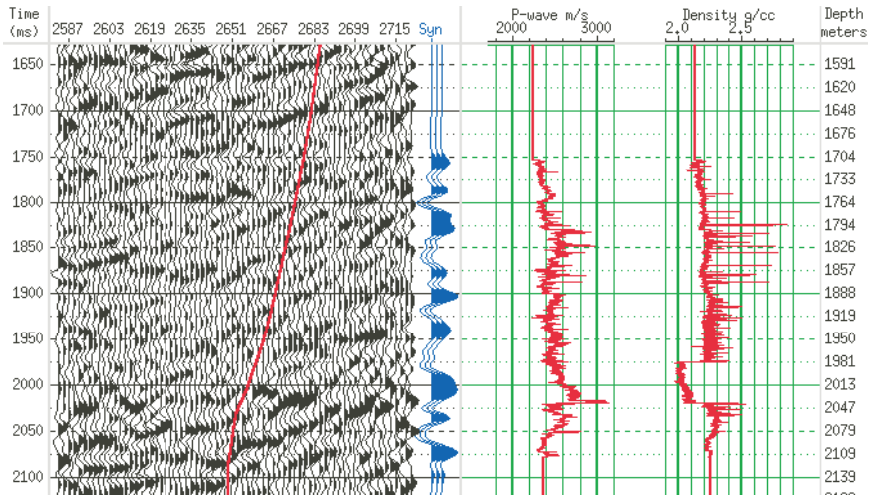

Figure 7.21: Well log and seismic correlation at well 1. V_p and density profiles on the right are for the condition after oil production, borrowed from Figure 7.19. Synthetic seismic trace in the middle produced from the V_p and density log are compared to the near-offset stack seismic data on the left. The curve shown in the seismic data is the deviated well trajectory of well 1.

Figure 7.22 shows an example of estimated acoustic impedance along section A, corresponding to the near-stack seismic section in Figure 7.15. Similar to the seismic section

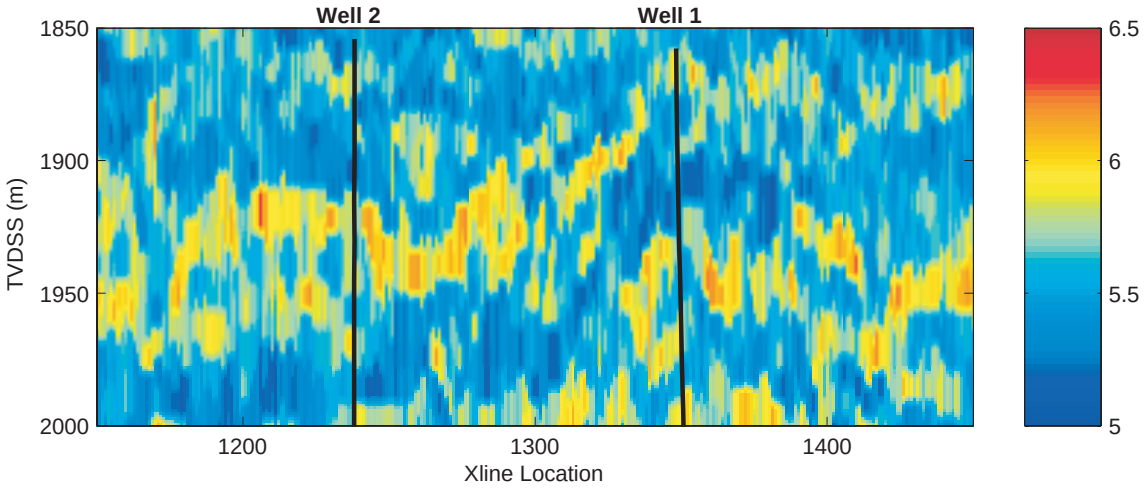

Figure 7.22: The acoustic impedance at section A, derived from the near-offset stack seismic section in Figure 7.15

in Figure 7.15, the impedance section does not show clear images of the sand bodies, because of the low impedance contrast between the shale and sands, as shown in Figure 7.20. However, dispersed low-impedance patches indicate sandy facies around the two wells, 1 and 5.

We derive the pseudo-density—defined in Equation B.8—at well 1, invert the far-offset stack seismic data, and estimate the elastic impedance profile, following the same procedure as the near-offset stack. An example of the elastic impedance profile at section A, corresponding to the seismic section in Figure 7.16, is shown in Figure 7.23. The low elas-

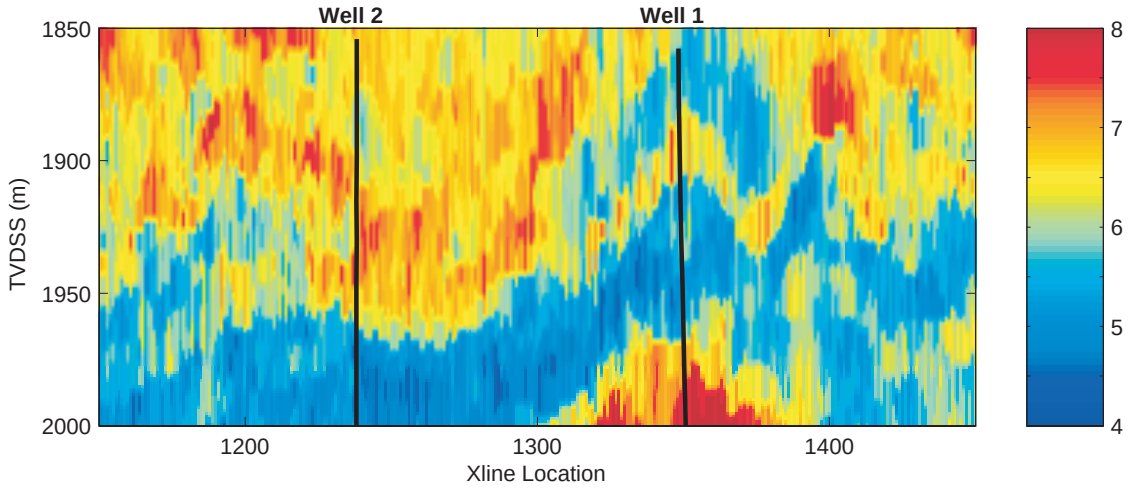

Figure 7.23: The elastic impedance profile at section A, derived from the far-offset stack section in Figure 7.16

tic impedance layer around a depth of 1,950 m in Figure 7.23 corresponds to sandy facies. However, the low-impedance zone is much more laterally continuous than the expected sandstone (Newton and Flanagan, 1993).

Figure 7.24 is a comparison of the well-log-derived and seismic-derived impedances close to the well location. In the well log profile in Figure 7.24-A, the top of the Alba reservoir at a depth of 1,900 m—a boundary between the overlying shale and the oil sand—is characterized by a significant decrease in the elastic impedance and a small decrease in the acoustic impedance. Both the acoustic and elastic impedances slightly increase at the

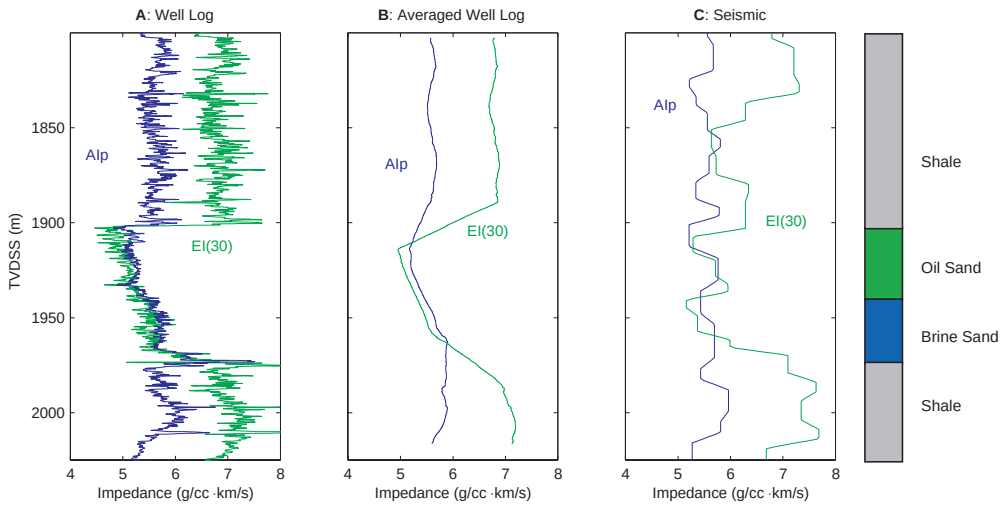

Figure 7.24: A comparison of the well-log-derived and seismic-derived impedances at well 1. **A** shows the acoustic impedance (blue) and the elastic impedance (green) plotted against the true vertical depth. Two curves in **B** are derived by taking the vertical moving averages of **A**. A time window approximately equal to a quarter of the seismic wavelength (30 m) is used for the averaging. **C** shows the acoustic and elastic impedances derived from near-offset and far-offset P-P partial stacks, respectively.

OWC. At the bottom of the reservoir, the greater cementation rate and higher water saturation make a spiky anomaly in the acoustic impedance. In addition, the elastic impedance gradually changes from the lower values of the sandy facies to the higher values of the underlying shale. Figure 7.24-B shows vertically averaged impedance curves derived from Figure 7.24-A. A 30 m wide moving window is used for averaging, which almost corresponds to the seismic resolution—a quarter of the dominant seismic wavelength. Since the Alba reservoir is thicker than the seismic resolution, the averaged well-log impedances capture major characteristics observed in the well-log impedances in Figure 7.24-A: significant decrease in the elastic impedance within the reservoir zone, small drop at the top of the reservoir and slight increase at the OWC in the acoustic impedance. The impedances derived from seismic inversions in Figure 7.24-C mimic the averaged well impedances in Figure 7.24-B. The blocky shapes of the seismic impedances are due to the algorithm used for the inversion.

Figure 7.25 is a cross-plot of the acoustic impedance and elastic impedance of the entire section A, shown in Figures 7.22 and 7.23. The bivariate pdfs, borrowed from Figure 7.20 and corresponding to error-free measurements, are overlain on the scatter data. The impedances from seismic inversion are much more widely distributed than the three

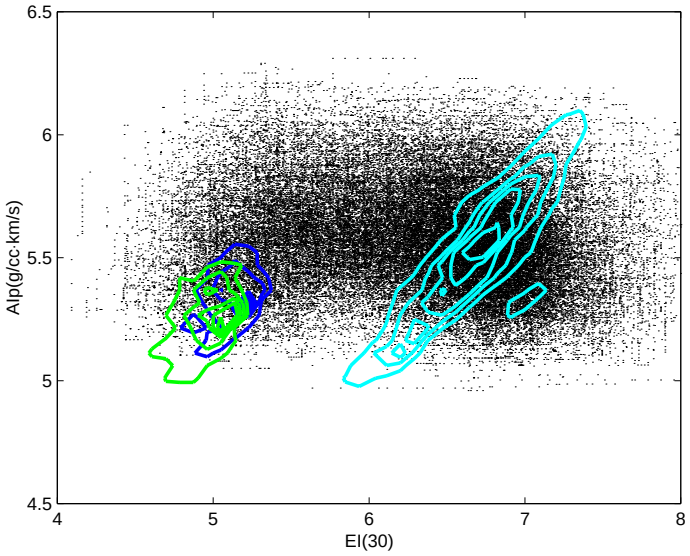

Figure 7.25: $AI_p - EI(30)$ cross-plot of the entire section A. The bivariate pdfs for oil sand, brine sand, and shale, borrowed from Figure 7.20 are overlain on the scattered data.

pdfs derived from well data. We assume that the discrepancy between the pdfs and the scattered data is due to measurement, processing, and inversion errors of the impedances derived from seismic data. The major causes of the errors include imperfect data quality, insufficient well control, and poor correlation between the well and seismic data due to the weak reflection from the reservoir. As discussed in section 4.3.1, the errors in deriving seismic attributes can be approximated by applying smoothing filters to the pdfs of error-free conditions.

We estimate the error function such that the smoothed pdfs covers most of the scattered data of section A. Figure 7.26 shows the estimated pdfs for oil sand, brine sand, and shale, corresponding to seismically observed impedances. Table 7.3 summarizes the statistics of facies prediction using the P-P impedances from seismic data.

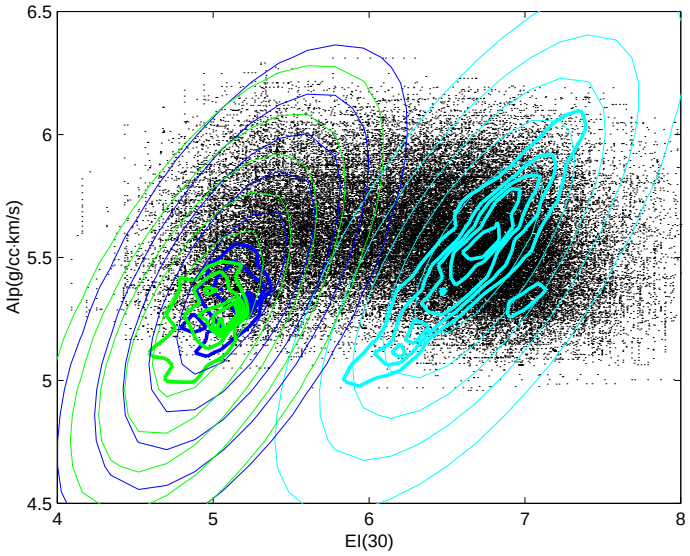

Figure 7.26: Estimated bivariate pdfs representing seismically observed acoustic and elastic impedances (thin outer contours). Scatter impedance data of section A, derived from seismic inversion, and bivariate pdfs for error-free measurements, derived from well data, are overlain.

Attribute	Success Rate	Mutual Inf.	Normalized Inf.
AI_p & $EI(30)$	0.83	0.22	0.34

Table 7.3: Information about facies provided by P-P near and far offset seismic impedances derived from seismic data.

7.4.3 P-S Data Inversion

We follow the similar procedure as the P-P data and invert the P-S far-offset partial stack. We derive the P-S pseudo-impedance at well 1, using the robust approximation as shown in Equation B.15. We use the impedance derived at well 1 only to build an initial model and update the impedance model using only P-S seismic data as the constraint. Figure 7.27 shows the P-S pseudo-impedance profile at section A. Even though the initial impedance model is horizontally layered, the estimated impedance section in Figure 7.27 includes discontinuous low-impedance anomalies. Figure 7.28 shows a comparison between the impedances derived from well 1 and from seismic data. In Figure 7.28, the P-S

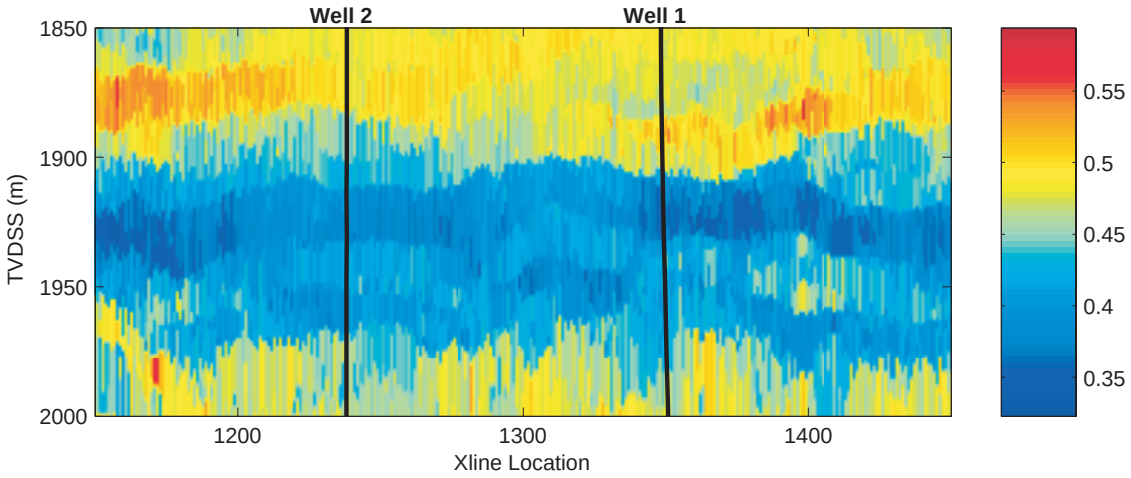

Figure 7.27: The P-S pseudo-impedance at section A, derived from the far-offset stack section in Figure 7.17

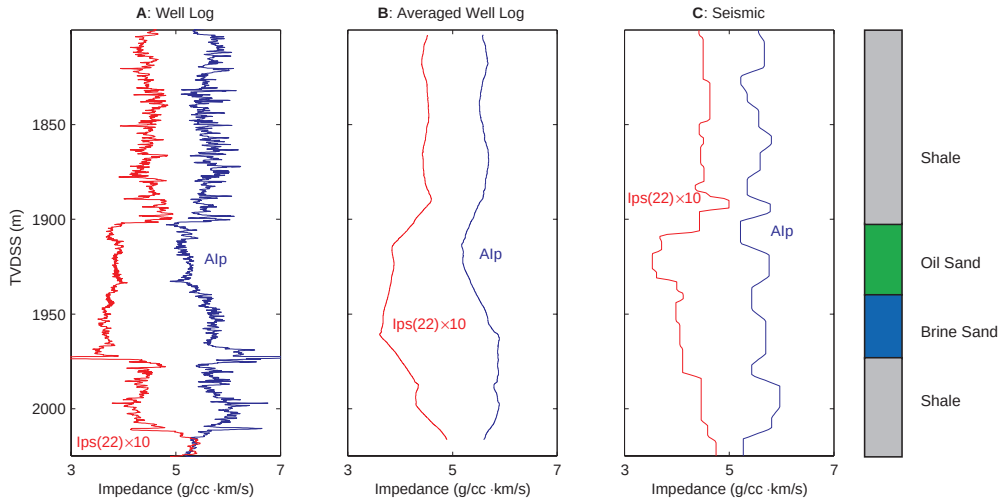

Figure 7.28: A comparison of the well-log-derived and seismic-derived impedances at well 1. **A** shows the acoustic impedance (blue) and the P-S pseudo-impedance (red) plotted against the true vertical depth. The two curves in **B** are derived by taking vertical moving averages of **A**. A time window equal to a quarter of the seismic wavelength (30 m) is used for the averaging. **C** shows the acoustic and P-S pseudo-impedances derived from P-P near-offset and P-S far offset partial stacks, respectively. The acoustic impedance curves in **A**-**C** are the same as in Figure 7.24.

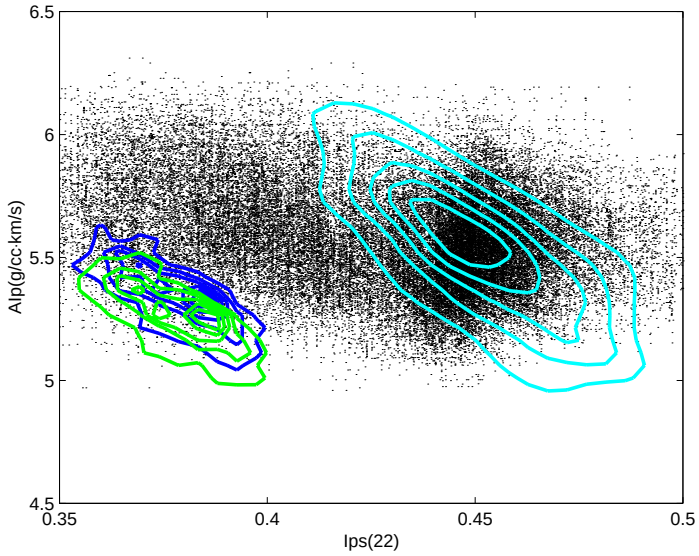

Figure 7.29: $AI_p - I_{ps}(22)$ cross-plot of the entire section A. The bivariate pdfs for oil sand, brine sand, and shale are overlain on the scattered data.

pseudo-impedance decreases at the top of the reservoir—from the overlying shale to the oil sand. The impedance, again, slightly decrease at the OWC, before it jumps up at the bottom of the reservoir. The seismically derived impedance clearly captures the characteristics at the top of the reservoir, although the small change of the impedance at the OWC is not seen.

Figure 7.29 is a cross-plot of the acoustic impedance and the P-S pseudo-impedance for the entire section A, derived from Figures 7.22 and 7.27. The distribution of the scattered points relative to the pdfs in Figure 7.29 is more limited than in the case of $AI_p - EI(30)$ in Figure 7.25. In the same way as Figure 7.26, we estimate pdfs representing seismically derived impedances such that the pdfs contain most of the scattered data of section A. Table 7.4 summarizes statistics of facies prediction, derived from the pdfs in Figure 7.30.

Attribute	Success Rate	Mutual Inf.	Normalized Inf.
AI_p & $EI(30)$	0.88	0.39	0.61

Table 7.4: Information about facies provided by P-P near-offset and P-S seismic impedances derived from seismic data.

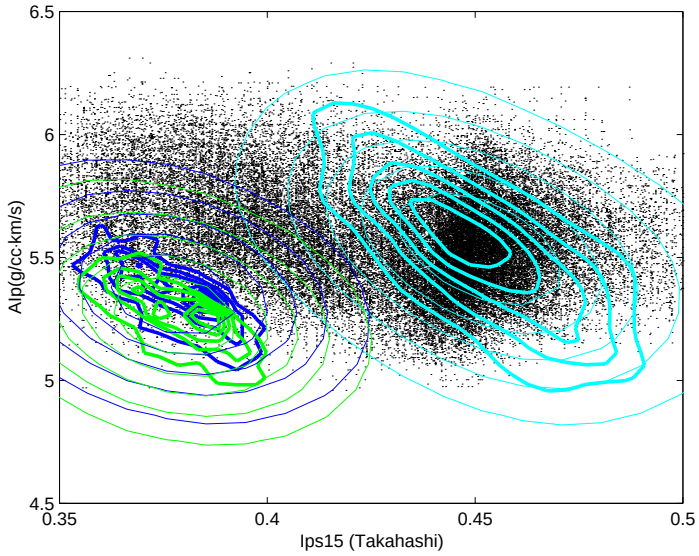

Figure 7.30: Estimated bivariate pdfs representing seismically observed acoustic and P-S pseudo- impedances (thin outer contours). Scatter impedance data of section A, derived from seismic inversion, and bivariate pdfs for error-free measurements, derived from well data, are overlain.

A comparison between Tables 7.3 and 7.4 shows that the combination of AI_p and I_{ps} allows better prediction than the combination of AI_p and EI, when the impedances are derived from seismic data. Since the facies separability of the two impedance combinations are almost equal in error-free conditions as shown in Figures 7.12 and 7.14, as well as in Tables 7.1 and 7.2, the different ability of facies prediction is due to more erroneous estimation of the P-P far-offset impedance than the P-S pseudo-impedance. P-wave propagation is more influenced by by fluids in the overlying layers than S-wave, and is more likely to be attenuated (Cadoret, 1993; Mavko et al., 1998). The fluid effects may degrade the quality of the P-P data more than the P-S data.

7.4.4 Facies and Fluid Prediction Using P-P and P-S Impedances

We use the established pdfs of seismic impedances for the estimation of lithology and pore fluids. In this study, we use few geological constraints for the facies prediction other than the seismic impedances and well log data from well 1, such that we can make a fair

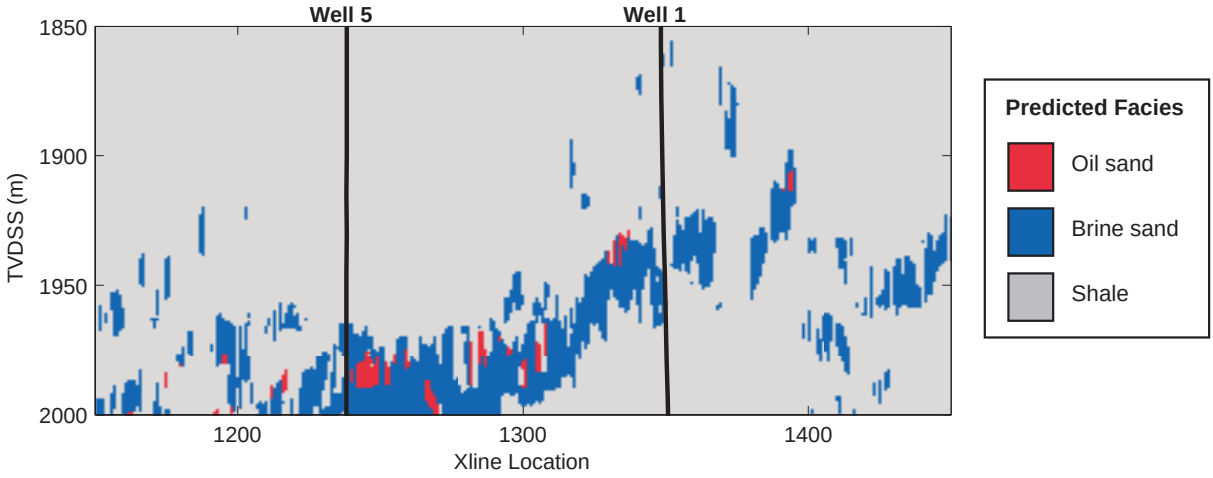

Figure 7.31: Lithology and pore fluids at section A, predicted by a combination of the acoustic and elastic impedances.

comparison between the P-P impedances and the P-S pseudo-impedance.

We first use the two impedances available from P-P surveys—the acoustic and elastic impedances—for the facies prediction. From the non-parametric pdfs of $AI_p - EI(30)$ for the oil sand, brine sand, and shale, as shown in Figure 7.26, we define the Bayes criteria for facies prediction. Based on the well-log data, we assume the prior probabilities for oil sand, brine sand, and shale to be 0.1, 0.1, and 0.8, respectively. We select the facies giving the maximum posterior probabilities—probabilities after observing the seismic impedances—as most likely. From the impedance profiles in Figures 7.22 and 7.23 and the established Bayes criteria, we predict lithology and pore fluids at section A, as shown in Figure 7.31. Following the same procedure, we also predict lithology and facies using a combination of the acoustic impedance and the P-S pseudo-impedance, as shown in Figure 7.32. In Figures 7.31 and 7.32, the distributions of the sandy facies are controlled by the elastic impedance and the P-S pseudo-impedance, respectively, rather than the acoustic impedance. On the other hand, pore fluids within the sandstone are mainly determined by the acoustic impedance.

Figure 7.33 compares the predicted facies from seismic impedances and the actual observations at wells 1 and 5. Well 1 was drilled into the northern part of the main Alba

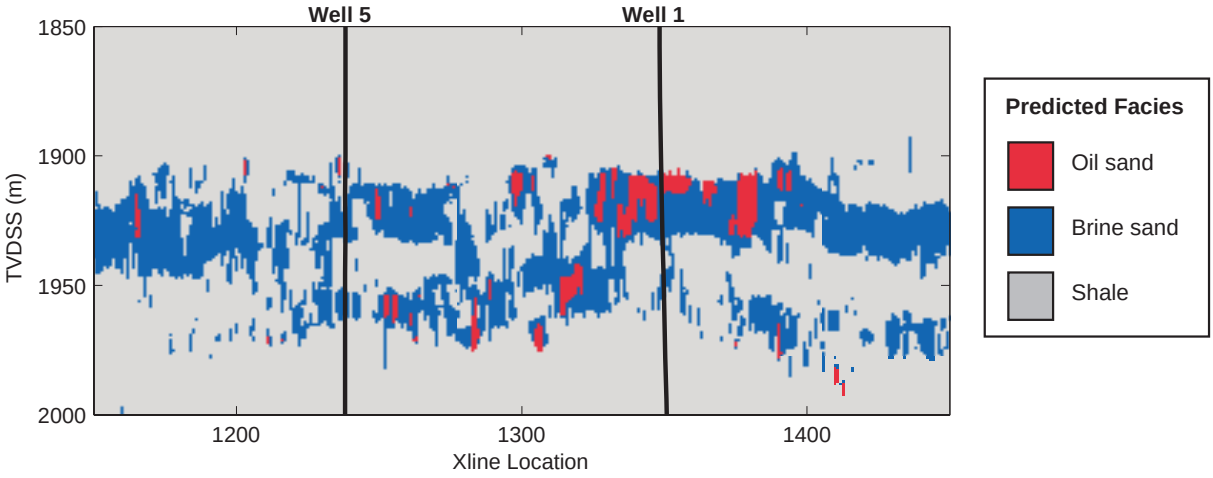

Figure 7.32: Lithology and pore fluids at section A, predicted by a combination of the acoustic impedance and the P-S pseudo-impedance.

channel, where a 70 m-thick massive sandstone was discovered and 40 m of oil column is expected at the time of the seismic data acquisition (Figure 7.19). Well 5 encountered several thin brine sand layers which are not connected to the main Alba channel (Newton and Flanagan, 1993). Since we used only the data from well 1 for building initial models in seismic inversion, the comparisons of the prediction and the observation at well 5 can be considered as blind tests.

Prediction results from the $AI_p - I_{ps}(22)$ combination in Figure 7.32 are more consistent with the well observations than the results from the $AI_p - EI(30)$ combination. A relatively thick oil sand on top of a brine sand is predicted around well 1, and several thin brine sand layers are identified at well 5. Figure 7.32 realizes the discontinuity between the main Alba channel (around well 1) and the isolated sand body at well 5. However, the predicted sands are more widely distributed along the lateral direction than is expected (Mattingly and Bretthauer, 1992), possibly due to the strong footprint of the horizontally layered initial impedance model in the seismic inversion, as well as the general lack of the horizontal resolution in surface seismic surveys. On the other hand, the $AI_p - EI(30)$ combination poorly predicts the lithology and pore fluids, as shown in Figure 7.31. The comparison between the predicted facies to well data and other geological information exhibits that the

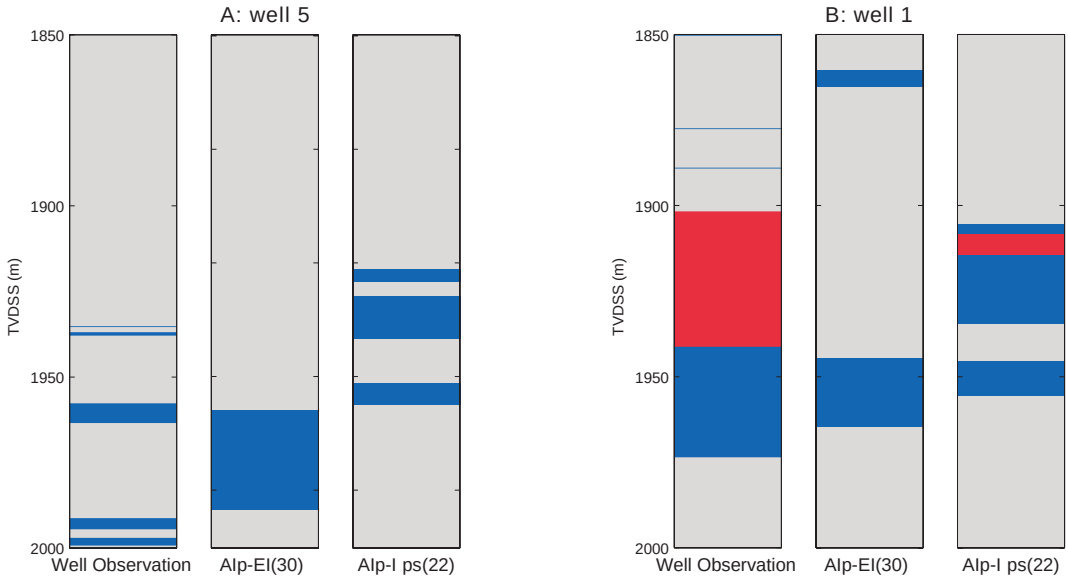

Figure 7.33: Comparisons of predicted facies from seismic impedances and actual observations at wells 5 and 1. Refer to Figure 7.31 for the legend.

combination of the P-P near-offset and P-S pseudo-impedances predicts lithology and pore fluids better than the combination of the P-P near and far offset impedances.

Although this result shows effectiveness of combining P-S data and P-P data, even better prediction can be possible by including additional information. Pre-stack depth migration of both P-P and P-S data will allow us to correlate different impedance sections better and reduce uncertainty caused by the mis-match between different data. The reservoir shape can become more geologically reasonable by adding the geological knowledge about the sedimentary facies and environment. Although the predicted pore fluids in Figures 7.31 and 7.32 include unreasonable distributions—brine sands over oil sands, these will vanish by using the information about the spatial order of individual facies (Eberle, 1998).

7.5 Conclusions

In this chapter, we explored P-S and P-P seismic data and well data of the Alba Oil Field and investigated how the P-S converted data help us to predict lithology and pore fluids. The results from rock physics diagnostic analysis showed the V_p-porosity relation of the Alba sandstone is well described by a constant pore stiffness curve, hence the porosity variation within the sand is controlled by the textural difference. The water-saturated sands show greater V_p and smaller porosity than the oil-saturated sands. These differences are explained by different cement fractions in the cementation model, and support a hypothesis that oil emplacements into sandstones slow down cementation.

By using statistical measures of information discussed in chapters 4 and 5, we investigated the dependence of the seismic impedances—P-P near and far offset and P-S impedances—on the lithology and pore fluids. We showed that the P-P near offset impedance is not very informative about lithology discrimination in the Alba Field. In contrast, the P-S pseudo-impedance and P-P far offset impedance are good lithology predictors. Our results showed that if perfectly error-free measurements are available, a combination of the P-P near and far offset impedances ($AI_p - EI$) predicts lithology and pore fluids as well as a combination of the P-P near offset impedance and the P-S pseudo-impedance ($AI_p - I_{ps}$).

Having performed seismic inversion for the P-P and P-S seismic data, we compared the well-derived impedances and seismically derived impedances, and established pdfs of impedances for the oil sand, brine sand, and shale. We defined Bayes decision criteria from the pdfs and predicted lithology and pore fluids from the $AI_p - EI$ combination, as well as from the $AI_p - I_{ps}$ combination. The prediction result from the $AI_p - I_{ps}$ combination is more consistent with a blind well and other geological information than the $AI_p - EI$ combination, which confirms the effectiveness of P-S converted shear data in the Alba Field.

Bibliography

Aki, K., and Richards, P., 1980, Quantitative seismology: Theory and methods: W.H. Freeman and Co., San Francisco.

Anselmetti, F., and Eberli, G., 1997, Sonic velocity in carbonate sediments and rocks *in* Palaz, I., and Marfurt, K., Eds., Carbonate Seismology: Soc. Expl. Geophys., 53–74.

Ash, R., 1965, Information theory: Dover Publications Inc., New York.

Avseth, P., Mavko, G., Dvorkin, J., and Rykkje, J., 1998a, The effect of sorting on the rock physics properties of sands: Stanford Rock Physics and Borehole Geophysics Project, **68**.

——— 1998b, Statistical discrimination of lithofacies from pre-stack seismic data constrained by well log rock physics: Application to a North Sea turbidite system: 68th Ann. Internat. Mtg., Soc. Expl. Geophys., Expanded Abstracts, 890–893.

Avseth, P., Dvorkin, J., Mavko, G., and Rykkje, J., 2000, Rock physics diagnostics of North Sea sands: Link between microstructure and seismic properties: Geophys. Res. Lett., in prep.

Avseth, P., 2000, Combining rock physics and sedimentology for seismic reservoir characterization in North Sea turbidite systems: Ph.D. thesis, Stanford University.

Bachrach, R., 1998, High resolution shallow seismic subsurface characterization: Ph.D. thesis, Stanford University.

Berryman, J., 1980, Long-wavelength propagation in composite elastic media: J. Acoustic Soc. Am., **68**, 1809–1831.

Berryman, J., 1992, Single-scattering approximations for coefficients in Biot's equations for poroelasticity: J. Acoustic Soc. Am., **91**, 551–571.

Berryman, J., 1995, Mixture theories for rock properties: Rock Physics and Phase Relations: A Handbook of Physics Constants, 205–228.

Berryman, J., 1999, Estimating rock porosity and fluid saturation using only seismic velocities: Stanford Exploration Project, **102**, 143–157.

Biot, M., 1956, Theory of propagation of elastic waves in a fluid saturated porous solid. I. Low frequency range and II. Higher-frequency range: J. Acoust. Soc. Am., **28**, 168–191.

Blair, D., 1996, Estimates of seismic attenuation using vibrational resonance and pulse transmission in four blocks of rock: Geophys. J. Int., **126**, 135–146.

Blangy, J., 1992, Integrated seismic lithologic interpretation: The petrophysical basis: Ph.D. thesis, Stanford University.

Bourbié, T., Coussy, O., and Zinszner, B., 1987, Acoustics of porous media: Gulf Publishing Co.

Box, G., and Tiao, G., 1992, Bayesian inference in statistical analysis: John Wiley and Sons, Inc., New York.

Bracewell, R., 1921, Fourier transform and its applications: McGraw Hill Co., Boston.

Brevik, I., 1995, Chalk data: Presented at workshop on effective media, Karlsruhe.

Brown, A., 1996, Seismic attributes and their classification: The Leading Edge, **10**, no. 15, 1090.

Cadoret, T., 1993, Effect de la saturation eau/gaz sur les propriétés acoustiques des roches: Ph.D. thesis, University of Paris.

Castagna, J., Batzle, M., and Eastwood, R., 1985, Relationships between compressional-wave and shear-wave velocities in clastic silicate rocks: Geophysics, **50**, 571–581.

Castagna, J., Batzle, M. L., and Kan, T. K., 1993, Rock physics – The link between rock properties and AVO response, *in* Castagna, J., and Backus, M., Eds., Offset-Dependent Reflectivity: Soc. Expl. Geophys., Investigations in Geophysics, 135–171.

Chen, Q., and Sidney, S., 1997, Seismic attribute technology for reservoir forecasting and monitoring: The Leading Edge, **16**, no. 5, 445–456.

Claerbout, J., 1993, Basic earth imaging: http://sepwww.stanford.edu/sep/prof.

Claerbout, J., 1999, Everything depends on $v(x, y, z)$: Stanford Exploration Project, **100**.

Cover, T., and Thomas, J., 1991, Elements of information theory: John Wiley and Sons, Inc., New York.

Deutsch, C., and Journél, A., 1998, GSLIB: Geostatistical software library and user's manual: Oxford University Press, New York.

Dilay, A., and Eastwood, J., 1995, Spectral analysis applied to seismic monitoring of thermal recovery: The Leading Edge, **14**, no. 11, 1117–1122.

Domenico, S., 1976, Effect of brine-gas mixture on velocity in an unconsolidated sand reservoir: Geophysics, **41**, 882–894.

Duda, R., and Hart, P., 1973, Pattern classification and scene analysis: John Wiley and Sons, Inc., New York.

Dvorkin, J., and Nur, A., 1996, Elasticity of high-porosity sandstone: Theory for two North Sea datasets: Geophysics, **61**, 1363–1370.

Eberle, N., 1998, Imposing sequence polarity on facies modeling: Stanford Center for Reservoir Forecasting, , no. 11.

Feynman, R., Leighton, R., and Sands, M., 1963, The Feynman lectures on physics: Wesley, Reading, MA.

Fink, M., 1999, Time-reversed acoustics: Sci. Amer., **281**, no. 5, 91–97.

Fukunaga, K., 1972, Introduction to statistical pattern recognition: Academic Press.

Gassmann, F., 1951, Über die elastizität poroser medien: Vier. der Natur. Gesellschaft, **96**, 1–23.

Gastaldi, C., Roy, D., Doyen, P., and Boer, L., 1998, Using Bayesian simulations to predict reservoir thickness under tuning conditions: The Leading Edge, **17**, no. 4.

Geertsma, J., 1961, Velocity-log interpretation: The effect of rock bulk compressibility: Soc. Pet. Eng. J., **1**, 235–248.

Goodway, B., Chen, T., and Downton, J., 1999, Rock parameterization and AVO fluid detection using Lamé petrophysical factors - λ, μ and $\lambda\rho$, $\mu\rho$: 61st Ann. Internat. Mtg., Europ. Assoc. Geocsi. Eng., Expanded Abstracts, 6–51.

Goovaerts, P., 1997, Geostatistics for natural resources evaluation: Oxford University Press, New York.

Gouveia, W., Moraes, F., and Scales, J., 1996, Entropy, information and inference: Project Review, Center for Wave Phenomena, Colorado School of Mines, **203**, 267–286.

Gouveia, W., 1996, Bayesian seismic waveform data inversion: Parameter estimation and uncertainty analysis: Ph.D. thesis, Colorado School of Mines.

Han, D.-H., 1986, Effects of porosity and clay content on acoustic properties of sandstones and unconsolidated sediments: Ph.D. thesis, Stanford University.

Hashin, Z., and Shtrikman, S., 1963, A variational approach to the elastic behavior of multiphase materials: J. Mech. Phys. Solids, **11**, 127–140.

Hilterman, F., 1989, Is AVO the seismic signature of lithology?: 59th Ann. Internat. Mtg., Soc. Expl. Geophys., Expanded Abstracts, 559.

Hilterman, F., Ed., 1998, Rock property framework for comprehending deep-water seismic response, proceedings GSH, 1998 spring aa symposium, 14^{th} Ann. SEG Gulf Coast Tech. Mtg. Soc. Expl. Geophys.

Houck, R., 1999, Estimating uncertainty in interpreting seismic indicators: The Leading Edge, **18**, no. 3, 320–325.

Jizba, D., 1991, Mechanical and acoustic properties of sandstones and shales: Ph.D. thesis, Stanford University.

Johnstad, S., and Dvorkin, J., 1999, Velocity-porosity trends in well log data: 69th Ann. Internat. Mtg., Soc. Expl. Geophys., Expanded Abstracts.

Kalkomey, C., 1997, Potential risks when using seismic attributes as predictors of reservoir properties: The Leading Edge, **16**, no. 3, 247–251.

Kennet, B., 1974, Reflections, rays and reverberations: Bull. Seismol. Soc. Am., **64**, 1685–1696.

Kennet, B., 1983, Seismic wave propagation in stratified media: Cambridge University Press, Cambridge.

Lewis, C., 1997, Seismic attributes for reservoir monitoring: A feasibility study using forward modeling: The Leading Edge, **16**, no. 5, 459–469.

Lonergan, L., and Cartwright, J., 1999, Polygonal faults and their influence on deep-water sandstone reservoir geometries, Alba field, United Kingdom Central North Sea: Amer. Assoc. Petr. Geol. Bull., **83**, no. 3, 410–432.

Lörtzer, G., 1990, An integrated approach to lithological inversion: Ph.D. thesis, Delft University of Technology.

Lucet, N., 1989, Vitesse et attenuation des ondes élastiques soniques et ultrasoniques dans les roches sous pression de confident: Ph.D. thesis, University of Paris.

MacLeod, M., Hanson, R., Bell, C., and McHugo, S., 1999, The Alba field ocean bottom cable seismic survey:Impact on development: The Leading Edge, **18**, 1306–1312.

Marion, D., and Nur, A., 1991, Pore-filling material and its effect on velocity in rocks: Geophysics, **56**, 225–230.

Marion, D., Mukerji, T., and Mavko, G., 1994, Scale effects on velocity dispersion: From ray to effective medium theories in stratified media: Geophysics, **59**, no. 10, 1613–1619.

Marion, D., 1990, Acoustical, mechanical, and transport properties of sediments and granular materials: Ph.D. thesis, Stanford University.

Mattingly, G., and Bretthauer, H., 1992, The Alba field; a middle Eocene deep water channel system in the UK North Sea, *in* Halbouty, M., Ed., Giant Oil and Gas Fields of the Decade, 1978 to 1988: Amer. Assoc. Petr. Geol., AAPG Memoir, 54, 78–88.

Mavko, G., and Jizba, D., 1991, Estimating grain-scale fluid effects on velocity dispersion in rocks: Geophysics, **56**, 1940–1949.

Mavko, G., and Mukerji, T., 1995, Seismic pore space compressibility and Gassmann's relation: Geophysics, **60**, 1743–1749.

Mavko, G., and Mukerji, T., 1998, A rock physics strategy for quantifying uncertainty in common hydrocarbon indicators: Geophysics, **63**, 1997–2008.

Mavko, G., Mukerji, T., and Dvorkin, J., 1998, Rock physics handbook: Cambridge University Press, Boston.

Mavko, G., 1979, Seismic wave attenuation in rocks: J. Geophys. Res., **17**, no. 6, 1155–1164.

Mayeda, K., Koyanagi, S., Hoshiba, M., Aki, K., and Zeng, Y., 1992, A comparative study of scattering, intrinsic, and coda Q^{-1} for Hawaii, Long Valley, and Central California between 1.5 and 15.0 HZ: J. Geophys. Res., **97**, no. B5, 6643–6659.

Menke, W., and Dubendorff, B., 1985, Discriminating intrinsic and apparent attenuation in layered rock: Geophys. Res. Lett., **12**, no. 10, 721–724.

Middleton, D., 1960, An introduction to statistical communication theory: McGraw-Hill Book Company, Inc.

Mindlin, R., 1949, Compliance of elastic bodies in contact: J. Appl. Mech., **16**, 259–268.

Mukerji, T., Jørstad, A., Mavko, G., and Granli, J., 1998, Near and far offset impedance: Seismic attributes for identifying lithofacies and pore fluid: Geophys. Res. Lett., **25**, no. 24, 4557–4560.

Mukerji, T., , and Mavko, G., 1999, Far offset impedance attributes for converted waves: Stanford Rock Physics and Borehole Geophysics Project, **74**.

Mukerji, T., 1995, Waves and scales in heterogeneous rocks: Ph.D. thesis, Stanford University.

Murphy, W., 1982, Effects of microstructure and pore fluids on the acoustic properties of granular sedimentary materials: Ph.D. thesis, Stanford University.

Newton, S., and Flanagan, K., 1993, The Alba field: evolution of the depositional model, *in* Parker, J., Ed., Petroleum Geology of Northwest Europe: Procfeedings of the 4^{th} Conference: Geological Society, 161–171.

Nur, A., Marion, D., and Yin, H., 1991, Wave velocities in sediments *in* Hovem, J.M. et al., Ed., Shear Waves in Marine Sediments: Kluwer Academic Publishers.

Nur, A., Mavko, G., Dvorkin, J., and Gal, D., 1995, Critical porosity: the key to relating physical properties to porosity in rocks: 65th Ann. Internat. Mtg., Soc. Expl. Geophys., Expanded Abstracts, 878.

Nur, A., 1992, Critical porosity and the seismic velocities in rocks: EOS, Transactions American Geophysical Union, **73**, 43–66.

Omre, H., and Tjelmeland, H., 1997, Petroleum geostatistics, *in* Baafi, E., and Shofield, N., Eds., Geostatistics Wollongong '96: Kluwer Academic Publishers, 41–52.

Picket, G. R., 1963, Acoustic character logs and their applications in formation evaluation: J. Petr. Tech., **15**, 650–667.

Scales, J., and Snieder, R., 1997, To Bayes or not to Bayes?: Geophysics, **62**, no. 4, 1045–1046.

Scales, J., and Tenorio, L., 1998, Prior information and uncertainty in inverse problems: Project Review, Center for Wave Phenomena, Colorado School of Mines, **292P**, 1–31.

Shannon, C., 1948, A mathematical theory of communication: Bell Systems Technical Journal, **27**, 379–423, 623–656.

Silverman, B., 1986, Density estimation for statistics and data analysis: Chapman and Hall Ltd., New York.

Steinmetz, R., Ed., 1992, The business of petroleum exploration Amer. Assoc. Petr. Geol., Tulsa, OK.

Strandenes, S., 1991, Rock physics analysis of the Brent Group reservoir in the Oseberg field: Stanford Rockphysics and Borehole Geophysics Project, Special volume.

Surdam, R., Dunn, T., Heasler, H., Jiao, Z., MacGowan, D., and Yin, P., 1993, Porosity prediction in sandstone/shale systems: A report prepared for Japan National Oil Corporation.

Takahashi, I., Mukerji, T., and Mavko, G., 1999a, Effect of thin-layering on seismic reflectivity: Estimation of sand/shale ratio using stochastic simulation and Bayes' inversion: 69th Conference, Soc. Expl. Geophys., Expanded Abstracts.

——— 1999b, A strategy to select optimal seismic attributes for reservoir property estimation: Application of information theory: 69th Conference, Soc. Expl. Geophys., Expanded Abstracts.

——— 1999c, Vp-Vs relation of sandstones and carbonates and their implication about the pore structure: Fall Meeting, American Geophysical Union.

Tarantola, A., and Valette, B., 1982, Inverse problems = Quest for information: J. Geophys., **50**, 159–170.

Tarantola, A., 1987, Inverse problem theory: Methods for data fitting and model parameter estimation: Elsevier Science Publication, Amsterdam.

Tjelmeland, H., and Omre, H., 1997, A complex sand-shale facies model conditioned on observations from wells, seismics and production, *in* Baafi, E., and Shofield, N., Eds., Geostatistics Wollongong '96: Kluwer Academic Publishers, 634–643.

Urmos, J., and Wilkens, R., 1993, In situ velocities in pelagic carbonates: New insights from ocean drilling program leg 130, Ontong Java: J. Geophys. Res., **70**, 7903–7920.

Uzcategui, O., 1998, Accuracy of velocities estimated by prestack depth migration: 68th Ann. Internat. Mtg., Soc. Expl. Geophys., Expanded Abstracts, 1309–1312.

Walton, K., 1987, The effective elastic moduli of a random packing of spheres: J. Mech. Phys. Solids, **35**, 213–226.

Wang, Z., and Nur, A., 1992, Seismic and acoustic velocities in reservoir rocks, vol. 2, theoretical and model studies: number 10 in Geophysics Reprints Soc. Expl. Geophys., Tulsa, Oklahoma.

Watanabe, T., and Sassa, K., 1995, Velocity and amplitude of P-wave transmitted through fractured zones composed of multiple thin low-velocity layers: Int. J. Rock Mech. Min. Sci. & Geomech. Abstr., **32**, no. 4, 313–224.

Watanabe, T., Sassa, K., Yuzuru, A., and Munemaru, K., 1989, Effects of low velocity zone consisting of multiple thin layeres on a P wave: Butsuri Tansa, **42**, no. 2, 75–81.

Weber, J., and Van Geuns, L.C., 1990, Framework for constructing clastic reservoir simulation model: J. Petr. Tech., **42**, no. 10.

White, R., 1991, Properties of instantaneous seismic attributes: The Leading Edge, **10**, no. 7, 26–32.

Widess, M., 1973, How thin is a thin bed?: Geophysics, **38**, no. 6, 1176–1180.

Worden, R., Oxtoby, N., and Smalley, P., 1998, Can oil emplacement prevent quartz cementation in sandstones?: Petroleum Geoscience, **4**, no. 2, 129–137.

Yale, D., and Jamieson, W., 1994, Static and dynamic rock mechanical properties in the Hugoton and Panoma fields: Kansas Society of Petroleum Engineers, Paper 27939. (Presented at the Society of Petroleum Engineers Mid-Continent Gas Symposium, Amarillo, Texas).

Yilmaz, O., 1987, Seismic data processing: number 2 in Investigations in Geophysics Soc. Expl. Geophys., Tulsa.

Zimmerman, R., 1991, Compressibility of sandstones: Elsevier, New York.

Appendix A

Using Time-Reversed Acoustics to Discriminate Intrinsic Absorption from Scattering Attenuation

"All truths are easy to understand once they are discovered; the point is to discover them."

— Galileo Galilei

A.1 Introduction - Motivation

This appendix presents a new method of distinguishing two physical phenomena which give rise to amplitude decays in seismic wave propagation through rocks.

Waves propagating through the Earth are always subject to the amplitude attenuation. Two different physical phenomena which brings about attenuation almost always coexist: intrinsic absorption and elastic scattering. Intrinsic absorption is a transform of wave energy to thermal energy, which is composed of several physical phenomena, including pore fluid-related mechanisms of Biot global fluid flow (Biot, 1956), squirt local flow (Mavko and Jizba, 1991), heterogeneity of saturation (Cadoret, 1993), and many others (Mavko, 1979; Mavko et al., 1998; Bourbié et al., 1987). On the other hand, elastic scattering is a redistribution of wave energy due to heterogeneity of elastic properties of media, which causes apparent amplitude decays (Aki and Richards, 1980).

In spite of the differences in their mechanisms, both intrinsic absorption and scattering share similar phenomenological outcomes: each one has velocity dispersion at a characteristic frequency, when the amplitude decay is at a maximum (Mavko et al., 1998). The characteristic frequency of scattering attenuation depends on the scale of heterogeneity, while rock properties that influence characteristic frequency of the intrinsic absorption are various and depend on the mechanisms causing the attenuation. Since subsurface properties of the Earth have a wide range of heterogeneity from microscopic to macroscopic scale (Weber and Van Geuns, L.C., 1990), virtually all practical frequencies of waves are subject to elastic scattering. Therefore, if a rock is absorptive, both effects are likely to coexist.

However, separation of the two effects, if possible, will enable us to extract more information about subsurface rock properties, since the individual mechanism is relatively well understood. For example, the intrinsic attenuation coefficient brings about information on fluid-related properties (*e.g.*, permeability and porosity) and scattering attenuation factor is related to the scale of subsurface heterogeneity. There have been many attempts to differentiate intrinsic absorption from scattering. By assuming proportionality between compressional and shear attenuation coefficients, as well as constant Poisson's ratio, Menke and Dubendorff (1985) numerically separated attenuation for scattering and intrinsic absorption. Blair (1996) estimated the two attenuation coefficients from his acoustic velocity measurements using vibrational resonance and pulse transmission, under assumptions of constant and non-constant-Q models, as well as a simple functional form for the scattering coefficient. Furthermore, from the coda energy decay of telesismic data, Mayeda et al. (1992) evaluated intrinsic and scattering attenuation using Monte Carlo simulations. Although these works successfully separated intrinsic and scattering attenuation, most of them have to do with simplification of physical phenomena and are valid for specific models, hence not general.

In contrast, the method proposed in this work focuses on the inherent difference between the two effects: Intrinsic absorption transforms wave energy to heat, while scattering redistributes wave energy. Therefore, the method is general and it does not require specific model for absorption nor scattering.

In this appendix, we first describe the basic concept of *time-reversed acoustics*. We then

present the experimental procedure of the proposed method and the derivation of the absorption and scattering quality factors. After verifying the method through seismic forward modeling, we summarize advantages of the method compared to conventional approaches and discuss simplification of the method. Finally, we conclude with a discussion about problems in its implementation.

A.2 Time Reverse Acoustics

The key concept of separating intrinsic and scattering attenuation is what is called *time-reversed acoustics*. Fink (1999) presented a concise summary of the technique. Figure A.1 explains basic idea of the method.

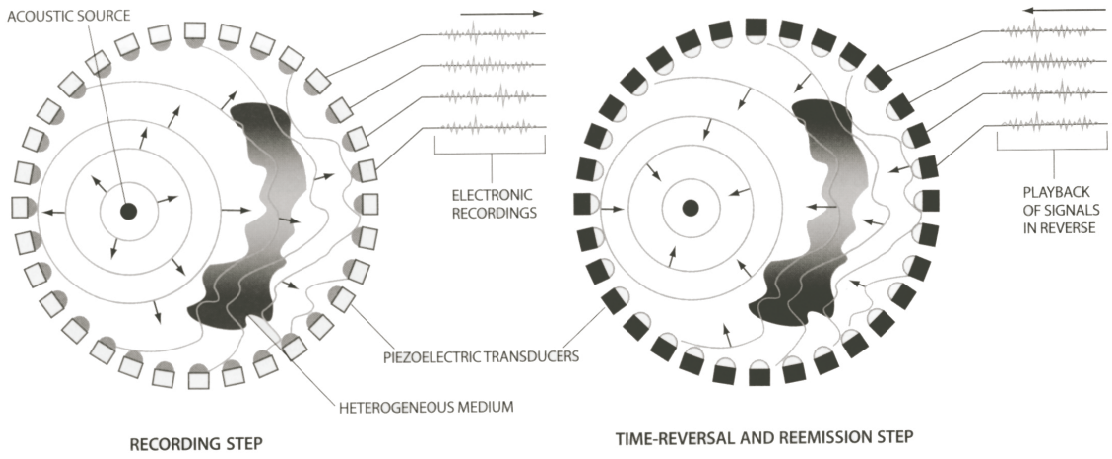

Figure A.1: Schematic picture of *time-reversed acoustics*. Forward propagation experiment (Step 1) in the left and the backward propagation experiment (Step 2) in the right. (From Fink (1999))

Time-reversed acoustics consists of two experiments. In Step 1 shown on the left of Figure A.1, a wave pulse is emitted from a point source, and the waves transmitted though a medium are recorded at the surrounding receivers. When the medium is heterogeneous, the waveforms may be deformed. Then the recorded waveform at each receiver is *flipped with respect to the time axis* and re-emitted to the medium, which is Step 2 shown on the

right of Figure A.1. The wave fronts converge towards the original source point as shown by inward arrows and *reproduce the original input wave form* which was emitted in Step 1. Fink implemented this concept in laboratory measurements, in which he successfully recovered the input waveforms.

Time-reversed acoustics is an elegant consequence of *the reciprocity* of wave phenomena. In fact, the time-reversed acoustics, focusing wave energy by back propagation, is nothing but the fundamental of all the migration techniques in seismic data processing (Yilmaz, 1987; Claerbout, 1993). Other practical applications extend from the detection of submarines in the ocean to breaking up kidney stones by acoustic energy focusing in medical science.

A.3 Proposed Method

We apply time-reversed acoustics to one of the important problems in rock physics: the distinction of intrinsic absorption from elastic scattering. This method presupposes an ideal condition and a geometry of typical core measurements, as shown in Figure A.2. We assume wave propagation through cores is one-dimensional, that is, the wavelength is far greater than the core diameter.

A.3.1 Procedure

- Input a pulse wave ($\mathbf{W}$) from one side of a core (side 1) and record the transmitted wave ($\mathbf{T}$) at side 2, as well as the reflected wave ($\mathbf{R}$) at side 1.
- Time reverse the two waveforms, $\mathbf{T}$ and $\mathbf{R}$, to produce $Rev(\mathbf{T})$ and $Rev(\mathbf{R})$, where Rev denotes flipping data with respect to the time axis.
- Simultaneously input $Rev(\mathbf{T})$ and $Rev(\mathbf{R})$ from side 2 and side 1, respectively, and record the output waveform ($\mathbf{D}$) at side 1.
- Compare the peak amplitudes of $\mathbf{W}$ and $\mathbf{D}$.

In the ideal case when the sample is heterogeneous and perfectly elastic, the recorded waves ($\mathbf{T}$ and $\mathbf{R}$) are distorted and differ from the original input, $\mathbf{W}$. However, the retrieved

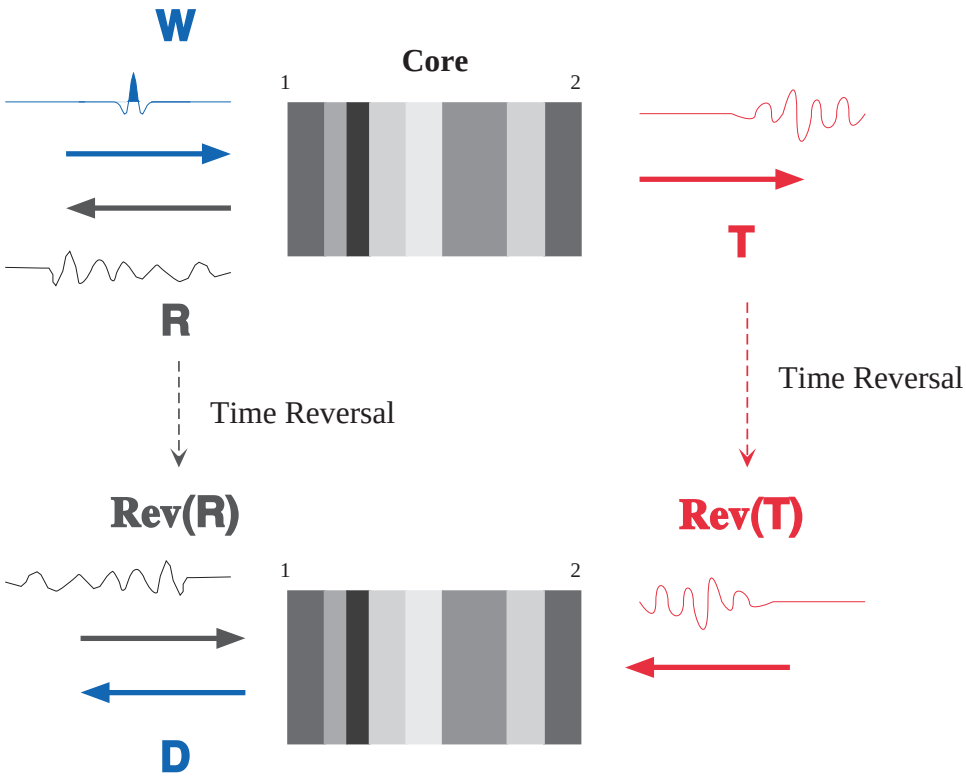

Figure A.2: Schematic picture of the proposed method.

waveform ($\mathbf{D}$) is exactly the same as the time-reversed version of the original input ($\mathbf{W}$), since the time reversal experiment focuses all the energy back. Hence, the peak amplitude of $\mathbf{D}$ is exactly the same as that of $\mathbf{W}$ in this case.

When a sample is both absorptive and heterogeneous, the amplitudes of recorded waves are decayed by the two phenomena. However, in the retrieved wave after time-reversal experiment, $\mathbf{D}$, all the scattered energy is focused back. Hence the difference in amplitude between $\mathbf{W}$ and $\mathbf{D}$ is only due to the intrinsic absorption. Therefore, we can compute intrinsic attenuation coefficient, α_i, as in section A.3.2.

A.3.2 Derivation of Attenuation Coefficients

The difference in the amplitudes of the retrieved wave and the input wave, $A_{\mathbf{D}}$ and $A_{\mathbf{W}}$, respectively, is only to the intrinsic absorption. Hence they are related by

$$A_{\mathbf{D}} = A_{\mathbf{W}} \exp[-\alpha_i(2d)] \tag{A.1}$$

where α_i is the intrinsic attenuation coefficient of the sample and d is the sample length. In Equation A.1, α_i is multiplied by $2d$, since the retrieved wave propagates through the core twice. Equation A.1 can be rewritten in terms of α_i as

$$\alpha_i = \frac{1}{2d} \ln \frac{A_{\mathbf{W}}}{A_{\mathbf{D}}} \tag{A.2}$$

Under an assumption that attenuation coefficients for intrinsic absorption and elastic scattering, α_i and α_s, respectively, are additive, *i.e.*, $\alpha_a = \alpha_i + \alpha_s$ (α_a represents apparent attenuation coefficient), we can describe the amplitude of the transmitted wave, $A_{\mathbf{T}}$, as

$$A_{\mathbf{T}} = A_{\mathbf{W}} \exp[-\alpha_a d] = A_{\mathbf{W}} \exp[-(\alpha_i + \alpha_s)d] \tag{A.3}$$

Given α_i from a time-reversed experiment, α_s can be derived from a comparison between the input wave amplitude and the transmitted amplitude as

$$\alpha_s = \alpha_a - \alpha_i = \frac{1}{d} \ln \frac{A_{\mathbf{W}}}{A_{\mathbf{T}}} - \alpha_i \tag{A.4}$$

Furthermore, from the apparent attenuation coefficient and the attenuation coefficients for intrinsic absorption and scattering, we can calculate the corresponding quality factors as

$$\frac{1}{Q_a} \approx \frac{\alpha_a V}{\pi f} \qquad \frac{1}{Q_i} \approx \frac{\alpha_i V}{\pi f} \qquad \frac{1}{Q_s} \approx \frac{\alpha_s V}{\pi f} \tag{A.5}$$

where f is the dominant frequency and V is the effective velocity of the sample.

A.4 Seismic Modeling

In this section, we show numerical examples of estimating the intrinsic and scattering quality factors using the proposed method.

A.4.1 Modeling Specifications

We simulate two wave propagations described in the procedure in section A.3.1, as well as depicted in Figure A.2: Step 1 consists of an input of the wavelet ($\mathbf{W}$) and recording of the reflection ($\mathbf{R}$) and the transmission ($\mathbf{T}$). Step 2 is after the time reversal manipulation and comprises simultaneous input of $Rev(\mathbf{R})$ and $Rev(\mathbf{T})$ and recording of $\mathbf{D}$.

For the following seismic modeling, we use the invariant imbedding method (Kennet, 1974; 1983) to realize complete wave propagation, including all orders of multiple reflections. Absorptive boundary conditions with no reflection are assumed on both sides. All of our core samples are 2.5 cm long, consisting of layers of either elastic or visco-elastic materials. The properties of the constituents are listed in Table A.1. As input waves, we use

Constituents	Velocity (km/s)	Density (g/cc)	Q^{-1} ($\times 10^{-3}$)	
c1	2.0	2.0	0	Elastic
c2	3.0	3.0	0	Elastic
c3	2.0	2.0	9.0	Visco-Elastic

Table A.1: Properties of materials consisting of the core models.

a Ricker wavelet with a center frequency of 500 KHz. Other specifications of the modeling are listed in Table A.2.

Core Length	2.5 cm
Input Wavelet	Zero phase Ricker
Center Frequency	500 KHz
Time Sampling Interval	80 ns
Record Length	2.62 ms

Table A.2: Forward modeling specifications.

A.4.2 Modeling Results

According to the procedure explained in section A.3.1, we conduct seismic forward modeling for three core models, estimate their quality factors, and compare them with true values.

Model 1: Heterogeneous and Elastic

First, we create a randomly layered elastic model, consisting of interbedded c1 and c2 in Table A.1, whose average layer thicknesses are 0.25 mm. In this model, the quality factor for intrinsic absorption (Q_i^{-1}) is 0. The resulting waveforms are shown in Figure A.3.

As mentioned, the input wave is a Ricker wavelet shown in Figure A.2-1), which is $\mathbf{W}$ in Figure A.2. The first experiment (Step 1) outputs the transmitted wave, 2), and reflected wave, 3). Since heterogeneity within the sample causes scattering attenuation, the amplitude of the transmitted wave is smaller than that of the input. From the comparison between 1) and 2), the apparent inverse quality factor of $\alpha_a = 9.6 \times 10^{-3}$ can be derived using Equation A.3. Then the transmitted and reflected waves are *flipped along the time axis* to make time-reversed waves in 4) and 5), before they are input back to the sample. Finally, the output, waveform $\mathbf{D}$ in Figure A.2, is recorded as 6). Comparison of 1) and 6) shows exact re-production of the input waveform by the backward propagation (Step 2), in spite of the chaotic input waves shown in 4) and 5). The peak amplitudes of 6) and 1) are identical, and Equation A.2 gives an estimate of Q_i^{-1} of 0.0, which is the true value. In addition, the difference between Q_a^{-1} and Q_i^{-1} gives a quality factor for scattering, $Q_s^{-1} = 14.6 \times 10^{-3}$.

Model 2: Homogeneous and Visco-Elastic

The second model is homogeneous and absorptive, consisting of the material c3 in Table A.1. In this mode, there is no scattering and the quality factor for intrinsic absorption is equal to that of c3, *i.e.*, $Q_i^{-1} = 9.0 \times 10^{-3}$. Six waveforms from the numerical modeling for Model 2 are shown in Figure A.4.

The transmitted wave in 2) has a similar shape with the the input, 1), since the medium is homogeneous and the intrinsic attenuation constant is relatively small. The ratio of the

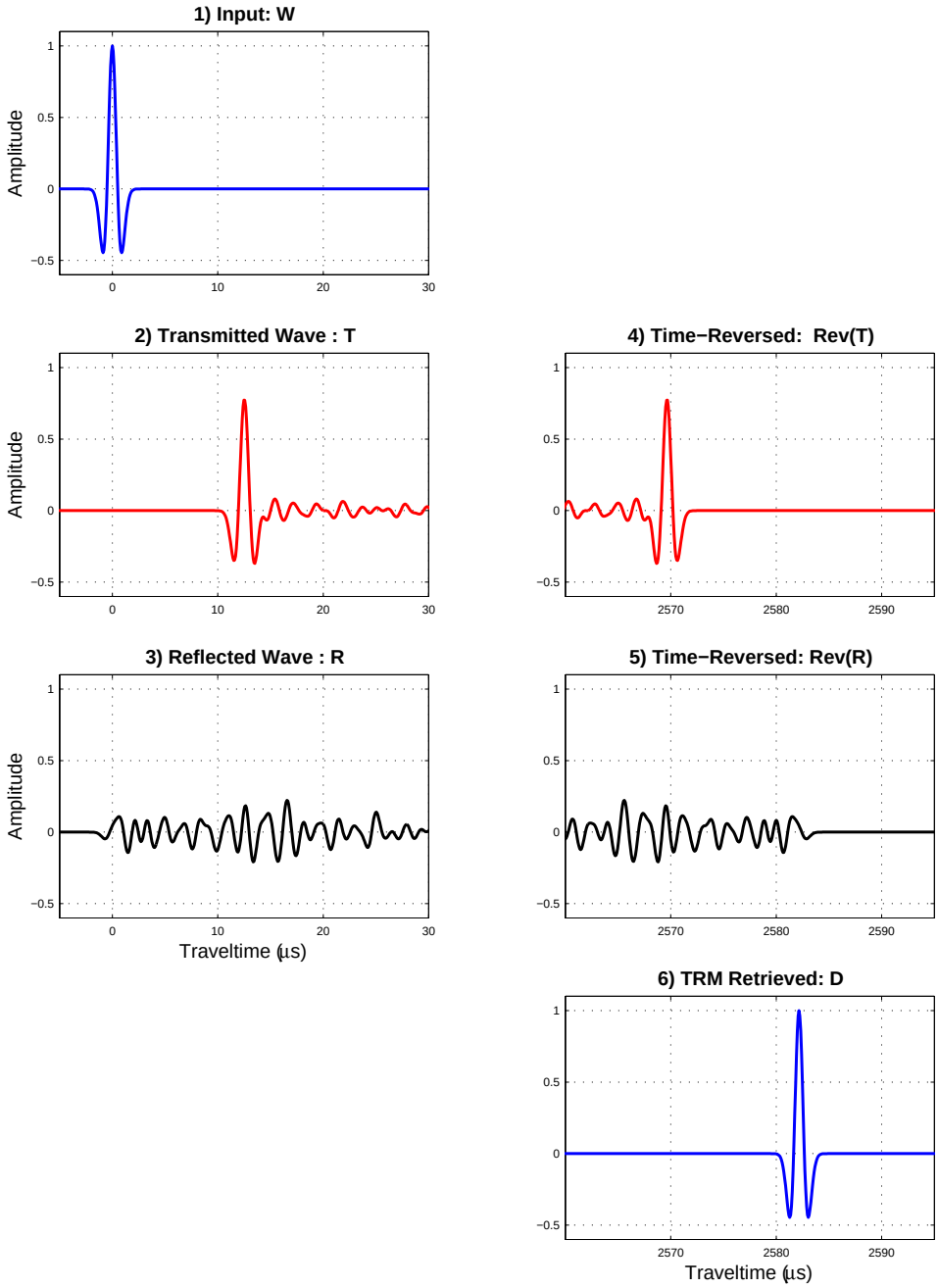

Figure A.3: Waveforms for Model 1: Heterogeneous and Elastic model.

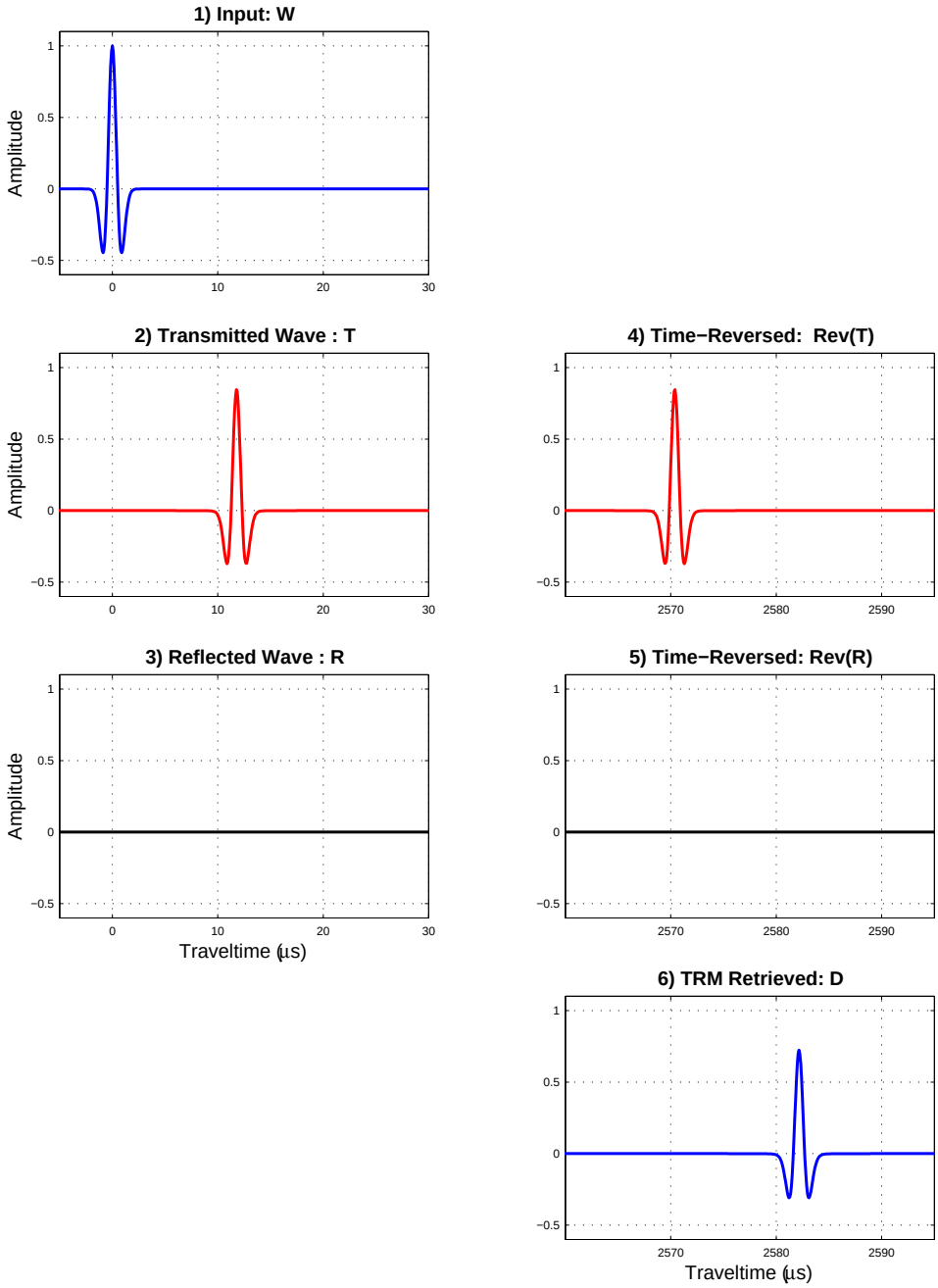

Figure A.4: Waveforms for Model 2: Homogeneous and Visco-Elastic model.

amplitudes in 1) and 2) gives an apparent inverse quality factor of $Q_a^{-1} = 9.5 \times 10^{-3}$. In 3), no reflected energy is recorded because of the homogeneity. Backward propagation after time reversal does not change the waveform significantly either, as shown in 6). Comparison of the input and the retrieved amplitudes predicts a Q_i^{-1} of 9.2×10^{-3}, and an estimate of the scattering quality factor, $Q_s^{-1} = 0.3 \times 10^{-3}$, near the true value.

Model 3: Heterogeneous and Visco-Elastic

The third model consists of layered elastic and visco-elastic materials, c1 and c3. Thicknesses of the individual layer are exactly identical to Model 1, *i.e.*, replacing layers of material c2 in Model 1 with c3 makes the Model 3. The true Q_i^{-1} of the model is 4.3×10^{-3}. Figure A.5 is the summary of the six simulated waveforms.

The transmitted wave in 2) is distorted and its amplitude is decayed. The apparent inverse quality factor (Q_a^{-1}) is 17.7×10^{-3}, which is much greater than the true intrinsic inverse quality factor because of scattering. The retrieved waveform after the time-reversed experiment is similar to the input wave, although noisy. From Equation A.2, the estimated inverse quality factor for intrinsic absorption (Q_i^{-1}) is 3.6×10^{-3}, which is near the true value. In addition, the difference between estimated Q_i^{-1} and Q_a^{-1} gives a Q_s^{-1} of 14.1×10^{-3}.

Summary of Modeling

Table A.3 summarizes the results of our seismic modeling. The apparent quality factor, which we observe in a conventional transmission measurement, does not allow the separation between intrinsic absorption and scattering. On the other hand, the proposed method using time-reversed acoustics correctly predicts the inverse quality factors in all of the three models. In addition, the estimated Q_s^{-1} for Models 1 and 3—models with the same velocity configurations but different quality factors—are almost equal. This result reveals that the scattering quality factor only depends on velocity structures and is independent of the intrinsic absorption.

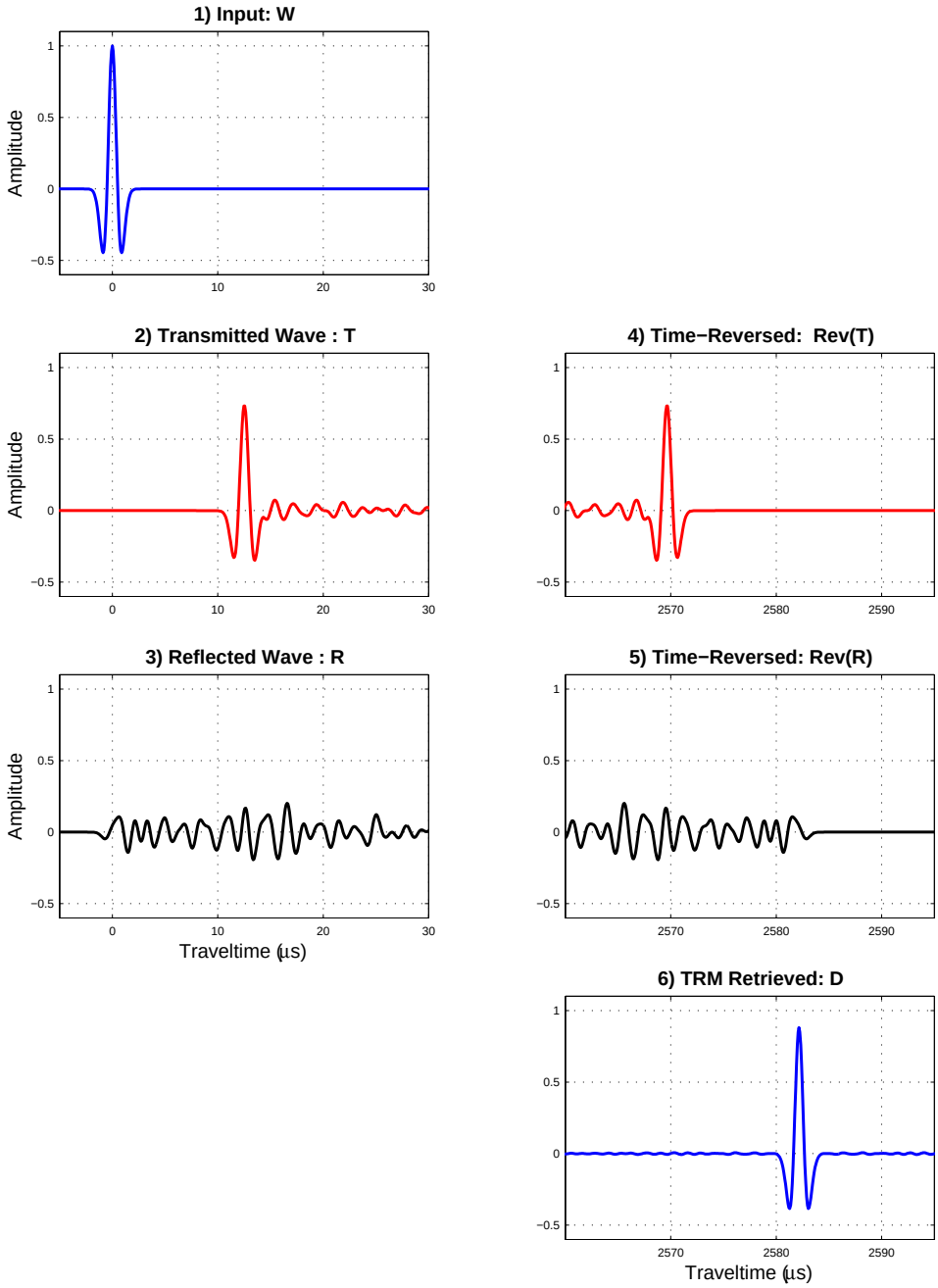

Figure A.5: Waveforms for Model 3: Heterogeneous and Visco-Elastic model.

Model		True Value		Apparent Value	TRM Estimate	
#	Property	Q_i^{-1}	Q_s^{-1}	Q_a^{-1}	Q_i^{-1}	Q_s^{-1}
1	Heterogeneous Elastic	**0**	-	14.6	**0.0**	14.6
2	Homogeneous Visco-Elastic	**9.0**	0	9.5	**9.2**	0.3
3	Heterogeneous Visco-Elastic	**4.3**	-	17.7	**3.6**	14.1
All values must be multiplied by 10^{-3}						

Table A.3: Estimated quality factors from forward modeling.

A.5 Discussions

This section discusses advantages and disadvantages of the proposed method, as well as further simplification of the method using deconvolution.

A.5.1 Advantages of the Proposed Method

The most profound advantage of the proposed method compared to conventional approaches is its generality. It is because the method takes advantage of the inherent difference of the two phenomena: intrinsic absorption is transform of wave energy to heat, hence *irreversible*, while scattering is redistribution of wave energy, hence *reversible*. Therefore, the proposed method does not require a specific model for intrinsic absorption nor a simple functional form for the scattering coefficient.

One possible alternative to the proposed method might be conducting only the forward propagation experiment (Step 1) and comparing the input wave energy and the output wave energy, the sum of the transmission and reflection. The difference between the input and the output corresponds to the energy dissipated by intrinsic absorption. However, strictly speaking, this method requires knowledge of seismic impedances at the two ends of the core in order to convert measured amplitudes to the wave energy. In contrast, the proposed method requires no conversion of wave amplitudes to energy, hence no knowledge of impedances.

Furthermore, the separation of absorption from scattering using energy comparison suffers much from random noise during experiments, since the noise energy of every time

sample may sum up and result in masking the genuine difference of the input and the output wave energy. On the other hand, the proposed method is less influenced by the random noise because the amplitude is picked only at the peak value, when the S/N ratio is the greatest.

A.5.2 Further Simplification

In this section we analytically describe the proposed method and look for simplification of the proposed procedure.

In Step 1 of the procedure, the input waveform ($\mathbf{W}$) and the outputs ($\mathbf{T}$ and $\mathbf{R}$) are related as

$$\mathbf{T}(\omega) = \mathbf{W}(\omega) \cdot \mathbf{I}_{12}(\omega) \tag{A.6}$$

$$\mathbf{R}(\omega) = \mathbf{W}(\omega) \cdot \mathbf{I}_{11}(\omega) \tag{A.7}$$

where $\mathbf{I}_{12}$ and $\mathbf{I}_{11}$ are impulse responses of the transmission (input at side 1 and record at side 2), and the reflection (input at side 1 and record at side 1), under the assumed conditions. (Waves are described in the frequency domain.)

In the frequency domain, the time reversal of a wave is realized by taking the complex conjugate as

$$Rev(\mathbf{T}(\omega)) = \mathbf{T}^*(\omega) \qquad Rev(\mathbf{R}(\omega)) = \mathbf{R}^*(\omega) \tag{A.8}$$

Using Equation A.8, we can describe Step 2 as

$$\mathbf{D}(\omega) = \mathbf{T}(\omega)^* \cdot \mathbf{I}_{21}(\omega) + \mathbf{R}(\omega)^* \cdot \mathbf{I}_{11}(\omega) \tag{A.9}$$

If the impedances at sides 1 and 2 are identical, the reciprocity states that

$$\mathbf{I}_{12} = \mathbf{I}_{21} \tag{A.10}$$

Hence, Equation A.9 can be rewritten as

$$\mathbf{D}(\omega) = \mathbf{T}(\omega)^* \cdot \mathbf{I}_{12}(\omega) + \mathbf{R}(\omega)^* \cdot \mathbf{I}_{11}(\omega) \tag{A.11}$$

Deconvolution allows us to retrieve impulse responses from the input and output waves in the ideal case (Yilmaz, 1987). From the outcome of Step 1, represented by Equation A.6 and A.7, $\mathbf{I}_{12}$ and $\mathbf{I}_{11}$ can be recovered as

$$\mathbf{I}_{12}(\omega) = \mathbf{W}(\omega)^{-1} \cdot \mathbf{T}(\omega) \tag{A.12}$$

$$\mathbf{I}_{11}(\omega) = \mathbf{W}(\omega)^{-1} \cdot \mathbf{R}(\omega) \tag{A.13}$$

Although the complete recovery of the impulse response is difficult in practice, the deconvolution allows us to skip Step 2, the time-reverse experiment; $\mathbf{D}$ is obtainable, since all terms on the right side of Equation A.11 can be given. Hence, only forward propagation experiment (Step 1) enables us to make the comparison between $\mathbf{D}$ and $\mathbf{W}$, and to estimate the intrinsic and scattering attenuation coefficients.

A.5.3 Problems in Practice

Section A.5.1 summarizes the advantages of the proposed method. However, there are several difficulties in implementing the method in the laboratory.

- Boundary conditions

  Although completely absorptive boundary conditions are assumed in the numerical modeling, there exists significant reflected energy at both sides of the core samples in real measurements. If wave energy once recorded by the transducer is reflected back into the sample, the energy will eventually return to the edge and will be recorded again. Multiple recording of the same wave energy makes amplitude comparison erroneous.

- Three-dimensional wave propagation

  If the wave propagation within a sample is three dimensional, *i.e.*, when the wavelength is far smaller than the core diameter, the phenomena becomes complicated.

Wave amplitudes are influenced by spherical divergence, in addition to the absorption and scattering decay. Moreover, wave propagation oblique to the sample axis, as well as reflections at the circumference, requires three-component receivers to recover the wavefield perfectly.

- Controlling source waveforms

  The input waveforms in Step 2 of the proposed procedure must be exactly identical to the time-reversed version of the recorded waves in Step 1, which are nearly arbitrary. Deficit reproduction of the waveforms results in incomplete retrieval of the final output. However, recent laboratory equipment may allow flexible waveform inputs to a required level.

These problems may or may not be significant to our objective, estimation of quality factors. The impacts of these effects on the estimation must be quantified through numerical modeling. Furthermore, the influences of these incomplete conditions may be relaxed by additional assumptions wave wave propagations. (Although the assumptions may cost the generality of the method, the deficit is not critical as long as they are for compensation of incomplete conditions.)

A.6 Conclusions

In this appendix, we proposed a method of discriminating the intrinsic absorption from the elastic scattering, applying *time-reversed acoustics*. In contrast to conventional approaches which have to involve simplifications of models for absorption and scattering, the proposed method focuses on the inherent difference between the two mechanisms, and is, consequently, very general. Our numerical modeling demonstrated correct predictions of true quality factors and verified the advantages of the method. The implementation of the proposed method will help us separate of the two effects and contribute to better understanding of wave attenuation phenomena in rocks.

Appendix B

Approximated Formulations of Seismic Attributes

This appendix presents the approximated forms of seismic attributes used in this thesis, including a new robust formulation of P-S pseudo-impedance derived in section B.

P-P Offset Reflectivity

For the calculation of offset reflectivity, the approximated form by Aki and Richards (1980) is used. P to P Reflectivity at an incidence angle of θ is given by

$$R_{pp}(\theta) = \frac{1}{2}\left(\frac{\Delta V_p}{\bar{V}_p} + \frac{\Delta \rho}{\bar{\rho}}\right) + \left[\frac{1}{2}\frac{\Delta V_p}{\bar{V}_p} - 2\frac{\bar{V}_s^{\,2}}{\bar{V}_p^{\,2}}\left(\frac{\Delta \rho}{\bar{\rho}} + 2\frac{\Delta V_s}{\bar{V}_s}\right)\right]\sin^2\theta + \frac{1}{2}\frac{\Delta V_p}{\bar{V}_p}\left[\tan^2\theta - \sin^2\theta\right] \tag{B.1}$$

where ΔV_p, ΔV_s, and $\Delta\rho$ are contrasts of, and $\bar{V_p}$, $\bar{V_s}$, and $\bar{\rho}$ are the averages of V_p, V_s, and density between the boundary as

$$\Delta V_p = V_{p2} - V_{p1} \qquad \Delta V_s = V_{s2} - V_{s1} \qquad \Delta\rho = \rho_2 - \rho_1 \tag{B.2}$$

$$\bar{V_p} = \frac{1}{2}(V_{p2} + V_{p1}) \qquad \bar{V_s} = \frac{1}{2}(V_{ps} + V_{ps}) \qquad \bar{\rho} = \frac{1}{2}(\rho_2 + \rho_1) \tag{B.3}$$

P-P AVO Gradient

Aki and Richards approximation in Equation B.1 leads to an AVO gradient, G, as

$$G = \frac{1}{2}\frac{\Delta V_p}{\bar{V_p}} - 2\frac{\bar{V_s}^2}{\bar{V_p}^2}(\frac{\Delta\rho}{\bar{\rho}} + 2\frac{\Delta V_s}{\bar{V_s}}) \tag{B.4}$$

Hilterman's approximation (1989) of AVO gradient, PR, is given by

$$PR = \frac{\Delta\nu}{(1-\bar{\nu})^2} \tag{B.5}$$

where $\Delta\nu$ and $\bar{\nu}$ are the contrast and the average of Poisson's ratio between the boundary as

$$\Delta\nu = \nu_2 - \nu_1 \qquad \bar{\nu} = \frac{1}{2}(\nu_2 + \nu_1) \tag{B.6}$$

P-P Offset Impedance (Elastic Impedance)

Elastic impedance is an analogue of acoustic impedance in non-zero offset case. In this thesis, the definition by Mukerji et al. (1998) based on the Aki and Richards approximation of reflectivity is used.

$$\begin{aligned} EI(\theta) &= \exp[2\int R(\theta)dt] \\ &= {V_p}^{1+\tan^2\theta}\rho^{1-4(V_s/V_p)^2\sin^2\theta}{V_s}^{-8(V_s/V_p)^2\sin^2\theta} \end{aligned} \tag{B.7}$$

where θ is the incident angle and $R(\theta)$ is the reflectivity at incident angle θ.

For practical inversion of P-P offset data to obtain the offset impedance, pseudo-density defined by Equation B.8 should be input into inversion software.

$$\rho(\theta) = V_p^{\tan^2\theta} \rho^{1-4(V_s/V_p)^2 \sin^2\theta} V_s^{-8(V_s/V_p)^2 \sin^2\theta} \tag{B.8}$$

P-S Pseudo-Impedance by Mukerji and Mavko

Similar to the P-P offset impedance (elastic impedance), Mukerji and Mavko (1999) derived an approximation of P-S converted wave offset impedance. The formulation by Mukerji and Mavko starts from the Aki and Richards approximation of P-S reflectivity (1980):

$$\begin{aligned} R_{ps} = &- \frac{\sin\theta_p}{2\cos\theta_s}\left[\left(1 - 2\frac{\bar{V_s}^2}{\bar{V_p}^2}\sin^2\theta_p + 2\frac{\bar{V_s}}{\bar{V_p}}\cos\theta_p\cos\theta_s\right)\frac{\Delta\rho}{\bar{\rho}}\right. \\ &\left. - \left(4\frac{\bar{V_s}^2}{\bar{V_p}^2}\sin^2\theta_p - 4\frac{\bar{V_s}}{\bar{V_p}}\cos\theta_p\cos\theta_s\right)\frac{\Delta V_s}{\bar{V_s}}\right] \end{aligned} \tag{B.9}$$

where θ_p and θ_s are P-wave incidence angle and S-wave reflection angle at the target boundary, respectively. These two angles are related by the Snell's law:

$$\sin\theta_p = \frac{\tilde{V_p}}{\tilde{V_s}}\sin\theta_s \tag{B.10}$$

where $\tilde{V_p}/\tilde{V_s}$ is the average V_p/V_s ratio above the target.

With an assumption

$$\frac{\bar{V_p}}{\bar{V_s}} = \frac{\tilde{V_p}}{\tilde{V_s}} \tag{B.11}$$

An integration of Equation B.9 leads the following approximated form of the P-S impedance:

$$I_{ps}(\theta_s) = \rho^a V_s^{\,b} \tag{B.12}$$

where θ_s is the angle of the reflected S-wave and a and b are given by

$$a = \frac{\tan\theta_s}{(V_s/V_p)}\left[2\sin^2\theta_s - 1 - 2\cos\theta_s\sqrt{(V_s/V_p)^2 - \sin^2\theta_s}\right] \tag{B.13}$$

$$b = \frac{4\tan\theta_s}{(V_s/V_p)}\left[\sin^2\theta_s - \cos\theta_s\sqrt{(V_s/V_p)^2 - \sin^2\theta_s}\right] \tag{B.14}$$

If the assumption in Equation B.11 is not valid, *i.e.*, when $\bar{V_p}/\bar{V_s}$ is large, or when θ_s is large, Equation B.12 can give unreasonable complex values.

Robust P-S Pseudo-Impedance

When the average V_p/V_s ratio of the overlying layers ($\tilde{V_p}/\tilde{V_s}$) is known, we can derive a more robust form of the P-S pseudo-impedance than Equations B.12 through B.14. From Equation B.9, we deduce another approximation of the pseudo-impedance in the same form as Equation B.12 as

$$I_{ps}(\theta_s, \theta_p) = \rho^a {V_s}^b \tag{B.15}$$

where

$$a = \frac{\sin\theta_p}{\cos\theta_s}\left(2\frac{V_s^2}{V_p^2}\sin^2\theta_p - 1 - 2\frac{V_s}{V_p}\cos\theta_p\cos\theta_s\right) \tag{B.16}$$

$$b = \frac{4\sin\theta_p}{\cos\theta_s}\left(\frac{V_s^2}{V_p^2}\sin^2\theta_p - \frac{V_s}{V_p}\cos\theta_p\cos\theta_s\right) \tag{B.17}$$

θ_s and θ_p must observe Equations B.10 for the given $\tilde{V_p}/\tilde{V_s}$. This formulation is more robust than Equations B.12 through B.14.